Montanuniversität

Dissertation

Steel laminates with highly improved fracture toughness

Dipl.-Ing. Roland Kasberger

Leoben, April 2018

Erich Schmid Institute of Materials Science
Austrian Academy of Sciences
Jahnstraße 12
A-8700 Leoben

Affidavit

I declare in lieu of oath,
that I wrote this thesis
and performed the associated research myself,
using only literature cited in this volume.

....
Roland Kasberger
Leoben, April 2018

Acknowledgements

The finalization of this thesis was made possible by the support of several people, who I want to thank in the following.

First and foremost, I sincerely thank my advisor, Prof. Otmar Kolednik of the Erich Schmid Institute of Materials Science, for the continuous support, numerous discussions and his contribution of valuable ideas and time.

I also sincerely thank Prof. Bruno Buchmayr for the productive time at the Chair of Metal Forming, which I could use to manufacture all the specimens, and for helpful discussions.

In addition, I want to thank all my colleagues at the Erich Schmid Institute, who always provided helpful input and debate, and especially Dr. Anton Hohenwarter and Peter Kutleša for support in the experiments. Working at the ESI was a rewarding and fun experience.

My student employee Andreas Palenik provided assistance in specimen preparation and testing, for which I am very thankful.

My colleague from MCL, Dr. Masoud Sistaninia, provided the finite element calculations and many helpful discussions. For that, and for a very enjoyable scientific conference on Rhodes, I am very grateful.

I thank the technical staff, Robin Neubauer, Franz Hubner and Silke Modritsch from ESI, as well as Ralph Ambrosch and Christian Stöckl from the Chair of Metal Forming for their help in the specimen preparation.

I also want to thank the voestalpine Stahl GmbH and especially Dr. Pichler and Dr. Hebesberger for providing material free of charge.

I am also very grateful for my friends, family and girlfriend, who always supported me throughout my studies.

Last but not least, financial support by the Austrian Federal Government and the Styrian Provincial Government within the research activities of the K2 Competence Center on “Integrated Research in Materials, Processing and Product Engineering”, under the frame of the Austrian COMET Competence Center Program, is gratefully acknowledged (strategic project A4.20-WP2).

Abstract

The aim of this thesis was to manufacture and test inhomogeneous steel-based laminates with a high resistance against fracture. These laminates exploit the material inhomogeneity effect as main toughening mechanism, which occurs independently to other toughening effects like delamination. This effect is caused by the presence of an inhomogeneity in Young's modulus or yield stress in front of a propagating crack. The basic mechanism is a strong reduction in the crack driving force, when the crack grows perpendicularly from a soft or compliant material into a stronger or stiffer material. This is also known as the shielding effect of the material inhomogeneity.

The hot press bonding process was used to manufacture steel-based multilayers with excellent interfacial strengths, using cold-working tool steels X210CrW12 or C45 as matrix and deep-drawing steel DC04 as soft interlayer(s). An empirical relation is given, which gives an estimate of the local thickness reduction and, therefore, the resulting composite geometry. Composites with varying number and thickness of the soft interlayer(s), as well as reference matrix specimen without interlayers were manufactured.

The improvement in fracture resistance caused by soft interlayer(s) was determined in fracture mechanics experiments. The reference specimens, which contained a single matrix/matrix interface each, fractured catastrophically after reaching a critical J-integral for the matrix, $J_{\mathrm{c}}^{\mathrm{M}}$. In specimen with one or more interlayers crack propagation initiated at $J_{\mathrm{c}}^{\mathrm{M}}$ as well, but the propagating crack arrested inside the interlayer. The load, measured in terms of the J-integral, had to be increased to cause final fracture at a critical J for the composite, $J_{\mathrm{c}}^{\mathrm{ML}}$. The ratio $J_{\mathrm{c}}^{\mathrm{ML}}/J_{\mathrm{c}}^{\mathrm{M}}$ is a measure of the effectiveness of the interlayer(s) as a crack arrester.

In X210CrW12/DC04 composites, the improvement is dependent on the interlayer thickness. For thin interlayers, $J_{\mathrm{c}}^{\mathrm{ML}}/J_{\mathrm{c}}^{\mathrm{M}}$ is in the order of 3-5, with thick interlayers the improvement is even higher. Numerical calculations are able to predict $J_{\mathrm{c}}^{\mathrm{ML}}/J_{\mathrm{c}}^{\mathrm{M}}$, when thermal residual stresses and the material inhomogeneity effect are taken into account.

In C45/DC04 composites, the arrested crack was rendered completely ineffective by the onset of debonding with further loading. The remaining specimen cross-section then behaves like tensile specimen and fails by reaching the plastic limit load. Compared to

X210CrW12/DC04 composites, the improvement J_c^{ML}/J_c^{M} is much higher and almost a factor 300.

The significant improvement of the fracture resistance by the material inhomogeneity effect was demonstrated in this thesis. An interesting feature observed in all fracture mechanics tests is the cleavage fracture mode of the DC04 interlayers. Cracks were successfully arrested despite the brittle fracture mode.

Kurzfassung

Das Ziel dieser Dissertation war die Herstellung und Erprobung inhomogener Schichtverbunde auf Stahlbasis, die einen hohen Bruchwiderstand aufweisen. Diese Laminate nützen den zähigkeitssteigernden Materialinhomogenitätseffekt aus. Dieser Effekt tritt unabhängig von anderen Mechanismen wie etwa Delamination auf und wird durch eine Inhomogenität von E-Modul und/oder Streckgrenze vor einem Riss hervorgerufen. Der grundlegende Effekt ist dabei die starke Abschwächung der risstreibenden Kraft, wenn der Riss von einem weicheren oder nachgiebigeren Material in Richtung eines festeren oder steiferen Materials wächst. Dies ist als der „shielding"-Effekt der Materialinhomogenität bekannt.

In dieser Dissertation wurde ein Schmiedeprozess verwendet, um mehrlagige Schichtverbundwerkstoffe auf Stahlbasis mit ausgezeichneter Interfacefestigkeit herzustellen. Dabei wurden die Kaltarbeitsstähle X210CrW12 und C45 als Matrixwerkstoffe, sowie der weiche Tiefziehstahl DC04 als Zwischenlagenwerkstoff verwendet. Eine empirische Formel wurde entwickelt, um die aus dem Schmiedeprozess resultierenden lokalen Umformgrade und damit die finale Verbundgeometrie abzuschätzen. Es wurden sowohl Verbundwerkstoffe mit variierender Anzahl und Dicke der Zwischenschichten, als auch Referenzproben aus Matrixmaterial hergestellt.

Die Verbesserung der Bruchzähigkeit durch den Einbau von weichen Schichten aus Tiefziehstahl wurde in Bruchmechanikversuchen ermittelt. Die Referenzproben, welche nur ein Matrix/Matrix Interface aufwiesen, brachen katastrophal beim Erreichen eines kritischen Wertes des J-Integrals für die Matrix, J_c^M. In Proben mit einer oder mehreren Zwischenlagen initiierte Risswachstum ebenfalls bei J_c^M, jedoch wurden die wachsenden Risse in diesen Zwischenlagen gestoppt. Um das Komplettversagen der Verbunde hervorzurufen, musste die Belastung auf einen kritischen Wert für den jeweiligen Verbundwerkstoff J_c^{ML} erhöht werden. Das Verhältnis J_c^{ML}/J_c^M ist ein Maß für die Effektivität der Zwischenlagen als Riss-Stopper.

In X210CrW12/DC04 Schichtverbunden ist dieses Verhältnis abhängig von der Dicke der Zwischenschicht. Bei dünnen Zwischenschichten ist J_c^{ML}/J_c^M in der Größenordnung 3-5, bei dickeren Zwischenschichten ist dieser Wert noch höher. Numerische Berechnungen

können J_c^{ML}/J_c^{M} prognostizieren, sofern der Materialinhomogenitätseffekt und thermische Eigenspannungen berücksichtigt werden.

In C45/DC04 Verbunden wurde der durch die Zwischenlage gestoppte Riss bei weiterer Belastung durch beginnende Delamination komplett wirkungslos. Der verbleibende Probenquerschnitt verhält sich dann wie eine Zugprobe und versagt erst durch Erreichen der plastischen Grenzlast. Im Vergleich zu X210CrW12/DC04 Schichtverbunden ist die Verbesserung J_c^{ML}/J_c^{M} viel größer und erreicht beinahe einen Faktor 300.

In dieser Arbeit wurde die signifikante Verbesserung der Bruchzähigkeit durch den Materialinhomogenitätseffekt demonstriert. Ein interessanter Aspekt der Bruchmechanikexperimente war der spaltflächige Bruch der Zwischenlagen. Trotz dieses spröden Bruchmodus wurden die laufenden Risse effektiv gestoppt.

Contents

1 Introduction

1.1 Motivation

The development of materials that excel in both strength and toughness is of considerable interest for a wide range of applications. The common approaches taken in materials science include changing alloy compositions, tailoring grain size and texture or exploiting second phase dispersions. In this thesis, a different, promising path is explored: Laminating.

The idea of laminating dissimilar materials to form composites is known since antiquity. (Wad2000). Compared to homogenous materials, laminating can dramatically improve many properties like fracture toughness, fatigue behavior or impact behavior (Wad2000). The improvements in damage resistance of laminates is typically explained with the effect of weak interfaces (Coo1964). The working principle of a delamination as toughening mechanism is easily understood: The delamination reduces the stress triaxiality by the generation of a new free surface ahead of the crack tip, Figure 1a. Furthermore, the crack tip blunts when the initial crack grows into the delaminated interface, Figure 1b. Usually, the crack then is arrested and a new crack has to nucleate in an adjacent layer.

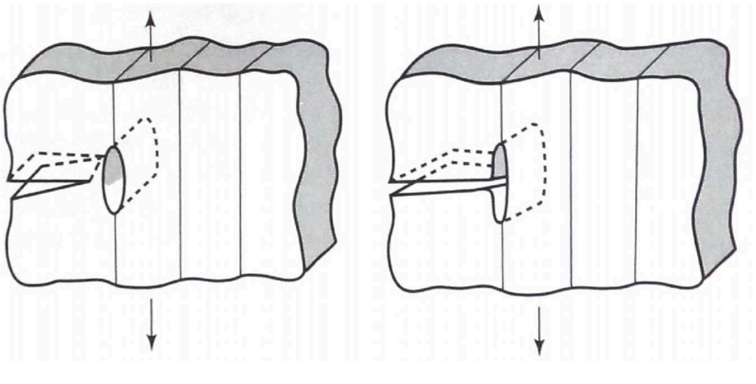

a) b)

Figure 1: Delamination at a weak interface in front of the crack tip a) reduces stress triaxiality and b) crack tip acuity (Her1996).

Embury et al. (Emb1967) soldered thin, mild steel plates and performed Charpy impact tests in crack arrester orientation, i.e. the crack grows perpendicularly to the interfaces. The dramatic improvement in toughness caused by delamination at the weak interfaces is depicted in Figure 2.

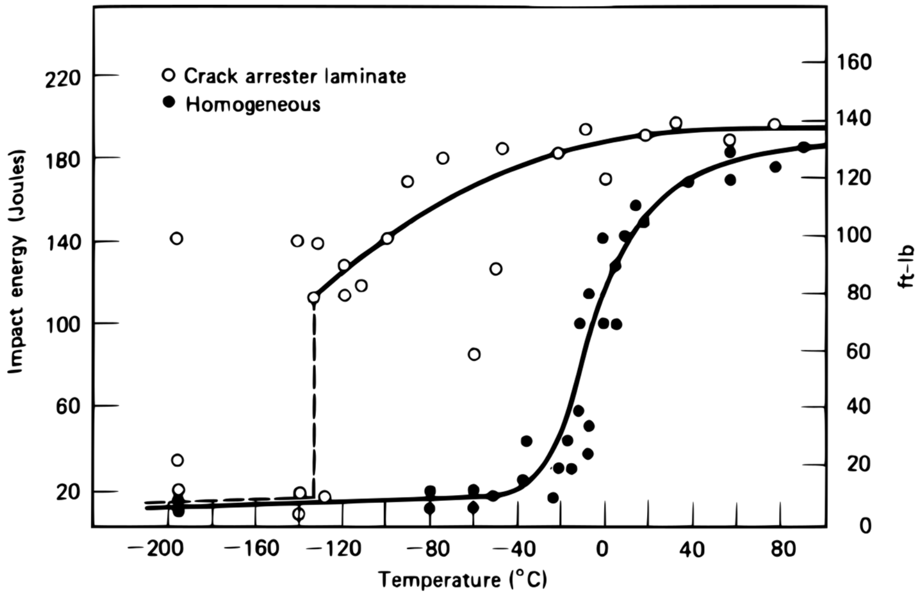

Figure 2: Comparison of Charpy impact energy of a homogeneous specimen with a mild steel laminate produced by soldering in crack arrester orientation (Emb1967).

Clegg and co-workers (Cle1990) also exploited the mechanism of crack deflection by weak interfaces, which they deliberately introduced in a ceramic material, to increase the apparent fracture toughness by more than a factor four compared to the monolithic material. Using weak interfaces to promote delamination has a disadvantage, however, as the strength of such composites perpendicular to the interfaces is strongly reduced.

While possibly predominant, a delamination is not the only relevant toughening mechanism. Various energy dissipating mechanisms occur in the process zone in front of a crack tip which increase the crack growth resistance, such as micro-cracking, plastic deformation or crack bridging. Bermejo and co-workers (Ber2006) exploited compressive residual stresses in Al_2O_3-ZrO_2 multilayers, introduced by the difference in thermal expansion coefficient, to improve the R-curve behavior of ceramic composites.

In laminates, there is an additional non-obvious mechanism, which provides a significant contribution to the damage tolerance. Laminates are heterogeneous materials, as the mechanical properties of the individual layers often strongly differ. Many researchers therefore studied the influence of such material inhomogeneities on the behavior of cracks. In the following, a concise overview is given. An extensive literature review can be found in (Sim2003).

Early papers treating the problem of *elastic* inhomogeneities perpendicular to the crack are e.g. the works of Zak and Williams (Zak1963), Erdogan and co-workers (Coo1972, Erd1973) and later Romeo and Ballarini (Rom1995). Summarizing the results, the stress intensity decreases when a crack lying in the elastically weaker material grows closer to the stiffer material. Directly at the interface, the local stress intensity approaches zero. Vice versa, the stress intensity increases when the crack approaches the interface to an elastically weaker material and reaches infinity at the interface. Experimental evidence for crack arrest due to Young's modulus inhomogeneities was found e.g. in adhesively bonded glass sandwiches (Lee2007, Par2014). After the crack arrest, final fracture occured by reinitiation of secondary cracks. (Mur2011) numerically studied crack propagation in the presence of a Young's modulus inhomogeneity using the phase field method. They observed a decrease in the crack driving force inside the interlayer, causing crack arrest when the driving force locally falls below a critical value. Further loading is required either to propagate the primary crack or to reinitiate a secondary crack in the matrix in front of the original crack tip.

The effect of plasticity in cracked bimaterials was taken into account e.g. by Shih (Shi1991), He et al., (He1992), Romeo and Ballarini (Rom1997) and Wang and Stähle (Wan2000). The effect of yield strength inhomogeneities was treated numerically in (Sug1995, Kim1997, Joy2003), where the authors showed that the near-tip J-integral, J_{tip}, which can be seen as the effective crack driving force, begins to deviate from the applied far-field value J_{far} when the plastic zone around the crack tip touches the interface. At a soft-hard transition $J_{\mathrm{tip}} < J_{\mathrm{far}}$, and at a hard-soft transition $J_{\mathrm{tip}} > J_{\mathrm{far}}$. Kolednik (Kol2000) derived analytical expressions based on global energy considerations, which quantify the effect of yield stress gradients on the crack driving force.

Using the concept of configurational forces, which will be introduced in a later chapter, a general description of the effects of material inhomogeneities was developed. A spatial variation of material properties in direction of the crack extension influences the crack driving force (Sim2003, Sim2005) and therefore affects the fracture toughness (Fra2007, Fis2007, Kol2010, Kol2011, Zec2013, Kol2014, Sis2014) or the fatigue crack growth rate (Kol2009, Kol2016). When a crack grows from a material with lower strength or stiffness into a material with higher strength or stiffness, the crack driving force decreases. This so-called shielding effect increases the apparent fracture toughness or reduces the crack growth rate. In the ideal case, the shielding effect can result in crack arrest. However, when a crack grows from a stronger (stiffer) into a weaker (more compliant) material, anti-shielding occurs and enhances the crack driving force. Accordingly, the anti-shielding effect reduces fracture toughness and increases fatigue crack growth rate compared to a homogenous material.

Sistaninia and Kolednik (Sis2014) studied the effect of single, soft interlayers on the crack driving force numerically using the configurational forces concept. Figure 3 shows a key result, which illustrates the aforementioned effects of an inhomogeneity. J_{tip}, which is the local crack driving force, varies with the distance L_1 of the crack tip to the first interface IF1 of the soft interlayer, as well as with the global loading parameter J_{far}. In contrast, for a homogeneous material J_{tip} would be constant, $J_{tip} = J_{far}$. Due to the presence of the hard-soft transition at IF1, the anti-shielding effect first causes an increase in J_{tip} close to IF1. When the crack tip is located within the interlayer, J_{tip} decreases due to the shielding effect exerted by the soft-hard transition at the second interface, IF2, until it reaches a minimum in the matrix just after IF2. The second interface is therefore a critical position for crack arrest, as at this point the crack driving force is at its lowest. The authors state that the optimum of the material inhomogeneity effect is reached when there is a factor 5 difference in yield stress between matrix and interlayer.

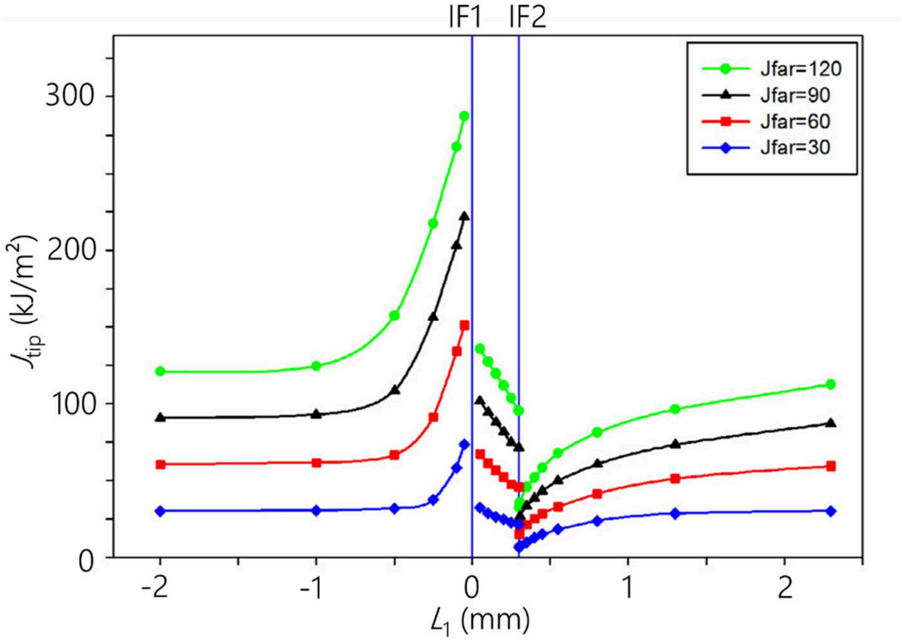

Figure 3: The crack driving force J_{tip} varies with the position of the crack tip respective to the first interface, L_1, and the loading parameter J_{far}. (Sis2014)

This so-called material inhomogeneity effect can be used to design fracture-resistant materials. Certain biological materials, such as the skeletons of deep see sponges (**Figure** 4a), serve as inspiration (Woe2006, Fra2007). The combination of high strength and stiffness with a high fracture toughness is made possible by the shielding effect of the thin, compliant protein layers (Kol2011).

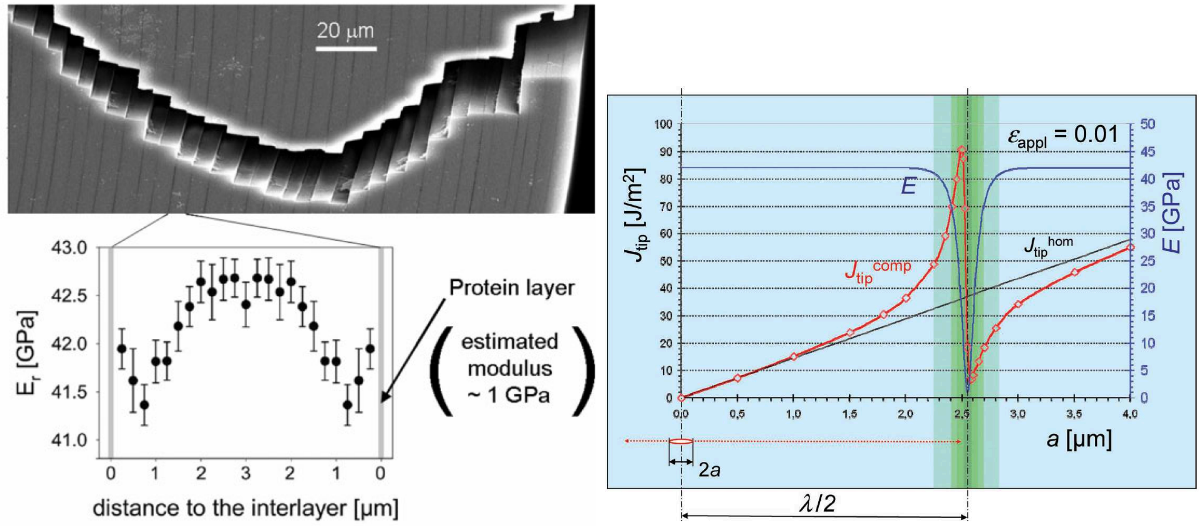

a) b)

Figure 4: a) Microstructure and variation of Young's Modulus in the deep-sea sponge *Monorhaphis chuni* (Woe2006, Fra2007). b) Variation of the crack driving force J_{tip}, when the crack approaches the protein layer indicated in green (Kol2011).

1.2 Aim and structure of the work

The main objective in this thesis is to produce and test damage resistant laminated metallic composites, which exploit the material inhomogeneity effect. Different production routes for such inhomogeneous materials are explored, and laminated metallic composites with sharp transitions in mechanical properties and excellent interfacial strengths are manufactured with a suitable process. To gain a better understanding of the material inhomogeneity effect, the number and thickness of the individual layers in the composites are varied. The improvement in damage tolerance due to material inhomogeneities is then studied with fracture mechanics experiments. The experimental findings are finally compared with numerical calculations using the configurational forces model, to gain a better understanding.

The thesis is structured as follows: Chapter 2 provides the reader with a basic theoretical background in fracture mechanics. Essential equations to determine J-Δa curves are mentioned in chapter 3, where the reader is also introduced to specifics regarding the application of the potential drop technique to determine crack lengths in laminated composites. Chapter 4 presents the configurational forces model and its application in the field of fracture mechanics. The implementation of this model in finite element modeling is mentioned as well. In chapter 5, the manufacturing of inhomogeneous materials is explored in detail. Lessons learned from preliminary forging experiments are used to manufacture suitable steel-based composite specimen for later fracture mechanics tests. The results from these fracture mechanics experiments are presented in chapter 6, together with numerical results using the configurational forces model. The mechanism of crack arrest and cleavage cracking in the interlayers is also discussed in detail. Finally, chapter 7 summarizes the findings of this thesis.

2 Fundamentals of Fracture Mechanics

In this chapter, an introduction into the wide subject of fracture mechanics is given. For a thorough assessment of this field, the reader is referred to dedicated books, e.g. the works by Anderson (And2005) or Gross and Seelig (Gro2011). In (Kol2012), a concise picture of fracture mechanics is drawn.

2.1 Generalized Crack Driving Force and Crack Growth Resistance

Fracture mechanics is a continuum mechanics tool, which is used to answer an important question: Can an existing crack in a loaded body grow (Figure 5) and if so, can it lead to catastrophic failure? In a generalized form, the condition for the growth of a loaded crack of length a_0 can be written as follows (Kol2012):

$$D_{\mathrm{gen}} \geq R_{\mathrm{gen}} \tag{2.1}$$

Depending on the stored elastic energy and the work of the applied forces, the crack will feel a "generalized crack driving force" D_{gen}, which aims to extend the crack. This driving force is a loading parameter for the crack. Its counterpart is the "generalized crack growth resistance" R_{gen}, which hinders crack extension, Figure 5a. R_{gen} is dependent on the material, the geometry of the body and the crack extension Δa. The crack cannot extend, when D_{gen} is smaller than R_{gen}. In the case of $D_{\mathrm{gen}} = R_{\mathrm{gen}}$, stable or equilibrium crack growth occurs. Crack growth becomes unstable, when $D_{\mathrm{gen}} \geq R_{\mathrm{gen.}}$

Knowledge of the fracture toughness of a material is paramount for the design and safety assessments of components. We measure this by conducting fracture mechanics experiments, where a specimen with a sharp crack is loaded, Figure 5a. During the experiment, the load F, the load point displacement v and the crack extension Δa are measured. From the F-v curve, the geometry of the body and the actual crack length $a = a_0 + \Delta a$ the crack driving force D_{gen} may then be calculated. Plotting D_{gen} over the crack length a or the crack extension Δa generates the so-called crack growth resistance curve (Figure 5c). At first, D_{gen} increases with increasing load. Only when D_{gen} reaches the R_{gen}, marked by "i" in Figure 5c), the first increment of crack extension occurs. The crack growth resistance $R_{\mathrm{gen,i}}$ at this point is a measure of the *fracture initiation toughness*. In the case of equilibrium crack growth, the crack growth toughness $R_{\mathrm{gen}}(\Delta a)$ can be determined similarly, since $D_{\mathrm{gen}} = R_{\mathrm{gen}}$. The R_{gen}-Δa-curve is denominated as the *crack growth resistance curve*.

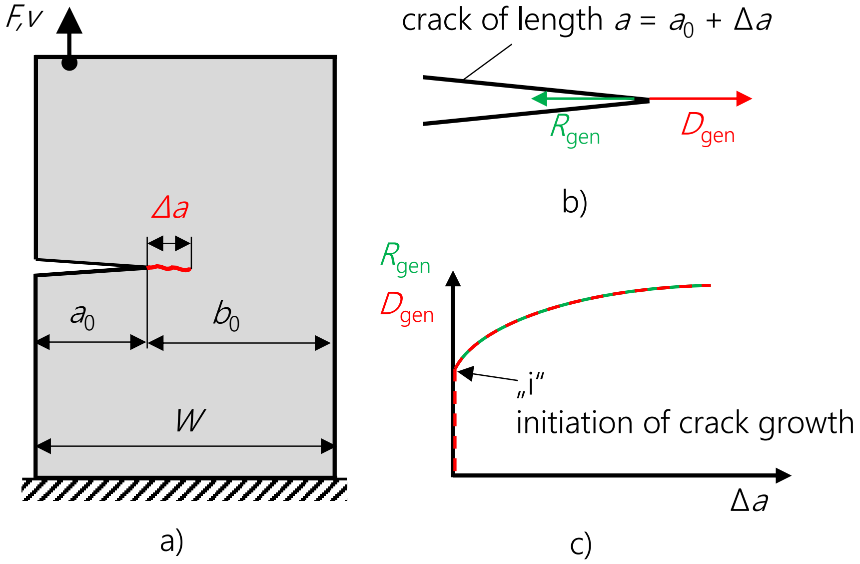

Figure 5: a) A body containing a crack of length a_0 under load. b) This crack can extend, when the generalized crack driving force D_{gen} is equal to or larger than the generalized crack growth resistance, R_{gen}. c) A plot of D_{gen} against the crack extension Δa is called a crack growth resistance curve (Kol2012).

The shape of the R_{gen}-Δa-curve determines whether stable or unstable crack growth occurs. In **Figure 6**a, a flat crack growth resistance curve is depicted. When the specimen with a crack of length a_0 is loaded by a stress σ_1, no crack extension can occur as $D_{\mathrm{gen}} < R_{\mathrm{gen}}$ at point (1). Upon increasing the load to σ_2, $D_{\mathrm{gen}} = R_{\mathrm{gen}}$ at point (2) and the crack can grow an increment. Crack growth will immediately become unstable as $D_{\mathrm{gen}} > R_{\mathrm{gen}}$ after the initial crack extension. **Figure 6**b shows a rising R_{gen}-curve as a comparison. Similarly, no crack extension can occur at point (1). Between point (2) and (3), stable crack extension can be continued by increasing the load from σ_3 to σ_3, maintaining the condition $D_{\mathrm{gen}} = R_{\mathrm{gen}}$. Upon reaching a critical crack length a_c at the load σ_3, cracking finally becomes unstable. With these observations, one can express the conditions for stable and unstable cracking as follows (And2005): Stable crack growth occurs when

$$\frac{\mathrm{d}D_{\mathrm{gen}}}{\mathrm{d}a} \leq \frac{\mathrm{d}R_{\mathrm{gen}}}{\mathrm{d}a} \tag{2.2}$$

and unstable crack growth when

$$\frac{\mathrm{d}D_{\mathrm{gen}}}{\mathrm{d}a} > \frac{\mathrm{d}R_{\mathrm{gen}}}{\mathrm{d}a} \tag{2.3}$$

Many factors determine the shape of the R-curve: A nearly flat R-curve is common for very brittle materials, as only the formation of new surfaces consumes energy and the surface energy is an invariant property. The formation of a plastic zone, for instance, causes a rising R-curve. A material failing by cleavage might show a falling R-curve, as the high strain rates during unstable crack propagation suppress plastic deformation. The size and geometry of the structure containing a crack may have an influence on the R-curve as well, due to the differences in stress triaxiality. A crack in a thin sheet tends to produce a steeper R-curve compared to a thick sheet (And2005).

Different parameters have been developed to characterize the crack driving force and the crack growth resistance. In the next chapter, an overview of these parameters and their validity conditions are given.

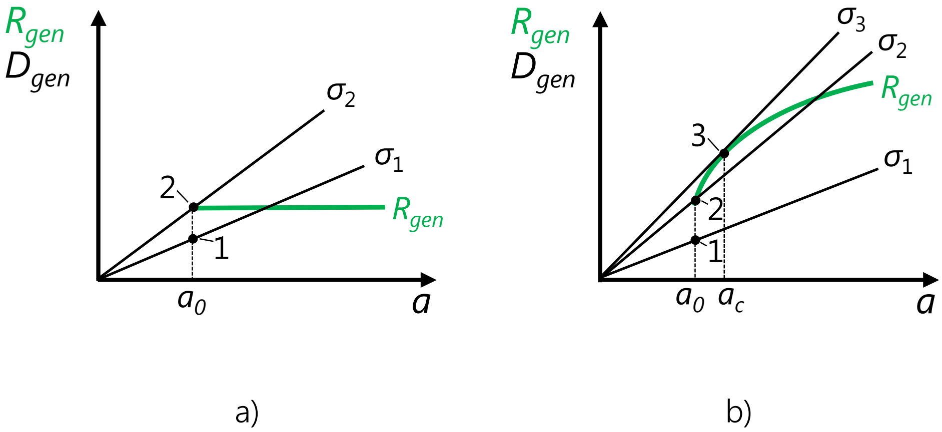

Figure 6: Different shapes of the crack growth resistance curve R_{gen} and schematic crack driving forces D_{gen} for different loading σ. a) Flat R-curve, b) rising R-curve. Adopted from (And2005).

2.2 Regimes of Fracture Mechanics

Many materials, especially under a small load, exhibit a linear elastic behavior, Figure 7a. In this case, linear elastic fracture mechanics (LEFM) can be applied. This is true even if a small process zone appears in front of the crack tip, where the behavior is nonlinear due to damage developing (Kol2012).

In elastic-plastic materials, a plastic zone develops which surrounds the process zone. If the radius of this plastic zone r_{pl} remains small in comparison to the crack length a and the ligament length b,

$$a, b << r_{\mathrm{pl}} \tag{2.4}$$

then so-called "small scale yielding" (ssy) conditions prevail (**Figure** 7b). In this regime, LEFM concepts can still be applied, however slightly modified. This is then called *engineering* LEFM. In **Figure** 7c and **Figure** 7d, large scale yielding (lsy) and general yielding (gy) is depicted. Under such conditions, and when the material in general exhibits non-linear behavior, elastic-plastic fracture mechanics (EP-FM) has to be applied (And2005, Kol2012).

In the next chapters, a brief introduction into LEFM and EP-FM is given.

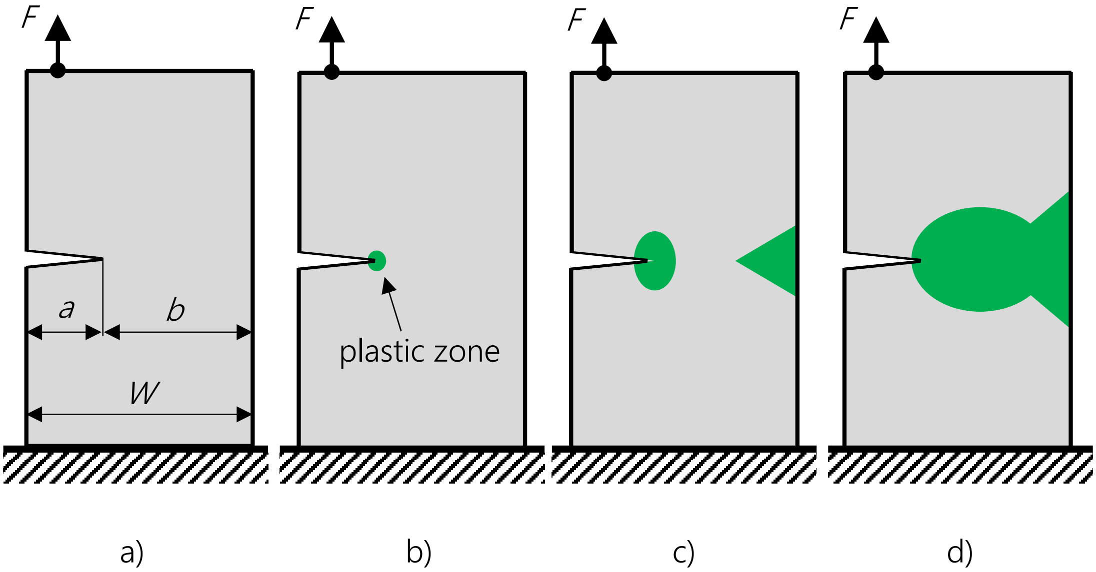

Figure 7: a) Strict LEFM, b) small scale yielding, c) large-scale yielding and d) general yielding (Kol2012).

2.3 Linear elastic fracture mechanics

2.3.1 The stress intensity concept

The following relation, derived assuming isotropic linear elastic material behavior (Wes1939, Irw1957, Wil1957), uses a single parameter K to describe stresses at a point P with polar coordinates r, θ in front of the crack tip (**Figure 8**a):

$$\sigma_{\text{ij}} = \frac{K}{\sqrt{2\pi r}} \cdot f_{\text{ij}}(\theta) + \text{nonsingular terms} \tag{2.5}$$

K is called the stress intensity factor, which determines the intensity of the near-tip field, and f_{ij} is a function only dependent on the crack plane angle θ. The nonsingular terms, which are of the order r^0, $r^{½}$, ... can be neglected for small r. The stress intensity factor K is dependent on the applied stress, the crack length a, and the geometry of the body:

$$K = \sigma_{\text{appl}} \sqrt{\pi a} \cdot f_{\text{K}}(\frac{a}{W}, \frac{H}{W}) \tag{2.6}$$

Solutions for K and the corresponding stress fields for common geometries are found in every fracture mechanics textbook, e.g. (And2005), or in dedicated books (Tad1985, Mur1987). Thereby, three different loading modes for the crack can be distinguished, see **Figure 8**b-d). Mode I, where the load axis is perpendicular to the crack plane, is the most critical out of these three. For that reason, fracture mechanics tests are usually performed under Mode I.

The condition for crack growth in terms of K can be written analogously to equation (2.1)

$$K \geq K_{\text{Ic}} \tag{2.7}$$

According to equation (2.7), a cracked material under Mode I loading can withstand a certain critical stress intensity K_{Ic}, before the crack can start to grow. This critical value is independent on the specimen geometry for

$$B, a, b \geq 2.5 \frac{K_{\text{Ic}}^2}{\sigma_{\text{y}}^2} \tag{2.8}$$

where B is the specimen with, a the crack length, b the ligament length, and σ_{y} the yield stress (**Figure 9**a). The critical value K_{Ic} is a static fracture toughness. However, after a short acceleration phase, a propagating crack can reach velocities of 1 000 *m/s* or more (Gro2011). During the dynamic crack extension, the *dynamic fracture toughness* K_{Id} determines whether the crack continues to grow or arrests, i.e. the condition

$$K_{\mathrm{I}} \geq K_{\mathrm{Id}} \tag{2.9}$$

has to be fulfilled at all times during crack extension. K_{Id} is a material property and depends in the first approximation on the crack tip velocity $\dot{a}$. A plot of $K_{\mathrm{Id}} = K_{\mathrm{Id}}(\dot{a})$ is shown qualitatively in **Figure 9**b. In this figure, c_2 is the propagation velocity of distortional waves, which is about 3200 m/s in steel. Even in brittle materials, cracks typically cannot become faster than $\dot{a}_{\mathrm{max}} \approx 0.5c_2$ (Gro2011). After an initial flat increase, K_{Id} rises significantly with increasing $\dot{a}$. A possible reason for that behavior may be a change in the separation mechanism within the process zone, which is suggested by the increase in roughness of the fracture surface with increasing velocity. Furthermore, it can be argued that K_{I} alone cannot characterize the crack tip field alone during fracture, as stresses and strains depend on the crack velocity as well (Gro2011).

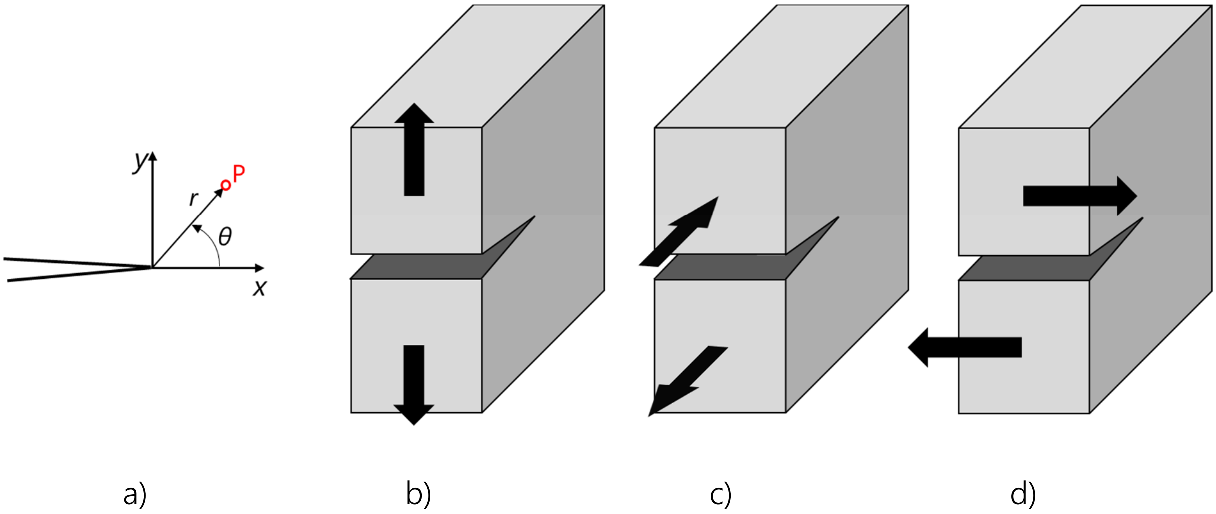

Figure 8: a) Polar coordinates (r, θ) of a point P in front of the crack tip and three possible crack opening modes: b) Mode I, c) Mode II and d) Mode III.

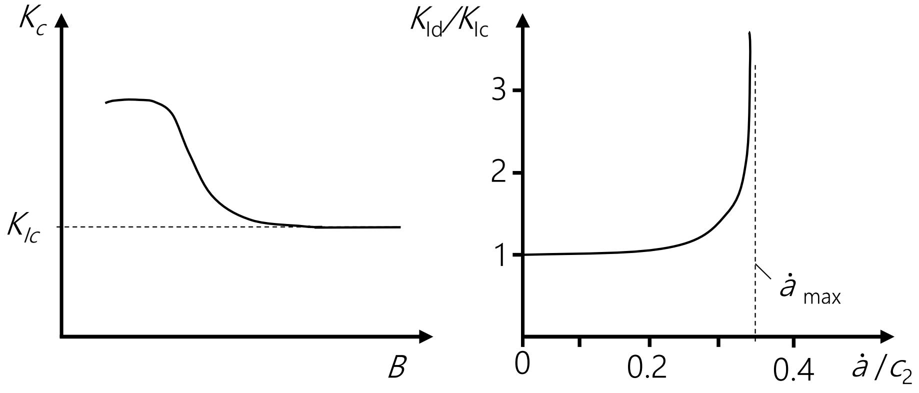

a) b)

Figure 9: a) The critical stress intensity K_c decreases with specimen thickness B. b) The dynamic fracture toughness K_{Id} is dependent on the crack velocity $\dot{a}$ (Gro2011).

2.4 The crack tip plastic zone

If a material can deform plastically, that is in elastic-plastic materials, a plastic zone will form around the crack tip. The size of this zone can be estimated after Irwin (Irw1961) as

$$r_{\mathrm{pl}} = \beta_{\mathrm{pl}} \frac{K^2}{\sigma_{\mathrm{y}}^2} \tag{2.10}$$

where β_{pl} equals 1/6π for plane strain, and 1/2π for plane stress. σ_y is the yield strength of the material.

Irwin's model, however, assumes a circular plastic zone centered around the crack tip, see Figure 10a. A simple elastic analysis using the von Mises-criterion yields a different shape, Figure 10b (And2005). Based on the results depicted in Figure 10b, the *dog bone model* assumes that in the middle of thick plates plane strain conditions prevail, while at the surface plane stress conditions predominate.

In reality, the plastic zone has a forward orientation and reaches its maximum extension at about an angle of $\theta = 70°$ (And2005).

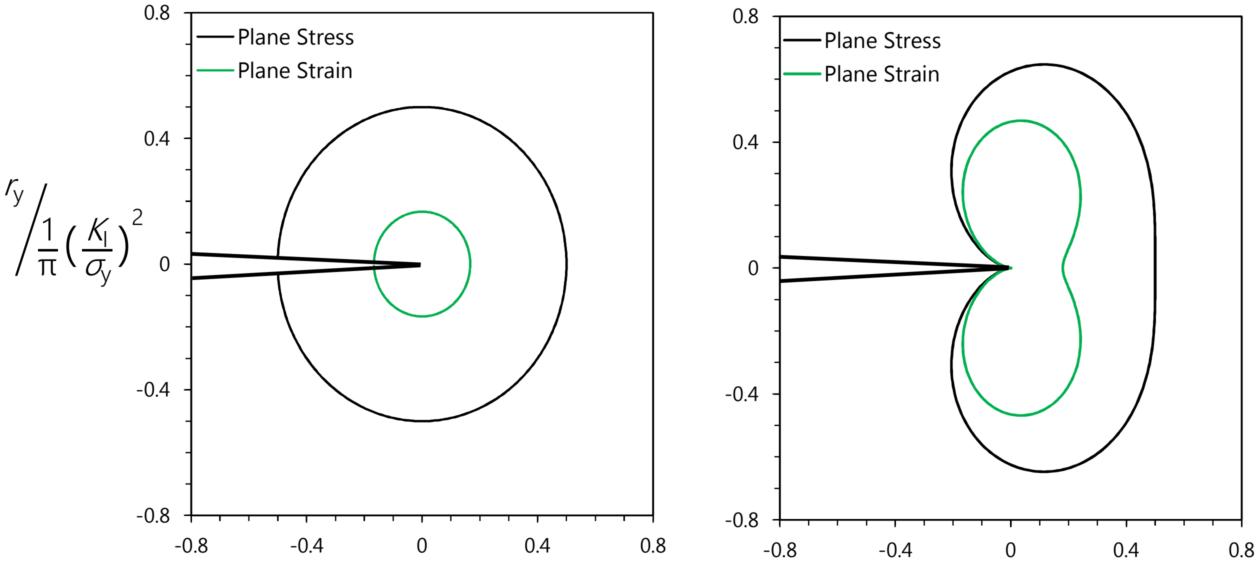

a) b)

Figure 10: Comparison of the shape of the plastic zone shape according to a) Irwin's model (Irw1961) and b) an elastic analysis using the von Mises-criterion (And2005).

2.5 Elastic-plastic Fracture Mechanics

Elastic-plastic fracture mechanics applies to materials that cannot be described using LEFM, that is, materials with nonlinear behavior like plastic deformation. Two parameters are used for such materials: The crack-tip-opening displacement (CTOD) and the *J*-integral. While both parameters describe crack-tip conditions and can be used as fracture criterions, the CTOD will only be mentioned briefly in the next chapter. More emphasis is put on the *J*-integral, which will be used for the evaluation of the experiments later in this thesis.

2.5.1 Crack-tip-opening displacement

(Wel1961) proposed the crack-tip-opening displacement δ as a measure of fracture toughness when he noticed that the degree of crack blunting δ_i before crack growth increased in proportion to the toughness of the material, Figure 11a. The two most common definitions of δ, namely the measurement at the original crack tip or at the 90° intercept, are illustrated in Figure 11b.

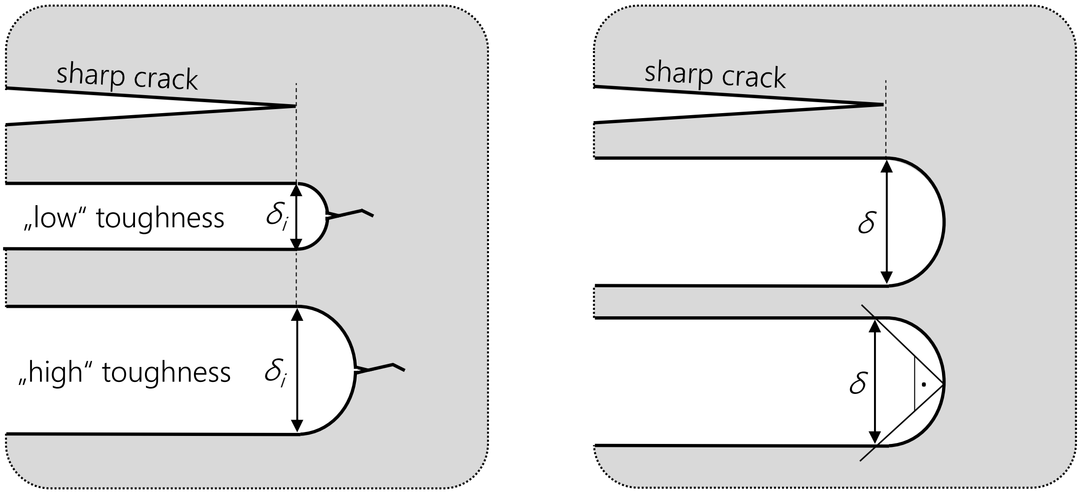

a) b)

Figure 11: a) Crack tip blunting in elastic-plastic materials. b) CTOD can be either determined at the original crack tip or at the intersection of a 90° vertex with the crack flanks. After (And2005).

In the regime of (engineering) LEFM, δ is related to K by (And2005)

$$\delta = \frac{1}{m}\frac{K^2}{E'\sigma_{ys}} \qquad \text{with } m = \begin{cases} 2 & \text{plane strain} \\ 1 & \text{plane stress} \end{cases} \tag{2.11}$$

$$\text{and } E' = \begin{cases} E/(1-\nu^2) & \text{plane strain} \\ E & \text{plane stress} \end{cases}$$

The condition for crack growth becomes, similar to equations 2.1 and 2.7,

$$\delta \geq \delta_i \tag{2.12}$$

where δ_i is the critical CTOD. Standard testing procedures are available for the determination of CTOD and crack growth resistance curves based on CTOD, such as the ASTM E1820 (E1820-13). Local values of CTOD can be measured from fracture surfaces with stereophotogrammetry (Kol1985).

2.5.2 *J*-Integral

In his fundamental paper, Rice (Ric1968a) showed that the difference in potential energy dP of two identical nonlinear elastic bodies with incrementally different crack lengths, Figure 12, can be expressed by a contour integral – the so-called J-integral. Thereby, he idealized elastic-plastic deformation as nonlinear elastic, see **Figure 13** for a schematic comparison. The J-integral is able to characterize stresses and strains in nonlinear materials (Hut1968, Ric1968b):

$$\sigma_{ij} = \sigma_0 \left(\frac{E\,J}{\alpha_{RO}\,\sigma_0^2\, I_n\, r} \right)^{\frac{1}{n+1}} \tilde{\sigma}_{ij}(n,\theta) \tag{2.13}$$

$$\varepsilon_{ij} = \frac{\alpha_{RO}\,\sigma_0}{E} \left(\frac{E\,J}{\alpha_{RO}\,\sigma_0^2\, I_n\, r} \right)^{\frac{n}{n+1}} \tilde{\varepsilon}_{ij}(n,\theta) \tag{2.14}$$

Equations (2.13) and (2.14) are known as the HRR field, where α_{RO} is a dimensionless constant, σ_0 is a reference stress and n is a hardening parameter varying between 1 for a linear elastic material and ∞ for an elastic-ideally plastic material. I_n and the functions $\tilde{\sigma}_{ij}$ and $\tilde{\varepsilon}_{ij}$ are tabulated as functions of the hardening parameter n.

J can therefore be seen as both a stress intensity parameter and as crack driving force. Similar to CTOD, equation (2.11), a relationship between the stress intensity K and J exists in the regime of (engineering) LEFM:

$$J_{\text{lin-el}} = \frac{K^2}{E'} \tag{2.15}$$

Inserting (2.15) into (2.11) yields the relation between CTOD and the J-integral,

$$J = m\,\sigma_{ys}\,\delta \tag{2.16}$$

which is also valid in the E-PFM regime.

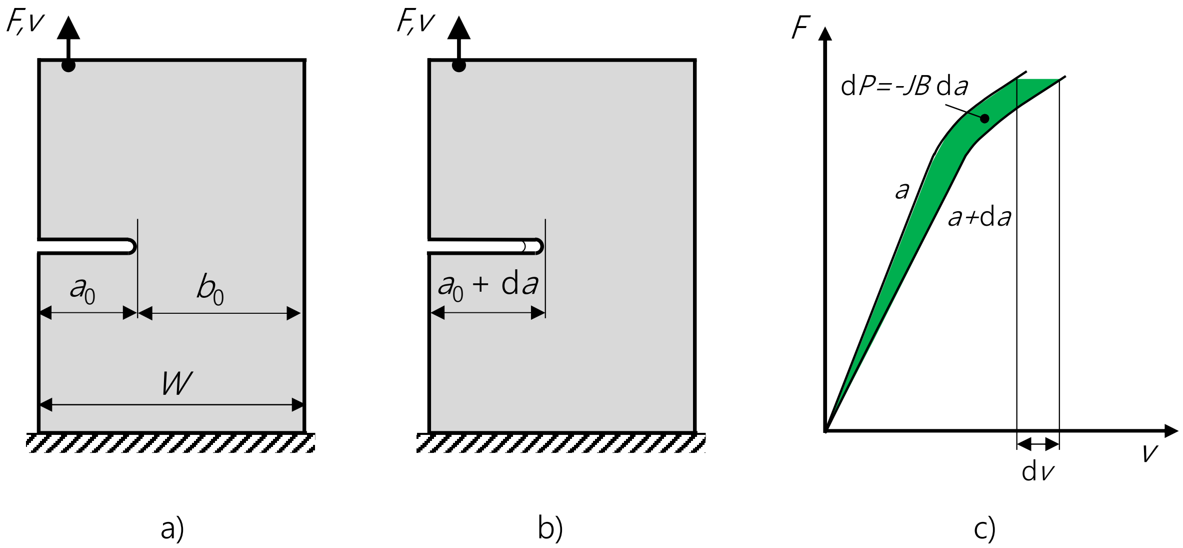

Figure 12: a-b) Two identical nonlinear elastic bodies with incrementally different crack lengths. c) The difference in the potential energy can be expressed with the *J*-integral *J*. After (Kol2012).

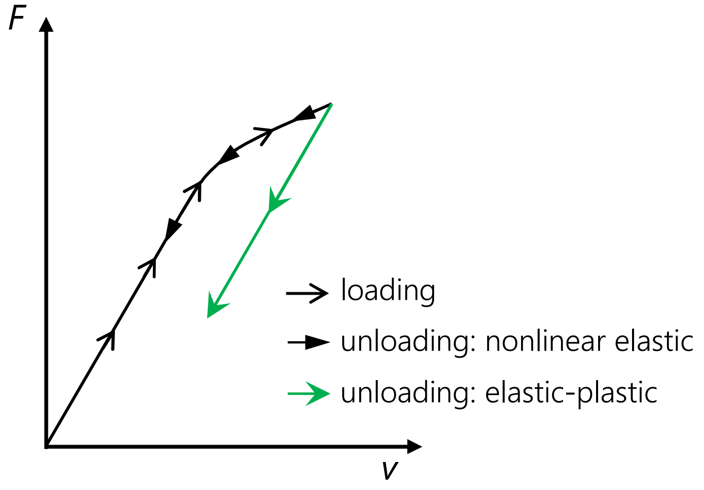

Figure 13: Different unloading behavior of nonlinear elastic and elastic-plastic materials.

The *J*-integral is path-independent in a homogeneous body. It is evaluated along an arbitrary contour Γ drawn counterclockwise from the lower to the upper crack flank, Figure 14, and defined as

$$J \equiv \int_{\Gamma} \left(\Phi \, \mathrm{d}y - \mathrm{T}_{\mathrm{i}} \frac{\partial u_{\mathrm{i}}}{\partial x} \mathrm{d}s\right) = -\frac{1}{B}\frac{\mathrm{d}P}{\mathrm{d}a} \tag{2.17}$$

where P is the potential energy (which can be seen in the F-v-curves, **Figure 12**c), Φ the strain energy density, and T_i and u_i the components of traction and displacement vectors, respectively. The strain energy density Φ,

$$\Phi = \int_0^{\varepsilon_{ij}} \sigma_{ij}\, \mathrm{d}\varepsilon_{ij} \tag{2.18}$$

can be calculated when the (i,j)-components of the stress $\boldsymbol{\sigma}$ and strains $\boldsymbol{\varepsilon}$ tensors along Γ are known, e.g. after a finite element analysis. The traction vector $\boldsymbol{T}$ is given by

$$T_i = \sigma_{ij} n_j \tag{2.19}$$

where n_j are the components of the unit vector normal to Γ.

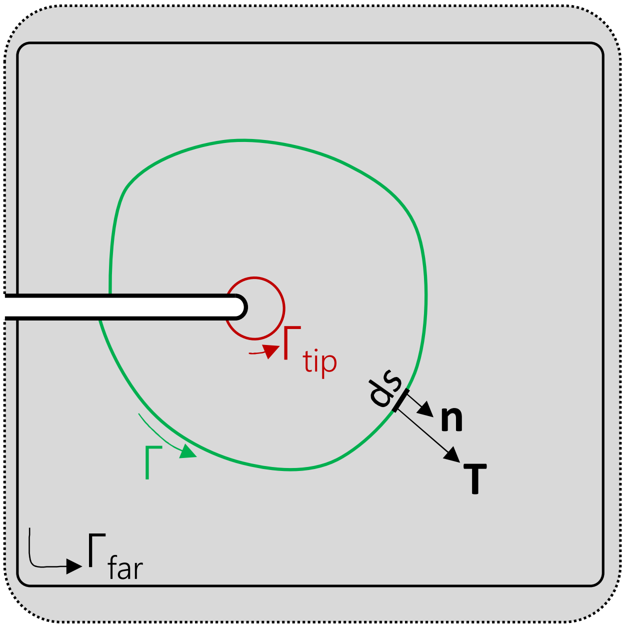

Figure 14: Evaluation of the J-integral along an arbitrary path Γ. In a homogeneous body, the J-integral is path independent.

3 Experimental J-Δa curve determination

This chapter deals with the specifics regarding the experimental determination of both J and the crack extension Δa. The approaches used in this thesis to plot results from fracture mechanics experiments as J-Δa curves are summarized at the end.

3.1 J-Integral

The evaluation of J using the equations (2.17)-(2.19) is not feasible in laboratory experiments. To that end, standards for the experimental estimation of J were developed, e.g. ASTM E-1820 (E1820-13). The experimental J is calculated from an elastic and a plastic component,

$$J = J_{\mathrm{el}} + J_{\mathrm{pl}} \tag{3.1}$$

The elastic part J_{el} is determined by

$$J_{\mathrm{el}} = \frac{K^2(1-\nu^2)}{E} \tag{3.2}$$

with K being the stress intensity, ν the Poisson's ratio and E the Young's modulus. K is calculated using the applied load P, the specimen thickness B, the width W and the crack length a:

$$K = \frac{P}{B\sqrt{W}}\mathrm{f}\left(\frac{a}{W}\right) \tag{3.3}$$

The dimensionless geometry factor $\mathrm{f}(a\,/\,W)$ is given in the literature, e.g. (And2005), and takes into account the geometry and tested specimen type. In this thesis, the single edge notched tension (SENT) specimen type is used. It can be loaded either via pins or via clamping, which has an influence on the geometry factor (**Figure 15**).

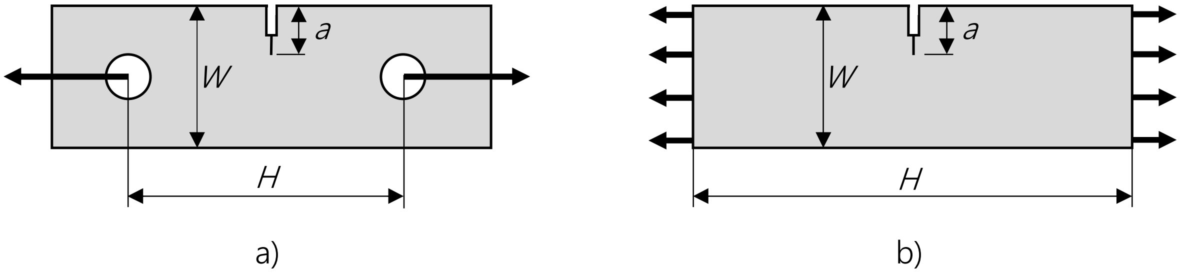

Figure 15: SENT specimen geometry loaded a) with pins or b) with clamps (Cra2007).

Cravero et al. (Cra2007) determined f(a / W) as a fifth-order polynomial function for both loading types and different geometries:

$$\mathrm{f}\left(\frac{a}{W}\right)=\xi_0+\xi_1\left(\frac{a}{W}\right)^1+\xi_2\left(\frac{a}{W}\right)^2+\xi_3\left(\frac{a}{W}\right)^3+\xi_4\left(\frac{a}{W}\right)^4+\xi_5\left(\frac{a}{W}\right)^5 \tag{3.4}$$

Table 1 lists the coefficients ξ for some of selected loading and geometry cases. When a SENT specimen is loaded via clamps, the clear span with H/W between the grips has a pronounced influence on f(a/W). It should be noted that, for pin-loading as well as clamped loading at an H/W = 4, there are analytical expressions available, e.g. in the standard ISO 12108:2002. In these cases, the relation given by (Cra2007) yields the same results as the analytical expressions.

Table 1: Coefficients for determining f(a/W) according to (3.4) (Cra2007)

	ξ_0	ξ_1	ξ_2	ξ_3	ξ_4	ξ_5
SENT$_{\text{pin}}$	-0.072	11.6294	-61.6928	223.4007	-355.5166	239.3969
SENT$_{\text{clamp}}$						
$H/W = 2$	0.2390	4.7685	-10.839	22.8483	-25.1329	13.8204
$H/W = 4$	0.2565	4.4604	-7.0538	18.6928	-19.4703	9.2523
$H/W = 6$	0.2681	4.1916	-4.5098	12.5442	-6.4726	0.7304
$H/W = 8$	0.2852	3.8168	-1.4522	3.5078	9.4071	-7.8491
$H/W = 10$	0.2832	3.8497	-1.4885	4.1716	9.9094	-7.4188

The plastic component of the J-integral, J_{pl}, is calculated as

$$J_{\mathrm{pl}}=\frac{\eta_{\mathrm{pl}}A_{\mathrm{pl}}}{Bb_0} \tag{3.5}$$

In (2.19), η_{pl} is a dimensionless factor, A_{pl} the dissipated plastic work, B the specimen thickness and b_0 the ligament length, with $b_0 = W - a_0$, a_0 being the initial crack length. The plastic work A_{pl} is determined by subtracting the elastic work A_{el} from the total applied work, which is the area under the load-displacement curve, Figure 16a. To evaluate A_{el} correctly, the specimen compliance C as a function of crack length has to be determined. The compliance can usually be calculated with expressions provided in standards like ASTM E1820 (ASTM1820-13) or determined with the unloading technique (e.g.

(Cra2007)). In this thesis, the specimen compliance before and after crack extension was estimated as depicted in **Figure 17**. Plastic deformation prior to the crack arrest is neglected.

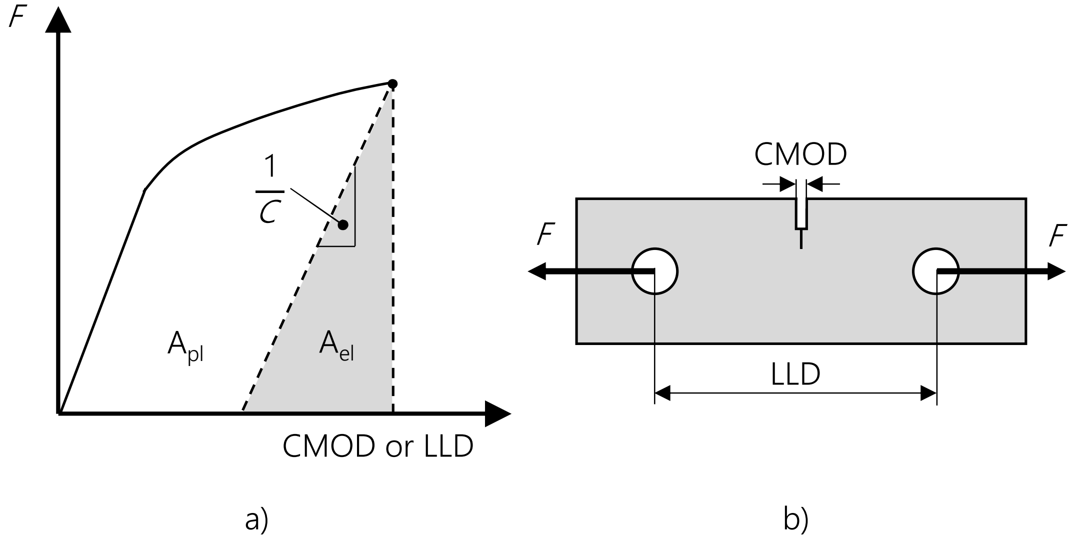

Figure 16: a) Definition of A_{pl} and A_{el}. b) Definition of CMOD and LLD (Cra2007).

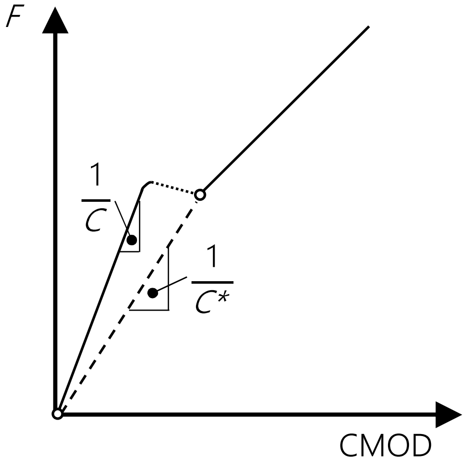

Figure 17: Estimation of the compliance C and C^* before and after crack extension, respectively.

The displacement can be measured in terms of either the load line displacement (LLD) or the crack mouth opening displacement (CMOD), which influences the calculated total applied work (**Figure 16**b). The factor η_{pl} then relates the plastic contribution to the strain energy with the J-integral and is given in literature as well. In the case of a SENT specimen geometry and a load-CMOD-record to calculate A_{pl}, (Cra2007) gives the relations

$$\eta_{\mathrm{pl,\,pin}}^{\mathrm{CMOD}} = 0.9167 + 0.0837(a/W) \tag{3.6}$$

$$\eta_{\mathrm{pl,\,clamp}}^{\mathrm{CMOD}} = 1.0398 - 0.6870\,(a/W) \tag{3.7}$$

for pin and clamp loading, respectively. When using the load line displacement instead of CMOD, no simple expressions are available as η_{pl} depends on a/W, H/W and the strain hardening coefficient. Instead, η_{pl} has to be determined from plots given in (Cra2007).

3.1.1 Correction of J for crack growth

The expressions stated above are valid only for small crack extensions Δa. In case of long crack extensions during the experiment, J has to be evaluated from an incremental procedure, which is also given in standards such as ASTM E1820. Thereby, J at a certain point k is evaluated using the current load P_k, the current crack length a_k, and a previous estimate for the plastic part, $J_{\mathrm{pl},k\text{-}1}$. The adapted expressions are as follows:

$$J_k = J_{\mathrm{el},k} + J_{\mathrm{pl},k} \tag{3.8}$$

$$J_{\mathrm{el},k} = \frac{K_k^2(1-\nu^2)}{E} \tag{3.9}$$

$$K_k = \frac{P_k}{B\sqrt{W}}\,\mathrm{f}\left(\frac{a_k}{W}\right) \tag{3.10}$$

$$J_{\mathrm{pl},k} = \left[J_{\mathrm{pl},k\text{-}1} + \frac{\eta_{k\text{-}1}}{b_{k\text{-}1}B}\left(A_{\mathrm{pl},k} - A_{\mathrm{pl},k\text{-}1}\right)\right] \cdot \left[1 - \frac{\gamma_{k\text{-}1}}{b_{k\text{-}1}}\left(a_k - a_{k\text{-}1}\right)\right] \tag{3.11}$$

For the SENT specimen geometry and load-CMOD records, Cravero et al. (Cra2007) give the following expressions for γ_k:

$$\gamma_{k,\mathrm{pin}}^{\mathrm{CMOD}} = -0.0833 + 0.0837(a_k/W) + \frac{0.0837(a_k/W - 1)}{0.9167 + 0.0837(a_k/W)} \tag{3.12}$$

$$\gamma_{k,\mathrm{clamp}}^{\mathrm{CMOD}} = 0.0398 - 0.6870(a_k/W) + \frac{0.6870(1 - a_k/W)}{1.0398 - 0.6870(a_k/W)} \tag{3.13}$$

Again, a differentiation between pin loading and clamp loading has to be made.

3.2 Determination of crack length

The crack extension Δa can be measured via the single specimen or the multi specimen technique. In the multi specimen technique, several similar samples are loaded to achieve different values of crack extension Δa. The crack extension itself is measuring optically from the fracture surfaces, after marking the original crack extension e.g. by heat tinting or fatiguing until final fracture.

In general, when evaluating the crack length optically, a has to be calculated from multiple measurements across the specimen width (**Figure 18**) to account for a crack front curvature. a is then calculated as

$$a = \frac{(a_1 + a_9)/2 + a_2 + \ldots + a_8.}{8} \tag{3.14}$$

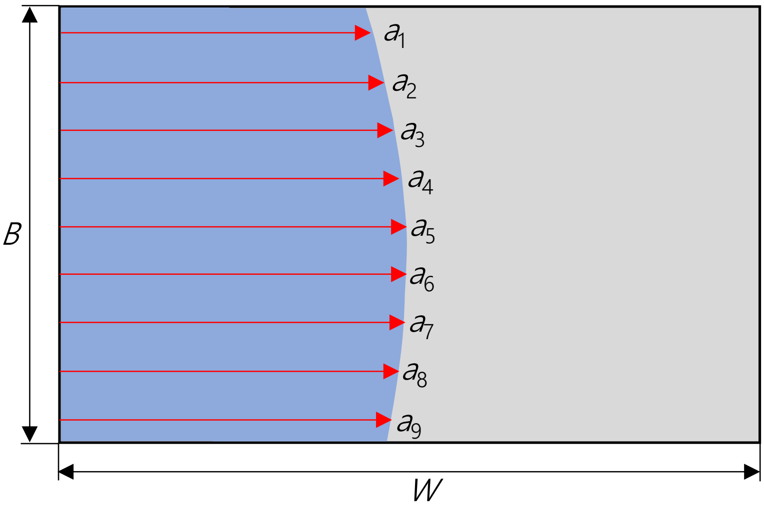

Figure 18: The crack length a is calculated from nine separate measurements across the specimen width B.

Commonly, J-Δa curves are determined using the single specimen technique, where the crack extension is measured by either the unloading compliance or the potential drop technique (And2005). The potential drop technique determines the crack length by applying a constant direct or alternating electric current to the specimen and measuring the potential V. As the resistance of the specimen changes with crack length, the instantaneous crack length can be calculated from the ratio of the current potential V and a reference potential V_0. The reference potential V_0 is not constant, but rather a function of the load P. Following the recommendations from ESIS (ESIS1992), it is determined by fitting a straight line through the steeply rising linear part of the load-potential record, Figure 19.

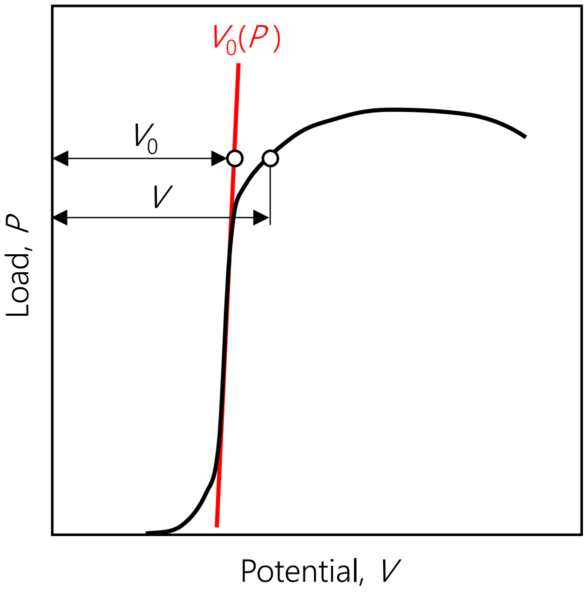

Figure 19: Determination of V and V_0 from a typical load-potential record. After (ESIS1992).

For SENT specimen, a is calculated with the relation given by Johnson (Joh1965):

$$a = \frac{2W}{\pi}\cos^{-1}\left\{\frac{\cosh\left(\frac{\pi y}{2W}\right)}{\cosh\left[\frac{V}{V_0}\cosh^{-1}\left(\cosh\left(\frac{\pi y}{2W}\right)/\cos\left(\frac{\pi a_0}{2W}\right)\right)\right]}\right\} \tag{3.15}$$

Thereby, $2y$ denotes the distance between the potential probes, and a_0 the initial crack length. This analytical expression is only valid for homogeneous specimen and cannot simply be used in the case of laminates, where the electrical conductivity γ differs between the layers. However, it is still possible to use the potential drop technique via the calculation of calibration curves, which relate the relative potential V/V_0 to a crack length a. This is demonstrated in the following chapter.

3.2.1 Calculation of calibration curves

As stated before, laminated composites complicate the crack length determination with the potential drop technique due to their difference in electrical conductivity. This is illustrated in Figure 20, which compares the distribution of current densities and equipotential lines for two simulated cases of a fracture mechanics experiment with a specimen containing a single interlayer. In Figure 20a, the interlayer is less conductive than the matrix, $\gamma_{IL}/\ \gamma_{matrix} = 0.2$. It is evident that the current density within the interlayer is lower than in the matrix, causing a distortion of the equipotential lines. In Figure 20b, the interlayer is significantly more conductive, i.e. $\gamma_{IL}/\ \gamma_{matrix} = 5$. In this case, most of the electric current is conducted through the interlayer. Again, a distortion of the equipotential lines is visible. It is clear that at the same crack length and current flow the potential probes attached next to the notch would measure different potentials for those cases. Simply applying equation (2.28) without accounting for the difference in conductivity would result in inaccurate crack lengths. This is especially true when the crack tip is located close to the interlayer.

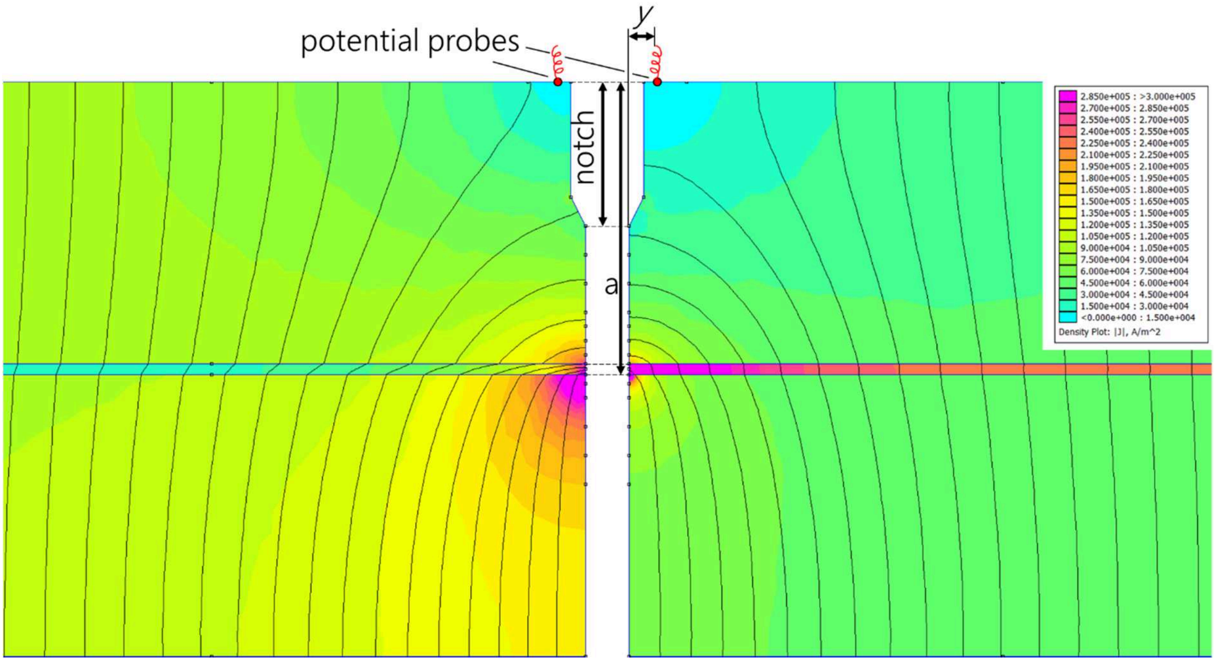

a) b)

Figure 20: A comparison of calculated current densities and equipotential lines in SENT specimen containing a single interlayer with conductivity γ_{IL}. The crack tip is located at the second interface. a) $\gamma_{IL}/\ \gamma_{matrix} = 0.2$, b) $\gamma_{IL}/\ \gamma_{matrix} = 5$.

Figure 20 was created with the free software package finite element magnetics (FEMM). With the same software it is possible to calculate calibration curves for arbitrary composite geometries, i.e. varying number and thicknesses of interlayers, to relate a relative change in potential with the crack length. An example is given in the following.

The experimental potential-load record of a fracture mechanics test with a single interlayer specimen is depicted in Figure 21a. In this specimen, X210CrW12 cold working tool steel and DC04 deep-drawing steel serve as matrix and interlayer material, respectively. Details on materials and manufacturing can be found in chapter 5.4.

During loading, the potential initially shows a linear rise with increasing load. From this linear region, the reference potential at a load P, $V_0(P)$, is extracted, compare also Figure 19. After reaching a load of ~4 500 N, a sudden crack extension causes the jump in potential. After this crack extension, the sample was unloaded, causing V to decrease. The decrease of V below the reference potential V_0 in the unloaded state is unexpected, given the crack extension during the experiment. A possible explanation for this is again the layered architecture and the fact that the crack arrested in the more conductive interlayer (see also Figure 21c). The current around the crack tip is then predominantly conducted in the interlayer, which results in a lower potential drop.

To determine the crack length from the potential measurement, calibration curves were calculated and plotted together with the location of the interlayer, Figure 21b. The dashed line indicates the analytical solution given by JOHNSON's equation (2.28), which is identical to the numerical calibration curve for a homogenous conductivity, i.e. $\gamma_{\text{IL}}/\ \gamma_{\text{matrix}} = 1$. Additionally, curves for $\gamma_{\text{IL}}/\ \gamma_{\text{matrix}} = 5$ and $\gamma_{\text{IL}}/\ \gamma_{\text{matrix}} = 10$ are plotted. The influence of the difference in electrical conductivity is clearly visible as a deviation from the linear, homogenous solution. Taking the relative potential $V/V_0 = 1.24$ at maximum load (Figure 21a), the crack lengths deduced from the calibration curves at $\gamma_{\text{IL}}/\ \gamma_{\text{matrix}} = 1$, 5 and 10 are marked as a', a'' and a''', respectively, in Figure 21b. It is evident that JOHNSON's relation significantly underestimates the real crack length, when $\gamma_{\text{IL}} > \gamma_{\text{matrix}}$.

To validate the calculations, the real crack tip position in the unloaded sample was marked by heat tinting, followed by fracturing of the sample. Figure 21c shows the fracture surface, with the DC04 interlayer in the middle. The blue and white colors indicate cracked and intact areas, respectively. The matrix in front of the interlayer fractured completely and the crack ultimately arrested in the interlayer at or before the second interface. The average total crack length was measured optically from the heat tinted fracture surface as a = 6.78 mm. Comparing this value with Figure 21b, it is evident that using $\gamma_{\mathrm{IL}}/\gamma_{\mathrm{matrix}}$ = 1 and 10 under- and overestimate the real crack length, respectively. The crack length a'' = 6.79 mm estimated with the calibration curve for $\gamma_{\mathrm{IL}}/\gamma_{\mathrm{matrix}}$ = 5, however, is very close to the actual crack length measured optically.

Typical values of γ from supplier datasheets are listed in Table 2. The cold-working tool steels X210CrW12 and C45 are used as matrix materials. The conductivity of pure iron is also listed, as it is comparable to the deep-drawing steel DC04 used as interlayer material (see also chapter 5.4). The effective relative conductivity between matrix and interlayer in the specimens cannot be determined accurately, however. The conductivity of the interlayer decreases due to carbon diffusion during manufacturing and heat treatment. Furthermore, in the fracture mechanics experiment plastic deformation of the interlayer occurs, which also decreases conductivity. In this thesis, a relative conductivity of 5 and 1.2 is used for X210CrW12/DC04 and C45/DC04 composites, respectively, to calculate calibration curves.

Table 2: Electrical conductivity γ of iron and steels.

Steel grade	γ / 10^6 [S/m]
X210CrW12	1.54
C45	8.33
Iron	10.00

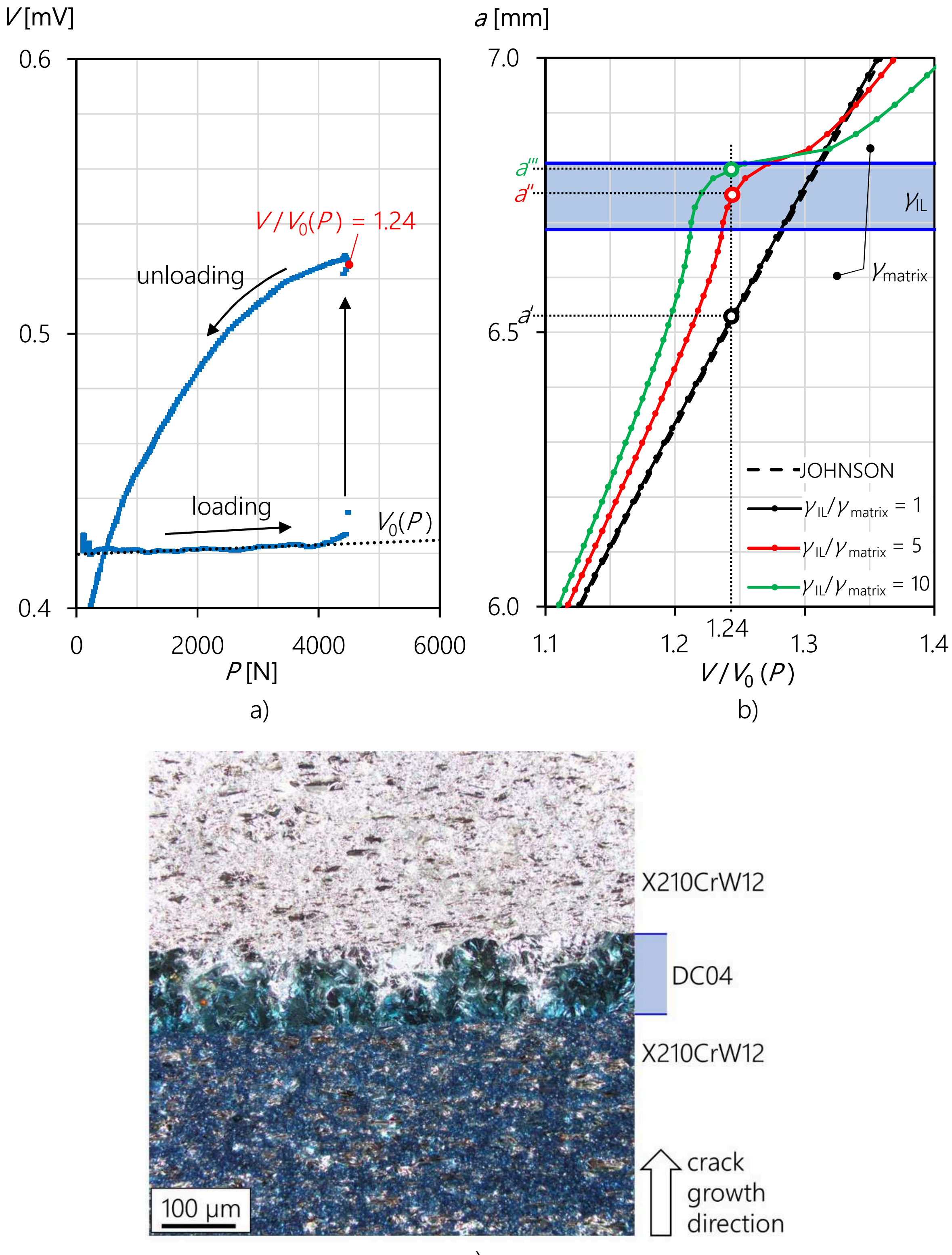

a) b)

c)

Figure 21: Example of a crack length determination using the potential drop technique. a) Plot of the potential V over the load P. At 4 500 N, a sudden crack extension is visible as a sharp increase in potential. b) Calculated calibration curves for different conductivity ratios $\gamma_{IL} / \gamma_{matrix}$. At a given relative potential V / V_0, the deduced crack lengths a' to a''' differ significantly. c) Real crack front marked by heat tinting.

3.3 Summary

In this thesis, J is evaluated from load-CMOD records as described in chapter 3.1. Unless stated otherwise, J is also corrected for crack growth, chapter 3.1.1. The crack length is determined as follows:

- The initial crack length a_0 is always measured post-mortem from the fracture surface as described in **Figure 18** and equation (3.14).
- In J-Δa plots, the crack extension Δa is calculated as

  $$\Delta a = a - a_0 \tag{3.16}$$

  where the total crack length a is determined using the potential drop technique and calculated calibration curves as described in chapter 3.2.1.

- In cases where the potential drop technique was not applicable, e.g. due to a detachment of wires during the experiment, the crack extension Δa is estimated optically from the fracture surface, similar to a_0.

4 The configurational forces concept

The configurational forces concept rests on ideas by Eshelby (Esh1951, Esh1970) and provides a convenient method for the quantitative description of the behavior of defects in materials. These forces are thermodynamic forces that are responsible for the movement of defects, such as grain boundaries, interstitial atoms, dislocations or cracks. A configurational force appears at a defect, when the total energy of the system varies for different positions of the defect in the material. As such, they are different from and less intuitive than the classical forces that enter the balance laws of classical Newtonian mechanics. However, in a series of experiments Bigoni and coworkers (Big2014, Big2015) experimentally demonstrated the existence of these configurational forces, using elastic beams with a moveable constraint. A physical interpretation of these configurational forces acting on dislocations and cracks was attempted in (Bal2016), by drawing the connection to classical Newtonian forces.

Three instructive examples are given in the next chapter, which should provide a basic understanding on *why* configurational forces appear. The framework for the concept as well as the specifics for its use in the field of fracture mechanics will be given afterwards. Finally, instructive results from numerical investigations using the configurational forces concept are described.

4.1 Introduction

The first illustrative example is shown in Figure 22. Eshelby (Esh1956) considered an elastic bimaterial beam with a junction between the stiffer and the more compliant part. Due to a load F, the beam bends and the load descends. If the junction is moved in direction of the stiffer material, the beam as a whole becomes more flexible, allowing the load to descend further. As this would cause the load to lose potential energy, a driving force appears at the junction to move it accordingly.

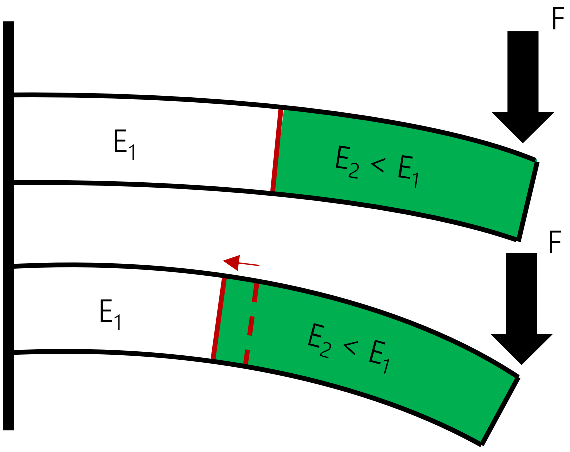

Figure 22: A bimaterial beam is bent by a force F. When the boundary moves in direction of the stiffer part, the beam as a whole becomes more compliant. The load descends and loses potential energy (Esh1956).

The similar train of thought can be used to predict the behavior of other kinds of defects. Figure 23 shows an interstitial atom near a free surface. This defect introduces stresses in the lattice due to the misfit of the atomic radii. We can now calculate the total energy of this system with a given position of this defect. As the total energy changes with the position of the defect, the defect feels a driving force to move towards the free surface, so that the total energy decreases (Figure 23b).

The last instructive example explores the influence of a material inhomogeneity on a growing crack (Kol2011). In Figure 24a, a cracked linear elastic homogenous body, made out of a material "1" with a Young's Modulus E_1, is depicted. An arbitrary point P within the crack tip field is chosen, and we will follow this point during a crack extension Δa to the position P'. As depicted, the elastically stored strain energy density in P and P', i.e. Φ_P and $\Phi_{P'}$, does not change – the crack extension does not generate any thermodynamic driving forces. The situation changes however, when material inhomogeneities are present.

In Figure 24b, the point P crosses the interface Σ into a material "2", which is more compliant than material "1". At the same strain, the stored elastic energy after the crack extension $\Phi_{P'}$ is now smaller than Φ_P before the crack extension. In other words, there is an excess in energy due to material "2" being more compliant, which is available for further crack propagation. Figure 24c depicts the reverse case, where material "2" is now stiffer than material "1". As can be seen, $\Phi_{P'}$ is now larger than Φ_P, i.e. more energy is needed for crack extension in order to move P across the interface. The excess or lack in energy caused by the material inhomogeneity cause configurational forces, which can hinder or facilitate crack propagation.

An important deduction can be made from **Figure 24**b and c: Crack propagation is hindered, when the crack grows into a material with higher Young's Modulus – we call this the *shielding effect* of the material inhomogeneity. The exact opposite is the case, when the crack grows into a more compliant material, which is then called *anti-shielding effect*, accordingly.

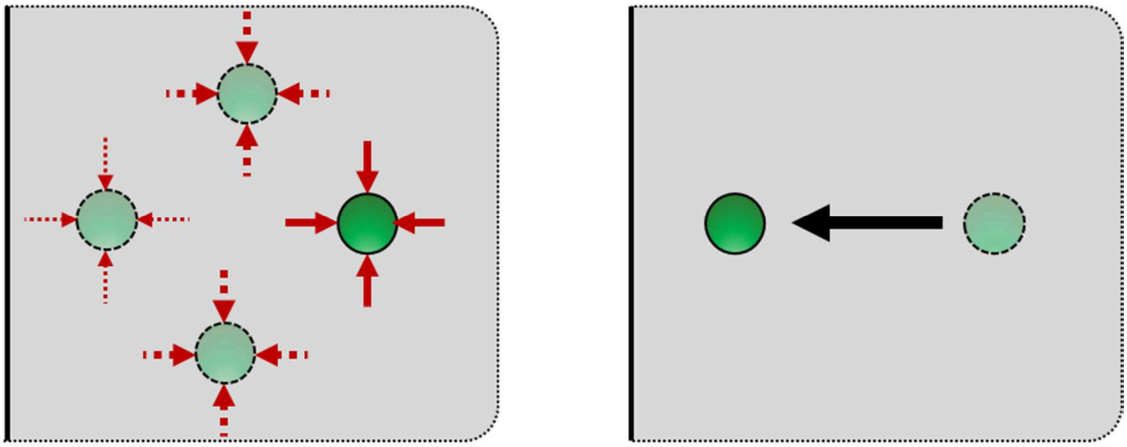

a) b)

Figure 23: An interstitial atom near a free surface. a) If the total energy of the system decreases with different positions of the atom, then a thermodynamic driving force will appear b) which aims to move the defect into a more favorable position.

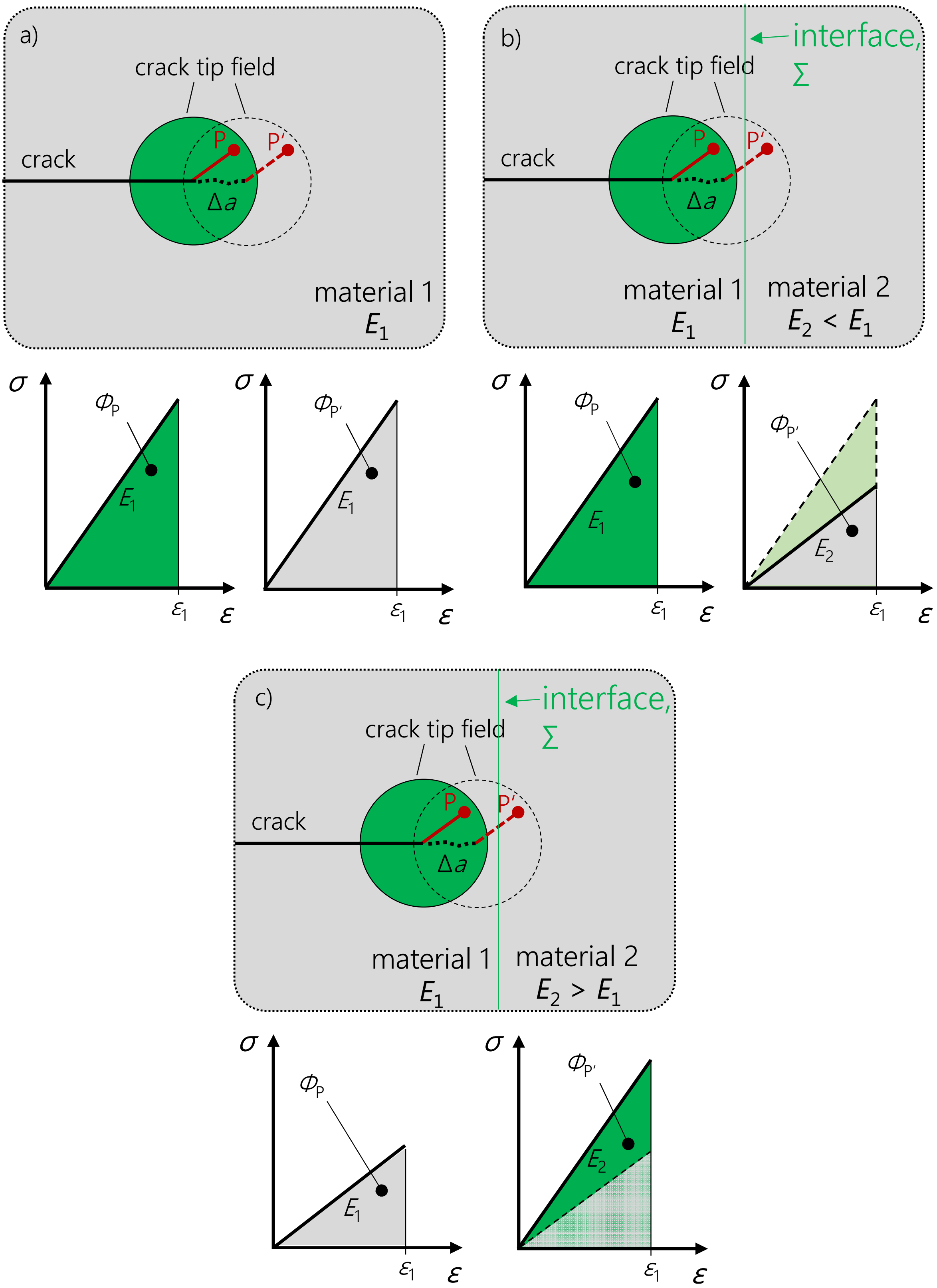

Figure 24: A comparison of the strain energy densities Φ for a point P and P' before and after crack extension for a) a homogeneus specimen, b) a bimaterial with a hard/compliant transition and c) a bimaterial with a compliant/hard transition. After (Kol2011).

4.2 The configurational forces framework

In this chapter, only the most important equations shall be given. For general information and the complete derivation of the concept, the reader is referred to the works of Maugin (Mau1993, Mau1995, Mau2011), Gurtin (Gur1996, Gur2000) or Kienzler and Herrmann (Kie2000).

As mentioned before, the basic idea of the configurational forces was introduced by Eshelby (Esh1951). His aim was to quantify the driving force on a defect.

In this approach, with the *configurational* forces a new force system is introduced in addition to the classical *deformational* forces. The deformational forces, like gravitation, act in the 'current' configuration and are responsible for e.g. changes in shape. In contrast, the configurational forces act in the reference configuration and are responsible for kinematic changes, e.g. the movement of a phase boundary or a crack tip (Sim2003), recall Figure 22 and Figure 24.

Eshelby found that the change in energy is completely defined by a tensor **C**, which is known as the 'Eshelby stress tensor', 'configurational stress tensor' or 'energy momentum tensor':

$$\mathbf{C}=\Phi\,\mathbf{I}-\mathbf{F}^{\mathrm{T}}\mathbf{S} \tag{4.1}$$

In equation 3.4, Φ is the strain energy density, $\mathbf{I}$ the unit tensor, $\mathbf{F}^{\mathrm{T}}$ the transposed deformation gradient tensor and **S** the first Piola-Kirchhoff stress tensor. The configurational force **f** in the bulk or at a defect is now the negative divergence of **C**:

$$\mathbf{f}=-\nabla\mathbf{C} \tag{4.2}$$

Equation (3.5) shows that a configurational force **f** appears where the divergence of the configurational stress tensor **C** does not vanish. This is the case e.g. at a defect or at deformation gradients within a plastic zone. The vector **f** determines now *magnitude* and *direction* of the driving force on the defect.

4.3 The configurational forces in fracture mechanics

The adaption of the configurational forces concept in fracture mechanics is discussed in detail in (Sim2003, Sim2005, Kol2010). Consider a cracked bimaterial body with a sharp interface, Figure 25. At the crack tip, the configurational force as given in equation (4.2) becomes for deformation theory of plasticity (Sim2003)

$$\mathbf{f}_{\mathrm{tip}} = -\lim_{\mathrm{r}\to 0}\int_{\Gamma_{\mathrm{r}}} (\mathit{\Phi}\mathbf{I} - \mathbf{F}^{\mathrm{T}}\mathbf{S})\mathbf{m}\,\mathrm{d}s \tag{4.3}$$

with $\mathbf{m}$ being the unit vector normal to the circle Γ_{r} centered at the crack tip. $\mathbf{f}_{\mathrm{tip}}$ is related to the crack driving force by:

$$\mathbf{J}_{\mathrm{tip}} = -\mathbf{f}_{\mathrm{tip}} \tag{4.4}$$

Multiplying the $\mathbf{J}_{\mathrm{tip}}$-vector with a unit vector $\mathbf{e}$ describing the direction of crack growth yields the scalar J-integral J_{tip}:

$$J_{\mathrm{tip}} = \mathbf{e}\mathbf{J}_{\mathrm{tip}} = \mathbf{e}\lim_{r\to 0}\int_{\Gamma_r} (\mathit{\Phi}\mathbf{I} - \mathbf{F}^{\mathrm{T}}\mathbf{S})\mathbf{m}\,\mathrm{d}s \tag{4.5}$$

The right-hand side of equation (4.5) is Rice' J-Integral evaluated at a contour Γ_{r} around the crack tip (Sim2003). As observed before in Figure 24, the change in mechanical properties at the interface will influence the crack driving force. The configurational forces along the interface $\mathbf{f}_{\Sigma}$ are given by

$$\mathbf{f}_{\Sigma} = -\left([[\mathit{\Phi}]]\mathbf{I} - [[\mathbf{F}^{\mathrm{T}}]]\cdot\langle\mathbf{S}\rangle\right)\mathbf{n} \tag{4.6}$$

Thereby, $[[a]]$ denotes the difference in a quantity a ($a_{\mathrm{right}} - a_{\mathrm{left}}$), and $\langle a \rangle$ the mean value of a ($\frac{1}{2}\cdot(a_{\mathrm{right}} + a_{\mathrm{left}})$) at the interface Σ. Correspondingly, if $\mathbf{f}_{\Sigma} \neq 0$, the configurational forces at the interface introduce a contribution to the crack driving force, C_{inh} (Sim2005):

$$C_{\mathrm{inh}} = -\mathbf{e}\cdot\int_{\Sigma}\left(\left[[\varnothing]\right]\mathbf{I} - \left[\left[\mathbf{F}^{\mathrm{T}}\right]\right]\langle\mathbf{S}\rangle\right)\mathbf{n}\,\mathrm{d}s \tag{4.7}$$

In equation (4.7), the integral (which gives a vector) was projected in the direction of crack extension by multiplying with $\mathbf{e}$, as before in equation (4.5). The material inhomogeneity term, C_{inh}, is a scalar quantity, denoting the energy that is released during a unit crack extension due to the material inhomogeneity at the interface. The effective, near-tip crack driving force, $\mathcal{J}_{tip}$, is the sum of the nominally applied far-field crack driving force $\mathcal{J}_{far}$ evaluated along a path at the boundary of the body and the material inhomogeneity term $\mathcal{C}_{inh}$ (Sim2003, Sim2005, Kol2010):

$$\mathcal{J}_{tip} = \mathcal{J}_{far} + \mathcal{C}_{inh} \tag{4.8}$$

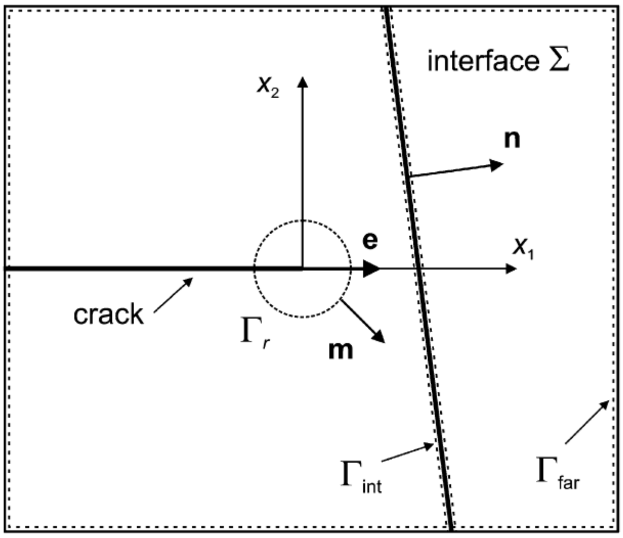

Figure 25: A two-dimensional bimaterial body containing a crack and a sharp interface (Kol2010).

$\mathcal{C}_{inh}$ quantifies the influence of the inhomogeneity on the crack driving force $\mathcal{J}_{tip}$. For small strain theory, equation (4.7) can be rewritten as (Sim2003, Sim2005)

$$\mathcal{C}_{inh} = -\mathbf{e}\int_{D} \frac{\partial\varnothing(\boldsymbol{\varepsilon},\mathbf{x})}{\partial\mathbf{x}}\,\mathrm{d}A \;-\; \int_{\Sigma} \left([[\varnothing]]\cdot\mathbf{I}-\langle\boldsymbol{\sigma}\rangle\cdot[[\boldsymbol{\varepsilon}]]\right)(\mathbf{n}\cdot\mathbf{e})\,\mathrm{d}s \tag{4.11}$$

$\partial\Phi/\partial x$ .... explicit spatial derivative of the strain energy density
$[[\ a\ ]]$ .... difference in quantity a (a_{right} - a_{left}) at the interface Σ
$<\ a\ >$ .... mean value of a (½·(a_{right} + a_{left})) at the interface Σ
σ.................... Cauchy stress tensor
ε.................... linear strain tensor
n.................... unit vector normal to the interface Σ
e.................... unit vector in direction of crack extension

The first term in equation (4.11) describes the contribution of a *gradient* within a region D (Figure 26a), the second term the contribution of a *jump* in a material property at an interface Σ (Figure 26b). In the case of multiple interfaces and property jumps (which is the case in laminated materials) the second term in equation (4.11) can be rewritten as a summation of the individual contributions of each interface Σ_i (Sis2017):

$$C_{\text{inh}} = -\sum_{i=1}^{k} \int_{\Sigma_i} \left([[\Phi]] \cdot \mathbf{I} - \langle \boldsymbol{\sigma} \rangle \cdot [[\boldsymbol{\varepsilon}]] \right) (\mathbf{n} \cdot \mathbf{e}) \, \mathrm{d}s \qquad (4.12)$$

The advantage of the configurational forces method is that a postprocessor - after a standard stress analysis using a finite element method (FEM) software like ABAQUS- can calculate C_{inh} using equation (4.7) or (4.12). The crack driving force J_{tip} can then be evaluated using equation (4.8), where J_{far} for a specific path is also readily obtained from FEM analysis.

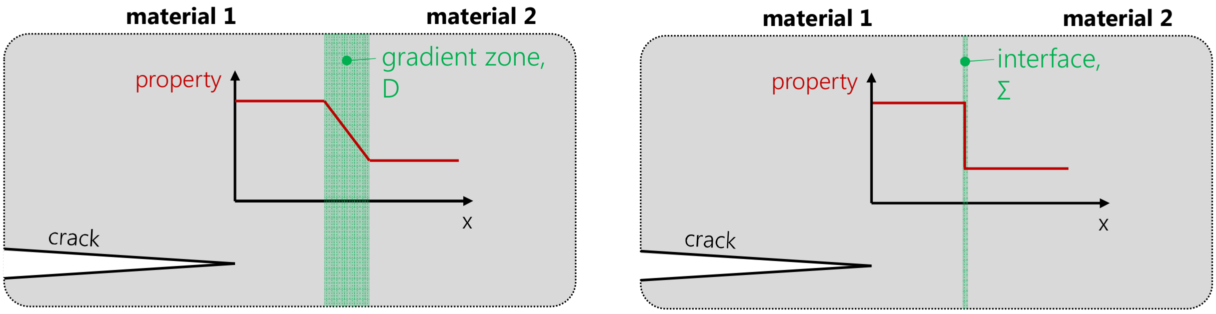

a) b)

Figure 26: C_{inh} can be calculated for a) gradients and b) jumps in material properties.

4.4 Finite element modelling

J-integrals for arbitrary integration paths can readily be determined with FEM-codes like ABAQUS, which use the virtual crack extension method of Parks (Par1977). It is also possible to evaluate the near-tip J-integral J_{tip} by choosing a suitable contour around the crack tip. As long as the contour does not touch an interface, J_{tip} should be path independent. Due to numerical reasons, this is not always the case (Kol2010). In contrast, the evaluation of the J_{tip} using the relation $J_{\text{tip}} = J_{\text{far}} + C_{\text{inh}}$ does not suffer from this shortcoming, as C_{inh} can be evaluated very accurately, even if the crack tip is close to an interface (Sim2005).

For the evaluation of C_{inh}, the configurational forces concept is implemented as a post-processing routine into ABAQUS, written in the Python programming language based on the works of Müller et al. (Mul2002, Mul2004) and Denzer et al. (Den2003). The configurational forces are calculated from the equilibrium stress and strain fields, with Φ being the total strain energy density. Therefore, deformation theory of plasticity is used in the post-processing.

In the numerical results given in the next chapter, no real crack extension is modelled. Instead, specimen with stationary cracks are considered, where the crack lengths a are varied to simulate the behavior of a growing crack. The materials are assumed to be isotropic and the elastic-plastic behavior is described using the incremental plasticity model provided by ABAQUS. With the assumed perfect bonding at the interfaces, no delamination can occur in the FE-simulation.

4.5 Numerical studies using the configurational forces model

As already mentioned in the introduction, Sistaninia and Kolednik (Sis2014) studied the effect of a single, soft interlayer on the crack driving force numerically using the configurational forces concept. They considered a compact tension specimen with a single interlayer of thickness $t = 0.3$ mm. The matrix and interlayer were modeled as having the same Young's modulus of $E = 70$ GPa and same Poisson's ratio of $\nu = 0.3$. The yield stress in matrix and interlayer was different, however, with $\sigma_y^{\mathrm{M}} = 500$ MPa and $\sigma_y^{\mathrm{IL}} = 200$ MPa for matrix and interlayer, respectively.

Figure 27 shows a key result, which illustrates the aforementioned effects of an inhomogeneity. J_{tip}, which is the local crack driving force, varies with the distance L_1 of the crack tip to the first interface IF1 of the soft interlayer, as well as with the global loading parameter J_{far}. In contrast, for a homogeneous material J_{tip} would be constant, $J_{\mathrm{tip}} = J_{\mathrm{far}}$. Due to the presence of the hard-soft transition at IF1, the anti-shielding effect first causes an increase in J_{tip} close to IF1. When the crack tip is located within the interlayer, J_{tip} decreases due to the shielding effect exerted by the soft-hard transition at the second interface, IF2, until it reaches a minimum in the matrix just after IF2. The second interface is therefore a critical position for crack arrest, as at this point the crack driving force is at its lowest. The authors state that the optimum of the material inhomogeneity effect is reached when there is a factor 5 difference in yield stress between matrix and interlayer and plasticity spreads across the whole interlayer. The optimum interlayer thickness t_{opt} can then be estimated as (Sis2014)

$$t_{\mathrm{opt}} \approx r_{\mathrm{pl}}^{\mathrm{IL}} = \beta \cdot \frac{J_{\mathrm{far}}^{\mathrm{CA}} \cdot E}{(\sigma_{\mathrm{y}}^{\mathrm{IL}})^2 \cdot (1 - \nu^2)} \tag{4.13}$$

where β = 1/6π for plane strain conditions and $J_{\mathrm{far}}^{\mathrm{CA}}$ is the loading parameter for a crack at crack arrest position.

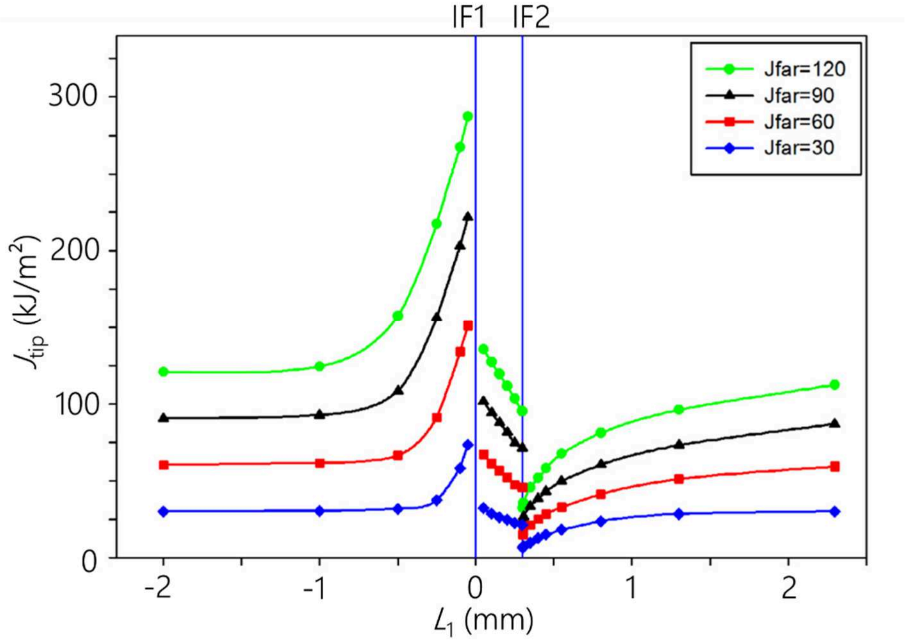

Figure 27: The crack driving force J_{tip} varies with the position of the crack tip respective to the first interface, L_1, and the loading parameter J_{far}. (Sis2014)

Sistaninia and Kolednik (Sis2017) introduced a dimensionless parameter $\psi_{\mathrm{IL}}^{\mathrm{CA}}$which quantifies the effectiveness of a single interlayer as a crack arrester,

$$\psi_{\mathrm{IL}}^{\mathrm{CA}} = \frac{J_{\mathrm{tip}}^{\mathrm{CA}}}{J_{\mathrm{far}}^{\mathrm{CA}}} \tag{4.14}$$

$\psi_{\mathrm{IL}}^{\mathrm{CA}}$ can be seen as the J-reduction coefficient, where under a given load $J_{\mathrm{tip}}^{\mathrm{CA}}$ and $J_{\mathrm{far}}^{\mathrm{CA}}$ denote crack driving force and far-field J-integral for a crack in the CA-position, respectively. This concept can be extended to the case of multilayers, where the J-reduction coefficient for a multilayer (ML) $\psi_{\mathrm{ML}}^{\mathrm{CA}}$ is given by (Sis2017)

$$\psi_{\mathrm{ML}}^{\mathrm{CA}} = \frac{J_{\mathrm{tip}}^{\mathrm{CA}}}{J_{\mathrm{far}}^{\mathrm{CA}}} \tag{4.15}$$

Using the configurational forces concept, Sistaninia and Kolednik explained how the multilayer geometry affects fracture strength and fracture toughness. They showed that there is an interplay of three length parameters in multilayered composites. In addition to the interlayer thickness t and the radius of the radius of the crack tip plastic zone r_y^{IL}, the interlayer spacing λ is important: If λ is smaller than r_y^{IL}, then the second interlayer deforms plastically. As the hard-soft transition is closer to the crack tip than the soft-hard transition, an anti-shielding effect is introduced. If r_y^{IL} is sufficiently large to reach multiple interlayers, then each interlayer will introduce an anti-shielding effect. This can be seen in Figure 28, which shows the ratio of the J-reduction coefficients $\Psi_{ML}^{CA}/\Psi_{IL}^{CA}$ as a function of r_y^{IL}/λ for different yield stress ratios. At $r_y^{IL}/\lambda \approx 1, 2, 3, \ldots$ the plastic zone reaches additional interlayers, which causes an increase in $\Psi_{ML}^{CA}/\Psi_{IL}^{CA}$. It is worth mentioning that interlayers in multilayers, while less effective compared to a single interlayers, still significantly reduce the crack driving force J_{tip}^{CA} (Sis17). Furthermore, the authors presented an iterative procedure to find the optimal interlayer spacing for a given load and known mechanical properties of matrix and interlayer. They found that the optimum value of λ is inversely proportional to the square of the applied stress.

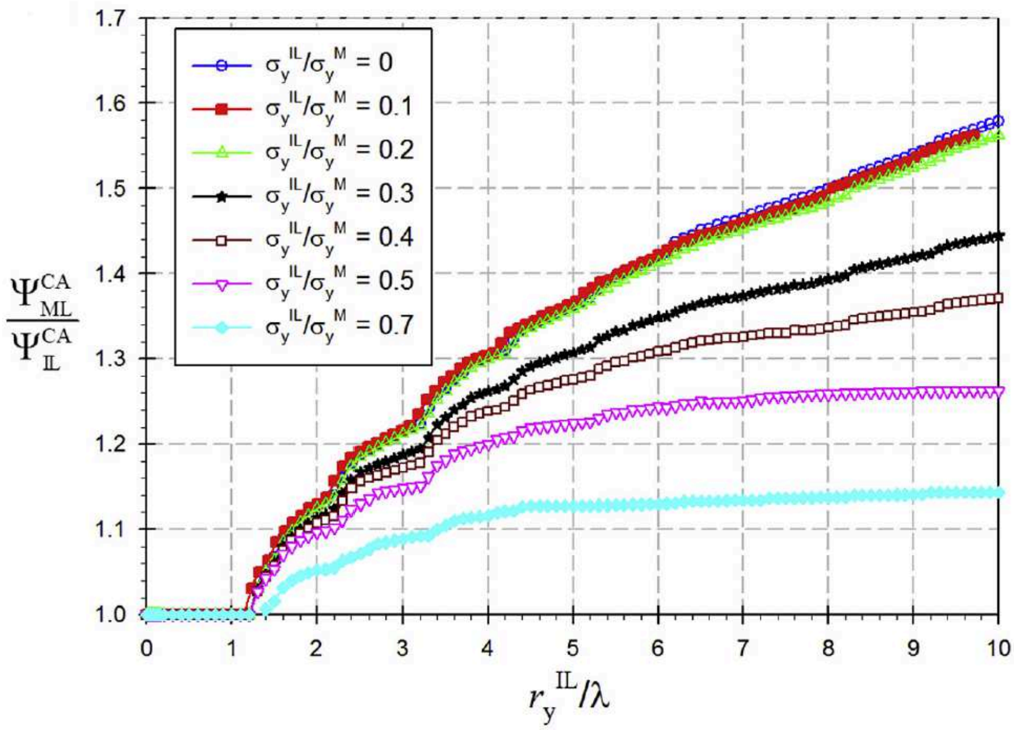

Figure 28: Ratio of the J-reduction coefficients $\Psi_{ML}^{CA}/\Psi_{IL}^{CA}$ as a function of r_y^{IL}/λ for different yield stress ratios at constant t and λ. (Sis2017)

5 Manufacturing of inhomogeneous materials

Many modern bulk metals and alloys already are high-performance materials. Through the addition of secondary phases, however, some properties can be further improved or tailored for specific applications. Metallic composites, or metal matrix composites (MMC), are a class of materials that can be distinguished according to their base metal, the manufacturing process or the type of reinforcement. An extensive overview can be found in (Kai2006). Figure 29 is a schematic overview of different approaches to introduce reinforcements to improve properties of a given matrix material.

The primary purpose of reinforcing with fibers or particles is to increase stiffness and strength (Kai2006). Regarding the exploitation of the aforementioned material inhomogeneity effect to improve the fracture toughness, it is possible to obtain gradients in local mechanical properties by introducing gradients in particle distribution and density (e.g. by centrifugal casting (Raj2010). However, this strategy might have adverse effects, as was studied e.g. in (Seg2003). The authors showed that an inhomogeneous particle distribution results in increased stresses and strains both within the particles as well in the matrix in-between. This leads to earlier onset of damage and a reduction of the composite flow stress and ductility. On the other hand, there is also evidence for the improvement of fracture toughness by particle reinforcement, e.g. in composites with an epoxy matrix. Interestingly, both the addition of rigid as well as soft particles, usually rubber, increase the toughness of the composite. Extensive reviews on particle reinforcement in epoxies can be found in (Gar1988) and, more recently, in (Bag2009).

Laminates, on the other hand, are ideal for the study of the material inhomogeneity effect both experimentally and numerically. For that reason, the production of metallic laminates will be discussed in more detail in this chapter.

The structure of this chapter is as follows: In 5.1, the basics of laminate fabrication via deformation bonding are covered, and 5.2 presents and compares the most common processes suitable for laminate production. Chapter 5.3 then explores the press bonding process - both in theory and with forging experiments. With the lessons learned from chapter 5.3, composite samples suitable for testing the material inhomogeneity effect were produced. The materials and experimental details are explained in chapter 5.4.

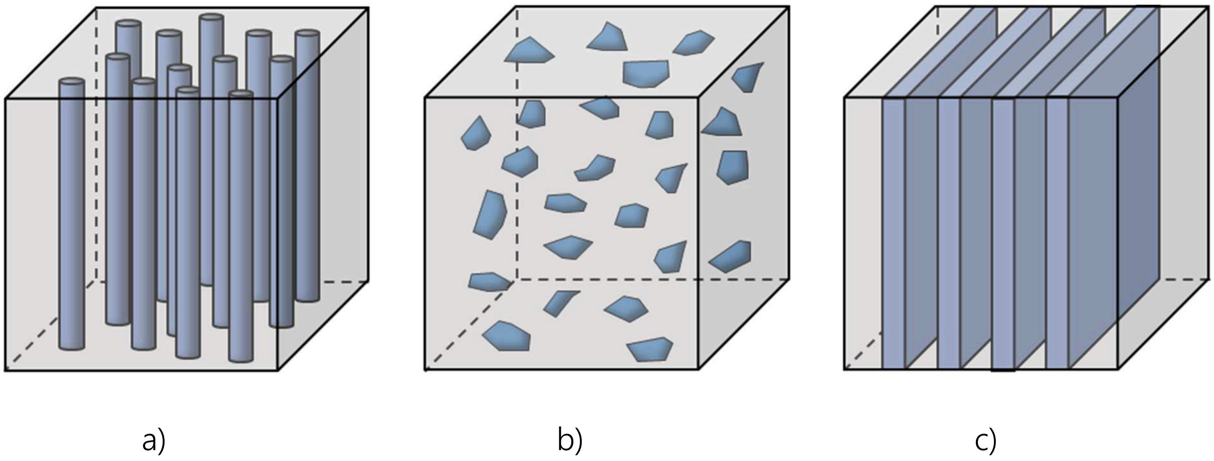

Figure 29: Schematic overview of metallic composites. a) Fiber reinforced composites, b) particle reinforced composite and c) laminated composite

5.1 Manufacturing of metallic laminates – the basics

The idea of laminating similar or dissimilar metals to create a composite material has already been known in the antiquity. In "The Iliad of Homer" (Hom) from 800 BC, Achilles' shield is being described as a composite with five distinct layers - bronze, tin, gold, tin, bronze. Up to 2000 years old laminated steel plates, tools and weapons have been found in countries like Egypt, Greece, Turkey or Japan (Wad2000).

Since the crude manual forging of that era, different production routes for laminates have been devised, see e.g. the review given in (Les1996). These can be classified in deposition or bonding techniques, see overview in Figure 30.

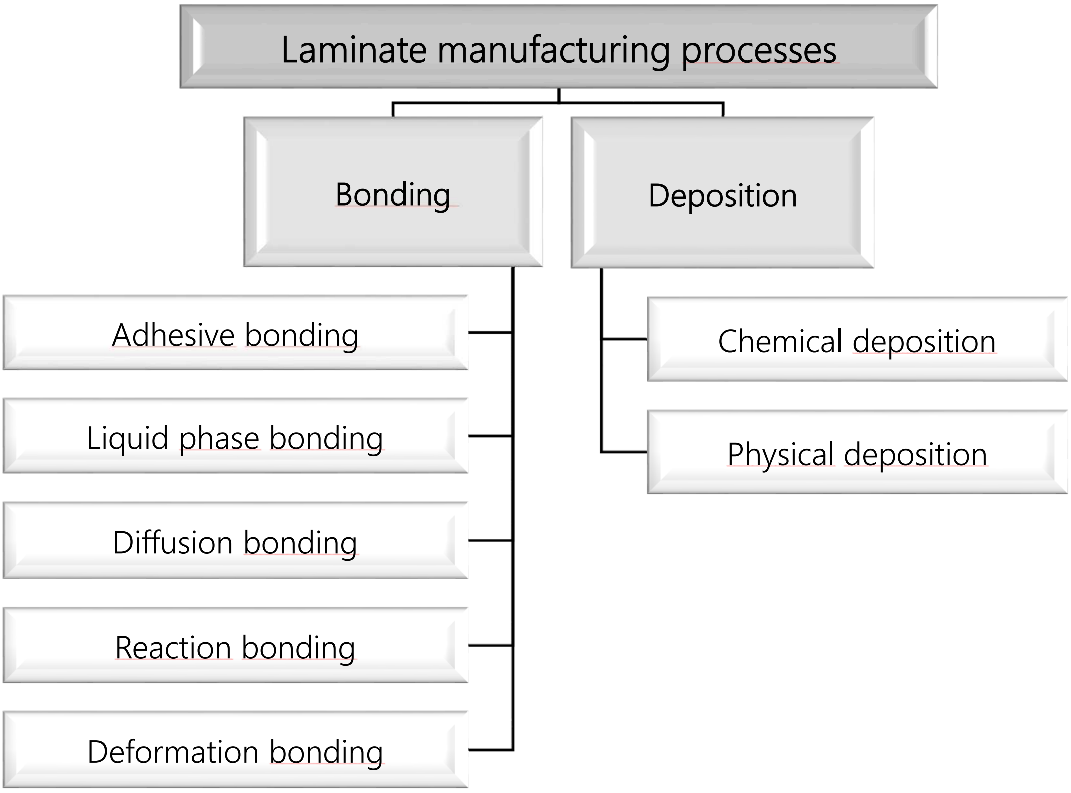

Figure 30: Overview over various process routes suitable for the production of laminates.

While the deposition route using e.g. chemical or physical vapor deposition (CVD or PVD), sputtering or electroplating excels in producing laminates with very thin individual layers, it is often too time consuming and too expensive for large scale components. Bonding processes, on the other hand, can be implemented more easily on an industrial scale. Laminates can be produced e.g. by using adhesives, welding, soldering and brazing, diffusion processes, chemical reactions or plastic deformation.

In deformation bonding, oxide films and contaminants on the interface between layers are broken up by extensive plastic deformation, enabling high interfacial strengths. In this chapter, the mechanisms governing bond formation and selected solid-state welding processes are discussed. It is based on the comprehensive reviews by Milner and Rowe (Mil1963), Li (Li2008) and Mori (Mor2013).

5.1.1 Bond formation in solid state welding

All solid state welding processes aim to develop a sufficient bond between the individual layers. Depending on the type of process and applied temperature range, different mechanisms like adhesion, mechanical interlocking, diffusion or the development of metallurgical bonds occur, which join prior separate pieces of metal together.

Different theories have been proposed to explain the mechanism of bond formation. The *energy barrier theory*, for example, states that is a certain energy barrier (e.g. from the misorientation of the crystals at the interface) must be overcome in order to initiate bonding, (Moh1975, Sem1961). Parks (Par1953) postulated that recrystallization of a deformed region on either side of the interface is an important mechanism. In contrast to the energy barrier theory, the *film theory* is thought to describe the more dominant mechanism governing bonding, especially when low temperatures are involved. This film theory is eludicated in the following.

As practical experience shows, two pieces of metal in contact do not “automatically” weld together. This is due to ever-existing contamination or oxide layers (Moh1975). A sufficiently large deformation is necessary to break up these layers of oxides, humidity, grease, or dust particles. Figure 31 depicts this film theory of bond formation (Bay1983).

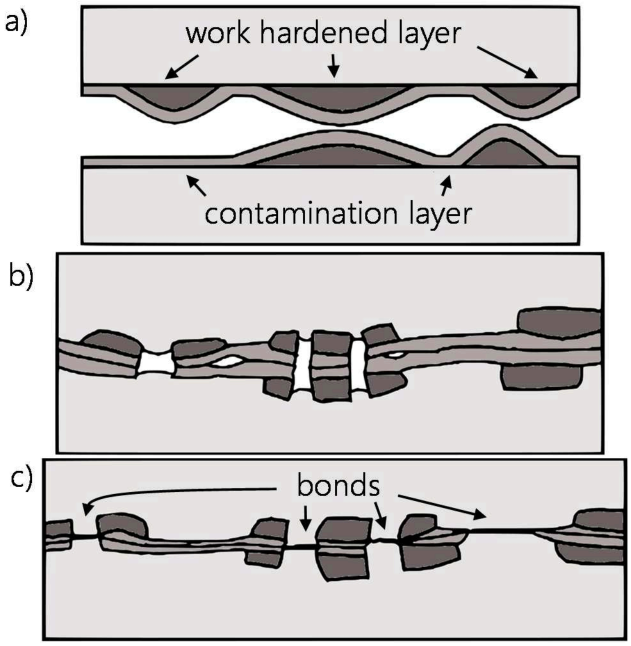

Figure 31: Model for bonding mechanisms during cold welding. a) Scratch brushed surface with a work hardened cover layer and a contaminant film. b) Extrusion of virgin materials through cracks in the cover layer. c) Bonding. Adapted from (Bay1983)

When the surface expands (e.g. during upsetting or rolling), brittle layers on top fracture. Driven by the applied pressure, uncontaminated base material is extruded through these gaps. Between two opposite extrusion sites, metallic bonds develop. It is clear that, if this model is appropriate, remnants of the former oxide and contamination layers should be present alongside the interfaces, and that the fracture surface should show distinctive features as shown schematically in Figure 32.

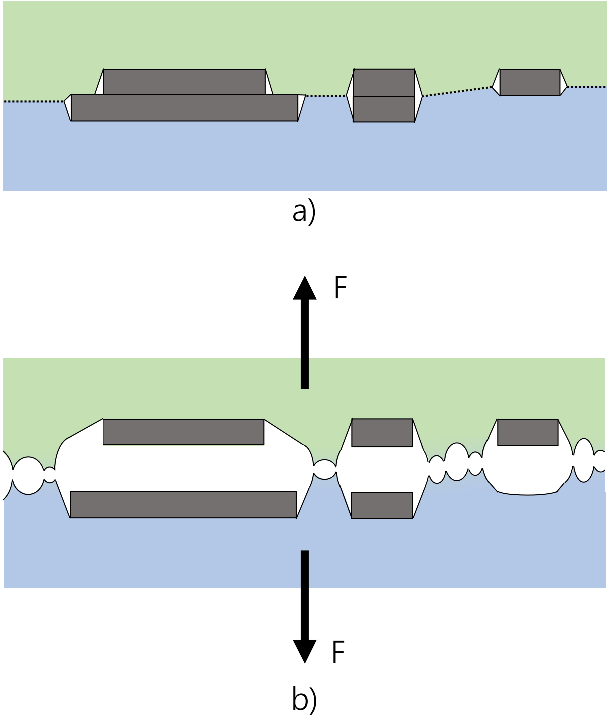

Figure 32: A schematic explaining the development of a typical fracture surface of an interface. a) Nonmetallic inclusions prevent completeness of the bonding between two layers. b) Upon separation of the layers by a force F, ductile pores develop where bonding was successful.

To show that this is indeed the case, an exemplary cross-section of an interface between two forged steel sheets was prepared, Figure 33a. The interface between the upper ferritic steel and the lower ferritic-pearlitic steel, as well as white non-metallic inclusions are clearly visible. Figure 33b shows a SEM image of the fracture surface of two separated layers. Ductile fracture occurs locally where metallic bonds were formed, and no bonding was possible where particles of the fractured surface layer are present.

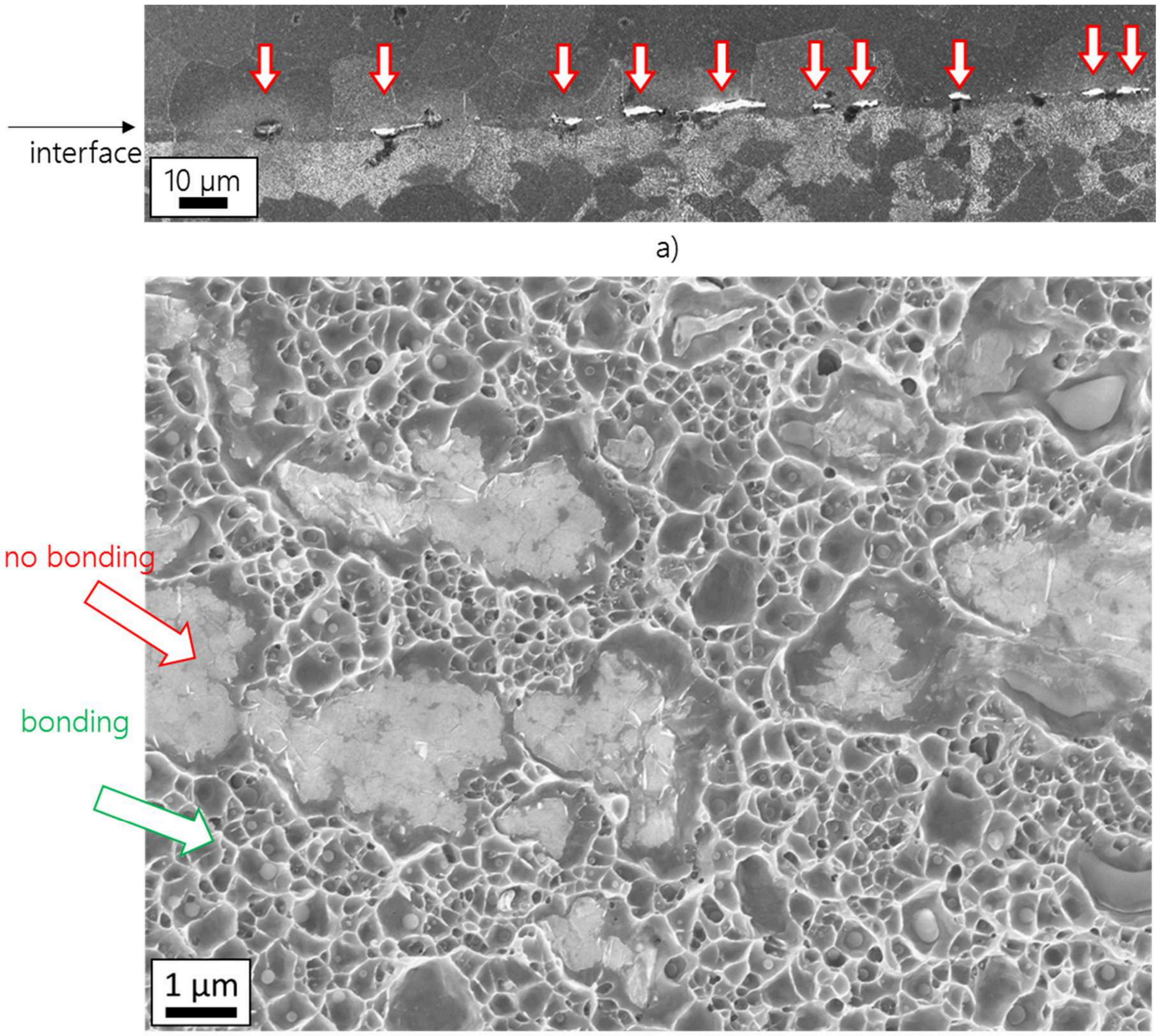

a)

b)

Figure 33: (a) Bonding defects alongside an interface are marked with red arrows. (b) A tensile test normal to the interface reveals ductile pores on bonding sites, whereas the remnants of the former cover layer are clearly visible.

5.1.2 Parameters affecting solid state welding

Different parameters have been identified, which have an influence on bond formation in solid state welding processes. It is generally accepted that the degree of deformation, the surface preparation and the welding temperature are the main factors governing the success and the quality of solid state welding processes. Other parameters affect the welding process as well, especially at ambient temperatures, such as the elapsed time between surface preparation and welding, the purity and lattice structure of the metals, the geometry of the deformation zone or a post-welding heat treatment (Eiz2008).

The aforementioned main three parameters will be discussed concisely in this chapter.

5.1.2.1 Degree of deformation

The importance of the creation of new surfaces in a solid state welding process is evident from the preceding chapter: the higher the deformation, the larger is the possible bonding area. This crucial parameter, the degree of deformation, can be expressed as a surface expansion X or as the degree of surface exposure Y (Mor2013):

$$X = \frac{A_1 - A_0}{A_0} \tag{5.1}$$

$$Y = \frac{A_1 - A_0}{\mathrm{A}_1} \tag{5.2}$$

A_0 and A_1 are the interface areas before and after deformation, respectively. Thereby, Y describes for a given contact area A_1 the fraction of 'fresh' surface created during forming, where metallurgical bonds can form. This parameter is equal to the thickness reduction e.g. during a rolling process.

A certain threshold surface exposure Y_{min} is necessary to form a stable bond between two parts. The reason for that is twofold and can be understood from the schematic drawn in Figure 34. The elastic deformation during pressure welding, $\varepsilon_{\mathrm{el}}$, tries to recover after the pressure is relieved, Figure 34a. This results in elastic springback stresses σ_{el} at the newly formed bondings, with their magnitude being determined by Young's Modulus and maximum stress during the process. As depicted in Figure 34b, the bond strength of the interface starts to rise only after reaching a certain surface exposure Y_0, where the first bonds are being formed, recall Figure 31. This initial threshold depends once again on the material and welding process (Bay1979), but particularly on the surface preparation as discussed in the next chapter. To achieve a lasting bond, the interfacial bond strength has to exceed the springback stress, which is the case at the threshold surface exposure Y_{min}. Figure 35 depicts shear strengths of several roll-bonded similar and dissimilar material combinations (Vai1959, McE1962). For severe thickness reductions, the bond strength can reach a plateau determined by the strength of the weaker component.

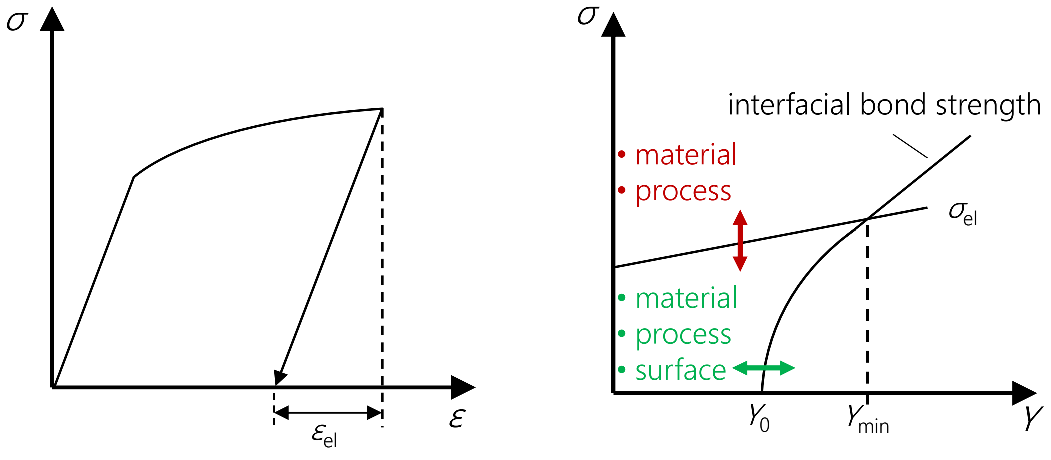

a) b)

Figure 34: a) Elastic deformation ε_{el} during pressure welding cause springback stresses σ_{el}. b) Bonds begin to develop after a certain threshold surface exposure Y_0. Due to the springback stress a minimum surface expansion Y_{min} is necessary to form a stable bond.

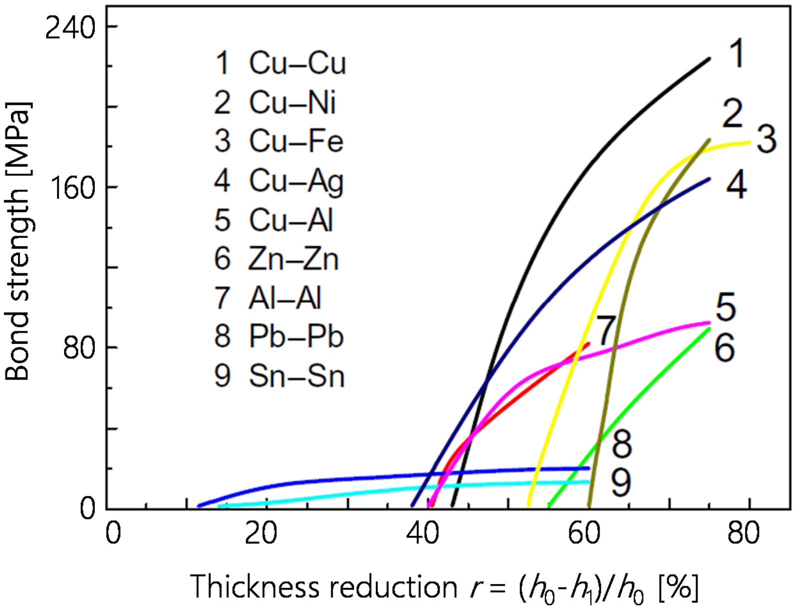

Figure 35: Bond shear strength as a function of the thickness reduction $r = (h_0 - h_1)/h_0$ for different material combinations (Vai1959, McE1962).

5.1.2.2 Surface preparation

While surface preparation is important for deformation welding processes in general, it is essential for cold welding processes. For example, surface oxides may be ablated using a diluted acid solution, while alkaline detergents efficiently remove oil or other organic matter (Li2011). Three types of preparation methods can be distinguished (Cle1986):

- chemical cleaning
- mechanical cleaning
- establishment of a brittle cover layer

While many different methods have been studied in the literature, e.g. (Cle1986), (Jam2011), commonly degreasing and subsequent scratch brushing with a wire brush yields good interface strengths in cold welding processes. However, the optimal surface preparation method depends on the material combination (Zha1997).

The surface roughness is crucial as well. Surface asperities can be sheared easily during deformation, destroying the contamination layers in the process. For that reason, polished surfaces are more difficult to weld (Moh1975).

5.1.2.3 Temperature

An obvious influence of the temperature on solid state welding processes is the decrease of the flow stress, as well as the increase of formability with increasing temperature. While the decrease in flow stress lowers the necessary forces during the welding process, it also reduces the elastic springback ε_{el}, compare Figure 34. In practice, an increase in temperature reduces the threshold surface exposure Y_{min}, as was e.g. shown for roll-bonding of aluminum sheets (Eiz2009).

(Nak1988) studied the influence of the homologue temperature T/T_m, T_m being the melting temperature, on the critical surface expansion ratio X_s (equation 5.1) necessary to obtain a bond strength exceeding 90% of the ultimate tensile strength of the base material. They found that with increasing T/T_m, X_s decreases remarkably and reaches unity at a certain homologue temperature. The homologue temperature T/T_m where X_s=1 is 0.5 for the welding of copper and nickel; for mild steel 0.55; for aluminum 0.7 and for stainless steel 0.8.

5.2 Deformation bonding processes – an overview

In this chapter, a short introduction into the most common deformation bonding processes, i.e. roll bonding, co-extrusion, impact welding, and press bonding shall be given, followed by a basic comparison. The press bonding process is discussed in more detail in a following chapter, as it is the process used in this thesis.

5.2.1.1 Roll bonding

Roll bonding is a cost-effective process to produce claddings or laminated composites and has therefore received much attention in the past decades, e.g. (Eiz2008, Eiz2009, Vai1959, Li2008, Li2011, Jam2011,).

Figure 36 gives an overview of successfully roll bonded material combinations, where it is evident that metals with a face centered cubic (FCC) crystal structure are easier to bond (Li2008). Steel-based laminates are commonly bonded at elevated temperatures and often in steps, see e.g. the reports for steel-Al (Buc2008, Jin2008), steel-brass (She1990) or steel-steel (Yin2013) laminates.

An example of the application of the roll bonding process to produce multilayered composites in a single rolling pass is the work of Chaudhari et al. (Cha2009), who studied the cold roll bonding of multi-layered Ti-Al bi-metal laminate composites both numerically and experimentally. They observed a preferential extrusion of the softer material, which could be reduced with

- increasing coefficient of friction
- decreasing thickness reduction (also decreasing interface strength)
- increasing the layer thickness of the soft material and
- increasing of the roll radius.

Since the introduction of the accumulative roll bonding (ARB) process by (Sai99) (Figure 37) it has been widely used to produce multilayered composites, e.g. Al-Cu (Eiz08-2), Al-Ni (Moz2010) or Al-Zn (Deh2011). However, in these studies necking and rupturing of the harder layer occurred at higher strains, in fact forming a dispersion strengthened composite. This rupturing is a general problem when producing bimaterial multilayers using ARB and can be an issue for applications where a continuous layer is desired, e.g. when exploiting the material inhomogeneity effect. To study the rupturing of the harder layer, (Gov2013) produced aluminum-copper and aluminum-brass multilayers with ARB. They found that the layer fragmentation is caused by the formation of shear bands and argue that a proper selection of strength ratio and work hardening of the involved materials can delay this effect. These shear bands could also be clearly observed in (Deh2011).

Roll bonding processes can be further improved when combined with asymmetric rolling to introduce an additional shear component into the process. For example, ultra-thin AA1050/AA6061 ARB foils with a thickness of 40 µm could be produced that way (Yu2013).

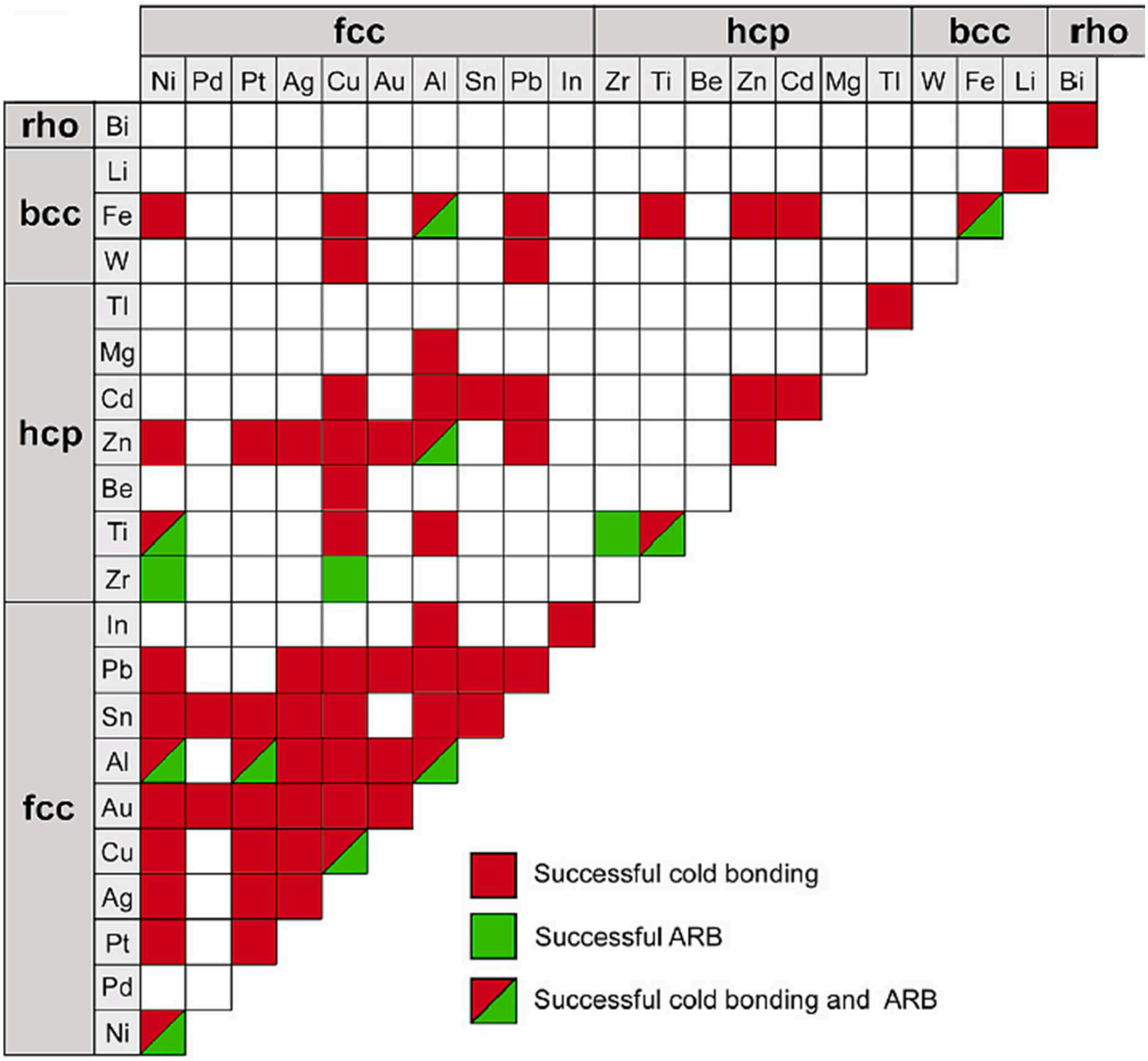

		fcc										hcp							bcc			rho
		Ni	Pd	Pt	Ag	Cu	Au	Al	Sn	Pb	In	Zr	Ti	Be	Zn	Cd	Mg	Tl	W	Fe	Li	Bi
rho	Bi																					🟥
bcc	Li																				🟥	
	Fe	🟥				🟥		◩		🟥			🟥		🟥	🟥				◩		
	W					🟥				🟥												
hcp	Tl																	🟥				
	Mg							🟥														
	Cd					🟥		🟥	🟥	🟥					🟥	🟥						
	Zn	🟥		🟥	🟥	🟥	🟥	◩		🟥					🟥							
	Be					🟥																
	Ti	◩				🟥		🟥				🟩	◩									
	Zr	🟩				🟩																
fcc	In							🟥			🟥											
	Pb	🟥			🟥	🟥	🟥	🟥	🟥	🟥												
	Sn	🟥	🟥	🟥	🟥	🟥		🟥	🟥													
	Al	◩		◩	🟥	🟥	🟥	◩														
	Au	🟥	🟥	🟥	🟥	🟥	🟥															
	Cu	🟥		🟥	🟥	◩																
	Ag	🟥		🟥	🟥																	
	Pt	🟥		🟥																		
	Pd																					
	Ni	◩																				

🟥 Successful cold bonding

🟩 Successful ARB

◩ Successful cold bonding and ARB

Figure 36: An overview of successful cold roll bonding and accumulated roll bonding ARB. FCC metals are easier to bond (Li2008).

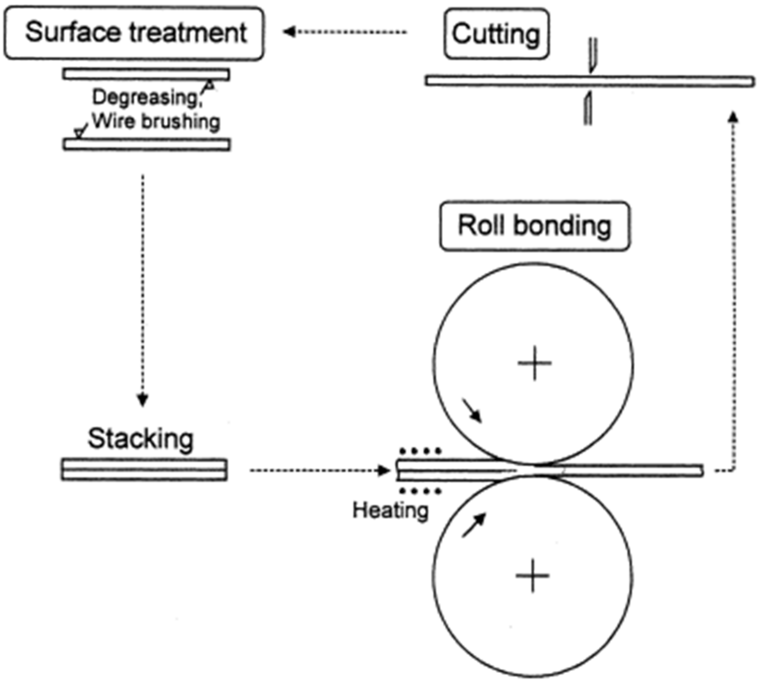

Figure 37: Schematic showing the accumulated roll bonding process. (Sai1999)

5.2.1.2 Impact welding

A big advantage of the impact welding process is the possibility of joining thick plates of significant dimensions, as it does not require extensive deformation. Metallic bonds are instead formed when two surfaces collide at very high velocities (up to several hundred m/s), causing impact pressures of up to several GPa. One way to achieve this rapid acceleration is using the energy of detonating explosives, another is to use electromagnetic pulse welding.

When joining two parts with this process, a very characteristic wavy surface structure develops. These patterns may be caused by reflected shock waves and the Kelvin-Helmholtz instability (Ben2010). The weld quality is mainly affected by the collision velocity, the angle of impact as well as the properties of the joined materials (Cow1971). The surfaces only need simple cleaning, such as wire brushing: Due to the high contact speeds involved in this process, surface contaminates are expelled in a fluid-like jet, leading to chemically clean surfaces and a metallurgical bond, see Figure 38. However, the setup of the process is complex and time consuming.

While it is relatively easy to produce a two-layer cladded material, three-layered sandwich laminates require virtually double the work as two separate (or, for symmetrical assemblies, two simultaneous) explosions have to be fired (Cle1983). The production of multilayers is possible, nevertheless. Bataev et al. (Bat2011) succeeded in producing a 21-layered composite using a low-carbon steel in three consecutive steps, see Figure 39. For the impact welding of a 23-layered aluminum–titanium composite, a single step was sufficient (Bat2012).

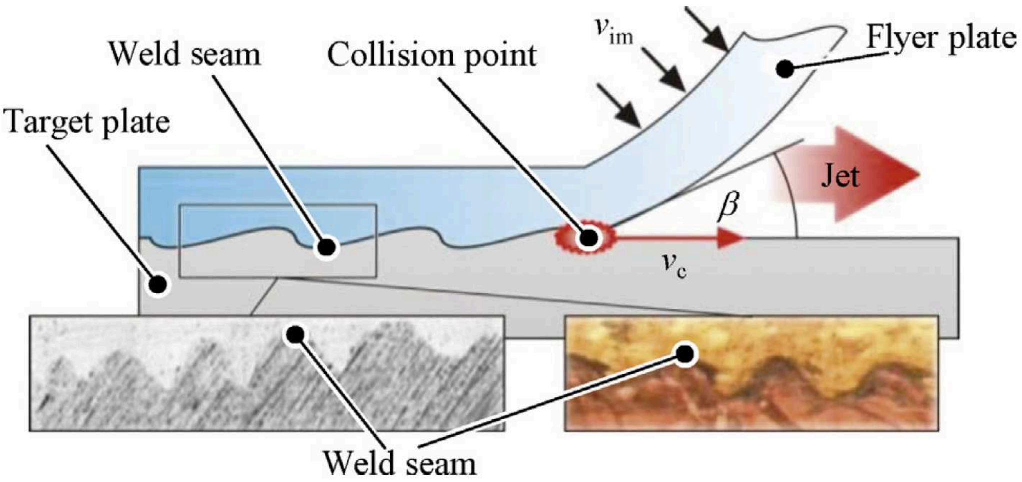

Figure 38: High impact velocities during the explosion welding process cause the wavy interface and the jetting effect (Ben2010).

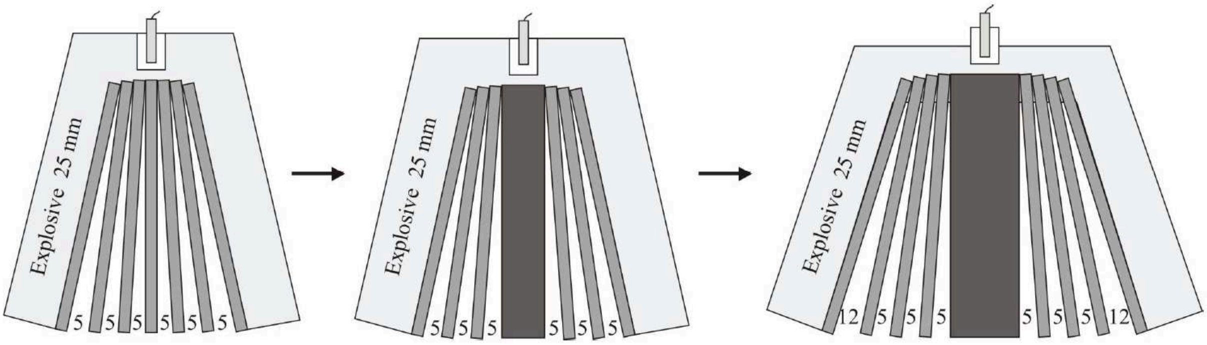

Figure 39: A 21-layered steel composite was produced via impact welding in three steps (Bat2011).

5.2.1.3 Extrusion

The simultaneous extrusion of rotational symmetric bimetallic rods, consisting out of the outer “sleeve” and the inner “core” material, is an economic way to produce composite materials. For example, (Eng2012) studied the co-extrusion of aluminum profiles with different sheet metals as reinforcing elements. While the Al-Mg laminate could successfully be extruded that way, both the steel and titanium reinforcement sheets fractured during the extrusion. (Wu2015) produced an Al-Mg sandwich laminate by extruding a round, Ø 80 mm bimetallic rod through a rectangular, 3 mm x 60 mm die. By repeating the extrusion step in an accumulative extrusion bonding process, (Xin2015) fabricated multilayered Al-Mg plates.

An adaption of the classical extrusion process uses the principle of equal channel angular extrusion, ECAE. The principle of ECAE is illustrated in Figure 40. Originally developed and patented by Segal (Seg1977) it served as a means to process metals and powders by simple shear, e.g. for powder consolidation or grain refinement (Seg1995). In 2007, Eivani and Taheri (Eiv2007) were the first to adopt this process to extrude bimetallic Cu-Al rods at elevated temperatures. They obtained improved interface shear strengths compared to a standard extrusion process. ECAE of Cu-Al rods at ambient temperatures was later shown to be feasible as well (Zeb2011). In addition to the metallurgical bonds formed during the process, mechanical interlocking of the layers also improve interface strength.

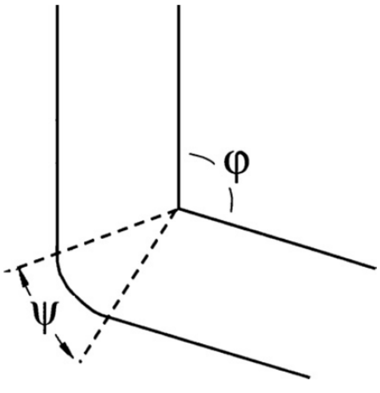

Figure 40: Illustration of the equal channel angular extrusion process with the extrusion angle φ and the curvature angle ψ (Zeb2011).

5.2.1.4 Press bonding

Press bonding is a process where two or more separate pieces of metal can be sufficiently deformed by the applied pressure so that metallic bonds form between the surfaces in contact. By choosing a proper die, material flow and flash formation can be controlled, which is a prerequisite for mass production. Excess flash can easily be machined afterwards. Being a discontinuous process, the separate metal sheets have to be cleaned, assembled and optionally heated each time before a part is welded together by forging.

Furthermore, high temperatures greatly assist in the formation of a strong bond by diffusion. However, press bonding is not to be confused with the more time consuming diffusion bonding process (Kaz1985), as the latter is performed on comparatively low stress and high temperatures ($T > 0.7\ T_m$).

In the literature press bonding is often combined with other processes for laminate production. For example, Sherby et al. (She1990) employed a variety of press bonding and hot rolling steps to produce laminates with alternating layers of ultra-high carbon steel (UHCS) and brass. All bonding procedures were performed below the A_1 temperature of the UHCS material of about 775 °C. After a selective heat-treatment, the difference in hardness between the hardened steel and soft brass layers was a factor 10.

(Web2013) produced two-layered steel plates with a total thickness of 9 mm by press bonding combined with hot roll bonding. The final laminate consisted of a 3 mm thick 0.45% carbon steel layer and a 6 mm 0.15% carbon steel layer. However, the authors did not state any details about initial plate thicknesses and parameters of forging and hot rolling.

Due to the variability of the press bonding process and the high forming forces offered by a hydraulic press, multilayered composites with varying geometry can be manufactured with high degrees of deformation. In chapter 5.3, this process will be discussed in more detail and used to manufacture steel-based multilayered composites.

5.2.1.5 Deformation bonding processes - a basic comparison

Table 3 presents a basic comparison of some of the characteristics of the deformation bonding processes discussed earlier. The final choice of the joining process for a specific material combination is dependent not only on the materials themselves, but also on parameters like geometry, setup time and cost. As such, no general recommendation can be made.

Table 3: Basic comparison of selected deformation bonding processes (Kas2014).

		Roll bonding	Press bonding	Extrusion	Impact welding
Characteristics		- continuous - Well-esablished process - With or without heating	- discontinuous - Simple setup - usually at high temperatures - optional use of dies	- (quasi-)continuous - High pressure necessary - High amount of wear on dies	- continuous - Complex setup - heat treatment after bonding - Shape restoration by subsequent pressing (thick clads) or rolling (thin clads)
Process limits	Geometry	- Flat strips and plates	- Flat - other simple geometries by use of dies	- typically round cross sections, flat also possible - limited by extrusion force	- Flat and curved plates - concentric tubes and rods
	Number and thickness of layers	- Suitable for cladding and multilayer production - Very thin layers possible with ARB - limited by maximum rolling force	- dependent on material combination and geometry - diffusion increases product range	- Suitable for cladding and multilayer production	- Very thick layers platable - Mostly used for cladding or sandwich laminates - multilayer laminates possible, but difficult
	Material combinations	**Medium** - hard metals more difficult to bond - Dissimilar metals difficult to bond - Possible improvements by asymmetric rolling	**Medium** - combinations limited by high temperatures (i.e. formation of brittle compounds) - More suitable for bonding of similar materials	**Medium** - combinations limited by maximum extrusion forces - Typically Al, Cu or Mg alloys - Formability is improved by high hydrostatic pressure in ECAE	**Very good** - Highly dissimilar metals weldable - no formation of intermetallic compounds, no diffusion - Bonding partners have to be ductile
Surface preparation		**Medium - High** - Degreasing - Optimum surface treatments depending on materials - prevention of reoxidation	**Medium** - Degreasing - prevention of reoxiation	**Medium** - degreasing - Preparation dependent on temperature and materials	**Low** - degreasing - explosive contact of metal surfaces expells contaminants

5.3 The hot press bonding process in laminate production

In this thesis, the hot press bonding process is used to manufacture metallic composites. First, influencing processing parameters are identified and preliminary forging experiments with multilayered steel composites are presented. A fracture mechanics experiment then highlights a key issue with this process. Further information about the process can be found in dedicated literature, e.g. (Doe2007).

5.3.1 General considerations and parameters

As mentioned earlier, press bonding works when both surfaces expand during upsetting. This is of consequence: composites with a high difference in flow stress can hardly be joined using such a process. The individual flow stress is dependent of the material itself, and a function of the degree of deformation, the deformation rate and the temperature, Figure 41a-c (Doe86). Therefore, an initial difference in flow stress can very well decrease during the press bonding process through preferential deformation and hardening of the softer phase.

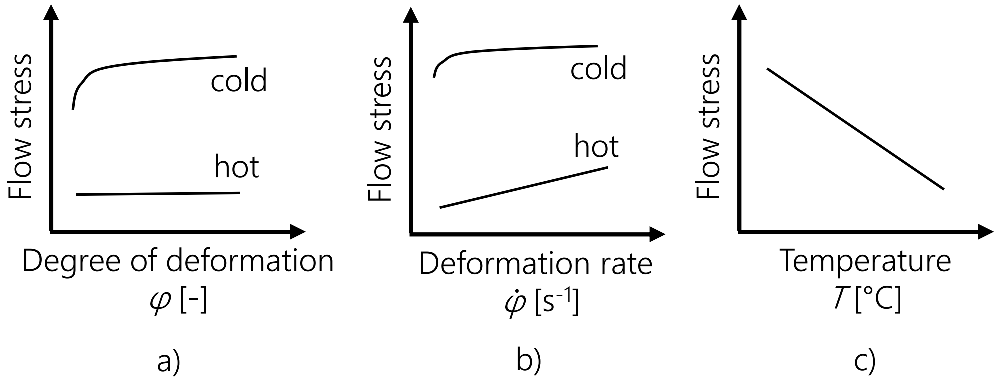

Figure 41: Schematic influence of a) degree of deformation, b) deformation rate and c) deformation temperature on the flow stress in metal forming (Doe86).

Lesuer et al. (Les1996) argue that press bonding requires a careful selection of temperature and strain rate of deformation. Figure 42a depicts two materials with a different strain rate-stress behavior; the behavior of laminate as a whole is defined by the shaded area in-between. At a given strain rate, the highest flow stress of the laminate is reached when each component of the laminate undergoes the same strain, i.e. isostrain behavior is dominant (Figure 42b). The lower bound in flow stress occurs under isostress conditions, where the softer phase is deformed preferentially and extruded from the laminate, Figure 42c. In practice, isostrain behavior can be reached when the individual layers are thin. Frictional forces and bonding between the layers thereby enforces uniform deformation. On the other hand, isostress behavior can be reached when the layers are very thick.

In general, materials and processing parameters should be chosen so that the individual components of the laminate have comparable flow stresses, which facilitates co-deformation of the layers. This processing window is larger for thin-layered systems (Les1996).

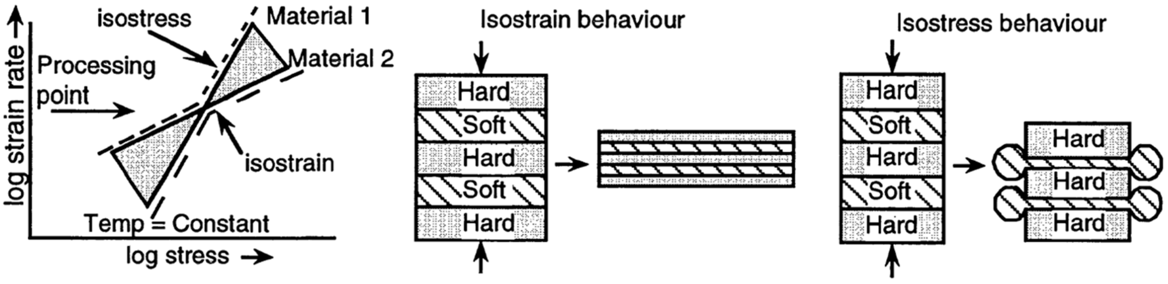

a) b) c)

Figure 42: a) Due to the different behaviour of the hard/soft phase during forging, an ideal processing window exists. b) For isostrain behaviour, co-deformation of the individual layers occurs. c) Isostress behaviour results in a preferred extrusion of the soft phase (Les1996).

5.3.1.1 Thickness reduction and degree of deformation

The thickness reduction in compression is calculated from the final height h and the original height h_0:

$$\text{thickness reduction [\%]} = (1-h/h_0) * 100 \tag{5.3}$$

As mentioned before, the thickness reduction is equal to the surface exposure, which is an important factor governing bonding. Instead of percentages, usually logarithmic strains are used to describe metal forming processes. The degree of deformation φ in an upsetting process is (Doe2007)

$$\varphi = \ln\left(\frac{h}{h_0}\right) = \ln(h) - \ln(h_0) \tag{5.4}$$

5.3.1.2 Strain rate

The strain rate $\dot{\varphi}$ is defined as

$$\dot{\varphi} = \frac{\mathrm{d}\varphi}{\mathrm{d}t} = \frac{\mathrm{d}\varphi}{\mathrm{d}h} \cdot \frac{\mathrm{d}h}{\mathrm{d}t} = \frac{1}{h} \cdot \frac{\mathrm{d}h}{\mathrm{d}t} \tag{5.5}$$

The change in height h with time t is the upsetting speed $\dot{v}$:

$$\dot{v} = \frac{\mathrm{d}h}{\mathrm{d}t} \tag{5.6}$$

It follows that

$$\dot{\varphi} = \frac{\dot{v}}{h} \tag{5.7}$$

The strain rate $\dot{\varphi}$ is therefore dependent on the stack height h. From equation (5.7), it is clear that at a constant value of $\dot{v}$ the deformation rate $\dot{\varphi}$ increases during the forging process, as the height h of the forging decreases. The relative increase in deformation rate during the forging process, $\dot{\varphi} / \dot{\varphi}_0$, can be calculated as follows:

$$\dot{\varphi}\Big/\dot{\varphi}_0 = \frac{v}{h}\Big/\frac{v}{h_0} = h_0\big/h \tag{5.10}$$

Figure 43 illustrates the change in the degree of deformation and the corresponding increase in deformation rate with decreasing specimen height during the upsetting process. When reaching a thickness reduction of 50%, i.e. $h / h_0 = 0.5$, the deformation rate increased by a factor of two. However, this estimation is only strictly valid for a homogenous and uniform deformation. If φ varies locally within the stack, then so does $\dot{\varphi}$. As an approximation, it is possible to calculate an average deformation rate for each layer, knowing the final degree of deformation as well as the forging time t_f:

$$\dot{\varphi}_{avg} = \frac{\varphi}{t_f} = \frac{\varphi}{(h_0 - h)/\dot{v}} \tag{5.11}$$

For example, with a press speed $\dot{v}$ of 6.23 mm/s and an absolute height reduction of $h_0 - h = 14$ mm, the forging time amounts to 2.25 s. A thickness reduction of 90% ($\varphi = 2.3$) results in an average deformation rate of $\dot{\varphi}_{avg} = 2.3/2.25 \approx 1$.

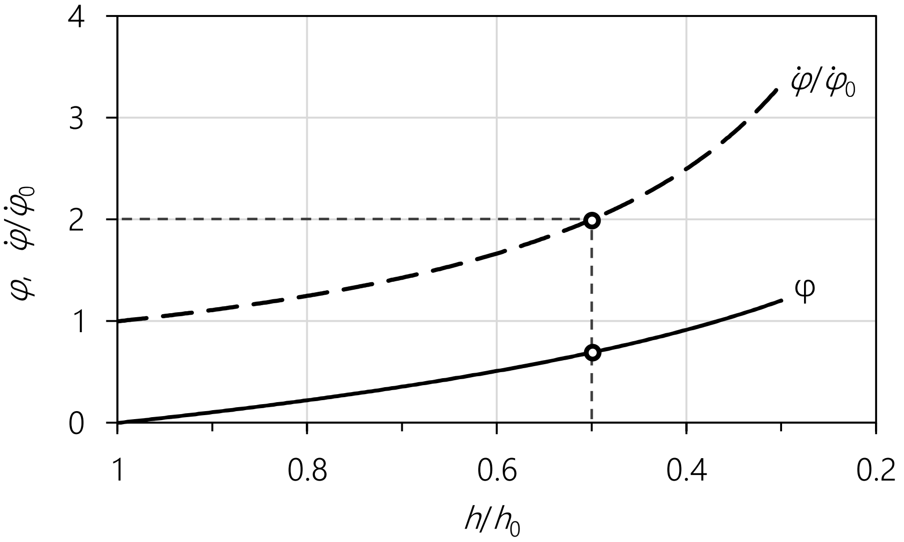

Figure 43: Increase of the degree of deformation φ and the relative deformation rate $\dot{\varphi}/\dot{\varphi}_0$ during the upsetting process.

5.3.2 Preliminary hot press bonding experiments

Using commercially available steel sheets, several multilayer configurations were hot press bonded. As hard matrix material commercially available 22MnB5 was used, which is a typical press hardening steel. Sheets from the non-hardenable deep-drawing steel grade DC04 were used as soft interlayer materials. The chemical compositions of these two steel grades are listed in Table 4.

Table 4: Chemical compositions of the constituents of the steel multilayer in weight-%

	C	Si	Mn	P	S	Cr	Al	B
22MnB5	0.20-0.25	<0.5	<2.0	<0.02	<0.005	<0.5	0.02-0.10	0.002-0.005
DC04	0.04	-	0.2	0.01	0.01	-	-	-

This material combination was selected, as a standard hardening procedure results in a high difference in yield stress between the individual layers. Technical stress-strain curves of hardened 22MnB5 sheets (austenitization at 900 °C/5 minutes, water quenching) and as-received DC04 steel sheets are shown in Figure 44.

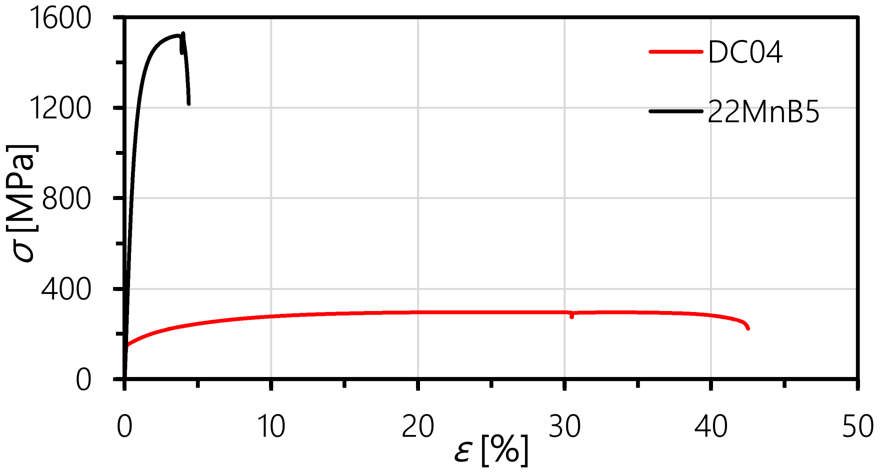

Figure 44: Technical stress-strain diagrams of DC04 and hardened 22MnB5 steel.

The as-received sheets were cut into preforms by waterjet cutting, Figure 45. The reason why this geometry was chosen instead of simple 68x176 mm rectangular sheets is twofold:

- Reduced contact area and therefore higher compressive stresses at a given load of the hydraulic press
- The high length to width-ratio (176:16 mm) within the parallel middle section of the composite ensures a defined deformation state during upsetting (where the material mainly flows to increase the width).

To further reduce the material volume during deformation, the DC04 interlayer preforms were cut at the shoulders, see Figure 45b.

Before forging, the surfaces were thoroughly cleaned with acetone and wire brushed, stacked and packed in heat treatment foil to prevent oxidation of the surfaces during heating to 1 150 °C. Pressure welding was then performed by upsetting at a constant press speed of $\dot{v}$ = 6.23 mm/s. The punches of the press were not pre-heated. The stacks are compressed until the maximum load of the hydraulic press of 1 MN is reached, which corresponds to a maximum stress of approximately 360 MPa. Subsequently, the forged stacks are cooled in air. The deformation behavior is then studied by comparing cross-sections taken from the middle part of the dog bone-multilayers. Etching with Nital produces a visible contrast between the 22MnB5 and DC04 layers, enabling local layer thickness reduction measurements.

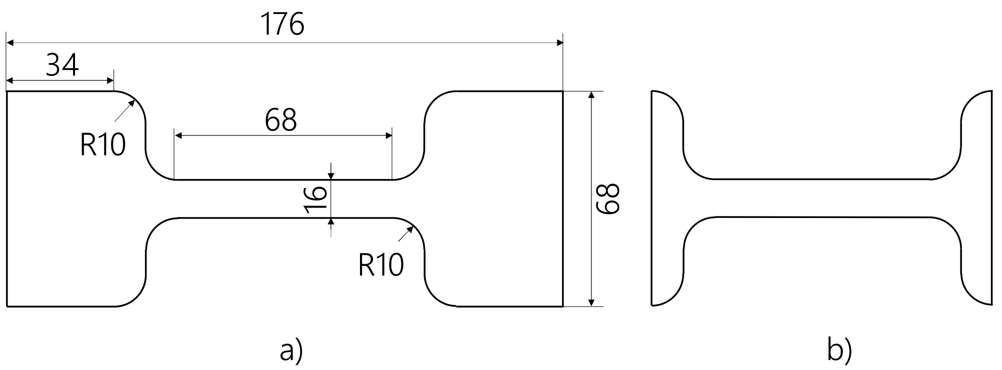

Figure 45: Sheets were cut into dogbone-shaped preforms. a) Dimensions of the 22MnB5 preforms, b) shape of the DC04 preforms.

5.3.2.1 The inhomogeneity of deformation

Two different sheet thicknesses were used of both the hard and the soft layers to assemble different multilayered composites. **Figure 46** shows the variation in stacking sequence of the first multilayers 'ML1' to 'ML4', with initial heights h_0 = 14.18, 11.98, 10.42 and 10.6 mm, respectively.

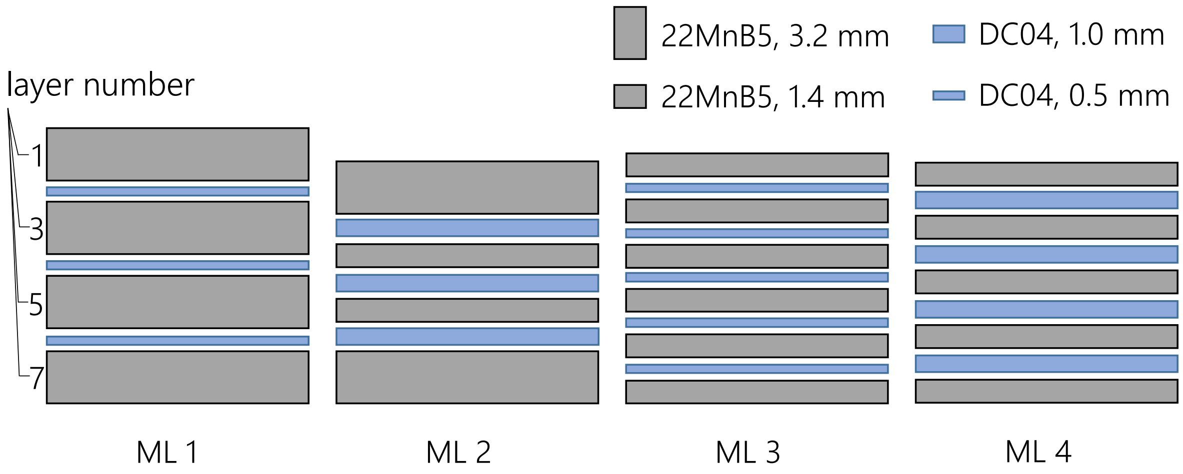

Figure 46: Stacking sequence of the multilayered composites designated 'ML 1' through 'ML 4'. Layers are numbered in ascending order from top to bottom.

The metallographic cross-sections and corresponding measurements of the thickness reductions for the seven-layered composites ML1 and ML2 are depicted in **Figure 47**. In the cross-sections, **Figure 47**a-b, a slight bending of the layers is evident. Representative for all figures in this chapter, the original width B_0 is indicated in **Figure 47**a. The local layer thickness was measured at eight equidistant positions between ± $B_0/2$. The calculated thickness reductions in **Figure 47**c-d, where each line corresponds to measurements within a single layer, reveal two significant deformation inhomogeneities: Layers located on the top and bottom of the composite (layers number 1 and 7) deform significantly less than layers located in the middle (layers number 3-5). Additionally, there is a difference in thickness reduction in the individual layers as measured across the specimen width. While the outer layers (1 and 7) experience a minimum in thickness reduction in the middle, the central layers deform there the most.

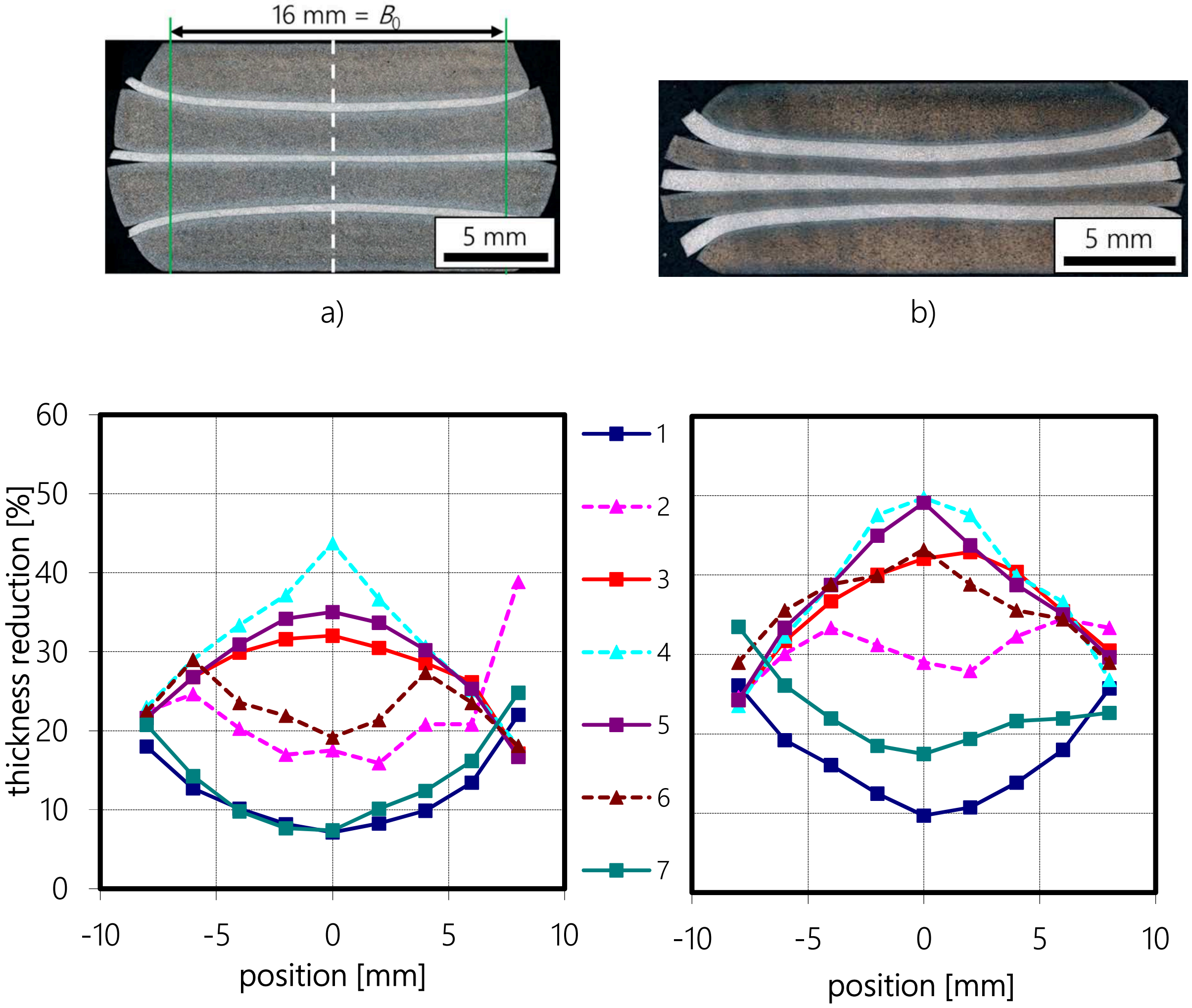

a)

b)

(c)

(d)

Figure 47: a-b) Cross-sections and b-c) local thickness reduction measurements of forged multi-layers ML 1 and ML 2, respectively. Solid lines correspond to 22MnB5, dashed lines to DC04 layers. The layers are numbered in ascending order from top to bottom.

Figure 48a-b show the cross-sections and **Figure 48**c-d the thickness reduction measurements of the composites ML 3 and ML 4, respectively. The same trend as before can be observed: all layers appear straight, but the measurements reveal the same deformation inhomogeneity as for specimens ML 1 and ML 2 in Figure 47.

The thickness reduction can directly be translated into the surface exposure. Weak bonding can therefore be expected in the outer layers and at the sides of these composites.

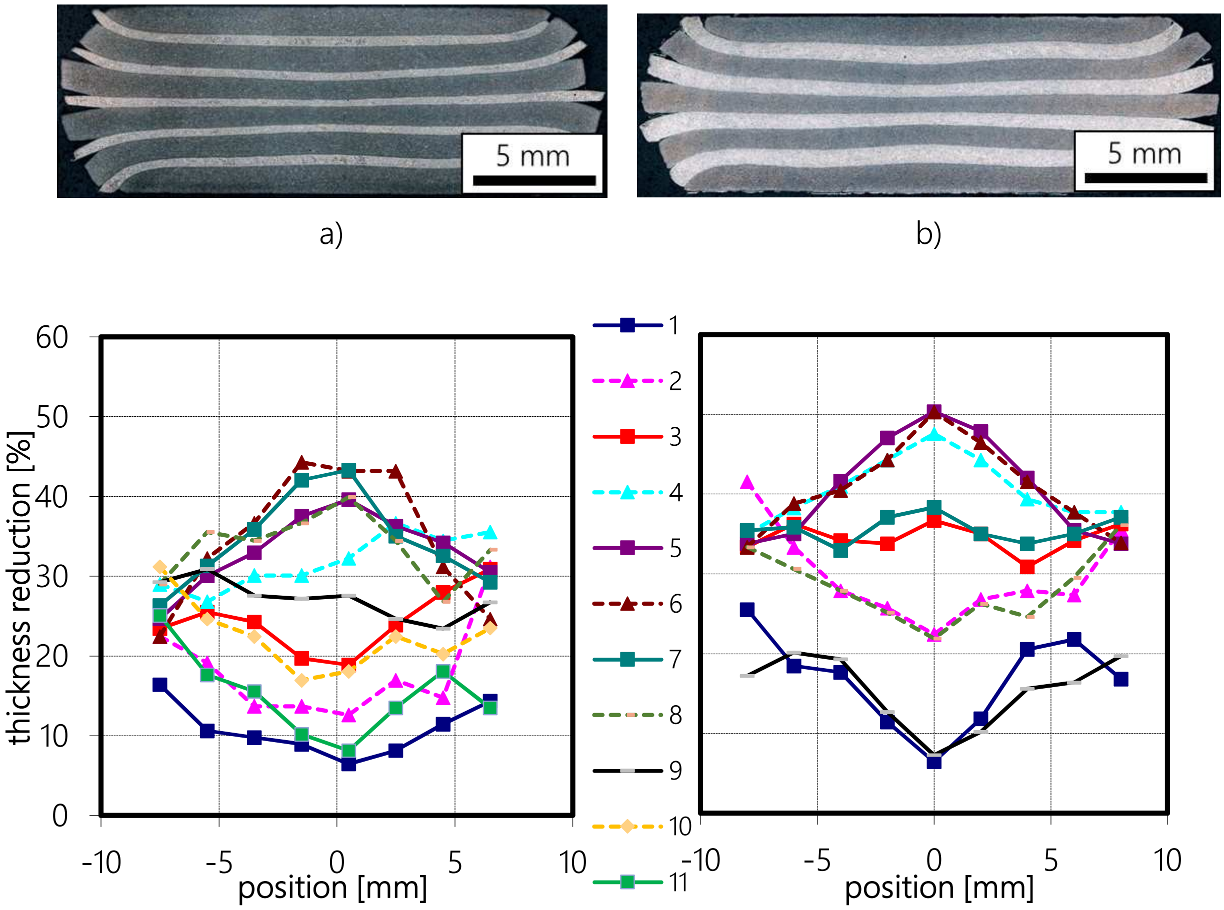

a) b)

c) d)

Figure 48: a-b) Cross-sections and b-c) local thickness reduction measurements of forged multi-layers ML 3 and ML 4, respectively. Solid lines correspond to 22MnB5, dashed lines to DC04 layers. The layers are numbered in ascending order from top to bottom.

Possible reasons for the deformation inhomogeneity are the following:

- Friction between the composite assembly and the forging tools hinders deformation of the outer layers.
- Heat transfer from the composite assembly into the forging tools (which are not pre-heated to forging temperature) effectively causes an increase in flow stress in the outer layers.
- The typical stress state exerted by the tools during upsetting (Doe2007).

5.3.2.2 The influence of the h_0/B ratio

In the next step the influence of the height/width ratio, h_0/B_0, is studied with two more multilayers. As shown in **Figure 49**, the composites ML 5 and ML 6 are assembled by using the same stacking sequence as for the composites ML 1 and ML 4, but with an increased number of layers.

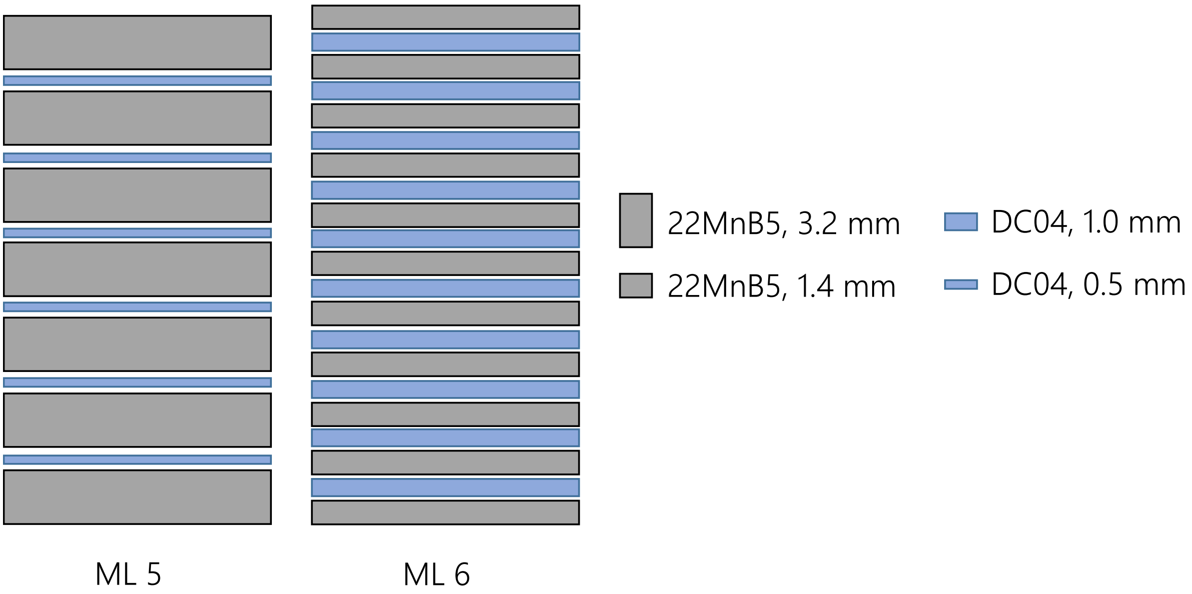

Figure 49: Stacking sequence of the multilayers ‘ML 5’ and ‘ML 6’, which are similar to ‘ML 1’ and ‘ML 4’.

The initial stack geometry, the final height h of the forged composites and the total thickness reduction of these four composites are compared in **Table 5**. By increasing h_0/B_0 of the assembly, the attainable thickness reduction under the same maximum load of 1 MN increased considerably. At a similar h_0/B_0 ratio, the composite ML 6 has a significant higher volume fraction of interlayer material compared to ML 5. The attained thickness reductions are, however, almost identical - the volume fraction of soft phase is therefore less important for the formability of the composites. It can therefore be argued that at forging temperature, the difference in flow stress of 22MnB5 and DC04 is negligible.

Table 5: Comparison of geometry and formability of selected composites

	h_0	h	h_0/B_0	volume fraction of soft phase	global thickness reduction
ML 1	14.18 mm	11.22 mm	0.87	10.5 %	20.8 %
ML 5	25.19 mm	13.33 mm	1.55	11.8 %	46.7 %
ML 4	10.6 mm	7.32 mm	0.65	36.4 %	31.0 %
ML 6	24.52 mm	13.12 mm	1.50	39.4 %	46.5 %

Figure 50 compares cross-sections and thickness reductions of specimen ML 1 and ML 5. The composite ML 1, Figure 50a, shows an onset of bending of the layers that is connected to the inhomogeneous deformation (Figure 47). This bending is much more significant in ML 5 (Figure 50b, and is symmetrical to the middle layer. The continuity of the highly deformed middle layers is still maintained. In Figure 50c-d the deformation behaviors are compared. Each data point in the figures represents the average from eight thickness reduction measurements in an individual layer, allowing for easier comparison. The standard deviation is thereby an indicator of the deformation inhomogeneity across the specimen width. The increase in global thickness reduction between ML 1 and ML 5 is accompanied by an intensification of the deformation inhomogeneity. While the highest local thickness reductions in the middle 22MnB5 layer reached more than 80%, less than 10% was measured in parts of the top and bottom layers. The warped appearance of the layers is a direct consequence of this result.

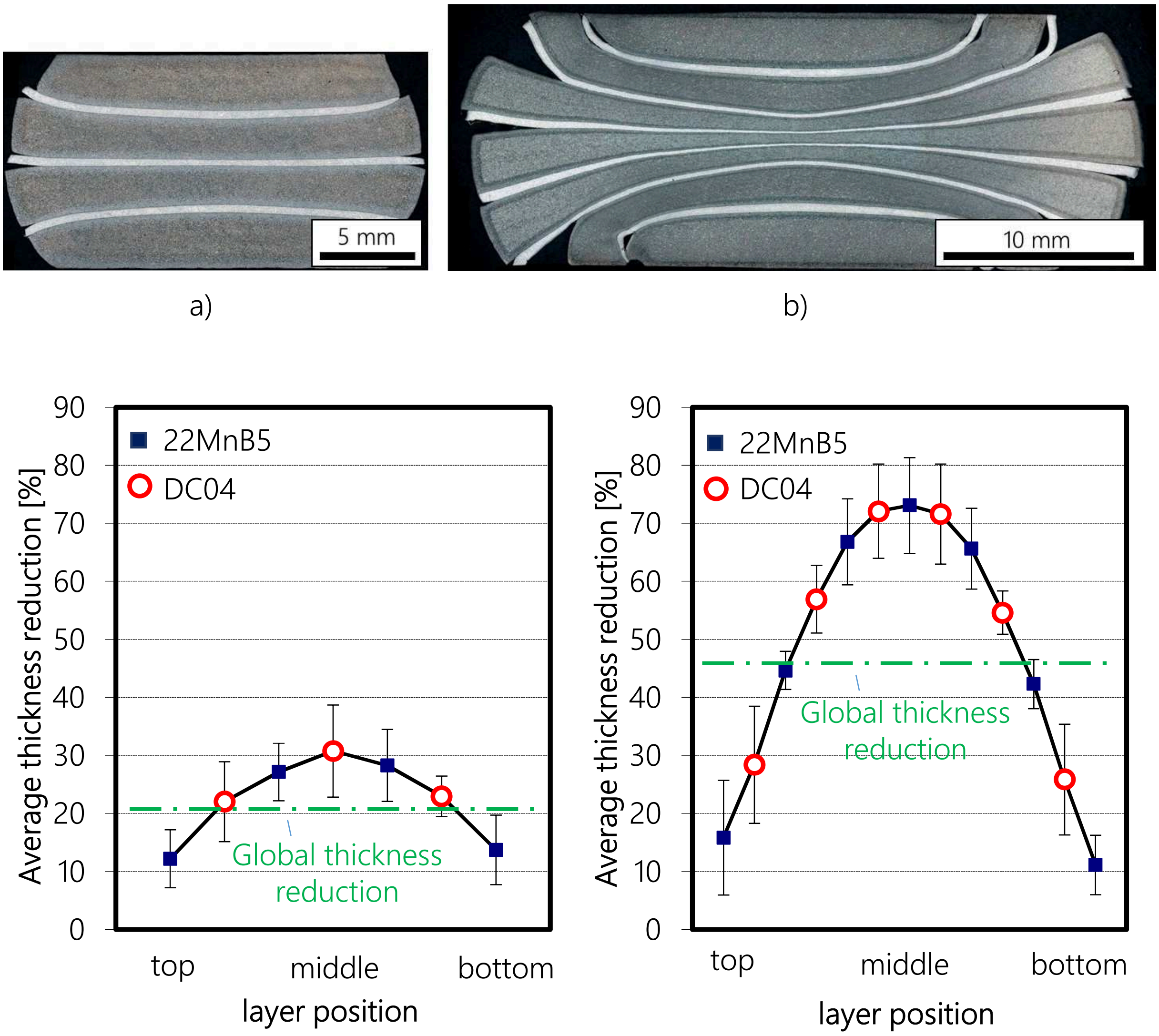

a) b) c) d)

Figure 50: Side-by-side comparison of the cross sections and average thickness reduction in each layer from top to bottom in the composites a) & c) 'ML 1', and b) & d) 'ML 5'

Figure 51 compares the behavior of the composites ML 4 and ML 6, which show the same trend as ML 1 and ML 5 - albeit the difference in volume fraction of the soft phase (compare **Table 5**). The conclusions which can be drawn from the observations until now are as follows: With increasing h_0/B_0-ratio, the attainable global thickness reduction, as well as the deformation inhomogeneity increases. The position of a layer within the composite thereby determines the amount of deformation, whereas the difference in flow stress can be neglected for this 22MnB5/DC04 material combination.

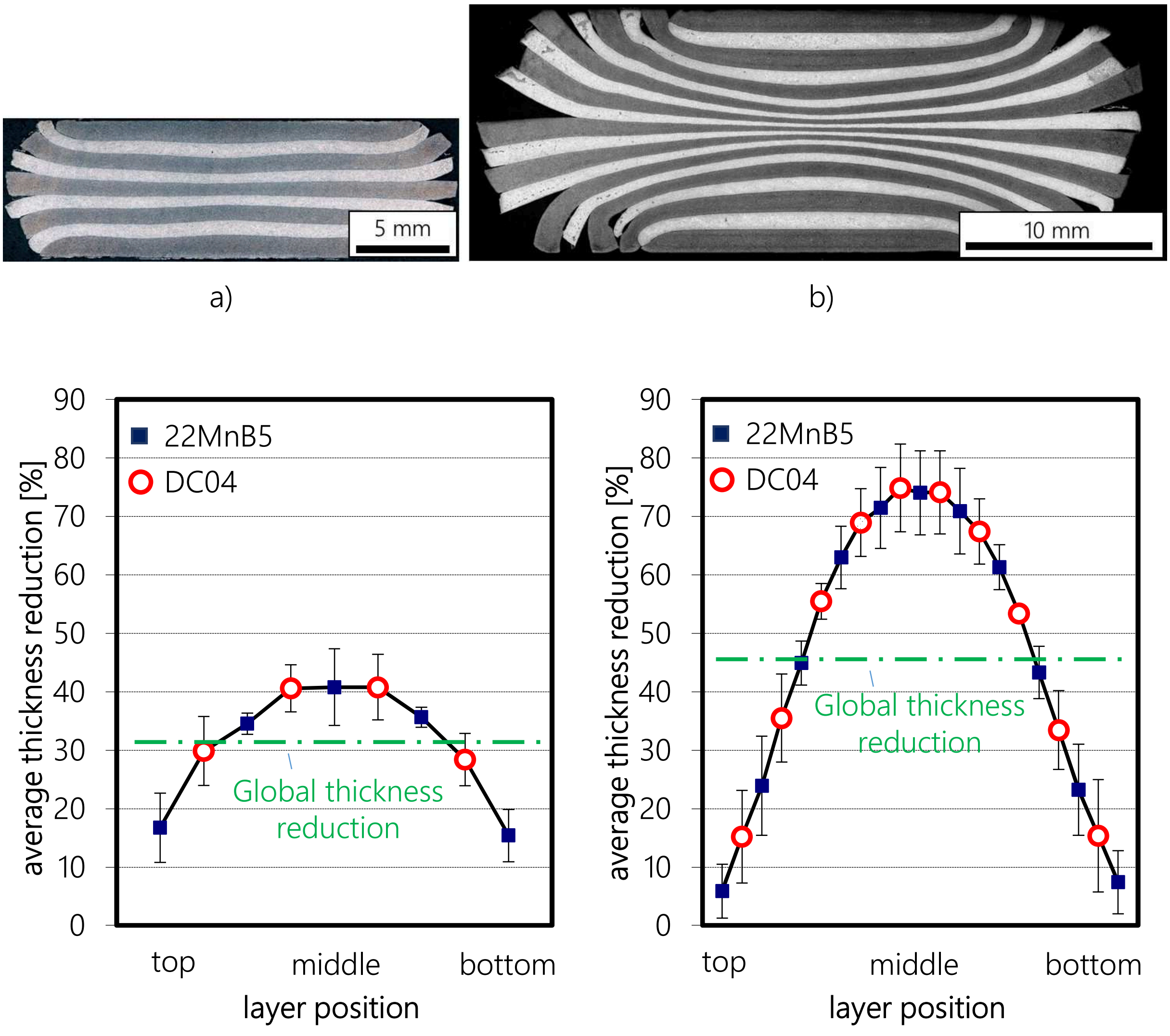

a) b)

c) d)

Figure 51: Side-by-side comparison of the cross sections and average thickness reduction in each layer from top to bottom in the composites a) & c) 'ML 4' and b) & d) 'ML 6'.

5.3.2.3 The influence of friction

Until now, no lubricants were applied during press bonding. In order to study the effect of friction, the stamps of the hydraulic press were coated with boron nitride, a lubricant suitable for high temperatures. A new specimen identical to ML 5 was assembled and bonded. Figure 52 compares the differences in a) local thickness reductions and b) layer appearance between lubricated and un-lubricated bonding. In general, at the same maximum load a higher global thickness reduction was achieved. This was expected, as lubrication reduces the deformation resistance which is a function of the flow stress of the composite and of the friction between composite and tools. Additionally, lubrication reduced the deformation inhomogeneity across the composite width, which is seen from the decrease in standard deviations given in Figure 52a. This significantly decreases warping of the layers, Figure 52b.

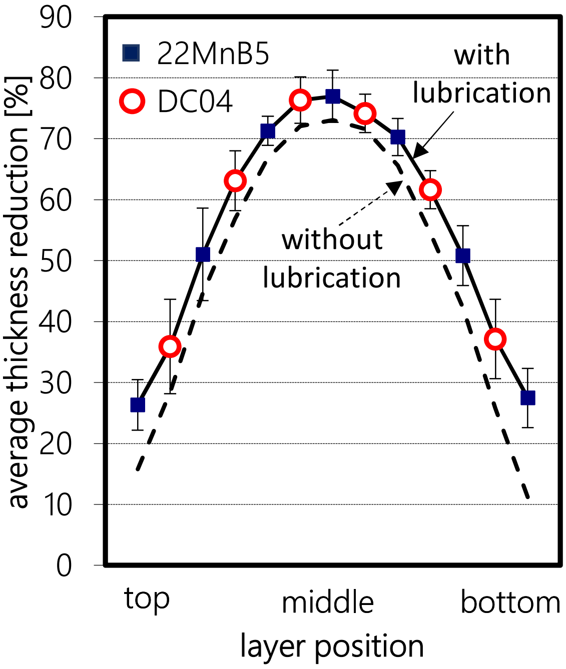

a)

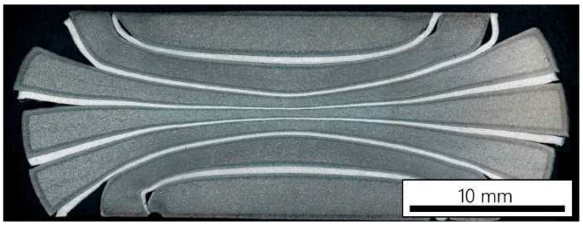

ML 5 without lubrication

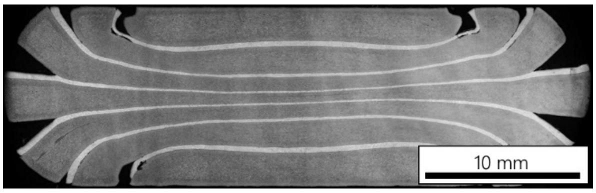

ML 5 with lubrication

b)

Figure 52: Comparison of the differences in a) the average thickness reduction and b) the appearance of the individual layers, when a boron nitride lubricant is applied to reduce friction during forging. The dashed line in a) is a simplified version of Figure 50 d).

5.3.2.4 Summary

Figure 53 summarizes the findings of the preceding sections schematically. Figure 53a recalls the basic geometry of a composite assembly with height h_0 and width B_0 before forging. The position of a layer within such a stack has a significant influence on its deformation, Figure 53b. Outer layers deform very little compared to layers in the middle of the assembly. Additionally, there is a deformation gradient within the layers across the width of the composite. The impact of the h_0/B_0-ratio is depicted in Figure 53c. With an increasing stack height, the attainable thickness reduction at the same maximum force increases significantly. However, the deformation inhomogeneity across the specimen height increases significantly as well. Lubrication reduces the deformation resistance of the composite, which is a function of the flow stress and friction. As such, higher thickness reductions can be obtained, Figure 53d. Additionally, the deformation inhomogeneity across the composite width is reduced, which is evident as reduced standard deviations of the average thickness reductions in Figure 53d.

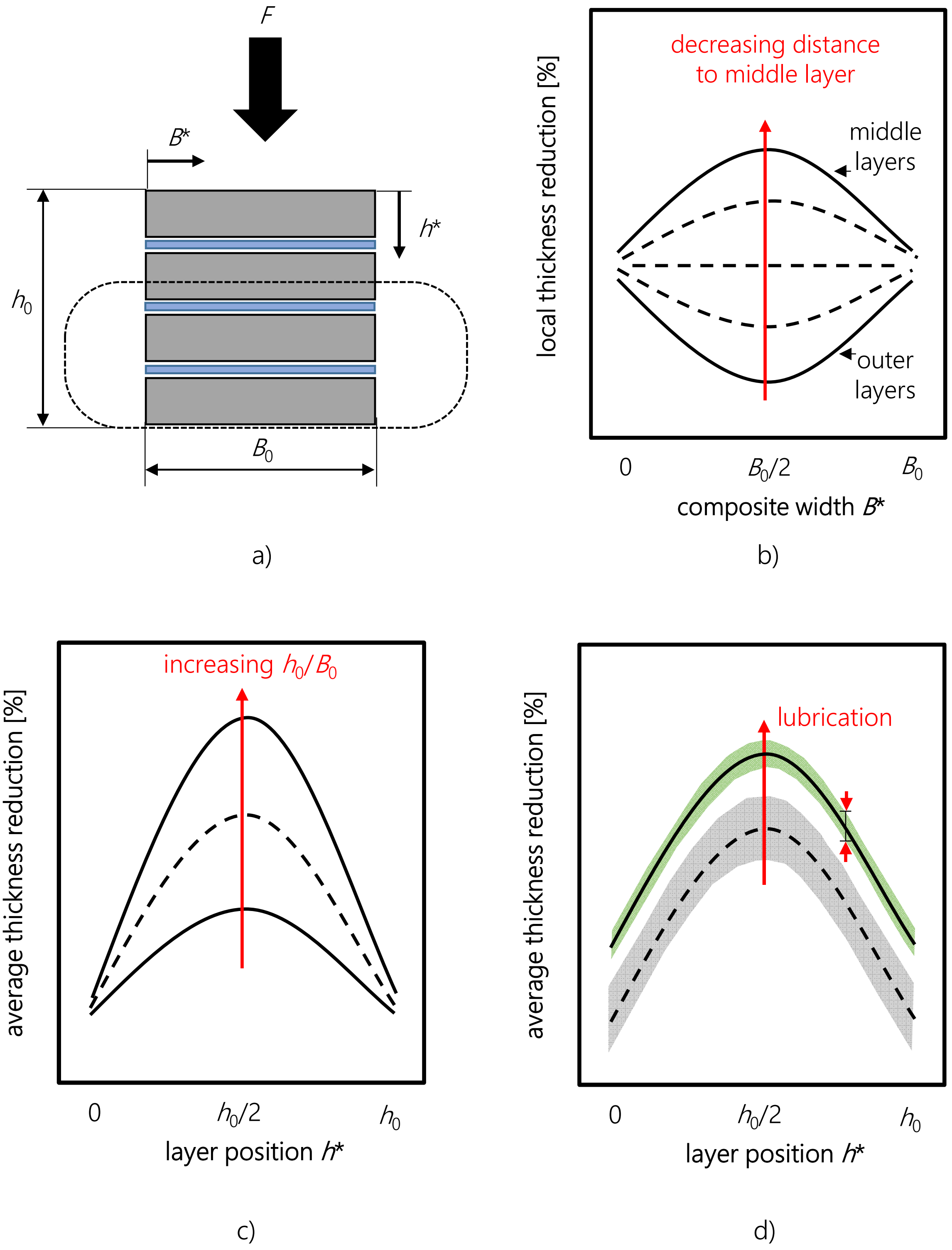

Figure 53: A summary of the basic influence factors in the pressure welding process of multilayered composites. (a) Geometry of the initial layer assembly before forging, b) influence of the layer position, c) influence of the h_0/B_0 ratio and d) influence of lubrication.

5.3.3 The issue of insufficient bond strengths

The previous chapter revealed locally low thickness reductions, which is an inherent problem of the press bonding process. The consequence of this is illustrated with an exemplary fracture mechanics test in this chapter.

5.3.3.1 A preliminary fracture mechanics test

Using the same procedure as described in chapter 5.3.2, a multilayered composite with 7 layers of 22MnB5 and 6 layers of DC04 was manufactured with lubrication to a total thickness reduction of 40%. This composite geometry was therefore similar to the composite 'ML 5' described in Figure 49 and Figure 52b.

The forged block was re-austenitized at 900 °C and water quenched. A dogbone-shaped single edge notched tension (SENT) sample with dimensions as depicted in Figure 54 was then prepared with water jet cutting. A sharp crack was then introduced by a wire saw and pre-fatiguing at a constant ΔK = 13.5 MPa$\sqrt{\text{m}}$. To study local deformations during the fracture mechanics test, a speckle pattern was sprayed onto the specimen, leaving only two stripes of blank metal surface to keep track of the individual layers. In the fracture mechanics test, the clamped sample with final dimensions W=14.8 mm, B=6.7 mm and a_0 = 5.2 mm was loaded in a Zwick tensile testing machine at a constant crosshead displacement rate of 5 mm/min.

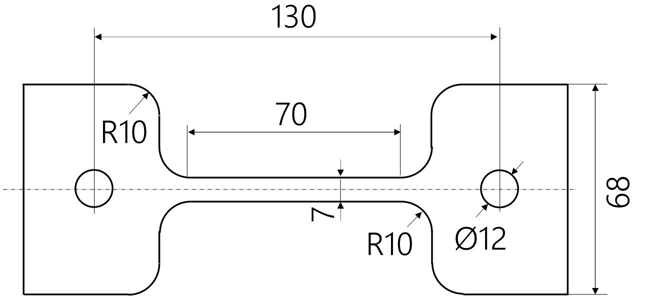

Figure 54: SENT sample geometry for a preliminary fracture mechanics test cut by a water jet.

Figure 55 displays the load-crack mouth opening displacement (CMOD) record of the fracture mechanics test, which resembles a simple tensile test. The CMOD was measured by digital image correlation. In this test, no critical values of J or K (J_c, K_c) for crack initiation were ascertained, as no crack extension could not be determined. Instead, seven points are marked in Figure 55 to discuss the behavior of the sample. The inserts in Figure 55 show the specimen at certain points during the test. The image corresponding to point

‘1’ shows the initial configuration of the specimen. From the second image at point ‘5’ it is evident that a delamination occurred during the test. Two more layer separations can be observed in the image corresponding to point ‘7’, which shows the specimen in the moment before final fracture. In contrast to the main delamination, these secondary delaminations can also be seen in the load-CMOD record as sudden load drops between points ‘6’ and ‘7’.

The development of delamination is studied in greater detail with digital image correlation (DIC) between the points ‘1’ to ‘4’. In DIC, strains at a given deformation stage are calculated by a comparison of two images showing the deformed and undeformed sample, respectively. Figure 56a-b show the tensile strains, ε_{yy}, and transverse strains ε_{xx}, respectively. The onset of delamination can be spotted at point ‘2’ in Figure 56b: positive transverse strains (red colour) indicate that layer separation in front of the crack tip already started. With increasing load, the area with $\varepsilon_{xx} > 0$ first extends to both sides of the crack, step ‘3’. At point ‘4’ the layer separation is already visible with naked eye and the image correlation software loses track of the local deformation due to the change in surface pattern alongside the delamination.

Further deformation of the sample in terms of tensile strains ε_{yy} is shown in Figure 57, note the change in color scale. At point ‘5’, which is past the load maximum, necking of the remaining ligament is evident, which further proceeds at points ‘6’ and ‘7’. The reason for the secondary delaminations can now be pinpointed as interface stresses caused by the lateral contraction of the remaining ligament.

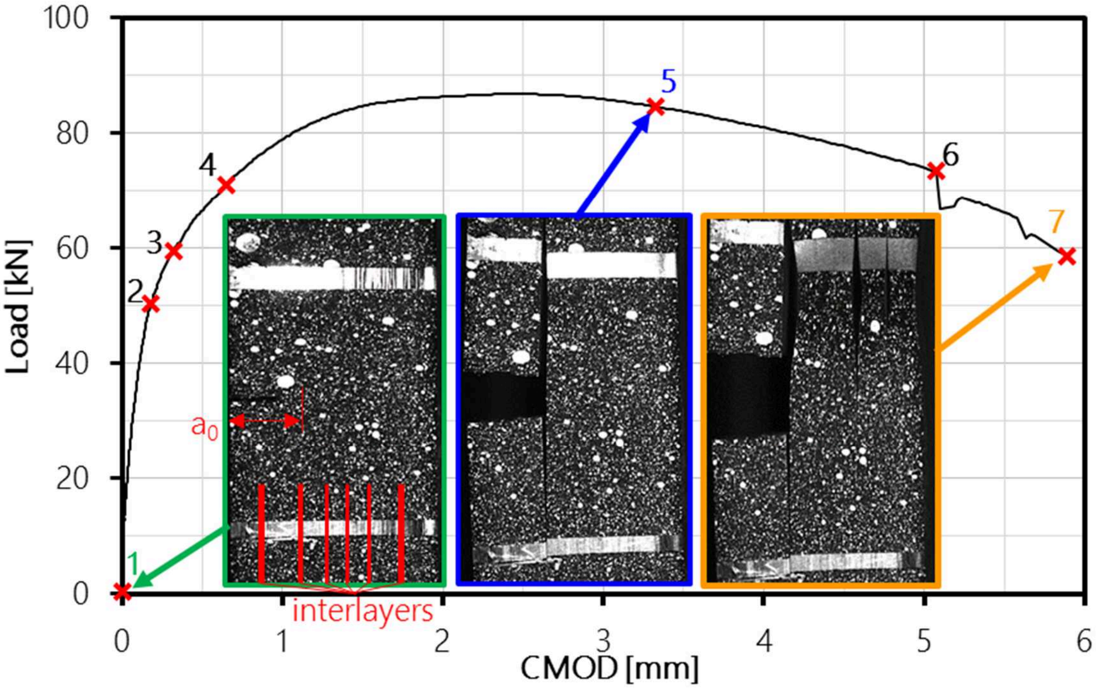

Figure 55: Load-CMOD record of a fracture mechanics test of a multilayered composite. The numbers 1 to 7 refer to specific points discussed in this chapter. The inserts show the specimen at the beginning (1), in the middle (5) and at the end of the test (7). The initial crack length a_0 and the interlayers are indicated in red in the first image.

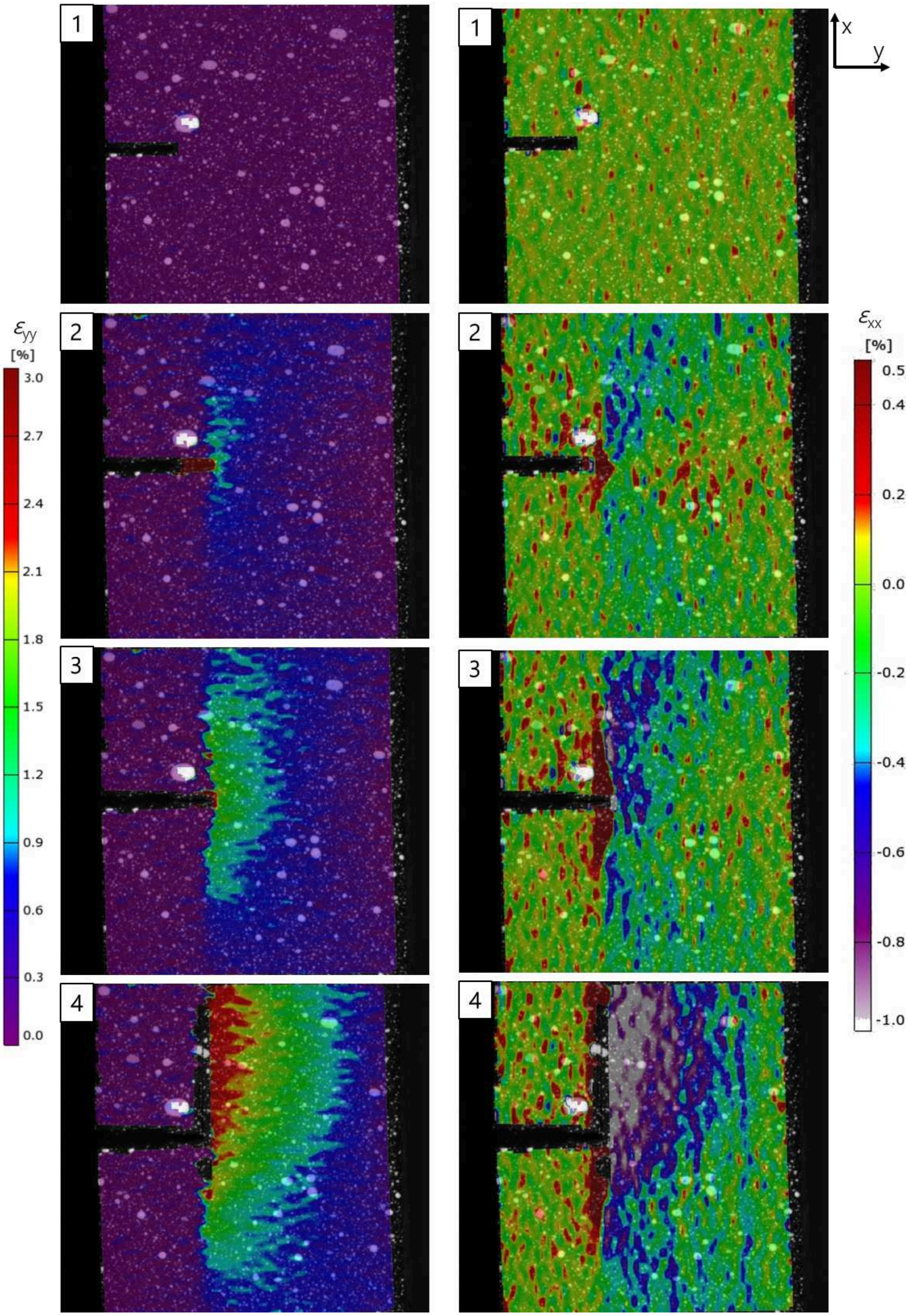

a) b)

Figure 56: a) ε_{yy} and b) ε_{xx} strain maps showing the onset of delamination in the fracture mechanics experiment. The images correspond to the points indicated in the force-CMOD-record in Figure 55 a).

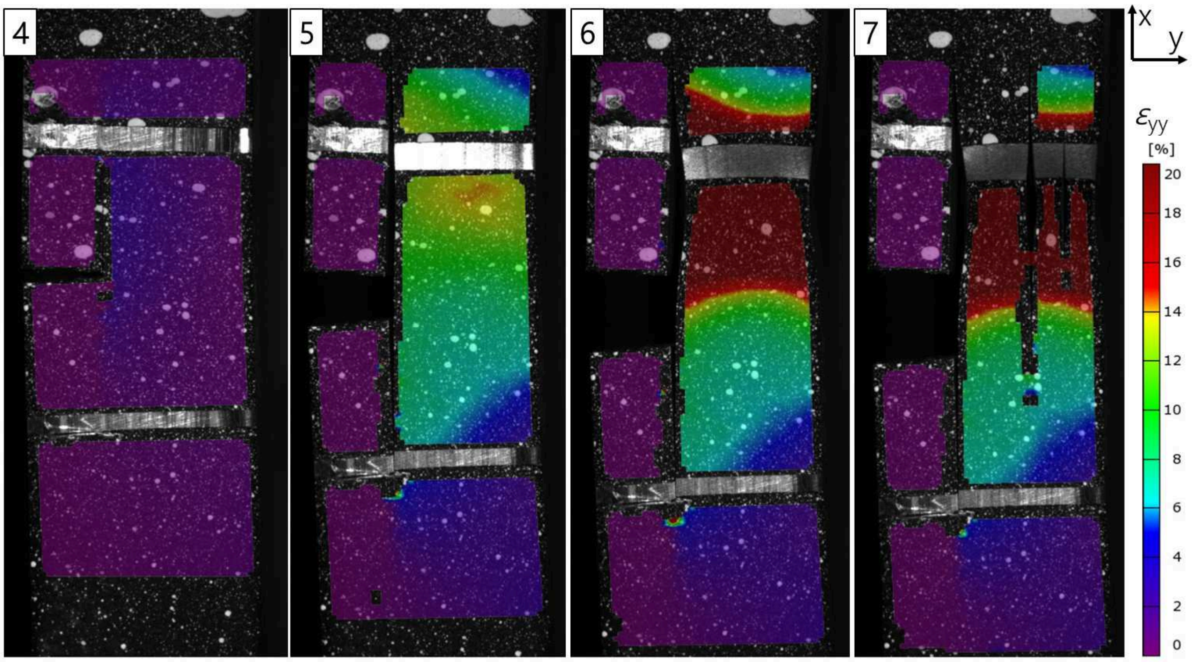

Figure 57: ε_{xx} strain maps corresponding to the points 4 to 7 marked in Figure 55 a).

The exemplary fracture mechanics test can be summarized as follows: The initial sharp crack causes early debonding at the interface in front of the crack tip. The sample subsequently behaves like a tensile test specimen, starts to neck and finally fails by reaching the plastic limit load. If this is true, then the stress σ_{max} at maximum load F_{max} should be equal to the ultimate tensile strength of the composite.

$$\sigma_{max} = \frac{F_{max}}{B \cdot (W\text{-}a_{CA})} = \frac{86\,830\ \mathrm{N}}{6.7 \cdot (14.8\text{-}5.2)\ \mathrm{mm}^2} = 1\,350\ \mathrm{MPa} \tag{5.12}$$

The theoretical ultimate tensile strength σ_{UTS} of the composite can be estimated by a rule of mixture from the tensile strength of the constituent materials. σ_{UTS}^{22MnB5} and σ_{UTS}^{DC04} were measured as 1 530 and 279 MPa, respectively (Figure 44). The volume fraction f^{DC04} of the soft interlayer phase DC04 in the remaining ligament of the composite is 11%.

$$\sigma_{UTS} = \sigma_{UTS}^{22MnB5} \cdot f^{22MnB5} + \sigma_{UTS}^{DC04} \cdot f^{DC04} = 1\,530 \cdot 0.89 + 279 \cdot 0.11 = 1\,392\ \mathrm{MPa} \tag{5.13}$$

The calculated composite tensile strength σ_{UTS} is only marginally higher than σ_{max} measured in the fracture mechanics test.

While this experiment demonstrates the effectiveness of weak interfaces as crack arresters, it serves little to study the effect of material inhomogeneities. This can best be shown when comparing the multilayered fracture mechanics sample from before, which contained soft interlayers, to a different multilayered sample without soft interlayers. A sample consisting of only 22MnB5 steel sheets was pressure welded to a total thickness reduction of 40% and similarly hardened (austenitization at 900°C, water quenching). The geometry of the SENT sample is depicted in **Figure 54**. The sample was notched with a wire saw and a sharp pre-crack of a_0 = 6.06 mm was introduced by fatiguing. The final B and W amounted to 6.6 and 13.2 mm, respectively. Testing of the clamped sample was then performed at the same crosshead displacement rate of 5 mm/minute. Unfortunately, the force-displacement record was lost due to a software crash. However, this test still serves as an illustrative example of the effect of delamination.

Figure 58 compares the fractured samples, whereas a) is the sample with interlayers and b) is the sample without. It is easy to see that the second sample fractured in the very same manner as the sample discussed before: a primary delamination at the first interface ahead of the original crack tip rendered the crack ineffective. Final fracture was then caused by reaching the plastic limit load.

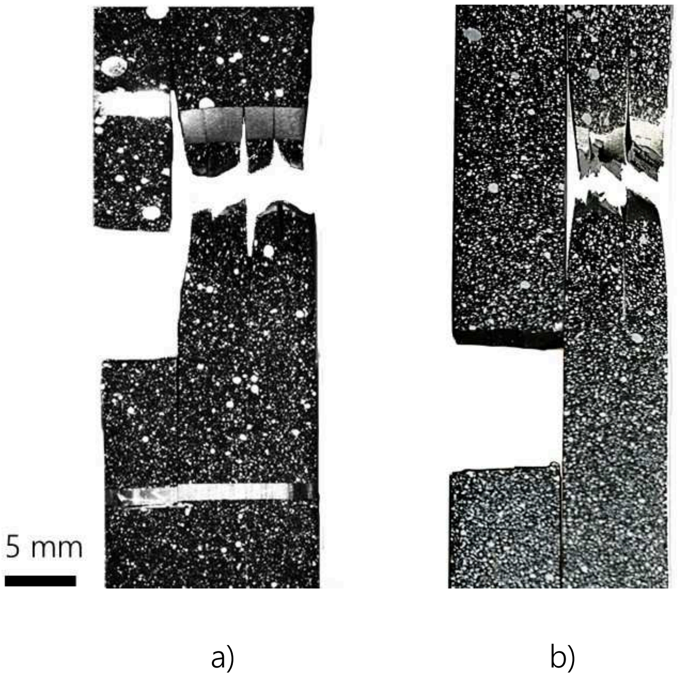

Figure 58: Comparison of tested fracture mechanics samples a) with six soft DC04 interlayers and b) without interlayers, but 18 22MnB5/22MnB5 interfaces in total.

A change in sample geometry to flat, rectangular SENT specimen was unsuccessful as well. In the example shown in **Figure 59**a, the crack arrested in the interlayer material. However, further loading was again interrupted by a layer separation. As evident from **Figure 59**b, the main problem of this sample geometry were shear stresses at the interfaces, caused by loading the specimen. This can be avoided, if the pins used for loading the specimen are oriented perpendicularly to the interfaces, **Figure 59**c.

To summarize, weak interfaces not only cause problems during fracture mechanics testing. Layer separation was sometimes observed also during heat treatment of the composites or during pre-fatiguing.

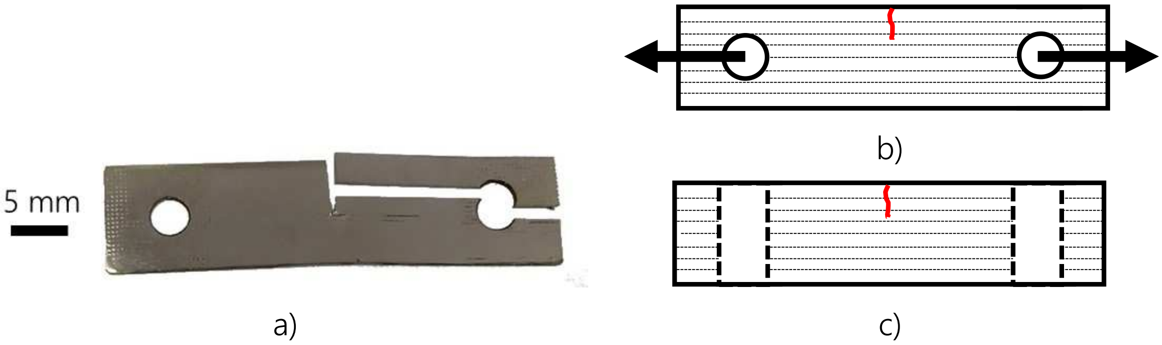

Figure 59: a) Delamination in a rectangular SENT specimen after crack arrest in the interlayer. b) and c) show schematics of the specimen, where dotted lines represent interfaces. In configuration c), shear stresses on the interfaces are reduced.

5.3.3.2 The ‚specimen window'

As was shown in the preceding chapters, the thickness reduction varies within hot press bonded composites. This is of important consequence: as the thickness reduction is equal to the surface exposure, it is an indirect measure of the bond strength between the layers. Critical positions for the onset of layer separation are therefore the outer layers, as well as the sides of the composites. It is therefore sensible to define a "specimen window", in which the local thickness reductions are sufficient to obtain satisfactory bond strengths, Figure 60a. The specimen window can be realized by removing the outer layers and the sides of the composite by milling or electric discharge machining, essentially only keeping the central part of the composite. This is illustrated in Figure 60b.

Another approach to reduce the chance of layer separation is to eliminate interfaces from outside this specimen window by a simple reduction of the number of layers. Instead of using multiple thin steel sheets, a single very thick steel bar could be used at the critical top and bottom position. We use this approach in the next chapter to manufacture fracture mechanics samples.

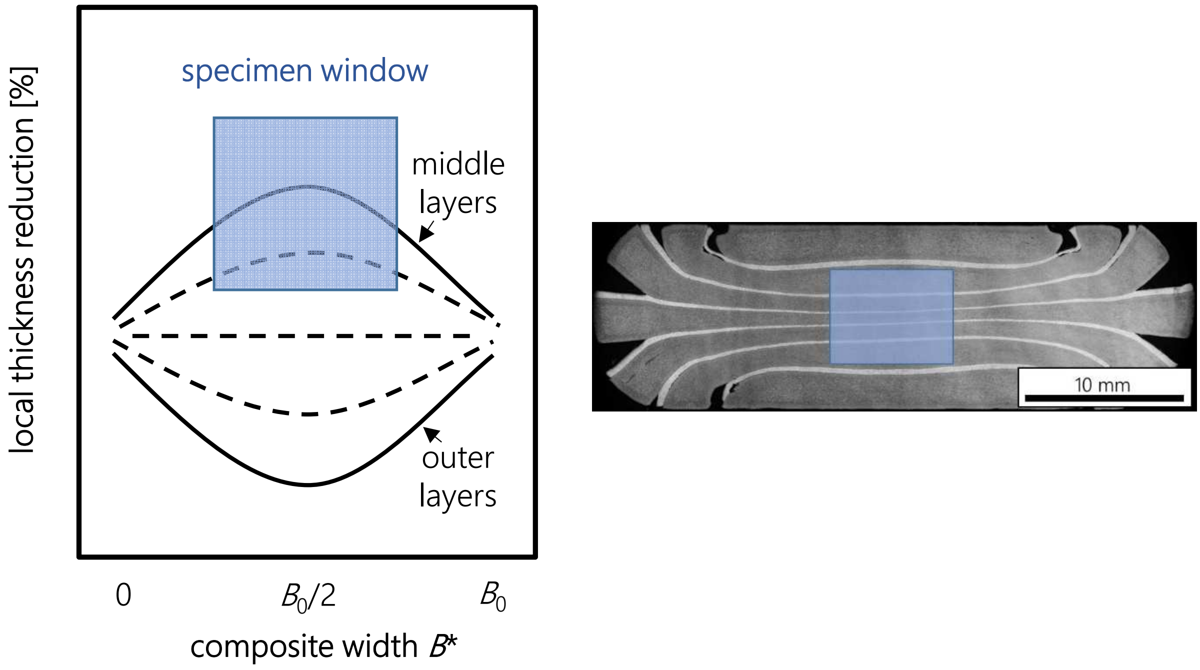

a) b)

Figure 60: a) Definition of the 'specimen window' and b) location of the specimen window in the multilayer ML 5 forged with lubrication.

5.4 Manufacturing of samples

This chapter presents the materials and process routes used to manufacture fracture mechanics specimen.

5.4.1 Materials

In further studies the commercially available cold-working tool steels X210CrW12 (1.2436) steel and C45 (1.1730) were employed as matrix materials. These were supplied as rectangular bars with dimensions 20x15x1000 mm. Figure 61a shows the ferritic-pearlitic microstructure of the as-received C45 steel. The X210CrW12 steel bars were delivered in the annealed state. In the vibropolished cross-section, Figure 61b, a significant content of carbides is visible. The size of these large, elongated carbides is in the range of several tens of µm, typically around 20 µm. However, even larger carbides with sizes of 50 µm or more have been observed as well. A second, smaller type of carbide is also present in the matrix. These carbides are finely dispersed and circular, with diameters of about 1-2 µm.

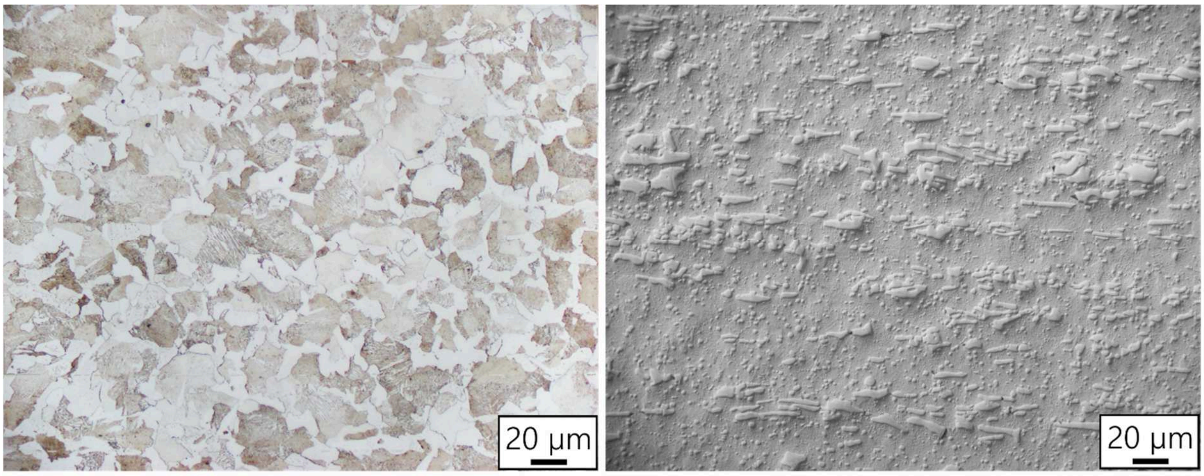

a) b)

Figure 61: a) Ferritic-pearlitic microstructure of the as-received C45 steel, etched with Nital. b) Microstructure of the as-received X210CrW12 steel, vibropolished.

As interlayer material, again the soft deep-drawing steel DC04 (1.0338) was used, which was available as cold-rolled sheets with thicknesses of 0.5 and 1.0 mm.

The chemical compositions of these steels are listed in Table 6. While the composition of the matrix steels X210CrW12 and C45 were determined from the supplier via chemical analysis, the composition of the DC04 interlayer material was taken from datasheets.

Table 6: Chemical compositions of the constituents of the steel multilayer in weight-%

	C	Si	Mn	P	S	Cr	W
X210CrW12	2.11	0.25	0.41	0.019	0.0003	11.21	0.65
C45	0.45	0.18	0.63	0.008	0.002	0.21	-
DC04	0.04	-	0.2	0.01	0.01	-	-

5.4.1.1 EBSD analysis

The as-received matrix materials were studied by EBSD in order to determine the presence of a texture. The C45 steel, Figure 62, thereby shows mainly equiaxed grains, with varying grain diameters of up to 60 µm. No pronounced texture is observable.

Compared to the C45 steel, in the X210CrW12 tool steel the grains are much more uniform and with diameters of approximately 10 µm also smaller, see Figure 63 (note the different length scale). A striking difference is the presence of primary carbides within the matrix. These carbides appear dark due to the overlay of the coloured inverse pole figure (IPF)-maps with the greyscale image quality maps, a darker grey tone thereby corresponding to a decreased quality of the Kikuchi-patterns.

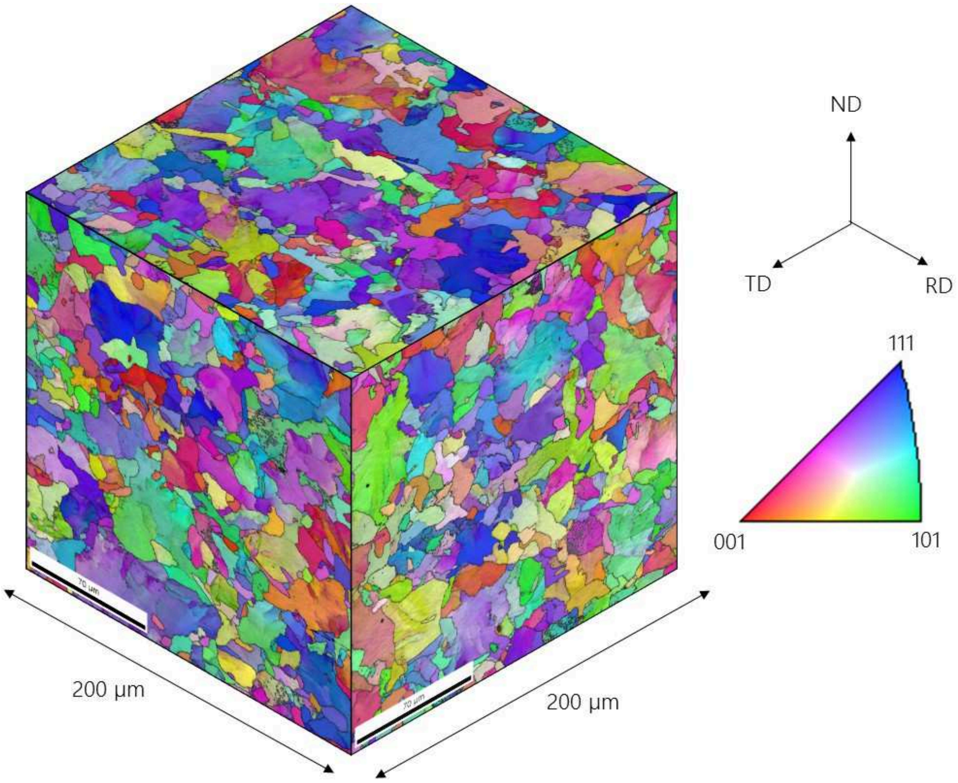

Figure 62: EBSD analysis of the as-received C45 tool steel.

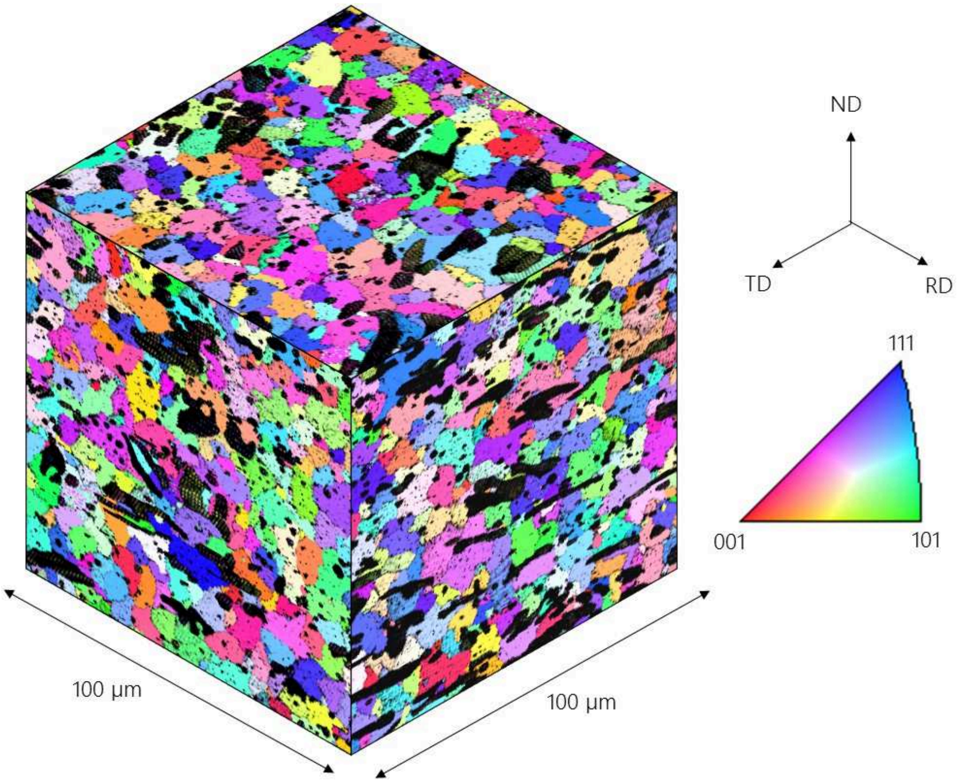

Figure 63: EBSD analysis of the as-received X210CrW12. Carbides appear dark due to a lower quality of the Kikuchi-patterns .

5.4.1.2 Flow curve determination

To determine the flow stress of the matrix materials, compression tests were performed using a servohydraulic compression testing machine (TMTS servotest). This machine allows for constant deformation rates at temperatures up to 1200 °C, where the samples are induction heated. The sample chamber and the punches, are pre-heated so no temperature loss occurs during upsetting.

Cylindrical specimens in ‘T’ and ‘N’ orientation were spark eroded, while specimens in ‘L’-orientation were machined from the as-received steel bars, see Figure 64. To reduce friction and maintain a uniaxial deformation state during the compression test, shallow pockets were machined on both the top and bottom specimen face, which can be filled with a lubricant. Additionally, a hole with Ø=1.1 mm was drilled into the side of the specimen to attach a thermocouple, which is used to control the induction heating of the specimen. Furthermore, the thermocouple also monitors temperature changes during deformation. Figure 65 shows the final dimension and a 3D-view of these so-called Rastegaev-specimens.

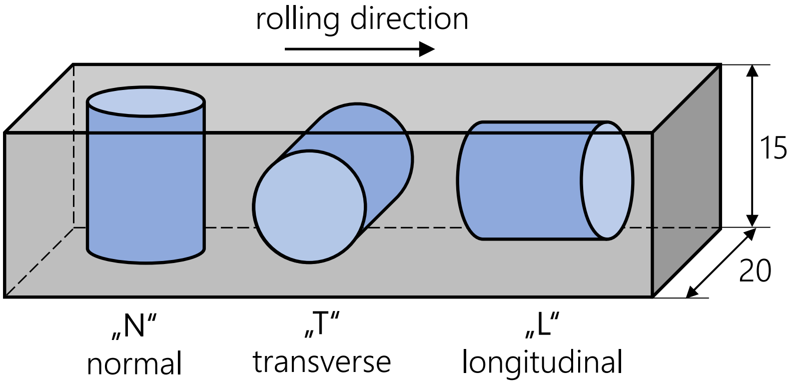

Figure 64: Orientation of the cyclindrical specimens machined or spark eroded from the steel bars with a cross-section of 20x15 mm

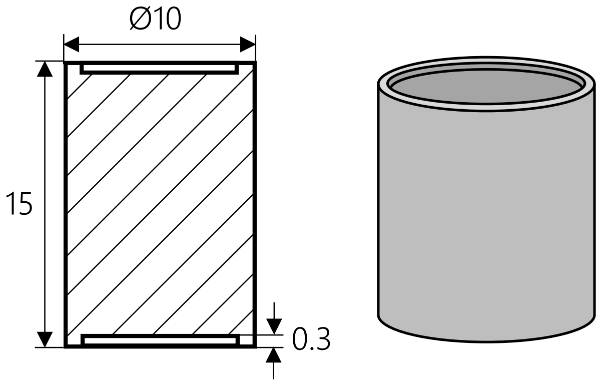

Figure 65: Dimensions and 3D-view of the cylindrical Rastegaev-specimens.

The hot flow curves from the DC04 interlayer material, which was supplied as thin 0.5 and 1 mm steel sheets, could not be determined that way. Instead, the flow curves were estimated using the following relation, which models the flow stress σ_f by multiplying a material specific initial value A by factors that express the influence of the conditions of deformation, i.e. forming temperature T, true strain φ and strain rate $\dot{\varphi}$ (Spi2009a):

$$\sigma_f = A \cdot K_T \cdot K_\varphi \cdot K_{\dot{\varphi}} \tag{5.14}$$

$$\sigma_f = A \cdot \underbrace{e^{m_1 T}}_{K_T} \cdot \underbrace{\varphi^{m_2} \cdot e^{m_4/\varphi} \cdot (1+\varphi)^{m_5 T} \cdot e^{m_7 \varphi}}_{K_\varphi} \cdot \underbrace{\dot{\varphi}^{\, m_8 T}}_{K_{\dot{\varphi}}} \tag{5.15}$$

In equation (5.15), the influence of T, φ and $\dot{\varphi}$ are considered with the exponents m_1 to m_8. **Table 7** lists the values of these exponents for the steel DC04 (Spi2009b). Flow curves calculated with eqn. (9) and the values from **Table 7** are valid for $\varphi < 1.5$ and forming temperatures between 900 °C and 1200 °C (Spi2009b).

Table 7: Material constant A and exponents m_1 to m_8 for flow curve modelling of the DC04 interlayer material using equation (5.15). (Spi2009b)

A	m_1	m_2	m_4	m_5	m_7	m_8
1561.21	-0.00226	0.31681	-0.00048	0.00057	-1.00839	0.000134

5.4.1.3 Flow curves

The calculated flow curves for the DC04 interlayer material at relevant forging temperatures and strain rates are given in Figure 66. The material model predicts significant softening effects, i.e. recovery and recrystallization, at deformations higher than φ=0.5.

Figure 67 and Figure 68 show the measured flow curves up to $\varphi = 1$ of the X210CrW12 and C45 steels, respectively. At 980 °C and low deformation rates of $\dot{\varphi}$ =0.2, the X210CrW12 behaves almost ideally plastic, see Figure 67a. At higher deformation rates, softening occurs to some extent at values of $\varphi > 0.25$. From Figure 67b, an orientation dependence of the flow stress is evident. Thereby, the 'N' orientation, indicated by the solid line, allows for easier deformation at the temperatures and strain rates studied. A decrease in forming temperature from 980 °C to 800 °C results in a significant increase in flow stress of more than a factor 1.5.

The flow curves of the C45 steel, Figure 68a, have been determined at 1050 °C for different forming rates; the influence of forming temperature is depicted in Figure 68b. In contrast to the X210CrW12 steel no orientation dependence of the flow curves was measured. When decreasing the forming temperature to 800 °C, the increase in flow stress amounts to approximately a factor of 2.

Using the data from Figure 66 to Figure 68, the relative flow stress $\sigma_\mathrm{f}^\mathrm{matrix}/\sigma_\mathrm{f}^\mathrm{DC04}$ at a given temperature and strain rate can be calculated.

Figure 69 plots $\sigma_\mathrm{f}^\mathrm{matrix}/\sigma_\mathrm{f}^\mathrm{DC04}$ for $\dot{\varphi}$ = 1/s at forging temperatures of 980 °C and 1050 °C for X210CrW12/DC04 and C45/DC04 composites, respectively. It is evident that co-deformation can easily be achieved when forging composites with a C45 matrix material, as $\sigma_\mathrm{f}^\mathrm{C45}/\sigma_\mathrm{f}^\mathrm{DC04} \approx 1$. In the case of X210CrW12/DC04 composites, the difference in flow stress between matrix and interlayer is almost a factor two. Through the influence of friction between the layers (see Figure 42), co-deformation may still be achieved. Note that the flow stress of the interlayer material $\sigma_\mathrm{f}^\mathrm{DC04}$ was only estimated.

It is worth mentioning that changes in temperature occur during the production of laminates via press bonding. As the stamps of the hydraulic press are colder than the specimen, heat is transferred from the top and bottom layers. This decrease in temperature increases the local flow stress, which reduces the local thickness reductions in these outer layers. On the other hand, heat is generated during deformation, which leads to a temperature increase and a decrease in flow stress.

The temperature increase during upsetting of the Rastegaev-specimens was measured with the attached thermocouple. Figure 70 depicts the increase of temperature ΔT for X210CrW12 specimens. At an initial deformation temperature of 980 °C and low deformation rates of $\dot{\varphi} = 0.2$, a ΔT of +15 °C was measured, while at $\dot{\varphi} = 10$ the temperature rise was $\Delta T = +45$ °C (Figure 70a). It is important to note that the temperature increase leads to softening, which is also directly reflected in the flow curves (compare Figure 67a). Figure 70b shows the influence of the deformation temperature on the generated heat, in which some curves are incomplete as some thermocouples detached during deformation. A comparison with Figure 67b reveals that a higher yield stress is associated with a larger temperature increase. The same trend can be seen in similar measurements with C45 specimens, see Figure 71.

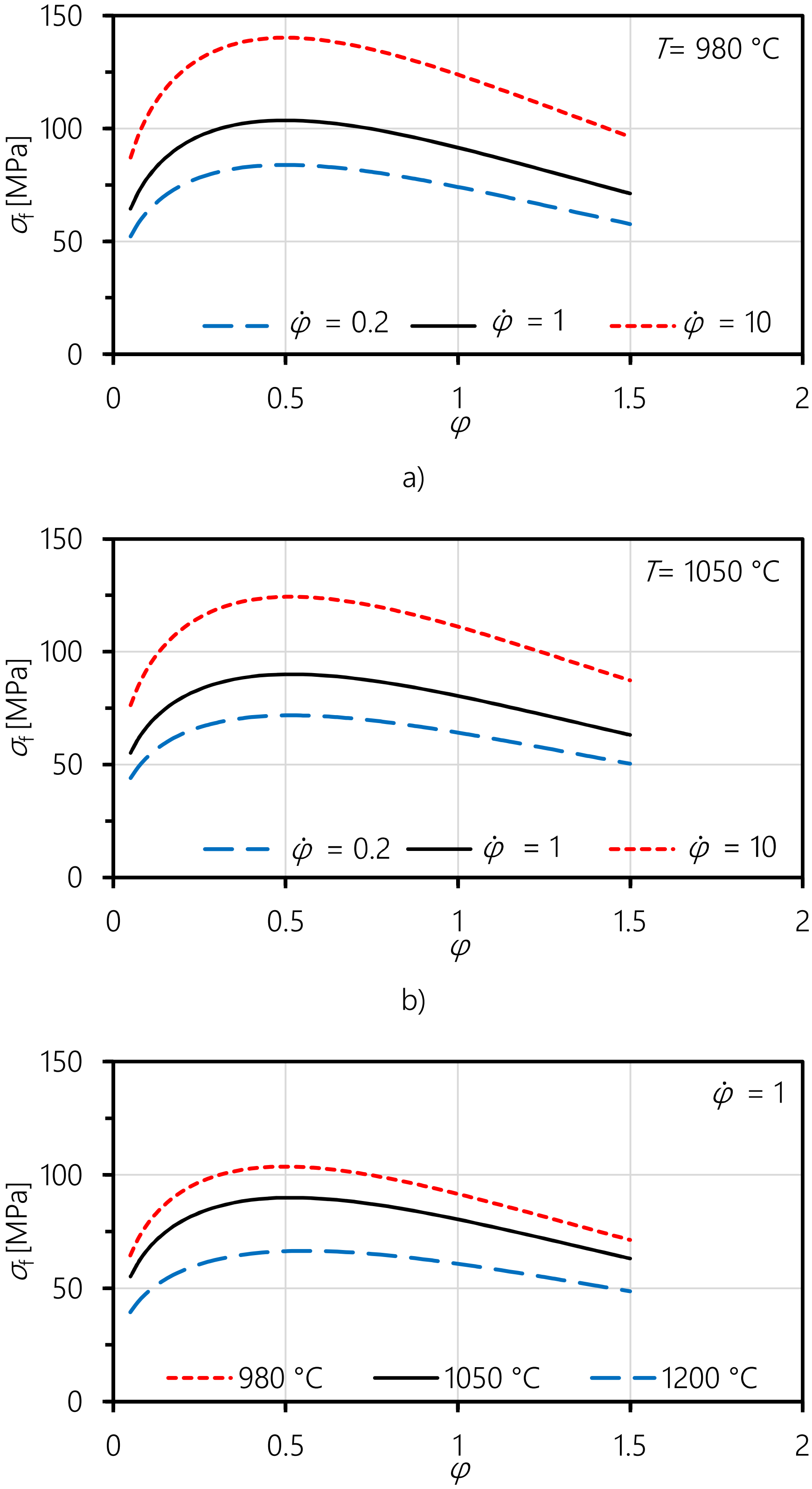

a)

b)

c)

Figure 66: Calculated flow curves for the DC04 steel at various temperatures and deformation rates. a) T = const = 980 °C, b) T = const = 1050 °C, c) $\dot{\varphi}$ = const = 1/s

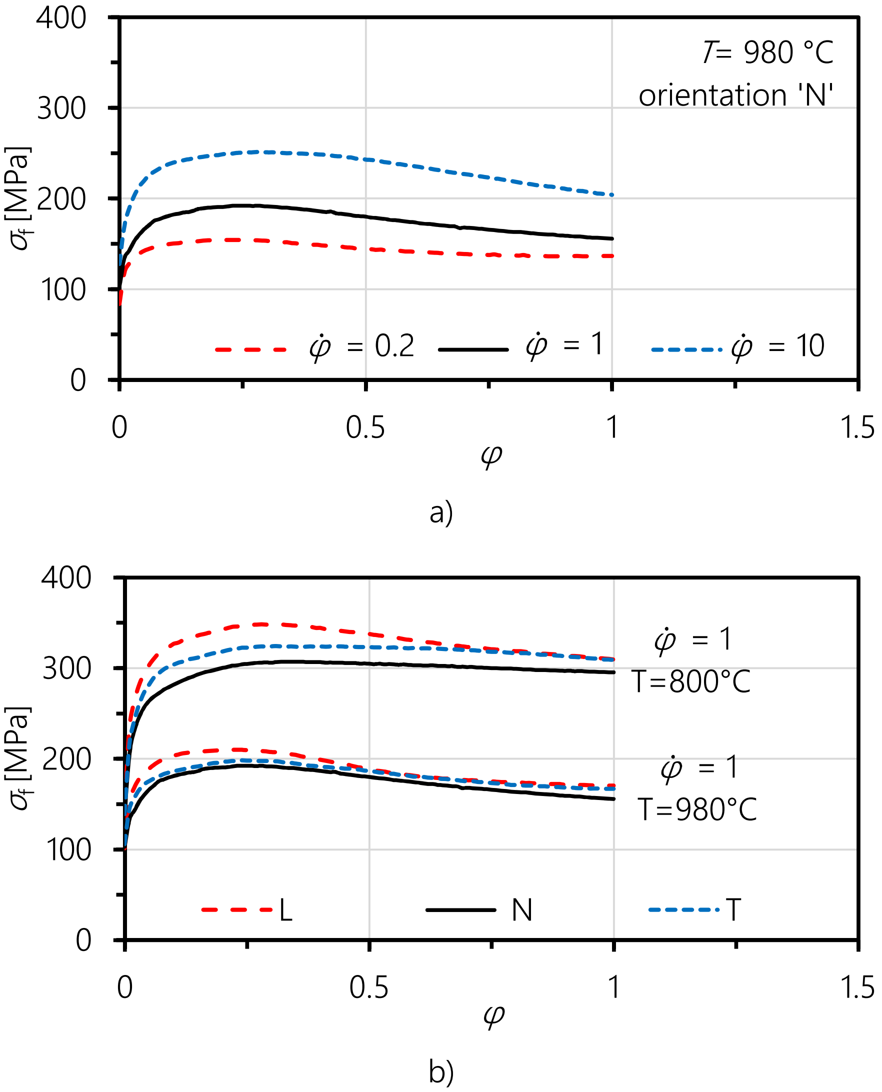

a)

b)

Figure 67: Influence of a) strain rate and b) orientation and temperature on the flow curves of the X210CrW12 steel.

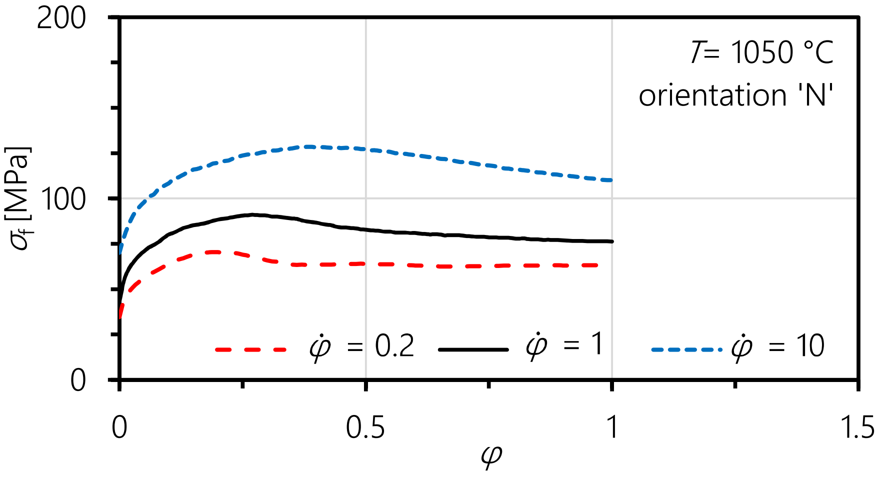

a)

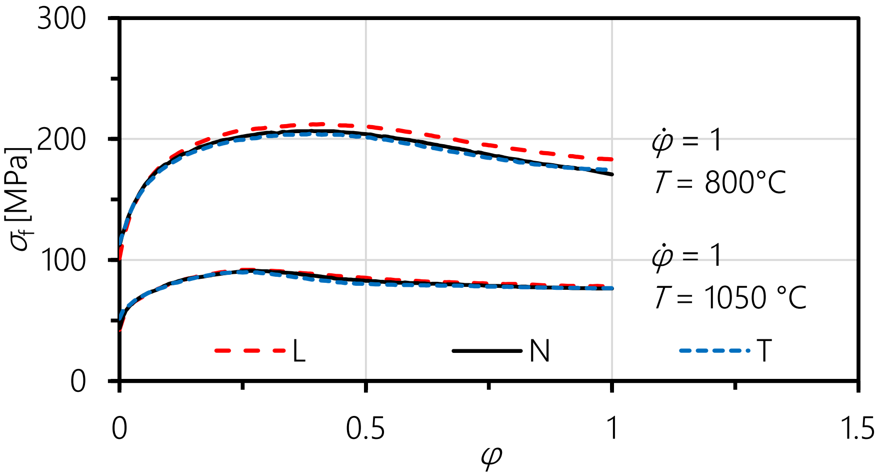

b)

Figure 68: Influence of a) strain rate and b) orientation and temperature on the flow curves of the C45 steel.

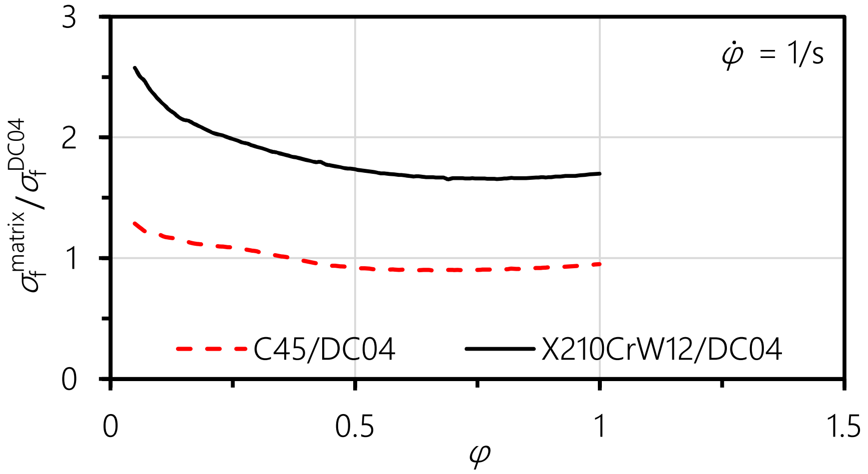

Figure 69: $\sigma_f^{matrix} / \sigma_f^{DC04}$ at $\dot{\varphi}$ = 1/s for C45/DC04 and X210CrW12/DC04 composites at 1050 °C and 980 °C, respectively.

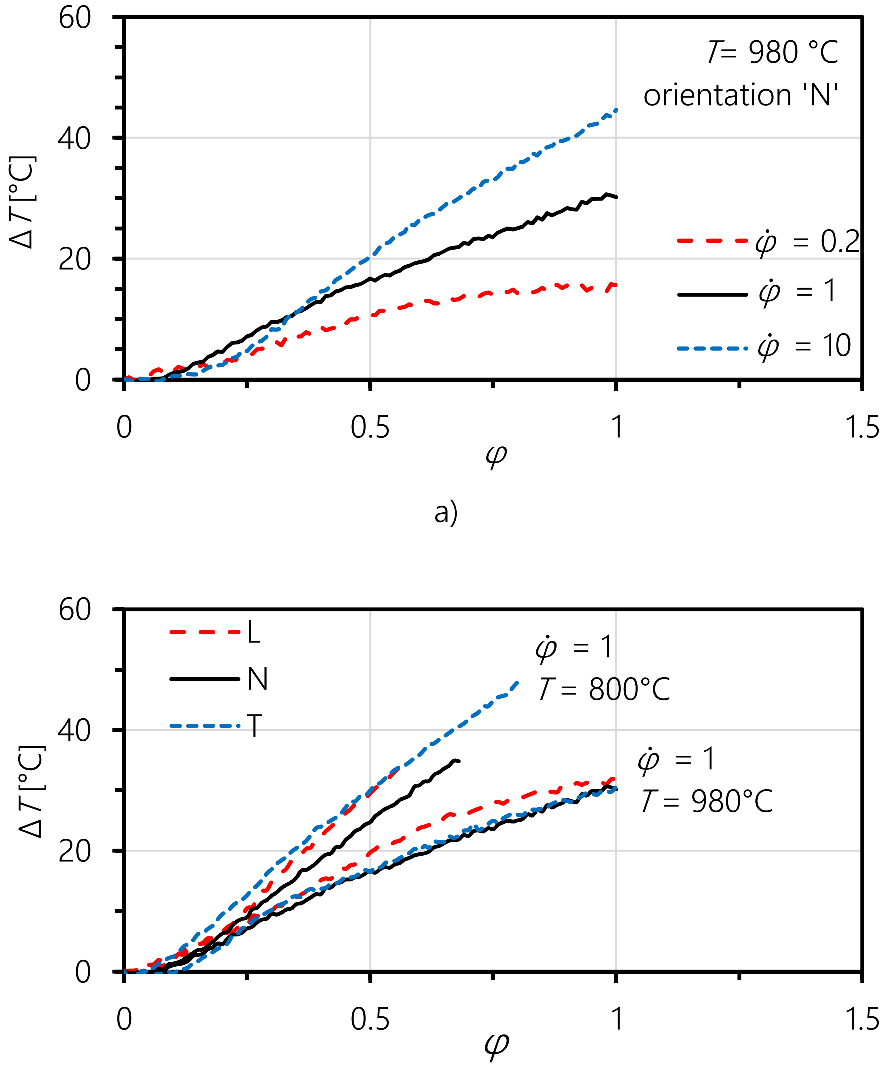

a)

b)

Figure 70: Increase in temperature ΔT of X210CrW12 specimens during deformation at a) different strain rates and b) different temperatures and orientations.

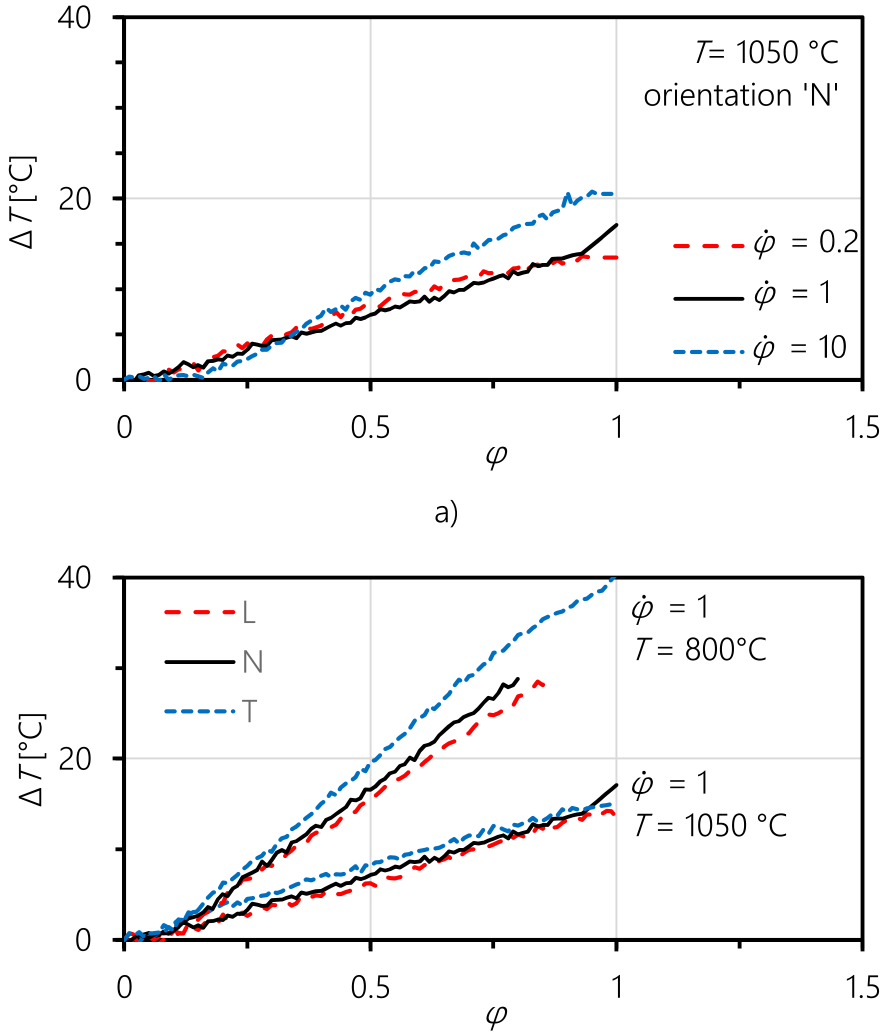

a)

b)

Figure 71: Increase in temperature Δ*T* of C45 specimens during deformation at a) different strain rates and b) different temperatures and orientations.

5.4.2 Processing route of X210CrW12/DC04 composites

Figure 72 summarizes the processing route of X210CrW12/DC04 composites. Rectangular sheets and blocks with dimensions 20x50 mm were prepared, thoroughly cleaned with acetone and ground with 380 grit paper. Depending on the desired multilayer configuration, stacks with a total height of h_0 were assembled, Figure 72a, and tightly wrapped in heat treatment foil, Figure 72b. The heat treatment foil reduces oxidation of the surfaces during heating and prevents displacement of the individual sheets during handling of the stack. The following temperature-time sequence is outlined schematically in Figure 72c. Preheating of the stack at 550 °C reduces temperature gradients within the tool steel. After fifteen minutes, the stack is transferred into a second oven set to 980 °C. Afterwards, the stack is press bonded at a constant deformation speed $\dot{v}$ of 6.23 mm/s to a global thickness reduction of 50%, using a pre-programmed hydraulic press. To reduce friction, the stamps of the press were coated with boron nitride lubricant. Subsequent soft annealing by re-heating to 980 °C and slow cooling in the oven is necessary to allow for machining of the composite.

From the forged blocks, samples are spark eroded, Figure 72d, and machined to the final SENT specimen geometry, Figure 72e. While already indicated for clarity, the notch is introduced only after the final heat treatment. The subsequent final heat treatment consists of re-austenitizing, air cooling and an annealing step (Figure 72f), which yields a high hardness difference between the thus hardened X210CrW12 matrix and the (mostly unaffected) DC04 interlayers.

To study the influence of the interlayer thickness and the effect of multiple interlayers, different composites with single or multiple interlayers were manufactured. The question arises, how the steel sheets in Figure 72a have to be assembled to achieve a desired final composite geometry. Recalling the preliminary forging experiments, Figure 53, it was postulated that the relative positon h^* in the stack is the governing factor of the final thickness reduction of a specific layer.

Figure 73 plots the measured thickness reductions for multiple press bonded X210CrW12/DC04 composites with a varying number of layers. It is evident that the local thickness reduction can very well be predicted by a second-degree polynomial fitting function. The local thickness reduction, and therefore the local surface exposure Y, is estimated by

$$Y = -6.0168\left(\frac{h^*}{h_0}\right)^2 + 6.0167\frac{h^*}{h_0} - 0.5756 \tag{5.16}$$

This empirical relation is strictly valid only for this stack geometry and for global thickness reductions of ≈50%. With a given stack assembly, this function can predict the composite geometry after forging. Equation (5.16) can also be used to calculate the necessary stack assembly to achieve a given composite geometry.

A simple example serves to illustrate the application of equation (5.16). Suppose that a composite with a single interlayer of thickness t = 0.1 mm has to be manufactured. The required initial DC04 layer thickness t_0 in the assembly is calculated as follows:

$$t_0 = \frac{t}{1-Y} = \frac{0.1\ \text{mm}}{1 - (-6.0168 \cdot 0.5^2 + 6.0167 \cdot 0.5 - 0.5756)} = 1.4\ \text{mm} \tag{5.17}$$

In equation (5.17), Y was evaluated at h^*/h_0 = 0.5, as the single interlayer is located in the middle of the stack. Now that the initial thickness of the interlayer is known, the required thickness of the X210CrW12 matrix pieces can be calculated, given that a total stack height of h_0 = 28 mm is required to apply equation (5.16). It follows that the DC04 sheet with t_0 = 1.4 mm has to be located between two X210CrW12 pieces of thickness 13.3 mm each. A global thickness reduction of 50% will then yield the desired composite geometry. In the case of multiple interlayers, an iterative procedure has to be applied.

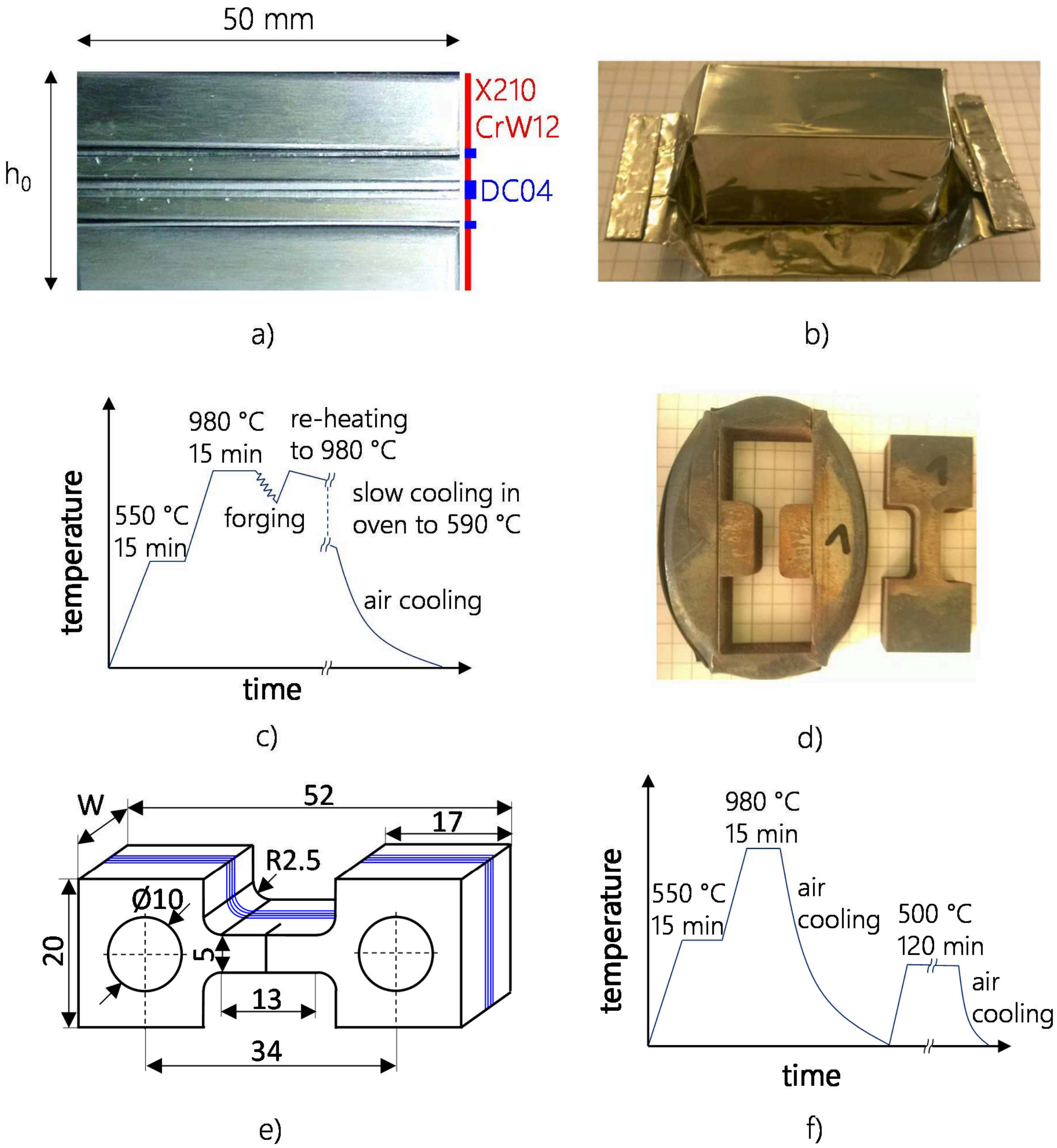

a) b) c) d) e) f)

Figure 72: Processing route of X210CrW12/DC04 composite specimen.

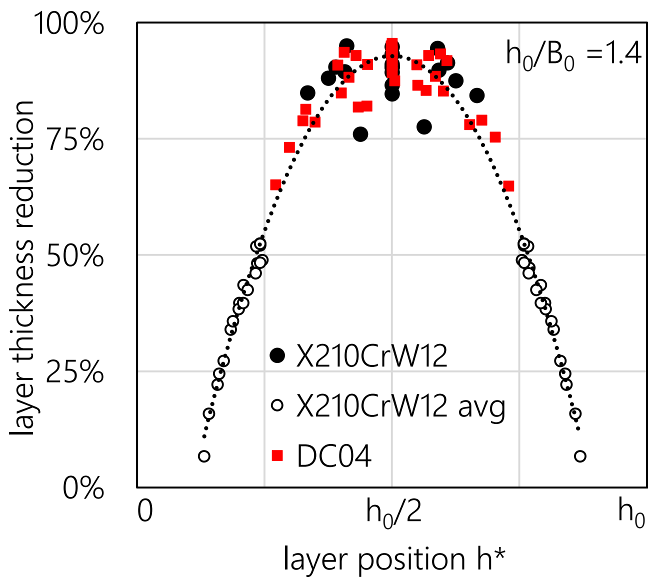

Figure 73: Dependence of layer thickness reduction on the position *h**. Empty circles correspond to the average thickness reduction of the top and bottom X210CrW12 layers.

In total, nine different single interlayer geometries and 12 different multiple interlayer geometries were produced with this method. Table 8 lists the composite geometry of those X210CrW12/DC04 samples, which are discussed in more detail in chapter 6.2.

Table 8: Geometry of X210CrW12/DC04 composites.

#interlayers	*t* [µm]	*B* [mm]	*W* [mm]
0	-	4.84	12.55
1	45	4.90	9.95
1	92	4.89	9.96
1	427	4.88	9.96
2	88/88	4.93	9.93
3	107/140/109	4.91	9.91

5.4.3 Processing route of C45/DC04 composites

The manufacturing route for the C45/DC04 composites is mostly similar to the X210CrW12/DC04 composites. The key difference is the higher forging temperature of 1050 °C, **Figure 74**a. After spark eroding and machining, the samples are heat treated according to the schematic in **Figure 74**b. In contrast to the X210CrW12 matrix, the C45 steel needs to be water quenched to achieve a high contrast in yield strength to the DC04 interlayer material. A subsequent annealing step aims to relieve some of the residual stresses.

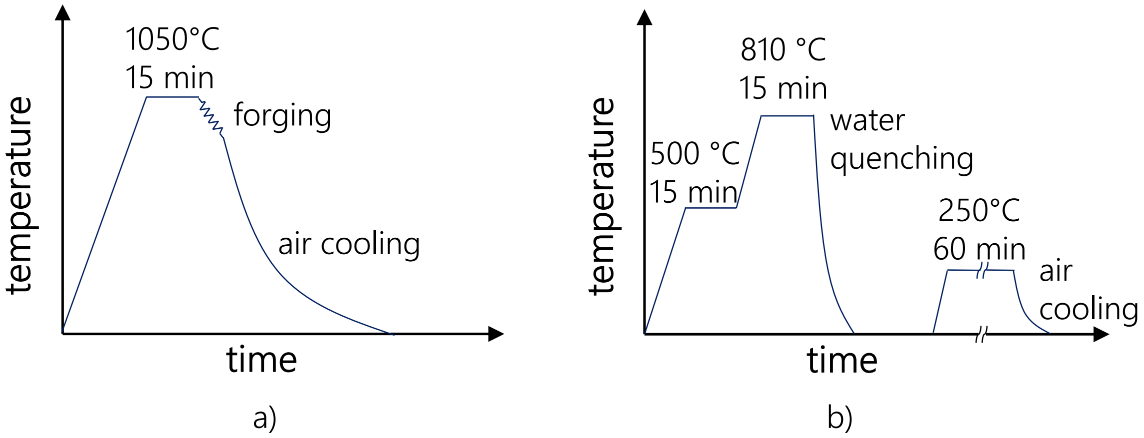

Figure 74: Schematic temperature-time route applied for a) forging and b) heat treatment of the spark eroded and machined C45/DC04 composites.

Table 9 lists the geometry of the manufactured composites with a C45 matrix. Apart from a reference specimen without interlayer, only single interlayered specimen were produced.

Table 9: Geometry of C45/DC04 composites.

#interlayers	*t* [µm]	*B* [mm]	*W* [mm]
0	-	4.89	11.45
1	75	4.88	11.82
1	120	4.87	11.62
1	55	4.86	11.75
1	120	4.93	11.67

6 Fracture behavior of laminated composites

6.1 Properties of interface and interlayer

Some properties of selected composites were studied to understand their behavior in fracture mechanics tests. The interface strength was quantified by tensile tests, and the grain size distribution and texture in the interlayer was determined by EBSD. Finally, nanoindentation measurements examine the hardness differences between matrix and interlayer.

6.1.1 Interface strength

In fracture mechanical experiments the interfaces between matrix and interlayer(s) are exposed to a multiaxial stress field caused by the crack, as well as plastic deformation of the interlayer. The strength of the matrix/interlayer interfaces is therefore a determining factor in preventing delamination.

6.1.1.1 Methodology

To quantify the interfacial strength, miniature tensile samples were prepared and tested according to the procedure developed in (Rat2013). Rectangular platelets were extracted with electro discharge machining from single interlayer composites with an X210CrW12 matrix, Figure 75a-b. The platelets were then heat-treated similarly to the fracture mechanics specimen and ground into tensile specimen with a round cross-section of Ø ≈ 800 µm (Figure 75c). The thickness of the single interlayers, each located in the middle of the tensile specimens, amounted to *t* = 90, 160, 350 and 790 µm, respectively. For comparison, a bulk matrix specimen, i.e. a specimen without interface, was also tested.

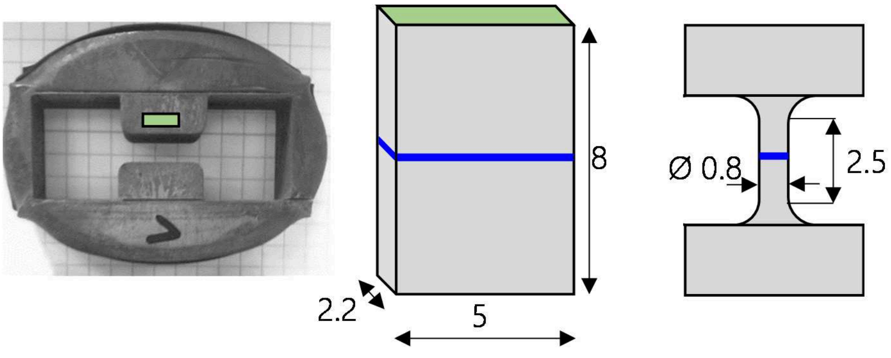

a) b) c)

Figure 75: Extraction of miniature tensile specimen. a) Location of the sampling site, b) dimension of the platelet and c) dimension of the ground miniature tensile specimen.

6.1.1.2 Results

Figure 76a compares the engineering stresses of the tested specimen with interlayers (solid lines) and without interlayer (dashed line) versus total elongation. Photographs of the corresponding specimen in the moment before fracture are shown in **Figure 76**b. The bulk specimen shows brittle fracture without prior plastic deformation. It is evident that the high surface exposure resulted produced excellent interfaces, as the interface strength exceeds the strength of the soft interlayer.

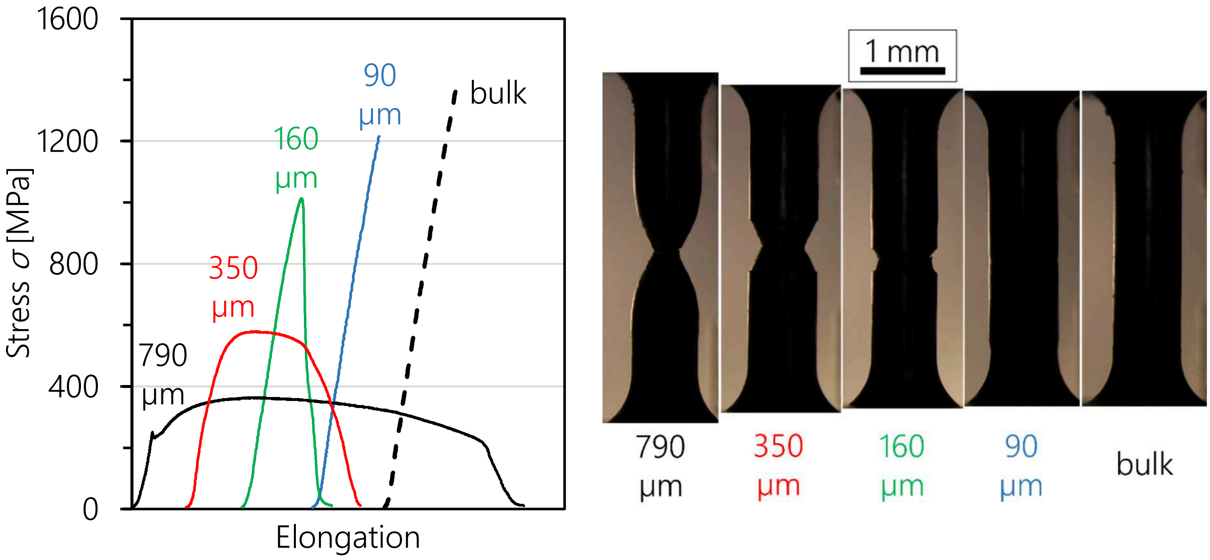

a) b)

Figure 76: a) Measured engineering stress-elongation curves and b) photographs of the corresponding specimens before fracture. The measures indicate the respective interlayer thicknesses t.

Assuming that all of plastic deformation is contained in the interlayer and the interfacial area remains constant throughout the test, the maximum engineering stress corresponds to the maximum true stress acting on the interface. Correspondingly, this maximum stress is a lower bound of the interface strength. From the specimen with an interlayer of thickness t = 90 µm, this lower bound is measured as 1 250 MPa. **Figure 77**a-b shows both fracture surfaces of this specimen, tilted by 45°. In **Figure 77**b, local debonding at the second interface is marked with black arrows.

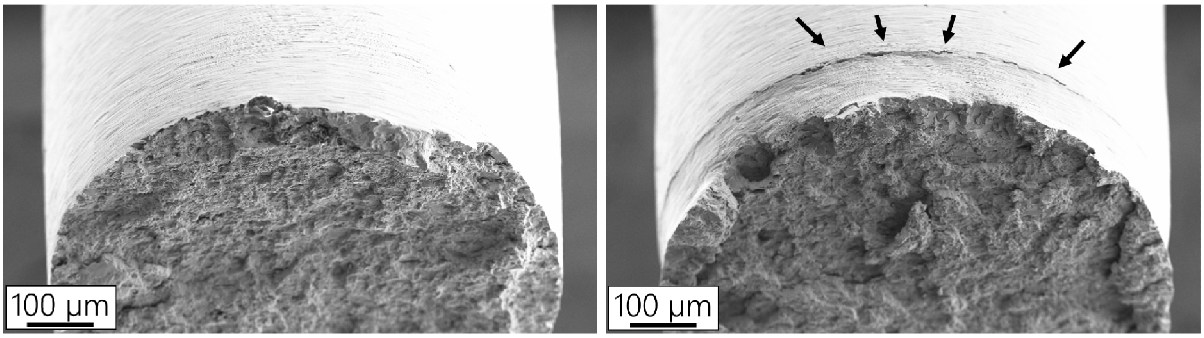

a) b)

Figure 77: (a) Upper and (b) lower fracture surface of the specimen with an interlayer of thickness *t* = 90 µm at a viewing angle of 45°. Debonding at the second interface is marked with black arrows.

6.1.2 Microstructure of the interlayer

Figure 78a shows an electrolytically polished metallographic cross-section of a single interlayer with *t* = 88 µm in an X210CrW12 matrix. Due to the carbon diffusion during the manufacturing and subsequent heat treatment, a ferritic-pearlitic microstructure develops in interlayers embedded in X210CrW12 tool steel matrix. In contrast, a single interlayer of similar thickness embedded in a C45 steel matrix is shown in Figure 78b. The microstructure of the interlayer is ferritic.

In the following, the grain structure of interlayers with different thicknesses is studied by EBSD. The scanned cross-sections were prepared after the fracture mechanics test from a cut about 1-2 mm below the fracture surface.

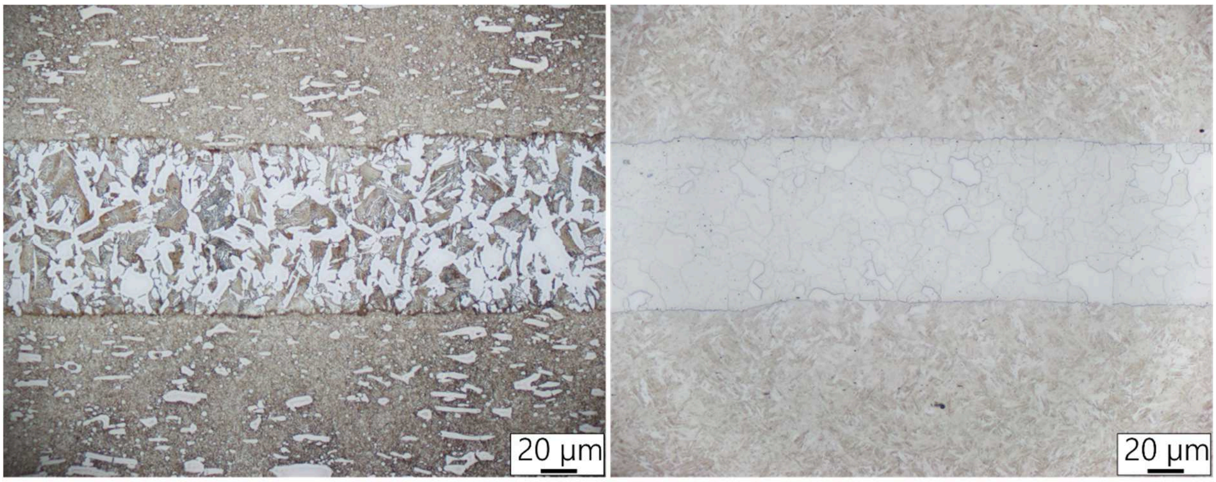

a) b)

Figure 78: Metallographic cross-section of a single interlayer with $t \approx 90$ µm embedded a) in X210CrW12 matrix and b) in C45 matrix after heat treatment.

Figure 79 compares parts of inverse pole figure + image quality maps from different interlayers in X210CrW12 matrix, denoted with numbers 1 to 5. The interlayers 1 to 4 thereby stand for single interlayers located in an X210CrW12 matrix, with t ranging from 45 to 427 µm. A multilayered composite with two interlayers was studied as well. The numbers 5-1 and 5-2 designate the first and second interlayer in that specimen, respectively. Some of the ferritic grains in the interlayers show a somewhat irregular shape. This could be caused by partial, needle-like formation of Widmanstätten ferrite upon cooling from austenitization temperature. Only in the middle of the thick interlayer 4, equiaxed grains dominate. The largest grains reach maximum lengths of about 50 µm. This is a relevant observation especially for thin interlayers: In interlayer 1, some grains are visible which span the whole thickness of the interlayer. To anticipate a later chapter, a potential cleavage crack in such a grain can easily cross the whole interlayer.

While Figure 79 offers some information about grain orientation, pole figures are more instructive to learn about a possible texture. (001) pole figures are plotted in Figure 80. A pronounced texture can be seen in the pole figures corresponding to the thick interlayer with t = 427 µm. However, it is worth noting that the possible scan size scales with the interlayer thickness, i.e. thick interlayers yield a better statistic. Figure 80 is interesting as it shows the orientation of the crystals regarding the (001) cleavage plane. It can be concluded that most cleavage planes are tilted with respect to the crack plane, yielding a ragged fracture surface in the case of cleavage cracking of the interlayer.

Figure 81 finally compares the grain size distributions within these interlayers. It is evident that the average grain size in the interlayer ranges from 15-20 µm, with some grains reaching diameters up to 40-50 µm. The thicker the interlayer, the higher the number of grain boundaries a crack growing through an interlayer has to cross.

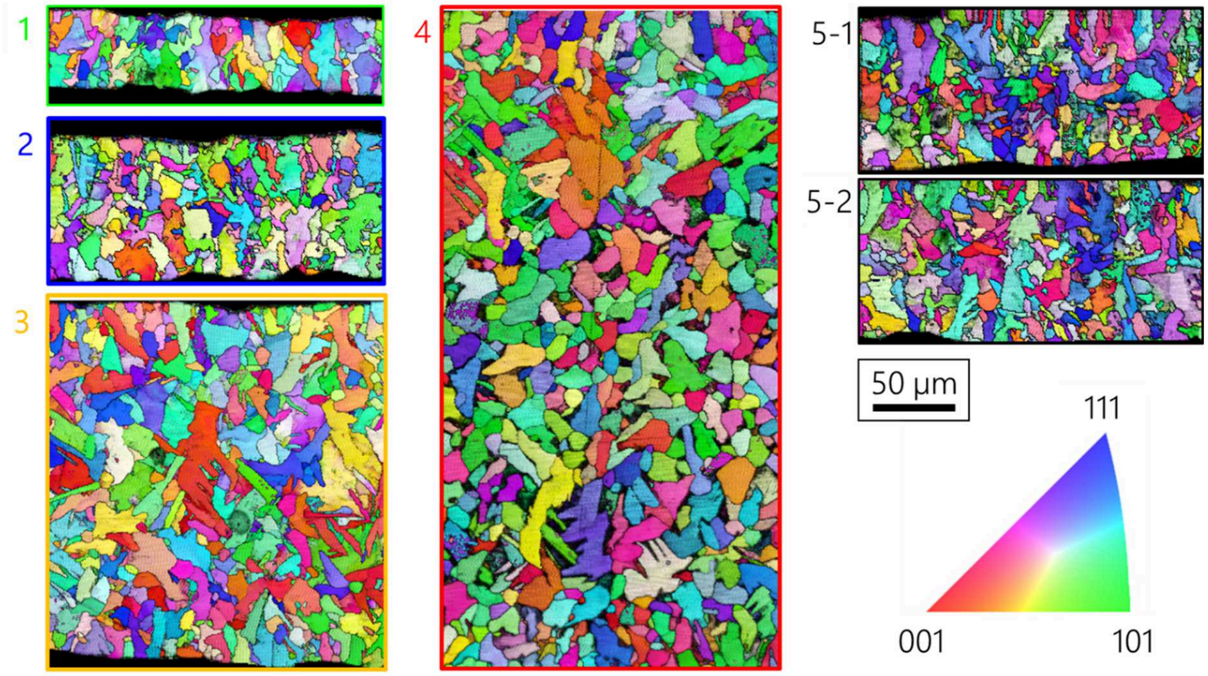

Figure 79: IPF + IQ maps for different DC04 interlayers. The numbers 1 to 4 correspond to interlayer thicknesses of t = 45, 92, 202 and 427 µm respectively. The numbers 5-1 and 5-2 correspond to two interlayers with $t_1 = t_2$ = 88 µm in a two-interlayer specimen.

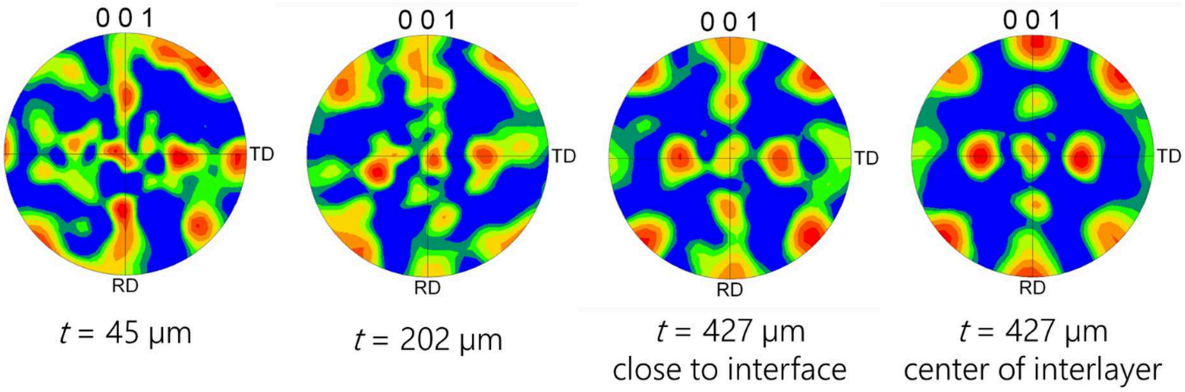

Figure 80: (001) pole figures of interlayers with varying thickness. With *t* = 427 µm, the texture is more pronounced at the center of the interlayer.

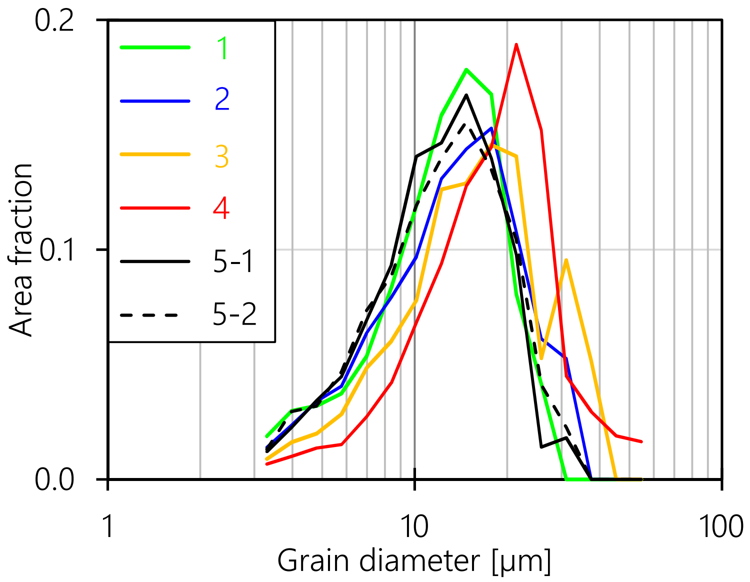

Figure 81: Grain size distribution in various DC04 interlayers. The numbers correspond to the interlayers shown in Figure 79.

6.1.3 Nanoindentation measurements

The extent of the material inhomogeneity effect is determined by the difference in yield stress or young’s modulus, respectively. The difference in mechanical properties are estimated via nanoindentation measurements using an indentation depth of 500 nm.

Due to the presence of carbides, a hardness scatter in the X210CrW12 matrix is to be expected. This is shown in Figure 82, which is a light microscopic image of nanoindents at a matrix/interlayer interface. The associated hardness values in GPa are given as well.

Figure 83 a) to d) shows the hardness variation measured in single interlayer specimens with an X210CrW12 matrix, while a two-interlayer X210CrW12/DC04 composite is depicted in Figure 83 e). The numbers in the interlayers correspond to Figure 79. The measurements are summarized in Figure 83 f), which plots the average hardness values of matrix and interlayer as a function of the interlayer thickness. The high variation of the measured matrix hardness is caused by the presence – or absence - of carbides. A sharp decrease in hardness at the matrix/interlayer interface is evident. Furthermore, no significant hardness gradients within the interlayers, e.g. as a result of carbon diffusion, is observed.

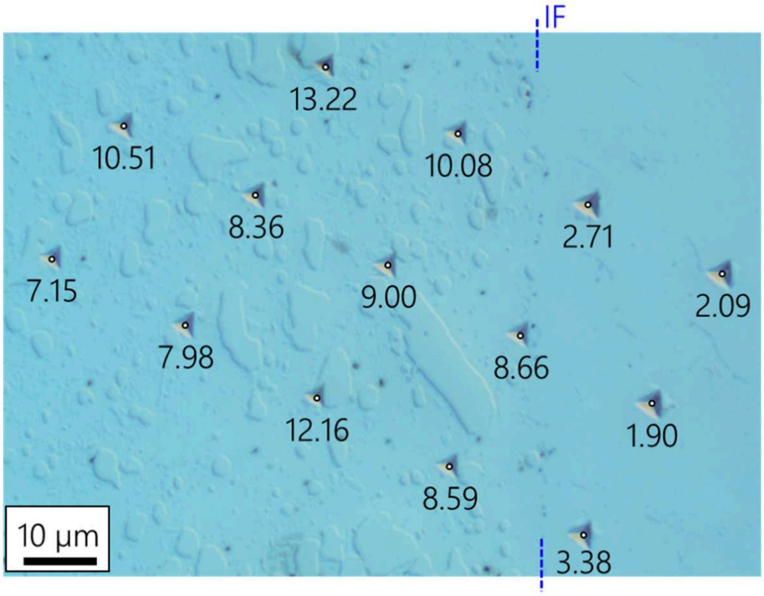

Figure 82: Location of nanoindents and hardness values in GPa at a matrix/interlayer interface..

As seen in Figure 83f, the average hardness of the X210CrW12 matrix and interlayer is 10 and 2.5 GPa, respectively. In measurements with a smaller indendation depth of 100 nm, the hardness of the carbides was measured as 24 GPa.

Table 10 lists the average values of Young's modulus and hardness. The slightly higher average modulus of the matrix can be attributed to the presence of the carbides, which are considerably stiffer.

Table 10: Average values of Young's Modulus and hardness as determined by nanoindentation.

	# indents	Young's Modulus [GPa]	Hardness [GPa]
Carbide	7	329.0	24.7
X210CrW12	163	242.3	9.6
DC04	138	220.5	2.5

No indentation measurements were performed with C45/DC04 composites, as the comparatively small carbon content also decreases diffusion into the interlayer. A sharp hardness transition is therefore also expected in C45/DC04 composites.

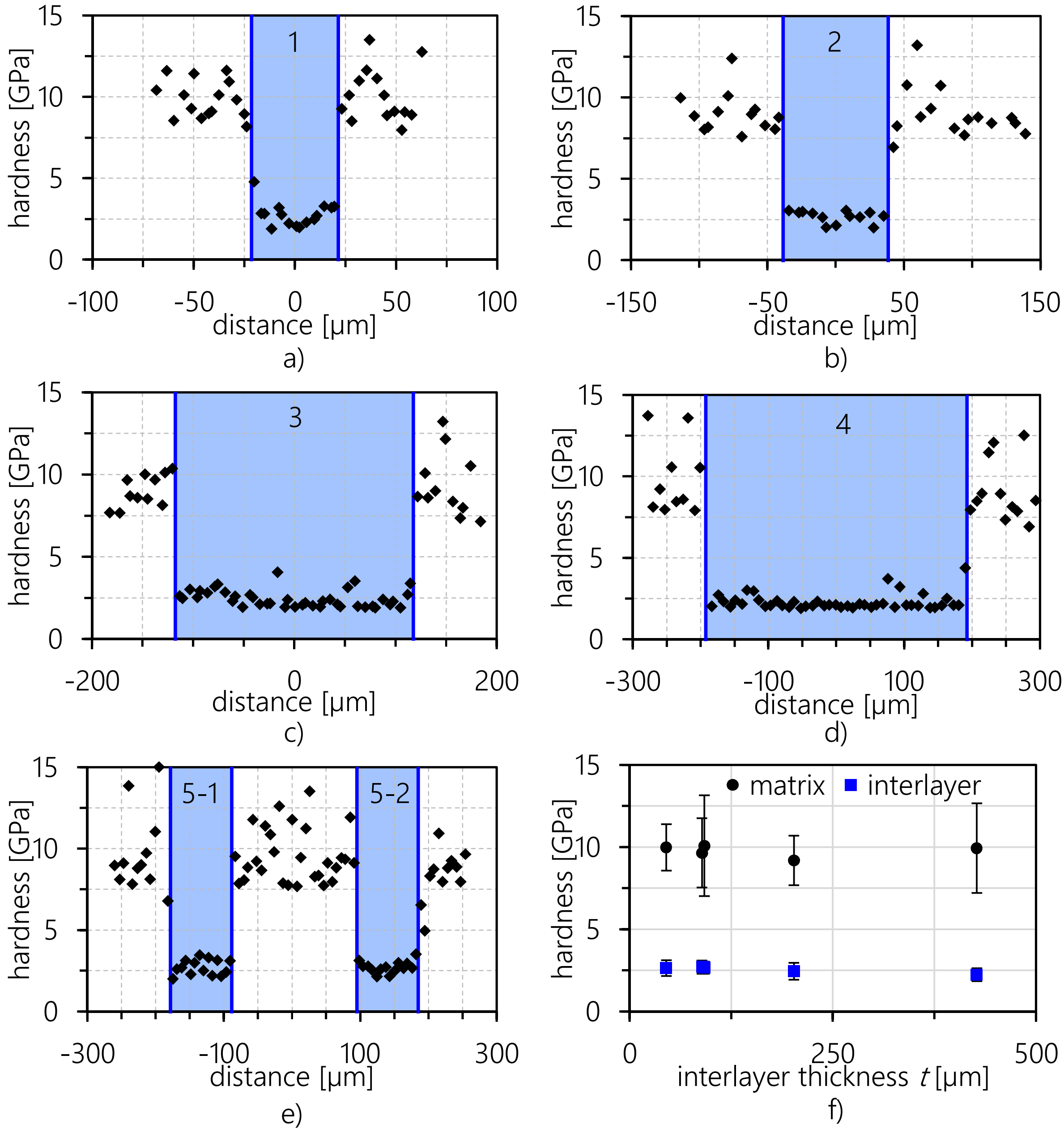

Figure 83: a) to e) Variation of local hardness in matrix and interlayer as measured by nanoindentation in different X210CrW12/DC04 composites. The numbers correspond to the interlayers shown in Figure 79. f) Variation of average hardness values as a function of interlayer thickness *t*.

6.1.4 Summary

In this chapter, selected properties of the composites were studied. In tensile tests with X210CrW12/DC04 laminates it was shown that the strength of the interface is superior to that of the interlayer. A lower bound of the interface strength was established as 1 250 MPa. EBSD showed ferrite grains with irregular shapes, but with similar grain size distributions in the interlayers studied. The average ferrite grain size is in the range of 15-20 µm, with the thick interlayer showing a tendency to larger grains. Maximum grain sizes are in the order of 30-50 µm. Nanoindentation confirmed the sharp transition between hard matrix and soft interlayer, as well as the absence of a hardness gradient within the interlayer. The average modulus of the X210CrW12 matrix is slightly higher compared to the DC04 interlayer, which is attributed to the presence of stiff carbides.

Similar conclusions can be drawn for C45/DC04 composites. Due to the same thickness reduction, a similar interfacial strength is to be expected. Owing to the reduced carbon content in the matrix, a sharp transition in hardness between matrix and interlayer is also anticipated, see also Figure 78. However, no nanoindentation or interfacial strength experiments were performed with these composites.

6.2 Fracture behavior of composites with X210CrW12 matrix

In this chapter, results of fracture mechanics tests with different thickness and number of interlayers and representative photographs and SEM-images from fracture surfaces are presented.

6.2.1 Fracture mechanics tests

Some experimental details and the results of the fracture mechanics tests are shown in the following. Before demonstrating the significant influence of soft interlayers, a specimen without interlayer, but containing a matrix/matrix interface, is presented. The sample geometry and critical J-values determined in the experiment are then summarized.

6.2.1.1 Sample preparation and testing

The production route and geometry of the fracture mechanics samples was covered in chapter 5.4.2. After the final heat treatment, the samples were polished to allow for better visibility of the future crack. A starter notch was then introduced by electro discharge machining or wire cutting and sharpened with a razor blade. The samples were then pre-fatigued in two steps. First, a fatigue precrack was introduced in compression at R = 10 and $\Delta K < 40$ MPa·m$^{0.5}$. After a precrack appeared on both specimen sides, fatiguing was carefully continued in tension at $R = 0.1$ and $\Delta K = 5$ MPa·m$^{0.5}$. If no crack growth occurred within 10 000 cycles, ΔK was raised carefully. Typically, $\Delta K = 7$ MPa·m$^{0.5}$ resulted in sufficient crack growth rates. Across all specimens, the maximum ΔK amounted to 13 MPa·m$^{0.5}$. The crack length was monitored optically and forces adjusted regularly to maintain constant values of ΔK. Fatiguing was stopped at $a_0/W \approx 0.36$. On average, the fatigue crack tip was located approximately 1 mm in front of the first interface of the first interlayer. The minimum fatigue crack length from the starter notch amounted to 0.95 mm.

The pre-fatigued specimen are then pin-loaded and tested with displacement control at a constant crosshead displacement rate of 0.3 mm/min using a Zwick tensile testing machine with a 100 kN load cell. The fracture mechanics experiments are analyzed by plotting experimental J-integral vs. crack extension (J–Δa) curves. Details on this evaluation can be found in chapter 3. The J-values incorporate both the elastic and the plastic part, i.e. $J = J_{\mathrm{el}} + J_{\mathrm{pl}}$.

The specimen were photographed at regular time intervals. From these photographs, the crack mouth opening displacement was measured directly on the edge of the specimen with digital image correlation using the free software GOM correlate (GOM). As DIC requires a random black/white pattern, the area around the notch was sprayed with commercially available white and black non-reflective paint.

6.2.1.2 Specimen without interlayer

A reference specimen without a soft interlayer was manufactured by press bonding. Due to that, a matrix/matrix interface was present in the specimen. Figure 84a shows the force-CMOD record of the fracture mechanics test. Point (1) marks the onset of loading of the specimen. It is evident that the specimen behaves linear elastic until a load of about 5 kN, point (2), upon which the composite fails catastrophically. The photographs in Figure 84b correspond to the points highlighted in Figure 84a. The initial crack length a_0 after pre-fatiguing as well as the approximate location of the matrix/matrix interface are indicated as well. The photographs also show that in this case the speckle pattern at the notch was insufficient for DIC, as a reflective paint was accidentally used. CMOD in this case was therefore measured with a clip gauge, which was attached to knives glued to the specimen surface. Figure 84c finally plots the experimental J–Δa curve, where the crack length was determined with the potential drop technique. This curve supports the observation already made in Figure 84a: The composite fails catastrophically upon reaching a critical value of J for the matrix, $J_c^M = 2.01$ kJ/m^2, without significant prior stable crack growth. Furthermore, the matrix/matrix interface provided no barrier to the rapidly propagating crack.

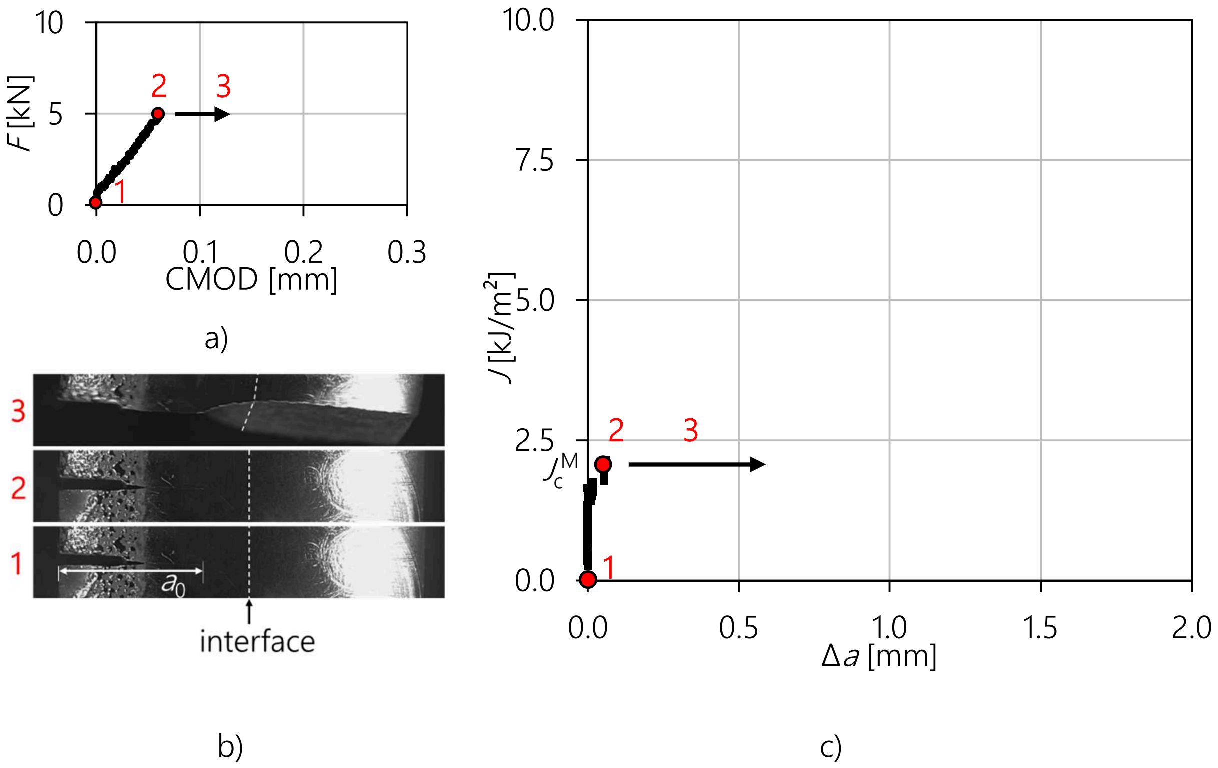

Figure 84: Fracture mechanics test of an X210CrW12 specimen with an interface. a) Load-CMOD curve. b) Photographs of the specimen at the points marked in a). The initial crack length after pre-fatiguing, a_0, as well as the interface are indicated. c) Experimental J-Δa curve.

6.2.1.3 Specimen with single interlayers

Figure 85 shows the results from testing a single interlayer specimen with interlayer thickness t = 45 µm. Figure 85a shows the load-CMOD curve. After an initial linear increase until point (1), an abrupt increase in CMOD at a slightly decreased load can be observed at point (2), hinting at a sudden crack extension. The load then increases until point (3), at which the sample fractures catastrophically. Figure 85b shows photographs of the specimen at the previously discussed points (1) to (4). The photograph corresponding to point (2) demonstrates that the pop-in observed in Figure 85a was caused by a crack extension, which was stopped by the DC04 interlayer. The experimental J-Δa curve is plotted in Figure 85c, where Δa was determined with the potential drop technique. After reaching a critical J-value in the matrix, J_c^M = 3.15 kJ/m^2, at point (1) the crack propagates very quickly but is arrested at the second interface of the interlayer, point (2). The increase in J between points (1) and (2) is caused by the increase in geometry factor f(a/W) with increasing crack length a, see equation (3.3).

The load has to be increased until J reaches a value of J_{max} = 12.3 kJ/m^2 (3). At this point, the specimen fractures completely (4). **Figure 85**b shows the corresponding load-CMOD curve. The sudden crack growth into the interlayer is evident as a sharp increase in CMOD, while the load only decreased slightly. **Figure 85**c finally shows photographs of the specimen at the points (1) to (4) marked in **Figure 85**a.

It is worth noting that no delamination occurred in this experiment.

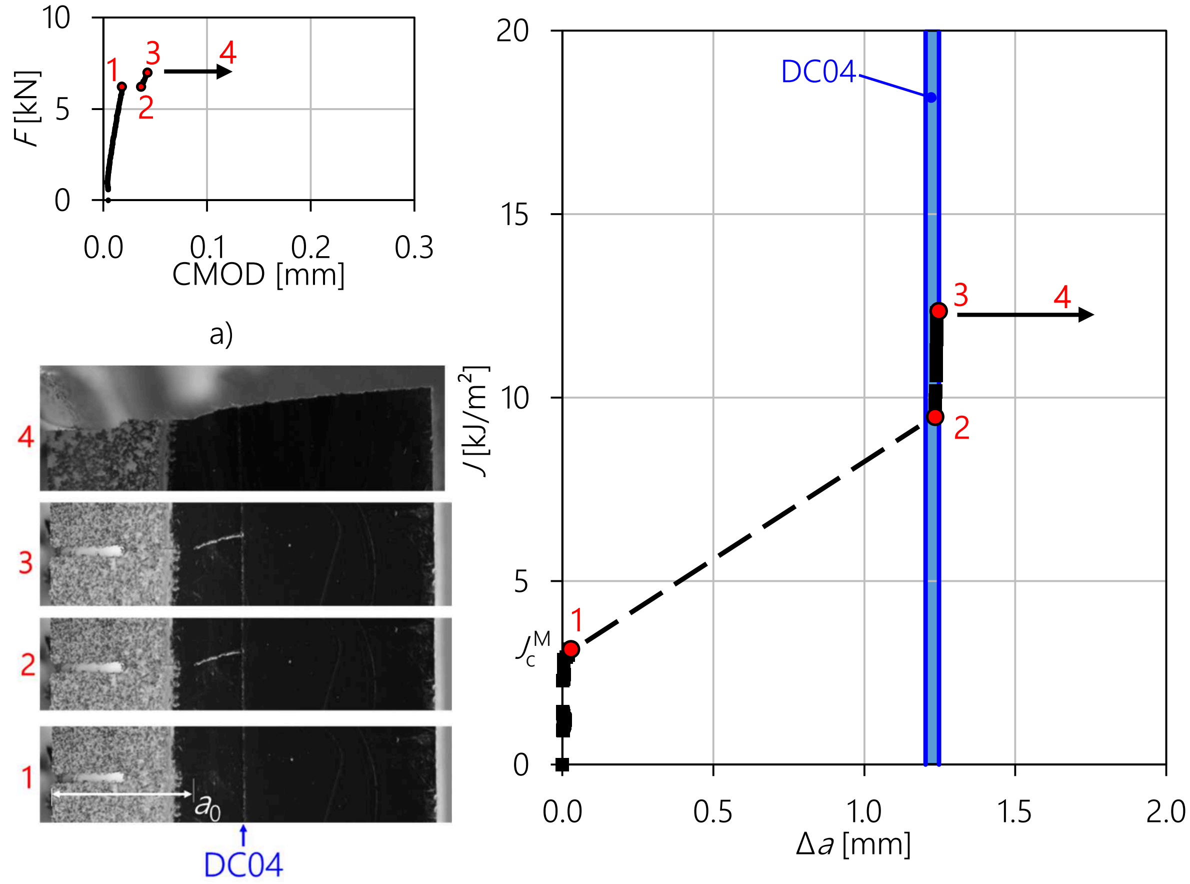

b)

c)

Figure 85: Fracture mechanics test of an X210CrW12 specimen with a single interlayer with t = 45 µm. a) Load-CMOD curve, where CMOD was measured with DIC. b) Photographs of the specimen corresponding to the points (1)-(4) marked in a). c) Experimental J-Δa curve. The interlayer is indicated in blue.

Figure 86 shows the results of a specimen with a single interlayer of thickness t = 92 µm. Also in this case the crack length was determined with the potential drop technique. The appearance of the load-CMOD curve, **Figure 86**a, is similar to the one shown in **Figure 85**a. Between points (1) and (2) a pop-in is visible, indicating sudden crack extension. Catastrophic final fracture occurred upon reaching point (3). Photographs of the specimen at the points (1) to (4) are shown in **Figure 86**b. **Figure 86**c finally plots the experimental J-Δa curve. After reaching J_c^M = 3.45 kJ/m^2, (1), the crack jumps into the interlayer and arrests at the second interface (2). Compared to the previous case, the maximum J sustained by the composite before fracture is higher, J_{max} = 19.4 kJ/m^2, point (3).

Also in this experiment, no delamination was observed.

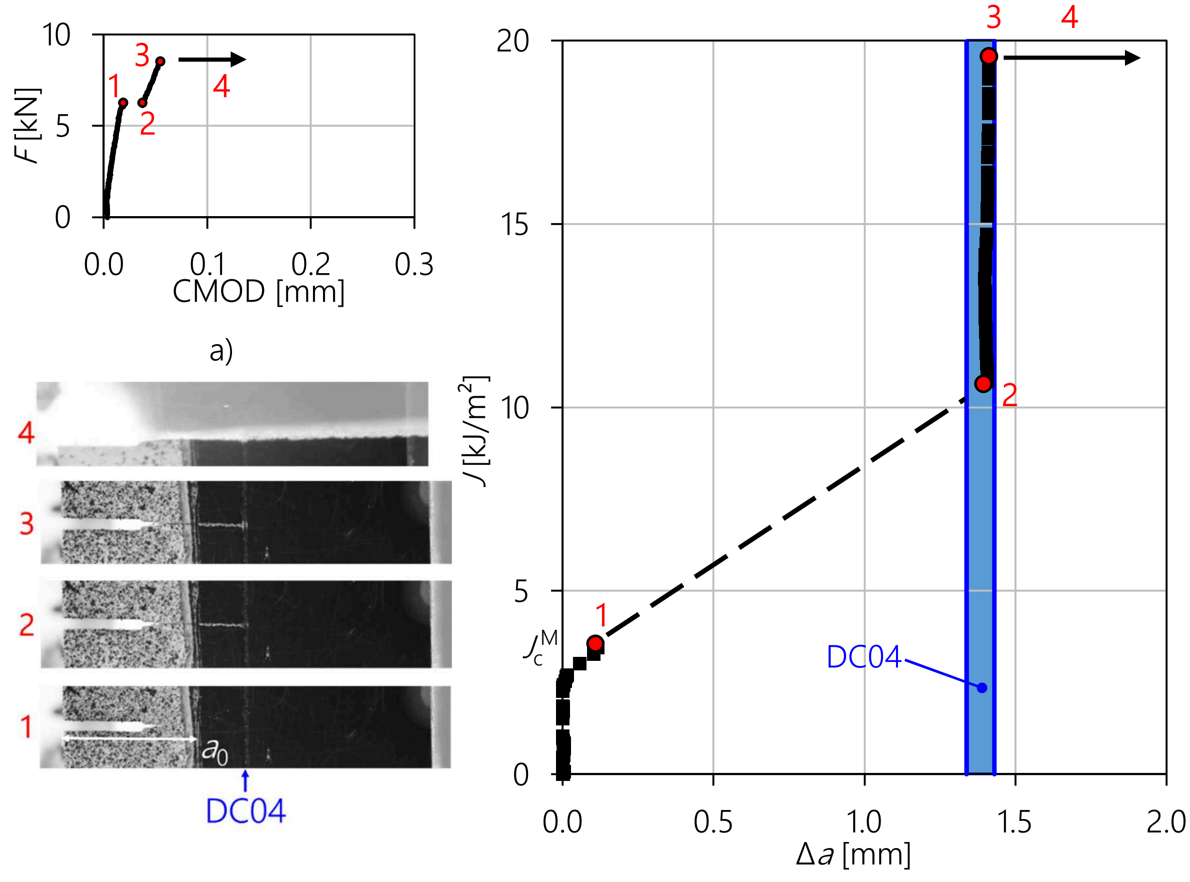

a)

b)

c)

Figure 86: Fracture mechanics test of an X210CrW12 specimen with a single interlayer with t = 92 µm. a) Load-CMOD curve, where CMOD was measured with DIC. b) Photographs of the specimen corresponding to the points (1)-(4) marked in a). c) Experimental J-Δa curve.

Finally, a specimen with a very thick interlayer with t = 427 μm is shown in **Figure 87**. Both the load-CMOD record (**Figure 87**a) the experimental J-Δa curve (**Figure 87**c) show a significant improvement: The maximum J-value before fracture, J_{max} = 153 kJ/m^2, is a factor 35 higher than the fracture initiation toughness of the matrix, J_c^M = 4.13 kJ/m^2. **Figure 87**c also shows that in this case, the crack arrested not at the second interface, but rather approximately in the middle of the interlayer. Further loading then causes blunting of the crack tip, which results in a slight increase in Δa.

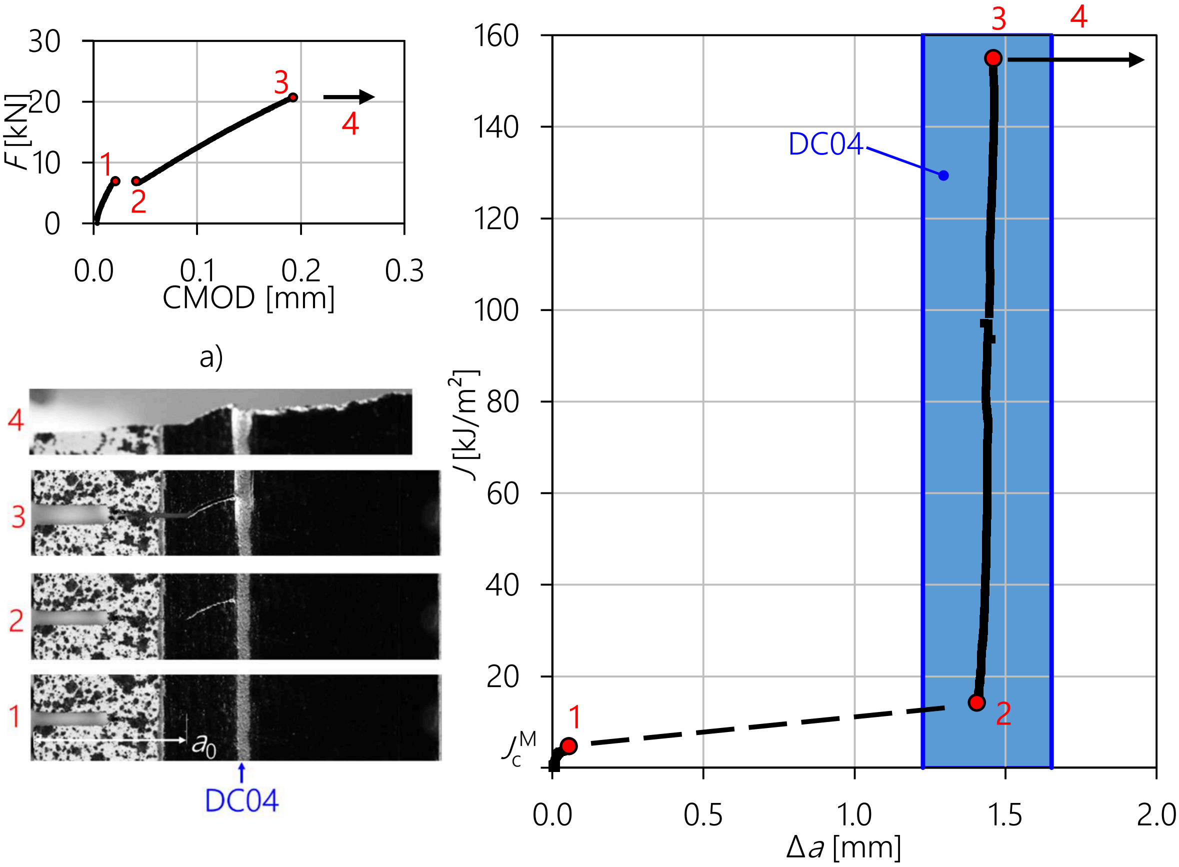

b)

c)

Figure 87: Fracture mechanics test of an X210CrW12 specimen with a single interlayer with t = 427 μm. a) Load-CMOD curve, where CMOD was measured with DIC. b) Photographs of the specimen corresponding to the points (1)-(4) marked in a). c) Experimental J-Δa curve.

6.2.1.4 Specimen with multiple interlayers

In **Figure 88** and **Figure 89**, the results of composites with two and three interlayers are demonstrated, respectively. While CMOD was again determined with digital image correlation, the crack lengths at the crack arrest positions were measured from the fracture surfaces as potential measurements were unsuccessful.

Figure 88 presents an X210CrW12/DC04 laminate with two interlayers of equal thickness, $t_1 = t_2 = 88$ µm. **Figure 88**a shows the load-CMOD record, which shows a single pop-in between points (1) and (2). The photographs of the specimen show that the crack arrested in the first interlayer, **Figure 88**b. Upon reaching point (3), crack growth reinitiated and the second interlayer could not stop the propagating crack. The experimental J–Δa curve, **Figure 88**c, further clarifies the specimen behavior. After reaching $J_c^M = 4.7$ kJ/m^2 (1), the crack quickly spread into the first interlayer and arrested there (2). The load had to be increased further to re-initiate crack growth (3). As already noted, the second interlayer could not stop the propagating crack at $J_{max} = 26.9$ kJ/m^2.

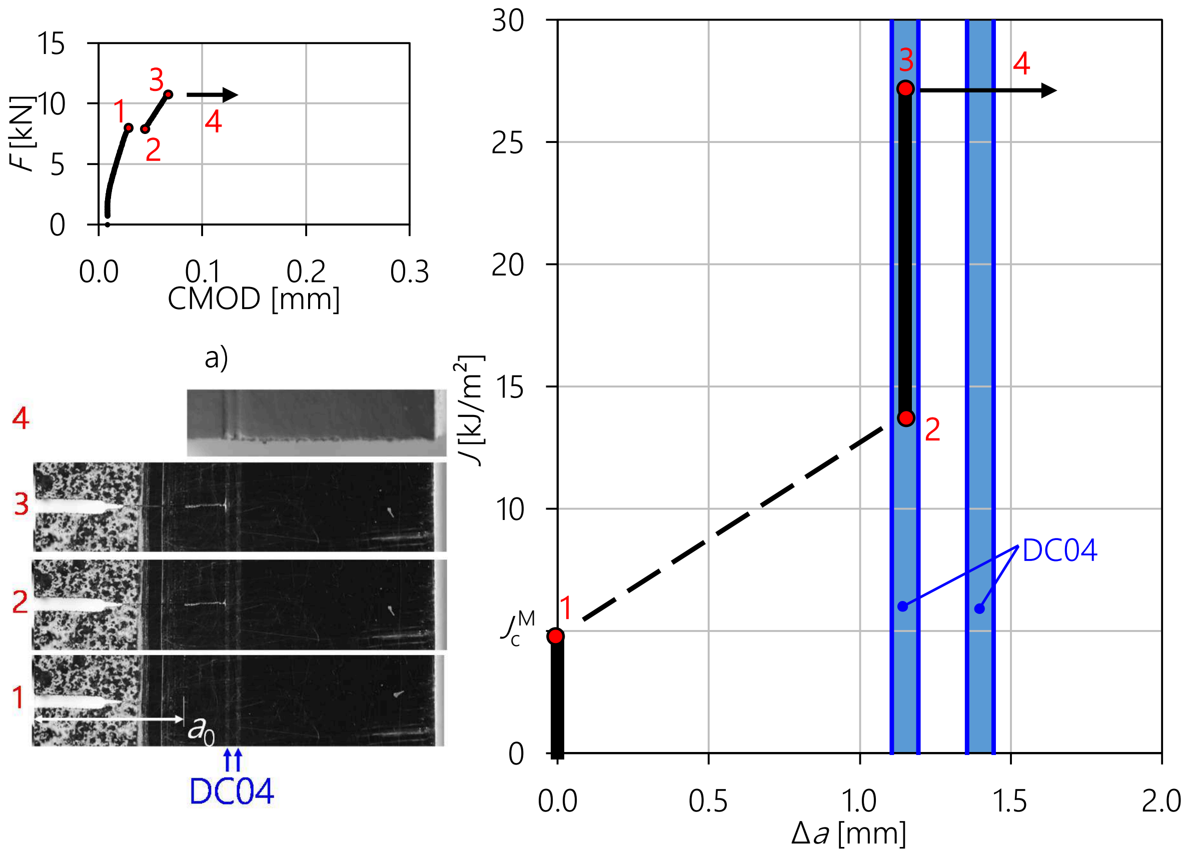

a)

b)

c)

Figure 88: Fracture mechanics test of an X210CrW12 specimen with two interlayers with thicknesses t_1 = t_2 = 88 μm. a) Load-CMOD curve, where CMOD was measured with DIC. b) Photographs of the specimen corresponding to the points (1)-(4) marked in a). c) Experimental J-Δa curve.

Figure 89 presents an X210CrW12/DC04 laminate with three interlayers of thickness 107, 140 and 109 μm, respectively.

The load-CMOD record (**Figure 89**a) shows a striking difference to the two-layered specimen from before. This time, two separate pop-ins are visible between the marked points (1)-(2) and (3)-(4), hinting at two sudden crack extensions. This is also clear from the photographs shown in **Figure 89**b, where crack arrest in the first and second interlayer is visible. At point (5), crack growth re-initiates once more. As the crack was not arrested by the third interlayer, final catastrophic failure of the composite occurs (6). The experimental J-Δa curve is shown in **Figure 89**c, where the two crack arrests in the first (2) and second interlayer (4) are clearly depicted. At point (5), J_{max} of this composite is reached at J_{max} =

37.8 kJ/m^2. The third interlayer cannot arrest the propagating crack and the specimen fails (6).

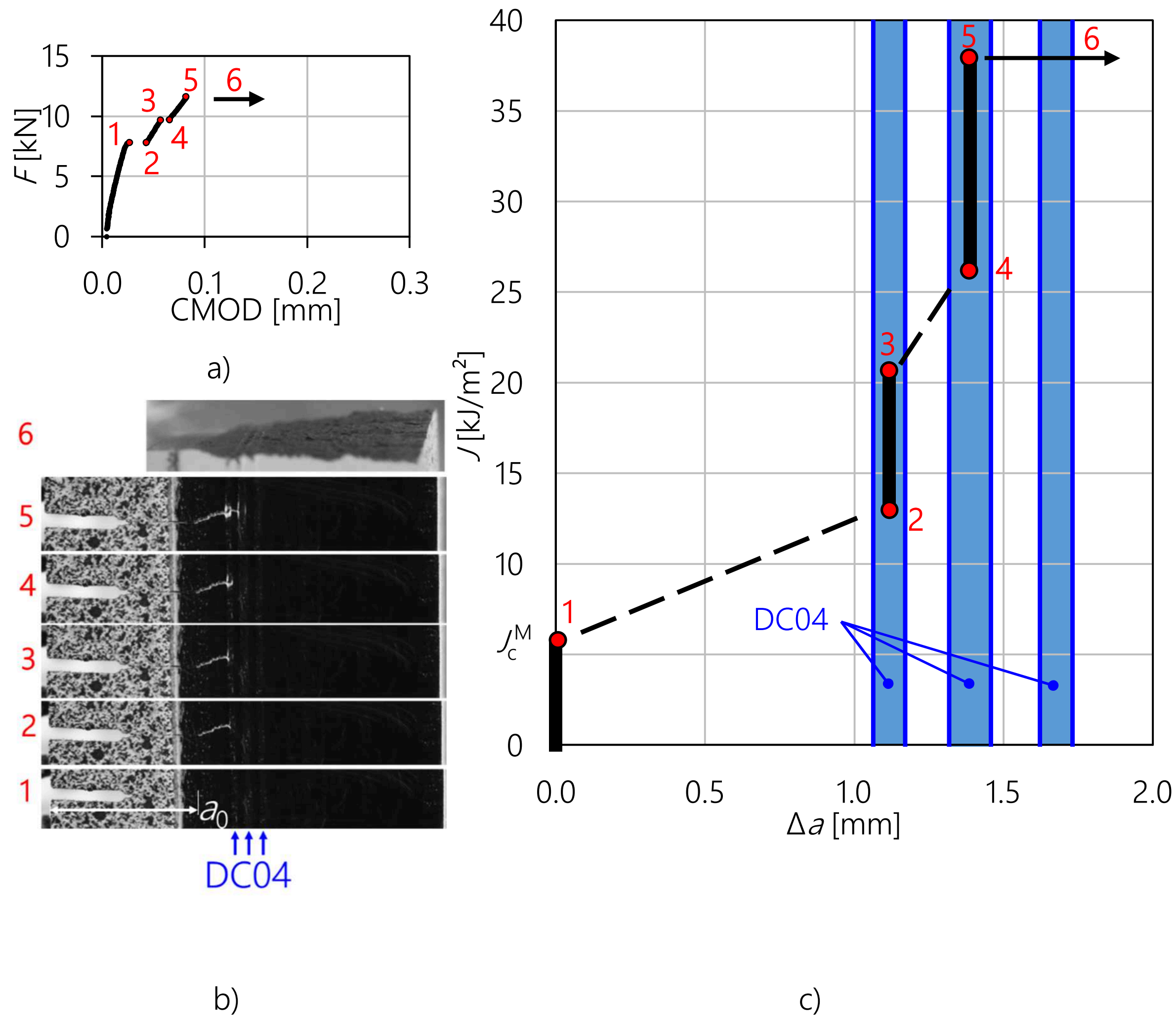

a)

b)

c)

Figure 89: Fracture mechanics test of an X210CrW12 specimen with three interlayers with thicknesses t_1 = 107, t_2 = 140 and t_3 = 109 µm. a) J-Δa curve. b) Load-CMOD curve, where CMOD was measured with DIC. c) Photographs of the specimen corresponding to the points 1-5 marked in a).

6.2.1.5 Summary

The geometry and critical J-values for matrix (J_c^M) and composite (J_{max}) are summarized in **Table 11**. A significant scatter in J_c^M is evident, as the measured values range from 2.01 to 5.37 kJ/m^2. This may be caused by the partly inhomogeneous distribution of large primary carbides, which preferentially are orientated along lines parallel to the crack front. Upon reaching this critical J-value, critical crack growth occurs, which immediately destroys the sample without interlayer. In the specimen with soft interlayer(s), the crack was arrested. The improvement caused by the soft interlayer(s) is significant: A factor 3.9 improvement between J_{max} and J_c^M was measured in the specimen with a 45 µm interlayer.

The volume fraction of the soft interlayer is in this case only 0.45%, which will only insignificantly reduce the overall composite strength. The improvement of the fracture resistance scales with interlayer thickness, but not linearly. In the case of a 427 µm thick interlayer, the improvement was more than a factor 35 compared to J_c^M. In the presence of several interlayers, it is possible for a crack to be arrested multiple times, as was seen in the sample with three interlayers.

From these experiments only, it is difficult to predict the critical J-value J_{max} for a given composite geometry. With the configurational forces model, a novel way to estimate these critical J-values is available, however. This is discussed in the next section.

Table 11: Geometry and critical J-values for different X210CrW12/DC04 composites.

#interlayers	t [µm]	B [mm]	W [mm]	a_0 [mm]	L_1 [mm]	J_c^M [kJ/m^2]	J_{max} [kJ/m^2]
0	-	4.84	12.55	5.06	-	2.01	2.01
1	45	4.90	9.95	3.67	1.20	3.15	12.30
1	92	4.89	9.96	3.59	1.34	3.45	19.41
1	427	4.88	9.96	3.71	1.23	4.19	153.30
2	88/88	4.93	9.93	3.68	1.11	4.70	26.93
3	107/140/109	4.91	9.91	3.57	1.06	5.37	37.80

6.2.2 Prediction of the fracture resistance of X210CrW12/DC04 laminates

The previous section demonstrated a significant scatter in the experimentally determined critical J-values for matrix (J_c^M) and composite (J_{max}). The necessary load increase to further propagate the crack is of significant interest for engineering applications. As was mentioned in the introductory chapter, numerical modelling in combination with the configurational forces model is a powerful tool to predict the fracture resistance of inhomogeneous materials. This is not straight-forward, as the fracture resistance of these layered composites is influenced by several factors:

- Fracture resistance of matrix and interlayer
- Interface strength

- Effect of a material inhomogeneity
- Effect of residual stresses

In the case of multiple interlayers, the distance between the individual layers is of importance. For example, a second interlayer in front a crack arrested in the first interlayer introduces an anti-shielding effect, which reduces the shielding effect of the first interlayer. In general, a multilayered specimen should therefore show a decreased fracture resistance compared to a specimen with a single interlayer.

Due to the differences in thermal expansion ratio between interlayer and matrix material, local residual stresses are introduced. The amount of residual stresses is governed by the local volume fraction of interlayer and matrix. Compressive residual stresses in the matrix would decrease the crack driving force in addition to the shielding effect of the material inhomogeneity.

In a recent paper, Sistaninia and co-workers (Sis2018) calculated the crack driving force with the configurational forces model, including both the effect of residual stress and material inhomogeneity. They showed that the crack driving force $J_{\mathrm{tip}}^{\mathrm{CA}}$ at a crack arrested in the interlayer becomes approximately equal to the critical J of the matrix, $J_{\mathrm{c}}^{\mathrm{M}}$.

The fracture resistance of a laminate with X210CrW12 matrix can therefore be estimated numerically, when the crack arrests at the interlayer/matrix interface. In the case of very thick interlayers this is not possible, as the crack arrests somewhere in the middle of the interlayer and starts to blunt. Final fracture may in this case be governed by reaching a critical tensile stress in the matrix.

The presence of brittle carbides in the X210CrW12 matrix adds another uncertainty factor. An inhomogeneous particle distribution results in increased stresses and strains both within the particles as well in the matrix in-between, which leads to earlier onset of damage and a reduction of the composite flow stress and ductility (Seg2003).

6.2.3 Fracture surfaces

Figure 90a-d compares photographs of selected fracture surfaces. **Figure 90**a shows the specimen without an interlayer. In **Figure 90**b-d the interlayer(s) have a glistening appearance and are therefore easily distinguishable from the matrix. This glistening is typical for cleavage fracture. Compared to the other three specimen, the matrix behind the thick interlayer, *t* = 427 µm, in **Figure 90**c shows a significantly higher roughness.

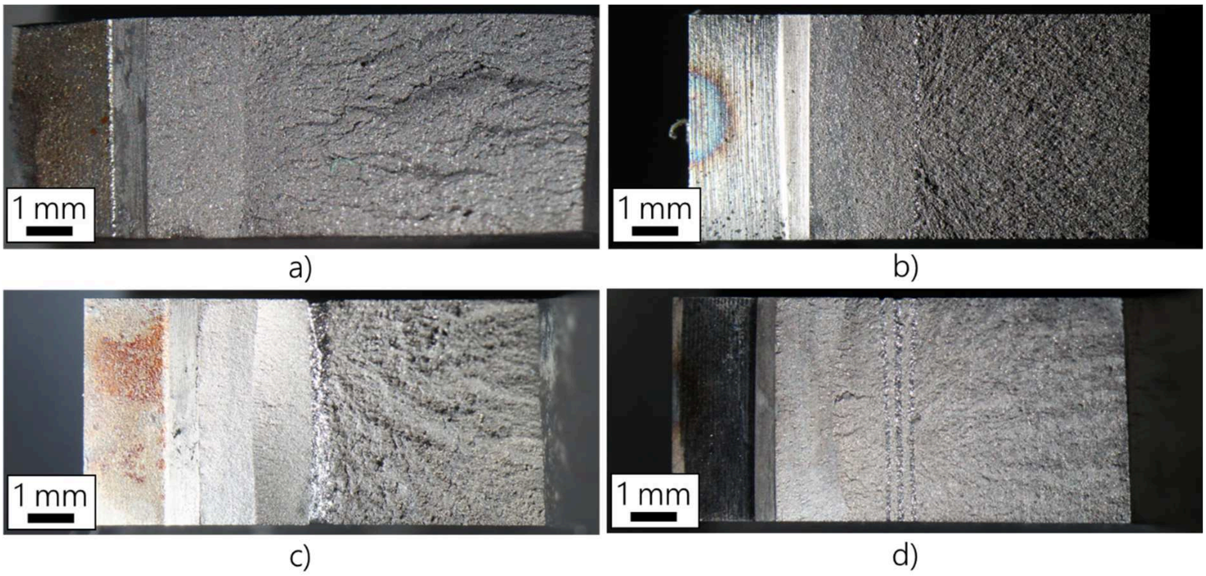

Figure 90: Photographs of X210CrW12 fracture surfaces. a) No interlayer, but an interface. b) Single interlayer with *t* = 92 µm. c) Single interlayer with *t* = 427 µm. d) Three interlayers with *t* = 107, 140 and 109 µm.

Figure 91 shows, for a specimen with a 92 µm thick interlayer and X210CrW12 matrix, SEM images of the fracture surface at different positions relative to the interlayer. **Figure 91**a-c are taken at a distance relative to the first interface of L_1 = -1000, -500 and -100, respectively. **Figure 91**d-f show the fracture surface at distances of L_2 = 100, 500 and 1000 µm behind the second interface. The increase in surface roughness thereby indicates an increase of the crack speed (Gro2012).

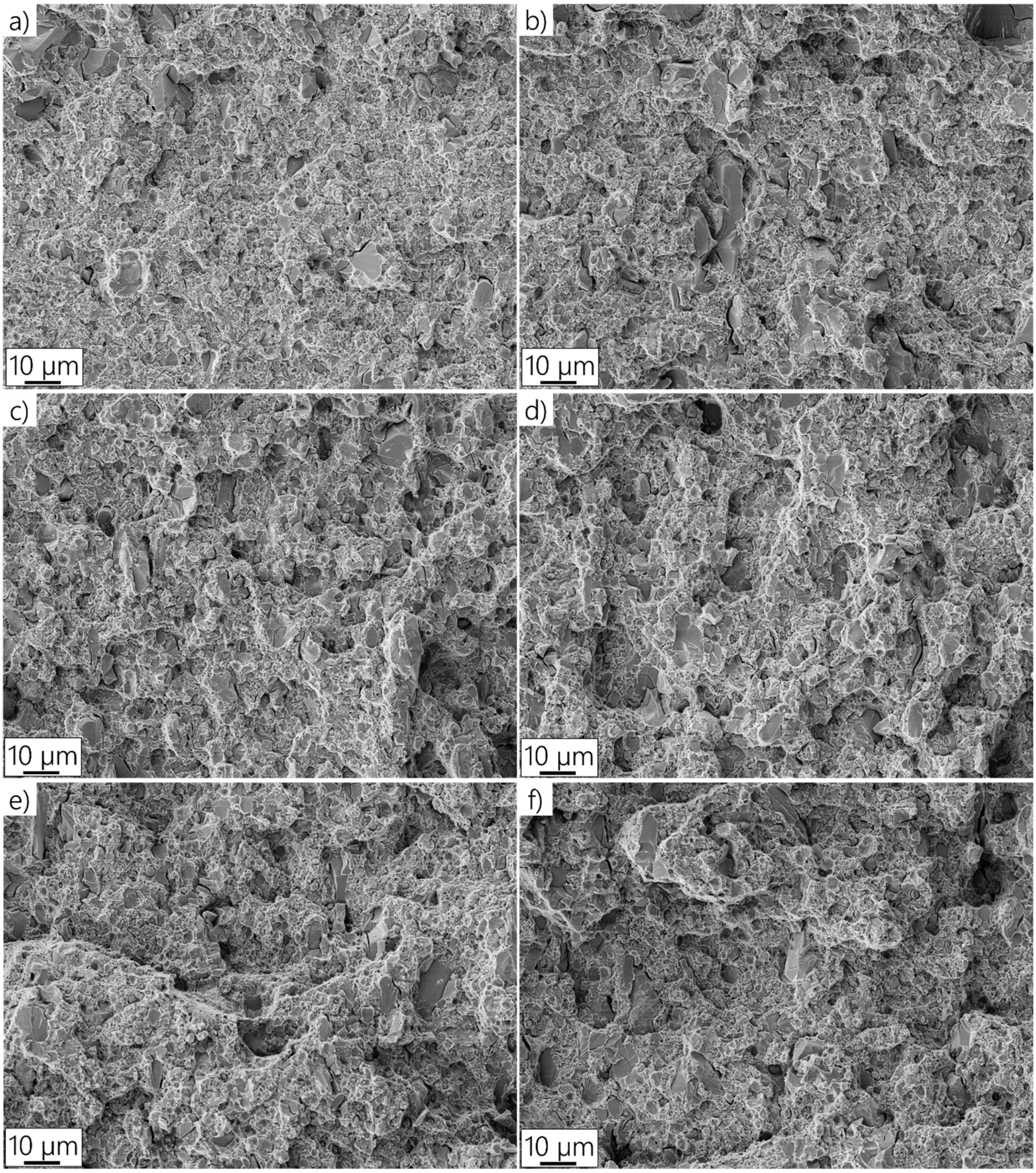

Figure 91: The roughness of the fracture surface increases with the crack length. a) L_1 = -1000 µm, b) L_1 = -500 µm, c) L_1 = -100 µm, d) L_2 = +100 µm, e) L_2 = +500 µm, f) L_2 = +1000 µm. Crack growth direction is from left to right.

Large, primary carbides within the matrix fracture in cleavage mode, Figure 92a. In the case of smaller carbides, both cleavage fracture as well as debonding between carbides and matrix can be observed. The matrix shows micro-ductile fracture, Figure 92b.

Due to its important role as a crack arrester, the fracture of the interlayer is shown and discussed separately in chapters 6.3 and 6.4.

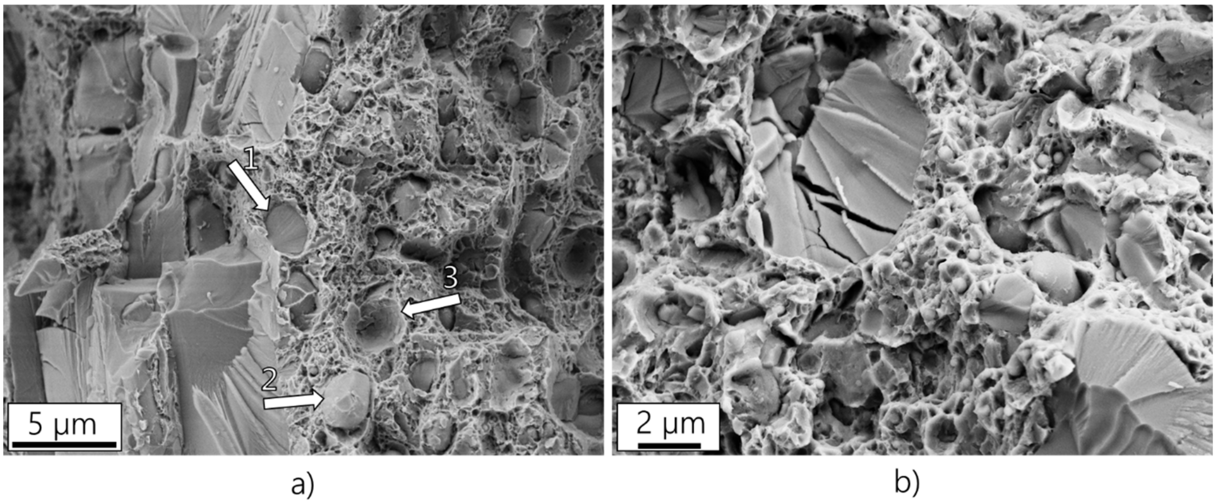

Figure 92: a) Cleavage fracture of large carbides in the X210CrW12 matrix. Smaller carbides embedded in the matrix can be (1) cleaved, (2) intact or (3) found on the corresponding fracture half. b) Micro-ductile fracture of the matrix.

6.3 Fracture behavior of the DC04 interlayer

To understand the behavior of the interlayers in the fracture mechanics tests, fracture surface observations are carried out in the SEM and explained in the following chapter. The cracking process is then further elaborated with crack profile measurements.

6.3.1 Observations on the fracture surfaces

Observation 1: The DC04 interlayer shows cleavage fracture in all X210CrW12/DC04 and C45/DC04 composites.

Observation 2: The crack path can be traced within the interlayer.

Figure 93a shows a SEM image of the fracture surface of an X210CrW12/DC04 composite with a thin single interlayer with thickness t = 45 µm. The interlayer can clearly be distinguished from the matrix due to the different fracture behavior. The river pattern caused by the cleavage fracture allows the identification of the crack path inside the interlayer, marked by white arrows in Figure 93b. It is evident that crack arrest occurred at the second interface, which is in agreement with the result from the potential drop technique used during the fracture mechanics test and with the numerical predictions of Sistaninia and Kolednik (Sis2014).

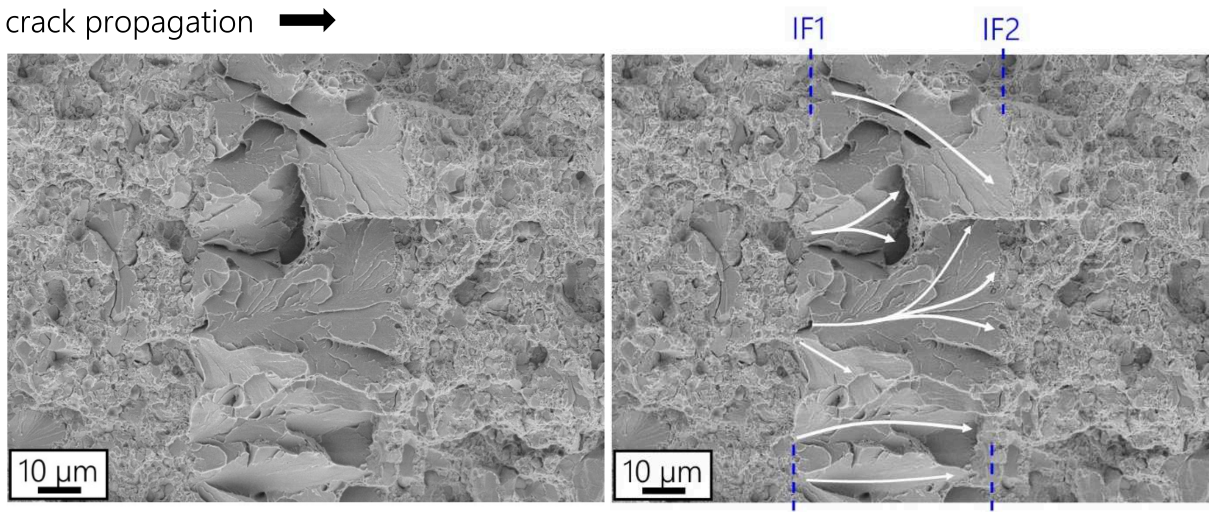

a) b)

Figure 93: a) Fracture surface of an X210CrW12/DC04 composite. The interlayer with t = 45 µm shows cleavage fracture and can be distinguished from the matrix. b) White arrows indicate the crack path inside the ferrite grains. The crack arrested at IF2.

Observation 3: Local crack growth against the global crack growth direction can be observed.

Some grains, even in very thin interlayers, may fracture in the opposite direction, Figure 94. In such a case ductile boundaries separate different stages of crack propagation. Figure 94a shows an enlarged view of a different region on the same specimen with *t* = 45 µm. Again, crack paths deduced from the river patterns are indicated with arrows in Figure 94b. Green arrows thereby show that locally a crack propagated in the opposite direction of the main crack. It is conceivable that the last remaining ligaments within the interlayer then fracture in a ductile mode as the stress state changes to plane stress.

Observation 4: Carbides frequently serve as crack initiation sites.

Often, the river patterns can be traced back to broken carbides located at the interfaces. Examples are marked with red circles in Figure 94b. This suggests that brittle second-phase particles may act as trigger points for cleavage cracking of the interlayer.

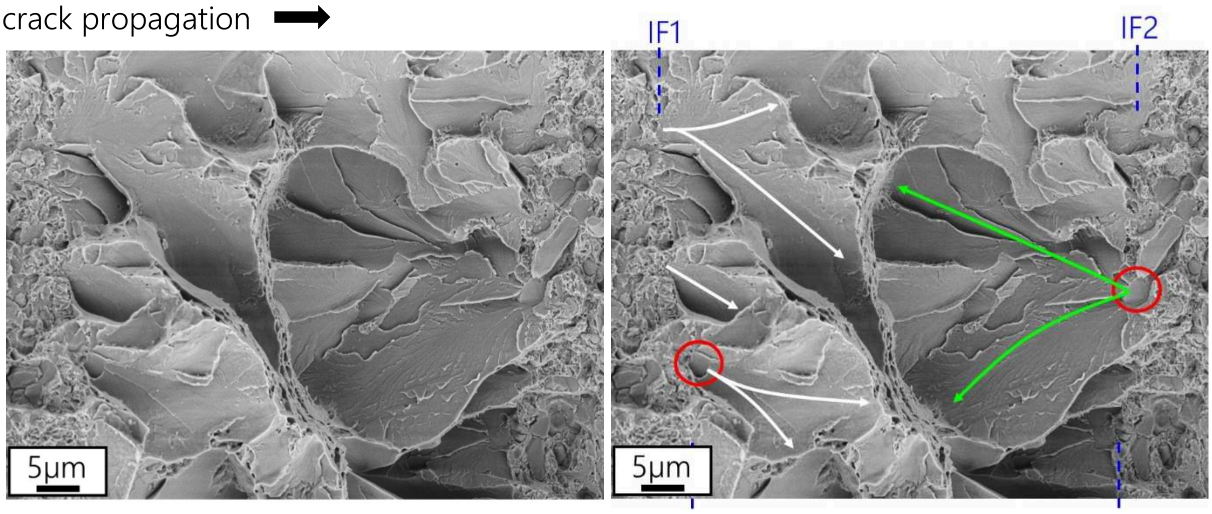

a) b)

Figure 94: a) Fracture surface of an X210CrW12/DC04 composite. The interlayer with *t* = 45 µm shows cleavage fracture and can be distinguished from the matrix. b) White and green arrows indicate crack propagation in direction of the main crack and in reverse direction, respectively. Two broken carbides at the interfaces IF1 and IF2, possibly serving as cleavage crack nucleation sites, are marked with red circles.

<u>Observation 5:</u> Stretched zones mark positions of local, temporary crack arrests.

Figure 95a shows the fracture surface of an X210CrW12/DC04 composite with a single, 427 µm thick interlayer. Approximately in the middle of the interlayer, a distinct stretched zone has been formed due to the local crack arrest and subsequent further loading of the specimen. The situation is explained in Figure 95b: White arrows mark the crack path when the crack propagated into the interlayer and arrested. The position of local crack arrest is identified with yellow arrows. These arrows therefore mark the transition from cleavage crack to a stretch zone. Following the stretched zone, a thin layer of ductile pores connects to a second cleavage fracture zone. The river patterns in this second zone indicate crack propagation to the left, as shown by green arrows.

<u>Observation 6:</u> Crack re-initiation occurs at interlayer/matrix interface or in matrix.

From the observations in Figure 95b, it can be concluded that after the crack arrest, the crack did not propagate directly from the stretch zone but rather re-initiated at the second interface or behind the second interface in the matrix. This can also be seen in Figure

96, which shows the fracture surface of an X210CrW12/DC04 composite with three interlayers, two of which are visible in **Figure 96**a. Two separate crack arrest events were observed in the fracture mechanics test, which is also reflected on the fracture surface. The fracture sequence is again clarified with arrows in Figure 96b. In the first step, the main crack propagated into the first interlayer IL1 and arrested there (white arrows). No significant blunting can be seen in the first interlayer, as the crack quickly re-initiated between the two interlayers IL1 and IL2. It then connected backwards with the main crack in IL1 (green arrows), but also propagated forwards into IL2 (white arrows) and arrested for a second time. After reinitiating once more, the sample fractured completely.

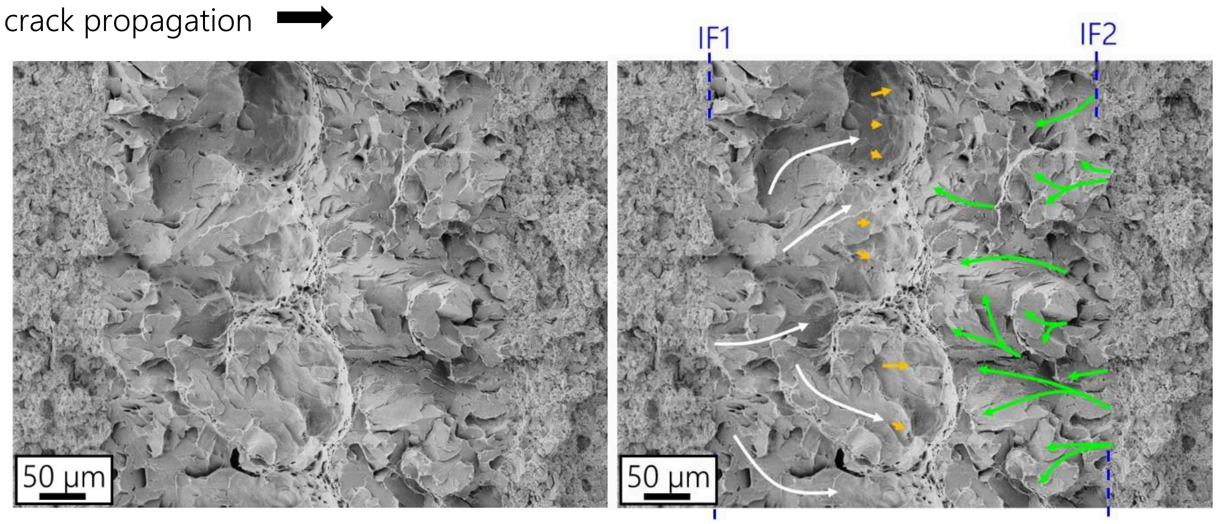

a) b)

Figure 95: a) Fracture surface of an X210CrW12/DC04 composite. The thick interlayer with t = 427 µm shows cleavage fracture and a distinct stretch zone, which marks the location of the temporary crack arrest. b) White and green arrows mark the local crack propagation in direction of the main crack and in reverse direction, respectively. Yellow arrows indicate the local crack arrest position.

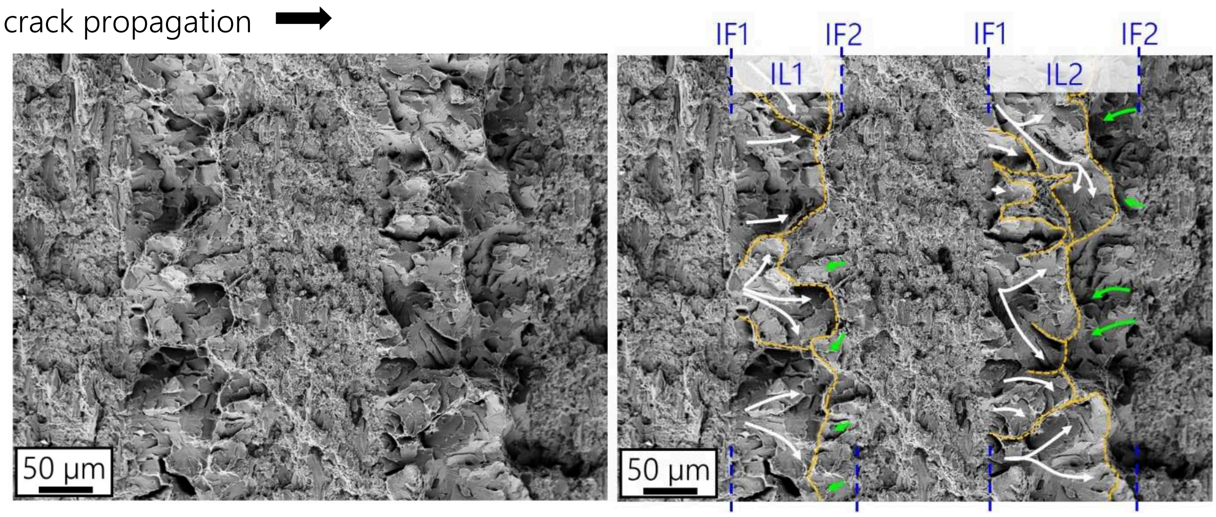

a)

b)

Figure 96: a) Fracture surface of an X210CrW12/DC04 composite with three interlayers. Temporary crack arrest occurred both in IL1 and in IL2 during the fracture mechanics experiment. b) White and green arrows indicate crack propagation in direction of the main crack and in reverse direction, respectively.

6.3.2 Crack profiles

The measurement of crack profiles offers insight into the fracture process. The methodology is explained in the following, and the crack profiles for two single interlayer specimens with t_{IL} = 90 and 427 µm are discussed in this chapter.

6.3.2.1 Methodology

The cracking sequence can be visualized using surface profiles measured on the same location on both fracture halves. Pioneering work was done by Kolednik and Stüwe (Kol1985, Kol1986), who used stereophotogrammetry to determine crack tip opening displacements. Stampfl et al. (Sta1996a, Sta1996b) later used an image processing software to reconstruct surface topographies from stereoscopic SEM micrographs. With the corresponding height profiles from both specimen-halves, crack tip opening displacements were determined.

Figure 97 summarizes the methodology schematically: In the first step, the height profile between two points 1 and 2 is measured on the lower fracture half, Figure 97a. The second height profile can be obtained on the other fracture half after finding the two corresponding points 1′ and 2′, Figure 97b. To simulate the process of putting the two fractured halves together, the second height profile is simply rotated by 180° and plotted together with the height profile of the bottom fracture surface in a single figure. Different stages of crack propagation can then be studied by moving one height profile along the y-axis. In this thesis, the surface was measured with a LEXT laser confocal scanning microscope and height profiles were extracted using the free software Gwyddion v2.48 (Gwy).

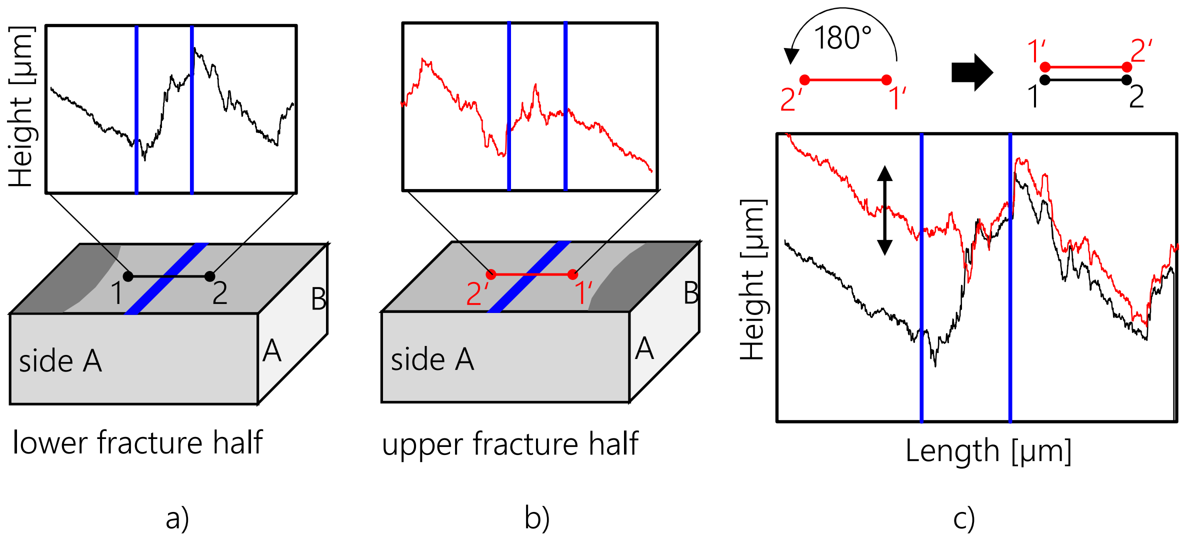

Figure 97: Schematic explanation of crack profile measurements using both fracture surfaces. a) Measurement of the first height profile between two points 1 and 2. b) Measurement of the second height profile between the two corresponding points 1′ and 2′. c) Rotating the second profile and superimposing with the first profile yields the crack profile, which can be studied for different crack openings by moving one height profile along the y-axis.

6.3.2.2 Crack profile of a single IL specimen with *t* = 427 µm

In Figure 98, the black and red curves correspond to the lower and upper fracture surface of a thick IL specimen as obtained with a laser confocal scanning microscope. Figure 98a shows the situation moments after the crack arrest in the interlayer. The arrest position of the primary crack propagating into the interlayer can easily be identified. Dark shaded areas are areas where the surfaces overlap, which indicates that plastic deformation occurred at a later stage. The situation is clearer after some further loading, Figure 98b. The arrested primary crack shows significant blunting, the remaining interlayer is still intact. However, a secondary crack formed in the matrix behind the interlayer. From Figure 98b it is possible to conclude that the secondary crack formed and opened, before triggering cleavage fracture in the interlayer. The formation of areas with ductile fracture in the interlayer becomes clear in Figure 98c. As cracks are located on both sides of the remaining interlayer ligament, the stress condition changes to plain stress, allowing ductile tearing. Figure 98 therefore supports the conclusions drawn from Figure 95.

6.3.2.3 Crack profile of a single IL specimen with *t* = 92 µm

Figure 99 shows a similar measurement near a single interlayer with *t* = 92 µm. The crack arrest position as well as the cleavage fracture within the interlayer can be identified in Figure 99a. The measured profiles furthermore suggest that already upon crack arrest, a secondary crack of length 50 µm forms at a distance of approximately 200 µm from IF2. With further loading, Figure 99b, blunting is less pronounced when compared to the thick interlayer specimen shown in Figure 98.

While the cracking sequence in Figure 98 is clear, from Figure 99 alone it is not possible to state whether final fracture in this specimen occurred due to a propagation of the primary crack, or due to a diametrical growth of the secondary crack. It is worth noting that these crack profiles only show the fracture behavior along a single path. Four crack profiles each were thus obtained on both specimens, and all showed a similar behavior as the profiles presented here.

6.3.3 Summary

The cracking sequence of the DC04 interlayer was reconstructed in this chapter using SEM imaging and crack profile measurements. It was shown that river patterns allow the deduction of the crack path within the interlayer, and that brittle second-phase particles, i.e. carbides, act as triggers for cleavage cracking of the interlayer. After the crack arrest, the crack does not propagate directly but rather re-initiates in the matrix behind the interlayer. This mechanism is especially pronounced in the specimen with a thick interlayer.

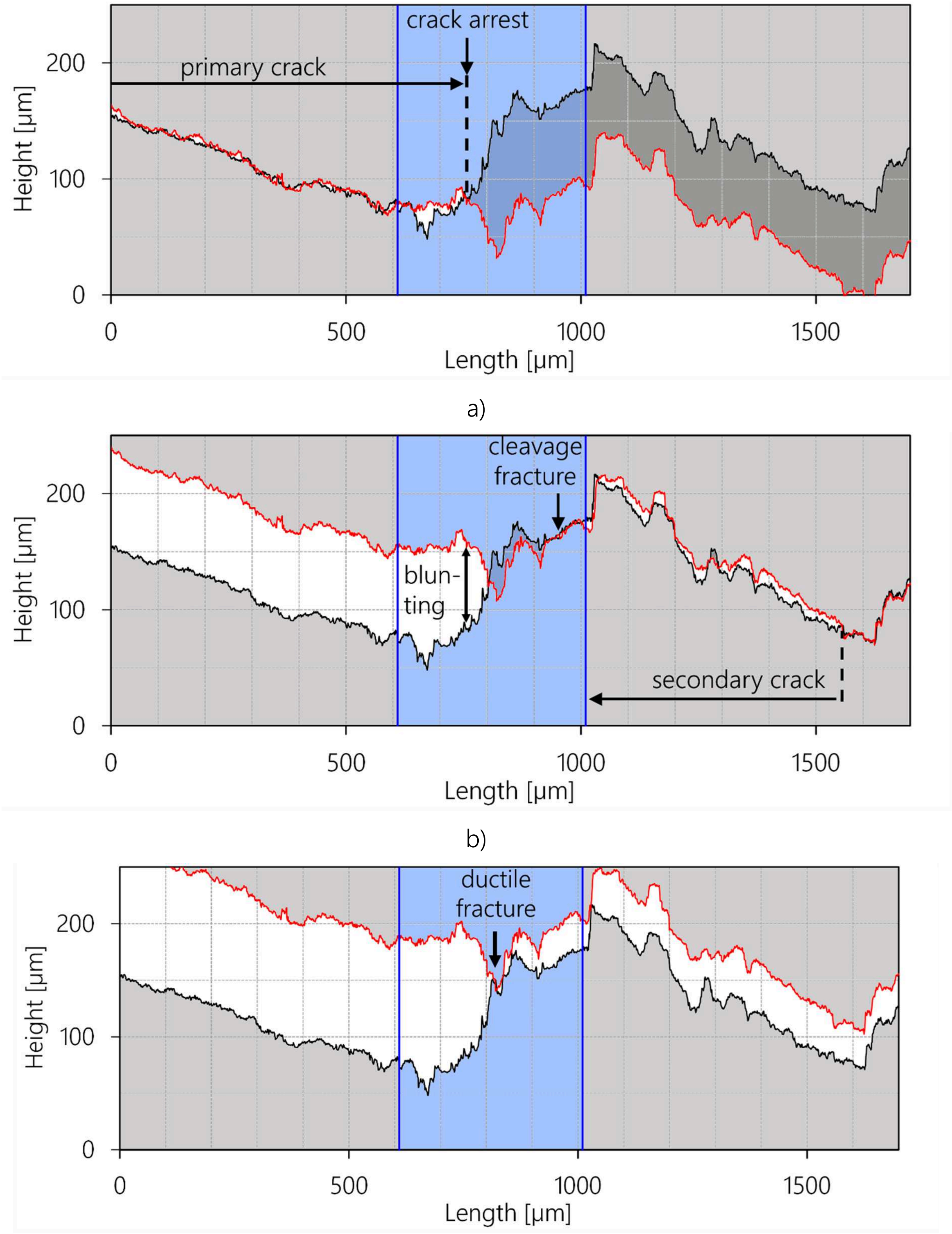

a)

b)

c)

Figure 98: Crack profiles in an X210CrW12/DC04 specimen with a thick single interlayer, *t* = 427 µm (blue color), demonstrating the cracking sequence. a) Crack arrest in the interlayer, b) significant blunting in the IL, initiation of a secondary crack in the matrix and c) ductile fracture of the remaining ligament in the interlayer.

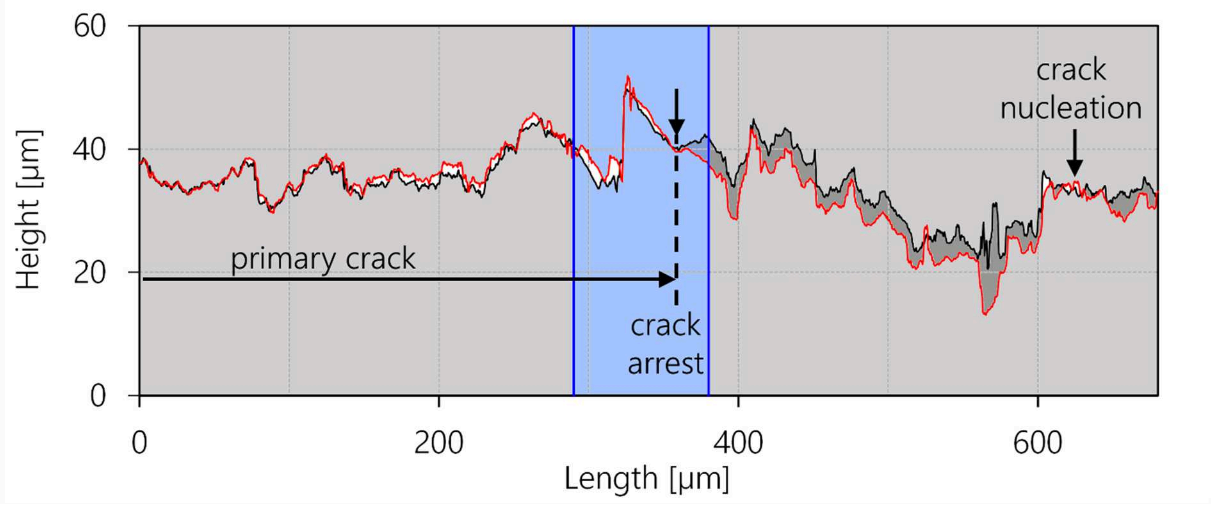

a)

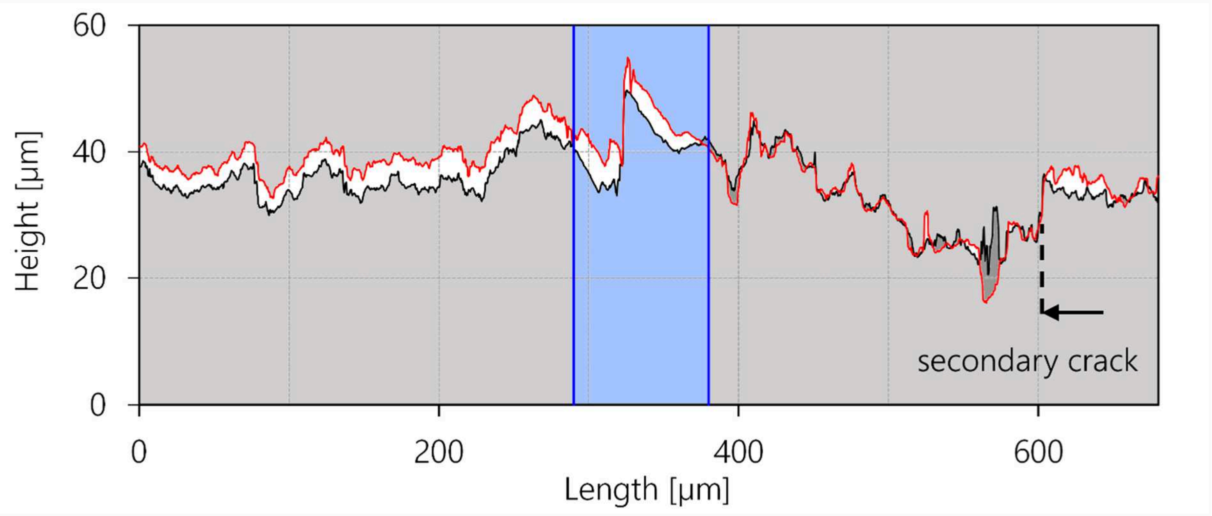

b)

Figure 99: Crack profiles in an X210CrW12/DC04 specimen with a thin single interlayer, *t* = 92 µm (blue color), demonstrating the cracking sequence. a) Crack arrest in the interlayer, b) moments before final fracture.

6.4 Cleavage cracking and crack arrest in the interlayer

The occurrence of cleavage fracture in the (ductile) interlayers at room temperature is, at the first glance, somewhat surprising. Possible reasons for the brittle fracture and why the crack arrested will be explained in this chapter. First, some basic information about cleavage fracture is given. The stress state within the interlayer during crack propagation and arrest is then analyzed with FEM for two composites with a single thin (*t* = 88 µm) and a single thick (t = 427 µm) interlayer. A possible influence of the strain rate is discussed at the end.

6.4.1 Basics of cleavage fracture

In most cases, cleavage fracture occurs when normal stresses exceed the cleavage fracture stress, $\sigma_{yy} > \sigma_f$, and a crack nucleus has been formed in front of the crack tip, which is able to extend (Che2015). According to Chen (Che2015), the cleavage fracture stress is independent of strain rate and temperature, but its magnitude depends on the critical (that is, the most difficult) event in the fracture process. For notched specimens, the critical event is the propagation of a crack nucleus into neighboring matrix grains, while for precracked specimen the creation of a crack nucleus is more difficult. No cleavage stress values for DC04 were found in the literature. Typically, the cleavage stress for precracked steel specimen are in the order of 2 GPa (Che2015). For a C-Mn steel with a grain size of 9.3 µm, Chen et al. (Che1996) reported values of 1.4 to 1.8 GPa.

Typical ductile-to-brittle transition temperatures for engineering materials are well below room temperature. In the upper ductile-to-brittle transition regime, cleavage cracking is preceded by a certain stable crack extension (Ros1983). The authors state that cleavage is then triggered when the stress field encounters a "trigger point", whose characteristics were not specified. In a later work, (Wan1997) stated that the amount of stable crack extension is determined by the stress triaxiality reaching a critical value T_c to prevent the crack nucleus from blunting. For a subsequent cleavage fracture, the normal stresses must exceed the cleavage fracture stress, $\sigma_{yy} > \sigma_f$, to propagate the sharp crack nucleus into neighboring matrix grains. This is thought to be the critical event for cleavage fracture. The amount of stable crack extension before cleavage measured in (Wan1997) was 0.5 mm and 1.0 mm for a 0.18% C, 1.49% Mn steel and a 0.07% C, 1.24% Mn steel, respectively. As a comparison, the extension Δa before the crack arrest within the interlayer in our samples ranged from 0.6 to 1.3 mm.

From literature it is well known that the tendency for cleavage fracture increases with

- grain coarsening
- solution hardening
- plastic deformation
- decrease in temperature
- increase in strain rate and
- high stress triaxiality.

With the exception of grain coarsening, all these parameters increase the yield stress, making it easier to reach the cleavage stress in a material. As reaching the cleavage stress is the decisive criterion, the stress states in front of the crack tip are studied numerically in the following.

6.4.2 Numerical stress analysis

Two cases of single interlayer specimens with different interlayer thicknesses are considered in the following. The finite element calculations, which were conducted by Masoud Sistaninia, consider residual stresses by assuming a stress-free state at the annealing temperature of 550 °C. Thermal residual stresses are then introduced numerically by cooling from annealing temperature to room temperature. The stress fields are then calculated for two different crack tip positions at the experimentally determined forces F_i and F_{max}, which are listed in Table 12.

From the stress fields, the stress triaxiality T can be calculated as

$$T = \frac{\sigma_m}{\sigma_{eq}} \tag{6.1}$$

where σ_m and σ_{eq} denote the mean and equivalent stress, respectively:

$$\sigma_m = \frac{1}{3}(\sigma_1 + \sigma_2 + \sigma_3) \tag{6.2}$$

$$\sigma_{eq} = \left\{\frac{1}{2}\left[(\sigma_1 - \sigma_2)^2 + (\sigma_2 - \sigma_3)^2 + (\sigma_3 - \sigma_1)^2\right]\right\}^{1/2} \tag{6.3}$$

Table 12: Specimen dimensions and experimentally determined loads and J-values at initiation and final fracture.

t_{IL} [mm]	W [mm]	B [mm]	t [µm]	F_i [kN]	F_{max} [kN]	J_c^{M} [kJ/m²]	J_c^{ML} [kJ/m²]
88	12.59	4.81	88	6.89	9.10	3.64	15.9
427	9.96	4.88	427	6.75	20.74	3.74	102.5

F_{i} = force at crack initiation, F_{max} = maximum force before final fracture,
J_c^{M} = critical J of the matrix material, J_c^{ML} = critical J of the composite

6.4.2.1 Single, soft interlayer with t = 88 µm

In the first case, a thin interlayer with t = 88 µm is considered. Figure 100 and Figure 101 compare the stress state in front of the crack tip when the crack is about to enter the interlayer and when the crack is arrested in the middle of the interlayer, respectively.

From Figure 100a it is clear that very high stresses σ_{yy} arise close to the first interface, IF1, although the DC04 has a low yield strength. With increasing distance to the crack tip, the stresses decrease but stay well above the uniaxial yield stress of the interlayer material. The stress triaxiality shown in Figure 100b is also amplified significantly directly at IF1, and decreases to a value of about 3 at IF2. The high stress triaxiality close IF1 is caused by a sharp decrease of σ_{eq} inside the interlayer, see (6.1). These results indicate a possible reason for cleavage cracking of the interlayer: The stress amplification directly at the interface can trigger cleavage fracture, maybe additionally promoted by a fracturing carbide near the interface (see Figure 94). The triggered crack is unable to blunt due to the high stress triaxiality. The normal stresses then propagate the cleavage crack into the interlayer.

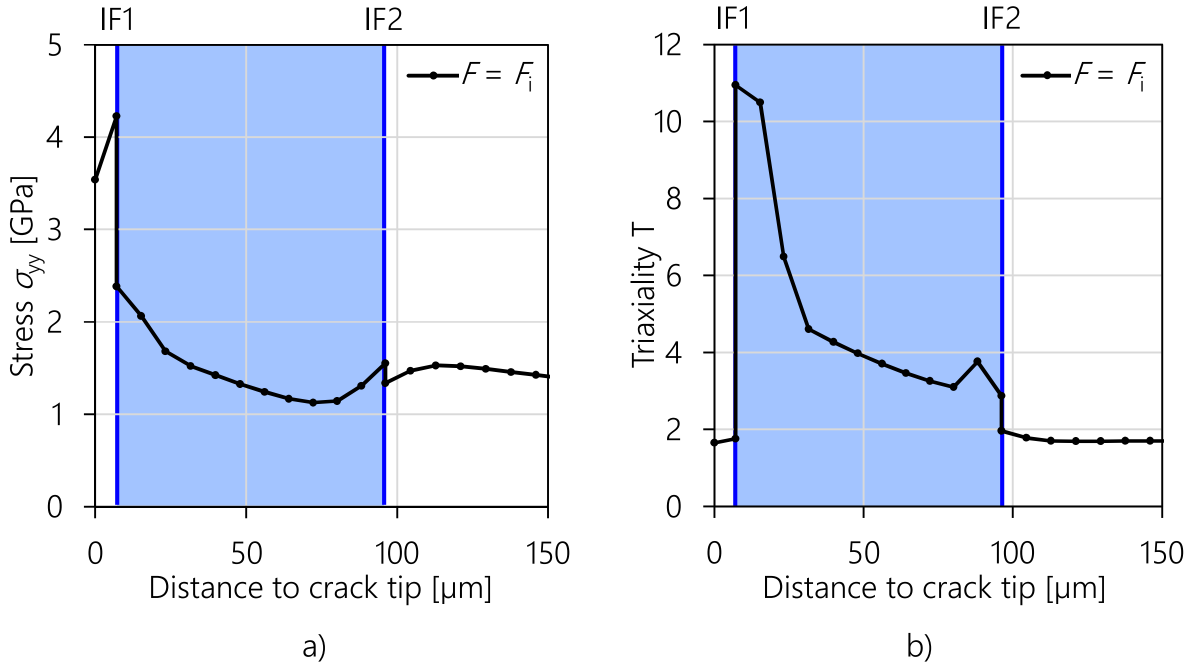

Figure 100: a) Normal stresses σ_{yy} and b) stress triaxiality at $F=F_i$ ahead of a crack tip located 7 µm in front of the soft interlayer with t = 88 µm.

Next, the stress fields are studied under the assumption of a crack arrest in the middle of the interlayer. The black curve in **Figure 101**a denotes the σ_{yy} stress field at the load $F = F_i$, i.e. at the same load as considered in **Figure 100**. The maximum normal stresses lie around 1 000 MPa. Upon increasing the load to $F = F_{max}$, σ_{yy} reaches 1 100 MPa. However, at this point no sharp cleavage nucleus is present in the interlayer, which could be propagated. This can be assumed from **Figure 101**b, which shows the stress triaxiality. A loss in constraint is evident, when the crack tip is located inside the interlayer. After the crack arrest, T is in the range of 2.1 and only increases to about 2.5 at the moment of final fracture.

In experiments with interlayer thicknesses below 100 µm, local crack arrests were observed between the middle of the interlayer and the second interface, see **Figure 21**. Two potential reasons for crack arrest may be discussed at this point:

I) The normal stresses σ_{yy} decrease below a critical value σ_c for cleave crack propagation. From **Figure 100**a, this critical value would be $\sigma_c \approx$1 100 – 1 200 MPa.

II) The stress triaxiality T decreases below a critical value T_c, which allows the crack tip to blunt. A change in fracture mode within the interlayer from brittle to ductile would follow. From **Figure 100**b, this critical value would be $T_c \approx$ 3 - 4.

It is worth noting that the numerical calculations, **Figure 100** and **Figure 101**, consider stationary cracks. The crack tip field for a propagating crack is different compared to a stationary one, however (Gro2006), and inertia of the quickly propagating cleave crack is neglected. The influence of grain size is also not taken into account. EBSD measurements, **Figure 79**, showed that single grains can span the whole interlayer thickness. A cleavage crack would likely not arrest in the middle of the grain, but would rather traverse the grain until it reaches the interlayer/matrix interface.

After the crack arrest, **Figure 101**, the conditions for cleavage fracture in the remaining interlayer are not fulfilled, apparently. Once arrested, the crack blunts and cannot continue as cleavage crack. The normal stress $\sigma_{yy} \approx 1\,200$ MPa is insufficient to initiate a new cleavage crack. However, in the previous chapters it was established that a secondary crack initiates in the matrix, which grows towards the remaining interlayer. It is clear that the appearance of a second (sharp) crack tip (close to IF2) will cause an additional increase both of normal stress and of triaxiality. As such, the conditions for cleavage cracking of the remaining interlayer may once again be fulfilled.

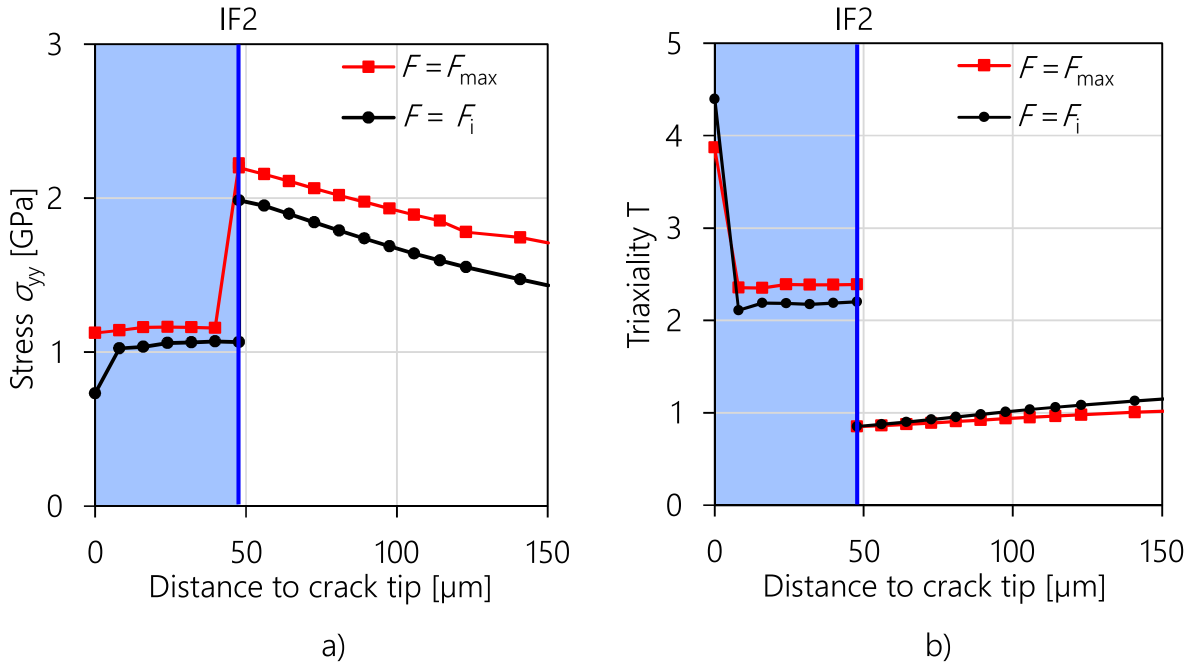

Figure 101: (a) Normal stresses σ_{yy} and (b) stress triaxiality at $F=F_i$ and $F=F_{max}$ ahead of a crack tip arrested in the middle of the soft interlayer with t = 88 µm.

6.4.2.2 Single, soft interlayer with $t = 427$ µm

In the second case, a specimen with a much thicker interlayer, $t = 427$ µm, is considered. Figure 102 and Figure 103 compare the stress state in front of the crack tip when the crack is about to enter the interlayer and when the crack is arrested in the interlayer, respectively.

Figure 102a shows the distribution of normal stresses σ_{yy}. Following high stress values at the first interface, σ_{yy} decreases to a plateau value of about 1 000 MPa. Interestingly, this plateau value is reached at a distance which is similar to the experimentally observed crack arrest position, CA_{exp}, which is between ⅓ and ½ of the interlayer. The stress triaxiality is plotted in Figure 102b. Similar to the situation with a thin interlayer, the triaxiality is very high close to IF1. T decreases further into the interlayer until it reaches a minimum of $T = 3$. Again, this minimum coincides with the experimental crack arrest position. A reason for the development of this minimum is the visible in Figure 102c, which shows that at this point the equivalent stress σ_{eq} decreases below the yield stress of the interlayer material, σ_y^{IL}. Accordingly, as $\sigma_{eq} > \sigma_y^{IL}$, the interlayer is plastically deformed between IF1 and the experimental CA position. This is an interesting finding, as plastic deformation increases susceptibility for cleavage cracking (Che2003).

From Figure 102 potential critical values for crack arrest can be derived, as established earlier. While $\sigma_c \approx 1000$ MPa is slightly lower, $T_c \approx 3$ is similar compared to the case of a thin interlayer.

The stress distribution after a crack arrest within the interlayer is shown in Figure 103. At $F = F_i$, the normal stress in the interlayer is approximately constant with $\sigma_{yy} \approx 1\,100$ MPa, while the triaxiality at F_i lies between 2.1 and 2.5 (black curves in Figure 103a-b). Under this stress and triaxiality, the arrested cleavage crack cannot propagate further. With a significant increase in load to $F = F_{max}$, both σ_{yy} and T reach a maximum close to IF2, with $\sigma_{yy} \approx 1\,350$ MPa and $T \approx 2.9$. The stresses within the matrix behind IF2 are much higher. With σ_{yy} reaching 3 000 MPa, crack initiation in the matrix is plausible.

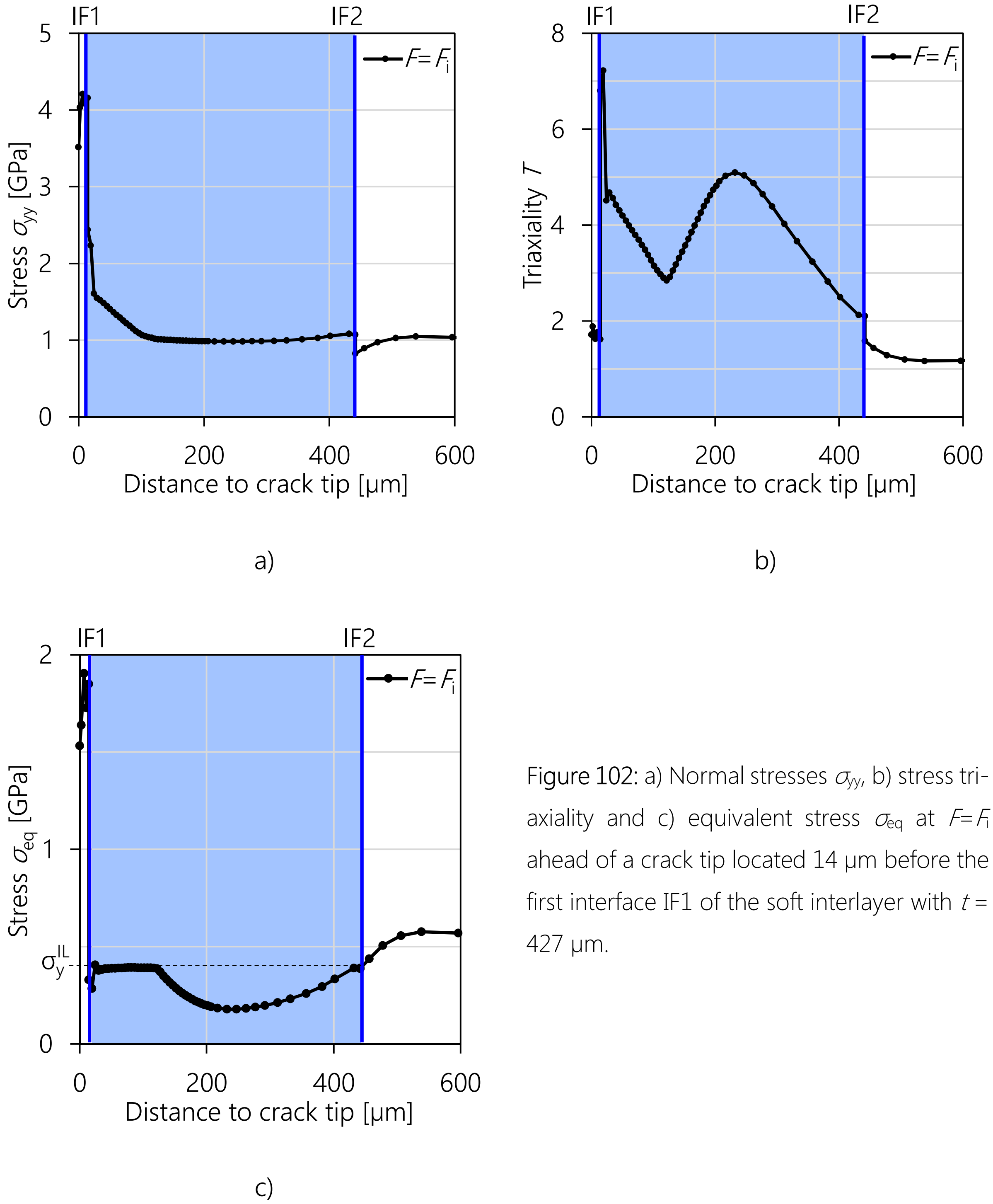

Figure 102: a) Normal stresses σ_{yy}, b) stress triaxiality and c) equivalent stress σ_{eq} at $F = F_i$ ahead of a crack tip located 14 μm before the first interface IF1 of the soft interlayer with t = 427 μm.

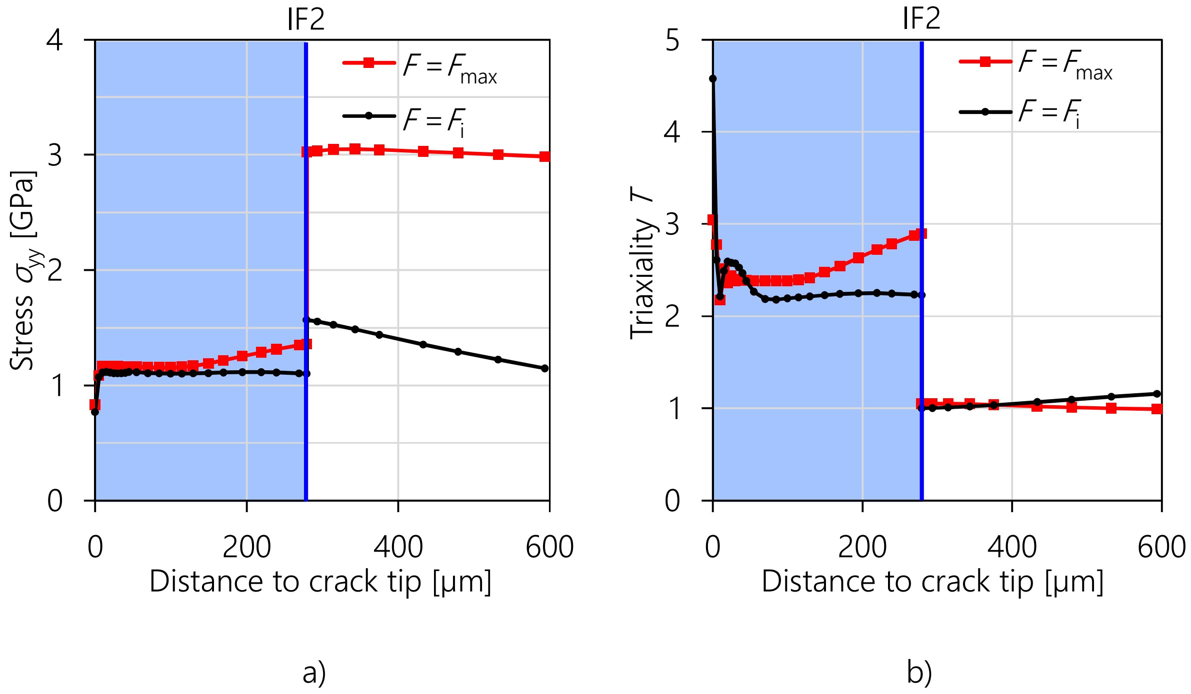

a) b)

Figure 103: a) Normal stresses σ_{yy} and b) stress triaxiality at F=F_i and F=F_{max} ahead of a crack tip arrested at 1/3 of the interlayer width.

6.4.3 Crack driving forces in the interlayer

Using the configurational forces concept, crack driving forces can be calculated numerically. The effect of single, soft interlayers on the crack driving force was studied in (Sis2014), recall Figure 27. The authors showed that the inhomogeneity effect in the interlayer results from a mixture between anti-shielding and shielding effect. As anti-shielding and shielding dominate at the first and second interface, respectively, a decrease of the crack driving force within the interlayer follows. Additionally, at one point within the interlayer the effect of shielding and anti-shielding even out. The local crack driving force J_{tip} is then equal to J_{far}.

Crack arrest within the interlayer would result if the condition $J_{tip} < R$, R being the crack growth resistance, is fulfilled. The crack growth resistance within the interlayer is difficult to determine, however, as it also depends on the fracture mode: cleavage fracture has a much smaller crack growth resistance than ductile fracture.

Due to these difficulties, the stress-based explanation for cleavage fracture and crack arrest in the interlayer from the previous chapter is more instructive.

6.4.4 Strain rate effect

In an early study (The1981), the authors' noted that a static analysis alone is not appropriate for the problem of a crack growing rapidly into an interface. Possible influences of the strain rate are discussed in the following.

Due to the high strain rates near the crack tip of an unstable cleavage crack, plastic deformation is suppressed and crack growth resistance is smaller compared to a stationary crack (And2005). As noted in (Fre1986), cleavage fracture ensues if local stresses reach a critical value before plastic flow diminishes these stresses. They also estimated the plastic strain rate in front of a moving crack in an iron single crystal to be in the order of 10^6 s^{-1} to 10^7 s^{-1}.

(Sri2013) studied the mechanical response and fracture toughness of mild steel at ambient temperature in a strain rate range between 10^{-5} and 10^2 s^{-1}. The lower yield strength is found to be dependent on the strain rate. This dependency is weak below strain rates of 10^{-2} s^{-1}. At higher strain rates, the yield stress increases linearly with increasing logarithmic strain rate. In impact tests specimens failed by nucleation, growth and coalescence of ductile voids up to strain rates of 10^0 s^{-1}. At 10^2 s^{-1} however, cleavage fracture occurred. The authors explained this with the occurrence of normal stresses that exceed the cleavage fracture stress, due to the increased dynamic yield stress and the stress concentration in front of the crack tip.

Furthermore, with increasing crack velocity the ratio σ_{yy}/σ_{xx} in front of the crack tip decreases, therefore influencing the stress triaxiality (Gro2011). The tendency for a crack propagation or material separation in planes perpendicular to the original crack plane increases accordingly.

The strain rate in our fracture mechanics experiments cannot be estimated due to a lack of data points. As the force-displacement record was obtained at 5 Hz frequency, the crack jumps occurred within a period of 0.2 seconds. A typical crack growth of Δa = 1.3 mm therefore results in a bottom estimate for the crack velocity of 6.5 mm/s. Final fracture of the specimen occurred within 0.2 seconds as well. A typical specimen ligament length (W-a) of 5 mm therefore fractured with a crack velocity of at least 25 mm/s. The actual crack tip velocities are believed to be much higher.

In our study, static numerical analysis was carried out to study the effectiveness of the interlayer as a crack arrester once the crack stopped. It cannot be excluded that, for example, inertia causes a crack to grow as cleavage crack a couple of grains into the interlayer before arresting. The exact mechanism of crack arrest as a dynamic problem could be the focus of a further study.

6.4.5 Summary

The reasons for cleavage fracture and crack arrest in the interlayer were studied in this chapter. Numerical stress analysis support the fracture mechanism clarified with crack profile measurements. The high stress triaxiality T prevents blunting of a nucleated cleavage crack (i.e. from a broken carbide), which then propagates driven by high normal stresses σ_{yy}. It was also shown in Figure 102c that the interlayer deforms plastically before cracking, which increases susceptibility for cleavage. Finally, cleavage cracking could be facilitated by the high strain rate at the propagating crack tip.

The crack arrest or crack blunting in the interlayer may then be caused by reaching critical values of normal stresses σ_{yy} and/or stress triaxiality T. In the following, a new crack has to re-initiate, triggered by high normal stresses in the matrix. Carbides thereby likely serve as initiation sites: Using acoustic emission, the onset of carbide fracture in uniaxial tension was studied in (Fuk2004). The authors found that fracture of M_7C_3 carbides with diameters around 20 µm begins at stresses as low as 1 100 MPa. Smaller carbides require higher stress levels.

6.5 Fracture behavior of composites with C45 matrix

In this chapter, the fracture behavior of composites with a C45 matrix is analyzed with fracture mechanics tests and fracture surface observations.

6.5.1 Fracture mechanics tests

After stating some experimental details, two representative fracture mechanics tests are presented: A C45/C45 composite with a single interface, and a C45/DC04 composite with a single, soft interlayer. The results are then summarized and compared with tensile test data for similarly heat treated C45 steel.

6.5.1.1 Sample preparation and testing

The production route and geometry of fracture mechanics samples with C45 matrix was covered in chapter 5.4.3. After the final heat treatment, the samples were polished to allow for better visibility of the future crack. A starter notch was then introduced by electro discharge machining or wire cutting and sharpened with a razor blade. The samples were then pre-fatigued in two steps. First, a fatigue precrack was introduced in compression at $R = 10$ and $\Delta K = 25$ to 30 MPa·m$^{0.5}$. After a precrack appeared on both specimen sides, fatiguing was carefully continued in tension at $R = 0.1$ and $\Delta K = 8$ MPa·m$^{0.5}$. Again, ΔK was raised incrementally if no crack growth should occur. The pre-fatigued specimen are then pin-loaded and tested at a constant crosshead displacement rate of 0.3 mm/min. CMOD is measured with a clip gauge attached to knives, which in turn are glued onto the specimen.

6.5.1.2 Specimen without interlayer

Figure 104 illustrates the results of the fracture mechanics test of a specimen forged from two pieces of C45 steel. As such, there is a single interface present in the middle of the specimen, approximately 3 mm in front of the initial fatigue crack of length $a_0 = 2.66$ mm. Figure 104a shows the force-CMOD record. The specimen behaves linear-elastic and fails catastrophically upon reaching a critical load at point (2). Figure 104b shows photographs of the specimen in the initial state (1), in the moment before fracture (2) and after final fracture (3). The experimental J-Δa curve is plotted in Figure 104c. After reaching a critical J-value of the matrix, $J_{\mathrm{c}}^{\mathrm{M}}$, the specimen breaks catastrophically. From this experiment, the critical J-value of the matrix J_c^M is measured as 10.5 kJ/m². It is worth noting that the C45/C45 interface is strong enough to prevent a deflection of the crack into the interface.

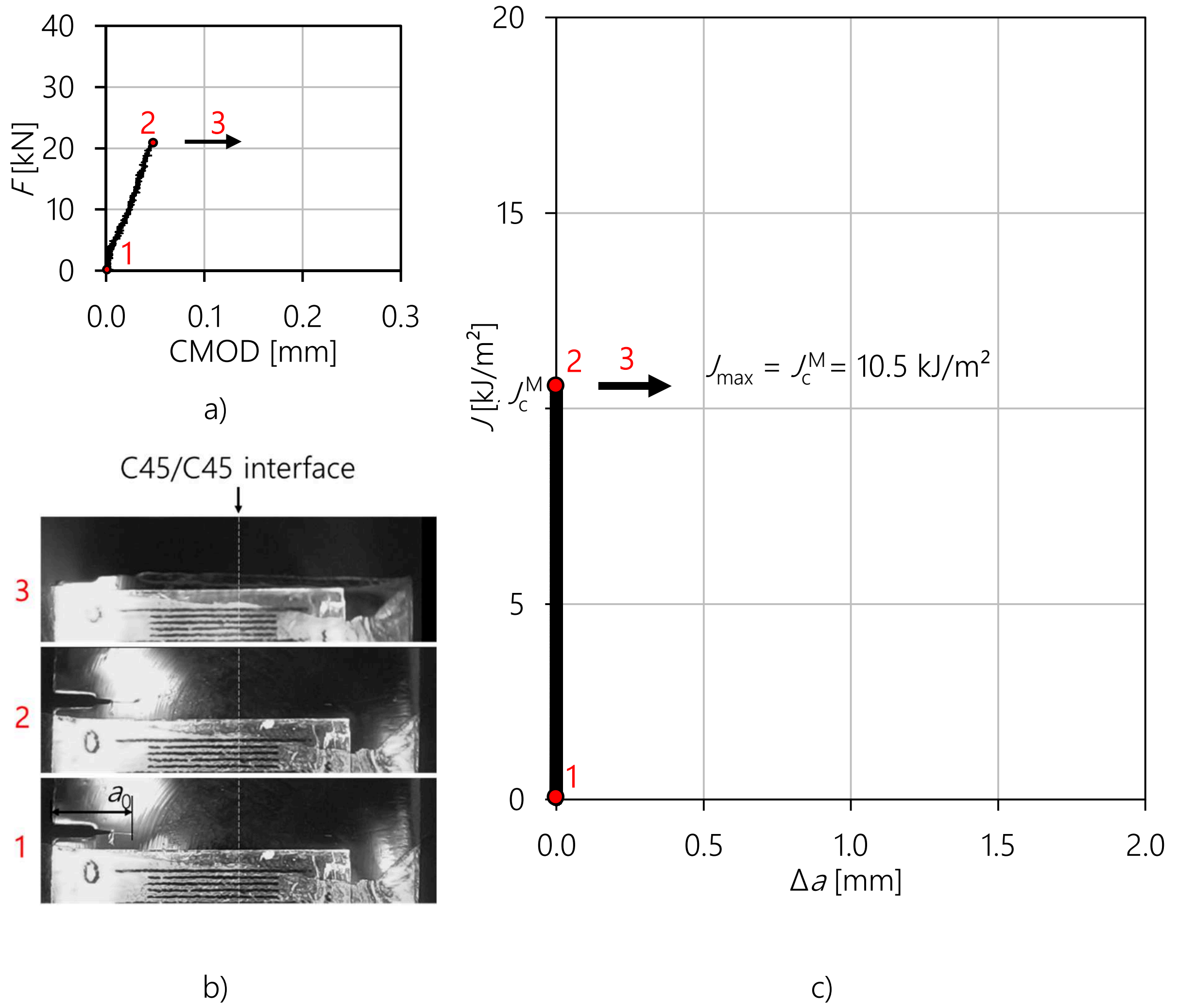

Figure 104: Fracture mechanics test of a C45 specimen without interlayer, but a C45/C45 interface. a) Load-CMOD curve. b) Photographs of the specimen corresponding to the points (1)-(3) marked in a). c) Experimental J-Δa curve.

6.5.1.3 Specimen with a single interlayer

Figure 105 illustrates the results of testing a composite with C45 matrix and a single DC04 interlayer of thickness t = 120 µm. The first interface of the interlayer is located 1.5 mm in front of the initial precrack of size a_0 = 4.02 mm. **Figure 105**a) shows the load-CMOD record, note the change in scale of the abscissa. Apart from the pop-in between the points (1) and (2), the load-CMOD curve resembles a tensile test. Photographs of the specimen before and after pop-in, points (1) and (2), as well as in the moment before fracture (3) are shown in **Figure 105**b). At (1), sudden crack growth occurs. In this case, the crack was arrested within the interlayer (2). With further loading debonding between interlayer and matrix occurs, which renders the crack completely inactive. The approximate onset of debonding is marked with an arrow in **Figure 105**a). The remaining ligament then behaves like a tensile specimen. **Figure 105**c) plots the experimental J-Δa curve. With $J_{max} \approx 3\ 140$ kJ/m^2, the improvement is about a factor 300 compared to a specimen without a soft interlayer.

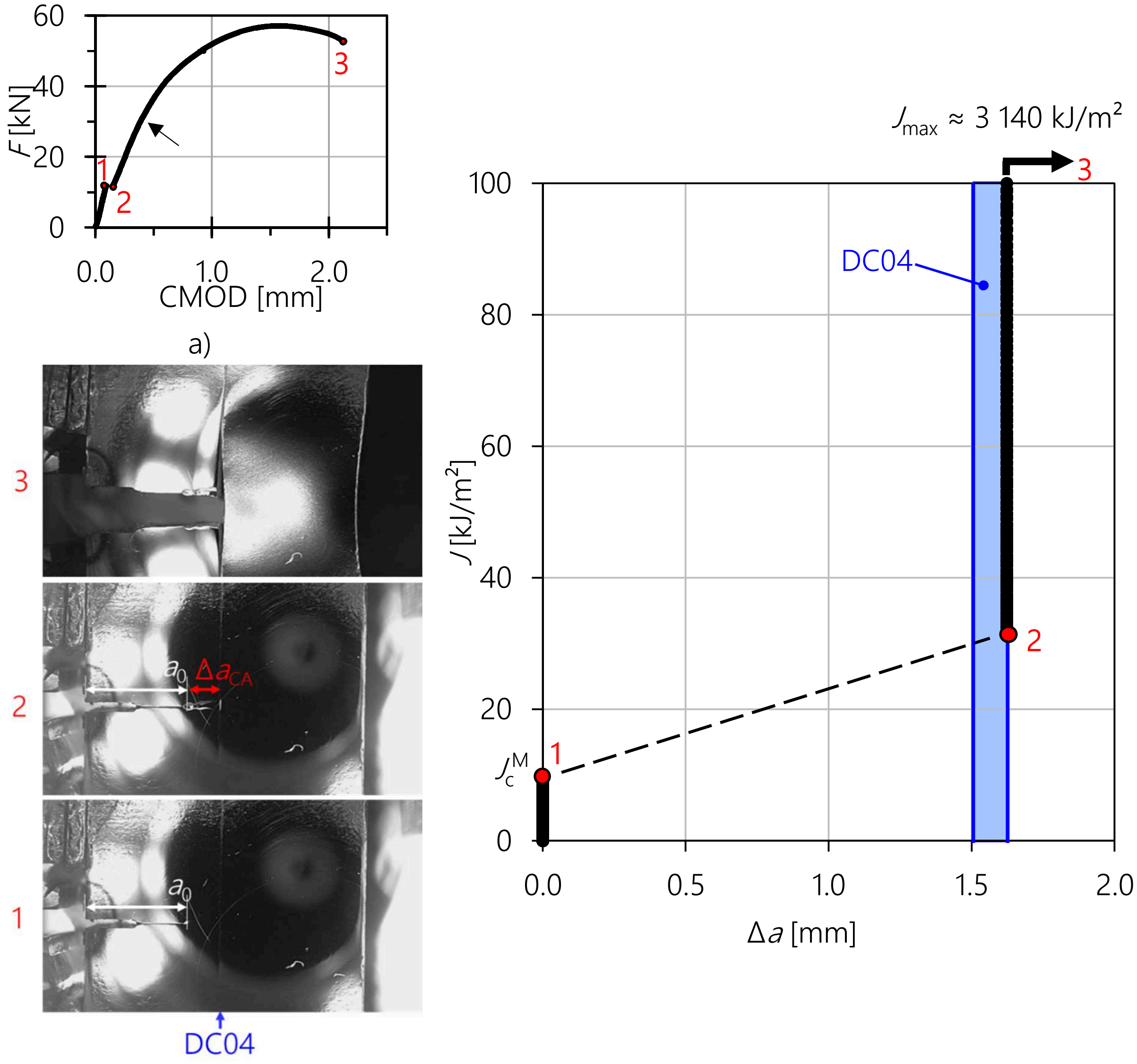

a) c)

Figure 105: Fracture mechanics test of a C45 specimen with a 120 µm interlayer. a) Load-CMOD curve. b) Photographs of the specimen corresponding to the points (1)-(3) marked in a). c) Experimental J-Δa curve.

Figure 106a-f shows the fracture sequence in more detail. The crack arrest and later delamination is clearly visible. It is worth mentioning that in **Figure 106**c, the thin white line in the interlayer does not indicate delamination but rather is an effect from lighting and lateral contraction due to plastic deformation of the interlayer. With further loading delamination occurs, **Figure 106**d-e. The remaining ligament then behaves like a tensile specimen, which fails by reaching the plastic limit load, **Figure 106**f.

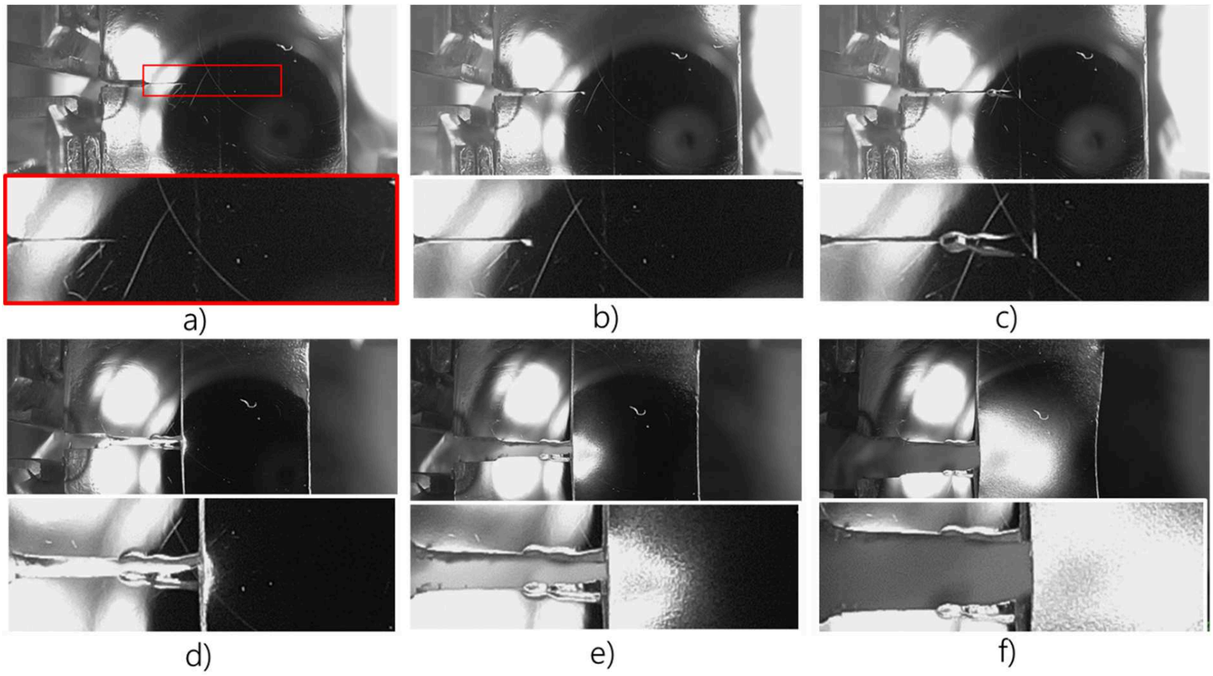

Figure 106: Fracture of a C45/DC04 composite with a single 120 µm interlayer. a) Initial stage, b) before pop-in, c) after pop-in, d) approximate onset of delamination, e) further delamination during straining and f) last image before fracture.

6.5.2 Prediction of fracture resistance of C45 composites

Other composites with different interlayer thicknesses were tested and are summarized in **Table 13**. All specimen showed a similar failure sequence as shown in **Figure 105** and **Figure 106**.

As the remaining ligament in C45/DC04 laminates behaves like a tensile specimen, the maximum force $F_{\max}$ measured in the fracture mechanics divided by the remaining cross-section $B\cdot(W\text{-}a_{CA})$ after crack arrest should be equal to the tensile strength σ_{UTS} of the matrix material,

$$\sigma_{\max,\mathrm{techn}} = \frac{F_{\max}}{B\cdot(W\text{-}a_{CA})} \approx \sigma_{UTS} \qquad (6.1)$$

In equation (6.1), a_{CA} is the total crack length after crack arrest. Compared with tensile tests of similarly heat-treated pure C45 steel, **Figure 107**, the stresses $\sigma_{\max,\mathrm{techn}}$ are slightly higher than the measured tensile strength σ_{UTS}. Albeit having the same heat treatment, the tensile samples were not deformed in the same manner as the composites. This may explain the difference between the measured strengths. However, the force maximum in fracture mechanics tests can be predicted with sufficient accuracy.

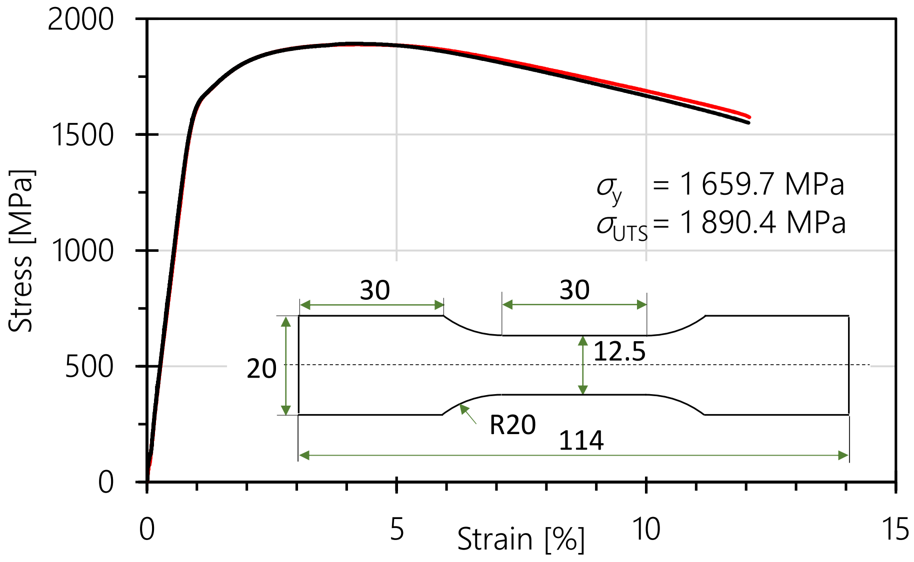

Figure 107: Technical stress-strain-diagram for C45 steel heat-treated similar to the composites.

The fact that the remaining specimen ligament behaves like a tensile specimen after a delamination was also observed with aluminum composites in (Zech2013). For this case, the authors derived the following approximate relation to estimate the value of J_{max}:

$$J_{\mathrm{max}} \approx \eta \cdot \sigma_{\mathrm{UTS}} \cdot \varepsilon_{\mathrm{f}} \cdot L \tag{6.2}$$

η is a geometry parameter similar to equation (3.6), ε_{f} the fracture strain of the matrix material and L the specimen length. Estimating J_{max} for C45 composites using equation (6.2) with η = 0.96, σ_{UTS}=1 890.4 MPa, ε_{f} = 0.12 (see **Figure 107**) and L = 13 mm yields

$$J_{\mathrm{max}} \approx 0.96 \cdot 1890.4 \cdot 0.12 \cdot 13 = 2830 \text{ kJ/m}^2 \tag{6.3}$$

This value is close to the value of J_{max} from **Figure 105**, which was determined by applying equations (3.8)-(3.11). Note that according to equation (6.2), the value of Jmax is independent of B and W-a_{CA}. However, compared to the critical J of the matrix, $J_{\mathrm{c}}^{\mathrm{M}}$ ≈10 kJ/m², the improvement is significant.

Table 13: Geometry, maximum force F_{max} and resulting maximum engineering stress $\sigma_{\mathrm{max,eng}}$ for different specimens with C45 matrix.

#inter-layers	t_{IL} [µm]	L_1 [mm]	a_0 [mm]	W [mm]	B [mm]	W-a_{CA} [mm]	F_{max} [kN]	$\sigma_{\mathrm{max,eng}}$ [MPa]
0	-	-	2.66	11.45	4.89	-	20.9	-
1	75	1.74	4.55	11.82	4.88	5.46	52.3	1 964
1	120	1.5	4.02	11.62	4.87	5.97	57.3	1 970
1	55	1.97	3.71	11.75	4.86	6.02	57.6	1 970
1	120	1.55	4.18	11.67	4.93	6.04	55.9	1 877

6.5.3 Fracture surfaces

Figure 108 exemplary shows fracture surface photographs of a) a C45 specimen with no interlayer, but a C45/C45 interface and b) a C45/DC04 composite, containing a single interlayer of thickness *t* = 120 µm. The differences are distinctive: No crack arrest occurred in the specimen without a DC04 interlayer (**Figure 108**a). In the composite showing crack arrest and delamination, **Figure 108**b, two regions can be distinguished: While the left side resembles a typical fracture mechanics specimen, the right side (which is the remaining ligament after the crack arrest) shows significant lateral contraction, which is typical for tensile specimens.

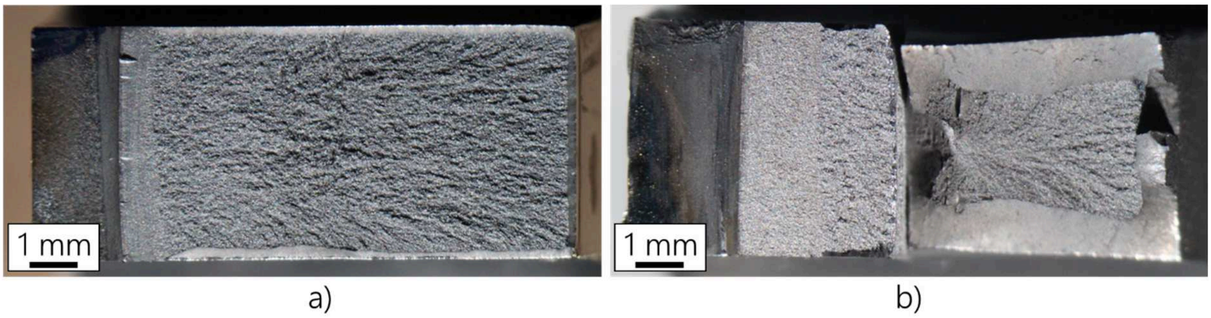

Figure 108: Photographs of the fracture surface of a) a C45 specimen with a single interface (no interlayer) and b) a C45/DC04 composite with a single interlayer with *t* = 120 µm and crack arrest.

The fracture surfaces were also observed in the SEM. In **Figure 109**a, the transition between the fatigue precrack and the fractured matrix is clearly visible. **Figure 109**b-c show the fracture surface of the C45 matrix, and **Figure 109**d shows part of an interlayer cracked in cleavage mode until the (later) delamination site. The irregular appearance of the fracture surface with both microductile and transgranular brittle fracture areas may be a result from the heat treatment, e.g. the tempering at 250 °C.

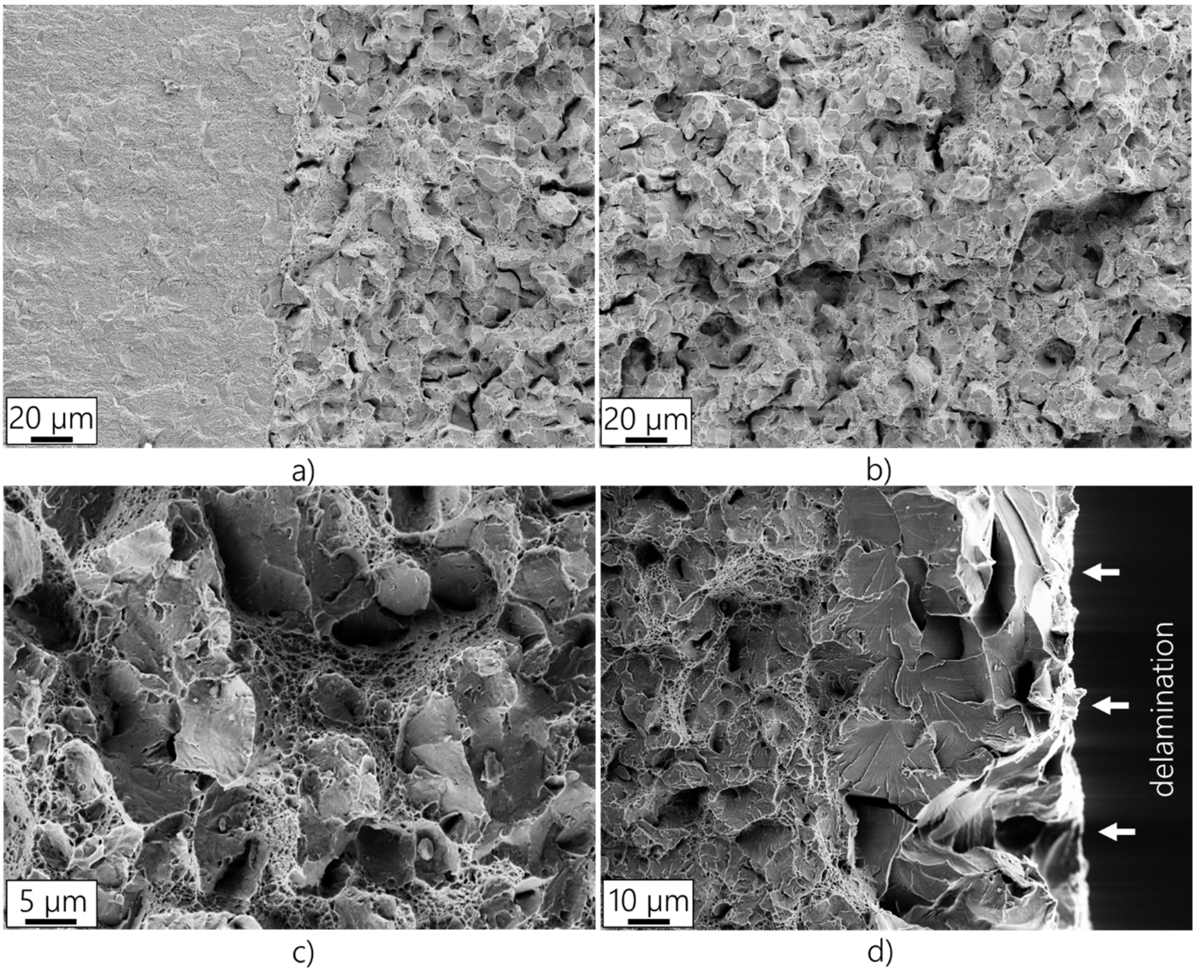

Figure 109: Details of the fracture surface of a C45/DC04 composite with a single 55 µm thick interlayer. a) Transition between fatigue and fracture, b) and c) fracture of the matrix and d) part of the interlayer fractured by cleavage.

7 Summary

In this thesis, inhomogeneous steel-based laminates with a high resistance against fracture were manufactured and tested. These laminates exploit the material inhomogeneity effect as main toughening mechanism, which occurs independently to other toughening effects like delamination. This effect is caused by the presence of an inhomogeneity in Young’s modulus or yield stress in front of a propagating crack. The basic mechanism is a strong reduction in the crack driving force, when the crack grows perpendicularly from a soft or compliant material into a stronger or stiffer material. This is also known as the shielding-effect of the material inhomogeneity. As was shown by earlier numerical studies for a yield stress inhomogeneity (Sis2014), a difference of a factor five in yield strength causes the best improvement.

Different deformation bonding processes were reviewed. The applicability of the hot press bonding technique to manufacture steel-based multilayered laminates was then explored in more detail. In preliminary experiments, several multilayer configurations were hot press bonded using steel sheets of commercially available 22MnB5 and DC04 as matrix and interlayer, respectively. It was found that the local deformation significantly varies across the composite cross-section, which results in low interface strengths in areas with low deformation. The highest deformation and interface strengths develop in the center of the composite, while outer layers deform very little. These outer layers are susceptible for debonding. It was demonstrated in a fracture mechanics experiment that debonding renders a crack completely ineffective, and final fracture of the specimen is then governed by the tensile strength of the matrix. While an effective and well-known way to toughen the composite, weak interfaces greatly reduce the composite strength in the transverse direction. To produce composites without weak interfaces in the following, thick steel bars were used for manufacturing instead of multiple thin steel sheets, so no interfaces were present in areas with low deformation.

Substituting the 22MnB5 matrix steel sheets, bars of the cold-working tool steels X210CrW12 or C45 were hot press bonded with sheets of DC04. Flow curves of the matrix materials at relevant temperatures and strain rates were measured. The difference in flow stress between C45 and DC04 at forging temperature is negligible, while a difference of a factor 2.5 exists between the X210CrW12 and DC04 steels. Nevertheless, the global thickness reduction of 50% during the hot press bonding process resulted in high local

thickness reductions of typically 90%, which produced excellent interface strengths. An empirical relation can predict the local thickness reduction during hot press bonding and therefore the resulting composite geometry. This relation is strictly valid only for the composite geometry used in this thesis.

The bond strength of the interlayers was measured with miniature tensile tests normal to the interfaces. The maximum engineering stress in a sample with a thin interlayer almost reached the strength of a reference X210CrW12 specimen without interfaces. Nanoindentation confirmed the sharp transition between hard matrix and soft interlayer, as well as the absence of a hardness gradient within the interlayer. The average Young's modulus of the X210CrW12 matrix is slightly higher compared to the DC04 interlayer, which can be attributed to the presence of stiff carbides.

Composites with varying number and thickness of the soft interlayer(s), as well as reference matrix specimen without interlayers were manufactured. The improvement in fracture resistance caused by soft interlayer(s) was determined in fracture mechanics experiments. The reference specimens, which contained a single matrix/matrix interface each, fractured catastrophically after reaching a critical J-integral for the matrix, J_c^M. In specimen with one or more interlayers crack propagation initiated at J_c^M as well, but the propagating crack arrested inside the interlayer. The load, measured in terms of the J-integral, had to be increased to cause final fracture at a critical J for the composite, J_c^{ML}. The ratio J_c^{ML}/J_c^M is a measure of the effectiveness of the interlayer(s) as a crack arrester.

In X210CrW12/DC04 composites, the improvement is dependent on the interlayer thickness. In a specimen with a single interlayer of thickness t = 45 µm, corresponding to a volume fraction of only 0.45%, J_c^{ML} was already a factor 3.9 higher than J_c^M. The improvement caused by a single interlayer with t = 427 µm was even more significant, as J_c^{ML}/J_c^M was a factor 35. It is worth mentioning that no delamination occurred in these experiments. The reason for the observed improvements is twofold: First, the differences in yield strength of interlayer and matrix cause the aforementioned shielding effect, which reduces the crack driving force. Secondly, the different thermal expansion coefficients of matrix and interlayer generate thermal residual stresses. Compressive residual stresses in the matrix further reduce the crack driving force. Numerical calculations are able to estimate J_c^{ML}/J_c^M, when both the material inhomogeneity effect as well as residual stresses are taken into account (Sis2018).

An interesting feature of the fracture mechanics tests is the cleavage fracture mode observed in the DC04 interlayers. Cracks were successfully arrested despite the brittle fracture mode. With numerical calculations, high normal stresses and a highly increased stress triaxiality were found at the matrix/interlayer interface, which may promote cleavage fracture of the interlayer. The exact location of the crack arrest as well as the fracture sequence in X210CrW12/DC04 composites was deduced by tracing river patterns in SEM images and by measuring crack profiles with a laser scanning confocal microscope. In thin interlayers, $t < 100$ µm, crack arrest is predominantly observed at the second interface, i.e. at the soft-hard transition. This is in agreement with the theoretical crack arrest position predicted with the configurational forces model, as at this point a minimum in crack driving force J_{tip} is reached (Sis2014). With increasing interlayer thickness, the experimental crack arrest position shifts into the interlayer. Both the river patterns as well as the analysis of crack profiles showed that a new crack initiated in the matrix, which subsequently grew against the main crack propagation direction and caused final fracture of the composites.

In C45/DC04 composites, the arrested crack was rendered completely ineffective by the onset of debonding with further loading. The remaining specimen cross-section then behaved like tensile specimen and failed by reaching the plastic limit load. Compared to X210CrW12/DC04 composites, the improvement $J_{\mathrm{c}}^{\mathrm{ML}}/J_{\mathrm{c}}^{\mathrm{M}}$ is much higher and almost a factor 300.

8 References

(And2005) Anderson, T.L., Fracture mechanics, Fundamentals and applications, Taylor & Francis (Boca Raton, FL), 3rd ed., 2005

(Bag2009) Bagheri, R.; Marouf, B. T.; Pearson, R. A., Rubber-Toughened Epoxies: A Critical Review, Polymer Reviews 49 (2009), issue 3, 201-225

(Bal2016) Ballarini, R., Royer-Carfagni, G., A Newtonian interpretation of configurational forces on dislocations and cracks. Journal of the Mechanics and Physics of Solids 95 (2016) 602-620. DOI: 10.1016/j.jmps.2016.05.008

(Bat2011) Bataev, I.A.; Bataev, A.; Mali, V.I.; Burov, V., Golovin, E., Smirnov, A., Prikhodko, E., Structure and Fatigue Crack Resistance of Multilayer Materials Produced by Explosive Welding, Advanced Materials Research 287-290 (2011) 108-111. DOI: 10.4028/www.scientific.net/AMR.287-290.108

(Bat2012) Bataev, I. A., Bataev, A. A., Mali, V. I., Pavlyukova, D. V., Yartsev, P. S., Golovin, E. D., Nucleation and growth of titanium aluminide in an explosion-welded laminate composite, The Physics of Metals and Metallography 113 (2012) 947-956. DOI: 10.1134/S0031918X12070022

(Bay1979) Bay, N., Cold Pressure Welding - The Mechanisms Governing Bonding, Transactions of the ASME Journal of Engineering for Industry 101 (1979) 121-127. DOI: 10.1115/1.3439484

(Bay1983) Bay, N., Mechanisms Producing Metallic Bonds in Cold Welding, Welding Research Supplement 62 (1983) 137-142

(Ben2010) Ben-Artzy A., Stern A., Frage N., Shribman V., Sadot O., Wave Formation Mechanism in Magnetic Pulse Welding. International Journal of Impact Engineering 37 (2010) 397-404. DOI: 10.1016/j.ijimpeng.2009.07.008

(Ber2006) Bermejo, R., Torres, Y.; Sanchez-Herencia, A., Baudin , C., Anglada, M., Llanes, L., Residual stresses, strength and toughness of laminates with different layer thickness ratios, Acta Materialia 54 (2006) 4745-4757. DOI: 10.1016/j.actamat.2006.06.008

(Big2014) Bigoni, D.; Bosi, F.; Dal Corso, F.; Misseroni, D., Instability of a penetrating blade, Journal of the Mechanics and Physics of Solids 64 (2014) 411-425. DOI: 10.1016/j.jmps.2013.12.008

(Big2015) Bigoni, D.; Dal Corso, F.; Bosi, F.; Misseroni, D., Eshelby-like forces acting on elastic structures: Theoretical and experimental proof. Mechanics of Materials 80 (2015) 368-374. DOI: 10.1016/j.mechmat.2013.10.009

(Buc2008) Buchner, M.; Buchner, B.; Buchmayr, B.; Kilian, H.; Riemelmoser, F., Investigation of different parameters on roll bonding quality of aluminium and steel sheets, International Journal of Material Forming 1, Issue Suppl. 1 (2008) 1279-1282. DOI: 10.1007/s12289-008-0136-7

(Cha2009) Chaudhari, G.P.; Acoff, V., Cold roll bonding of multi-layered bi-metal laminate composites, Composites Science and Technology 69 (2009) 1667-1675. DOI: 10.1016/j.compscitech.2009.03.018

(Che1996) Chen, J.H., Wang, G.Z., Wang, H.J., A statistical model for cleavage fracture of low alloy steel. Acta Metallurgica 44 (1996) 3979-3989. DOI: 10.1016/S1359-6454(96)00041-9

(Che2003) Chen, J.H., Li, Z., Wang, G.Z., Effects of tensile prestrain on the notch toughness of low-alloy steel. Metallurgical and Materials Transactions A: Physical Metallurgy and Materials Science 34 (2003) 1055-1068. DOI: 10.1007/s11661-003-0126-9

(Che2015) Chen, J. H., Cao, R., Micromechanism of Cleavage Fracture of Metals - A Comprehensive Microphysical Model for Cleavage Cracking in Metals. Butterworth-Heinemann, 1st edition (2015) ISBN 978-0-12-800765-5

(Cle1983) Cleland D.B., Basic Consideration for Commercal Processes. In Explosive welding, forming, and compaction, T. Z. Blazynski, Ed. Applied Science; Elsevier Science Pub. Co, London, New York, (1983) 159-188.

(Cle1986) Clemensen, C., Juelstorp, O., Bay, N., Cold Welding: Part 3. Influence of surface preparation on bond strength, Metal Construction 18 (1986) 625-629

(Cle1990) Clegg, W. J.; Kendall, K.; Alford, N. McN.; Button, T. W.; Birchall, J. D., A simple way to make tough ceramics. Nature 347 (1990) 455-457. DOI: 10.1038/347455a0

(Coo1964) Cook, J., Gordon, J.E., A mechanism for the control of crack propagation in all-brittle systems. Proceedings of the Royal Society A: Mathematical, Physical and Engineering Sciences 282 (1964). 508-520. DOI: 10.1098/rspa.1964.0248

(Coo1972) Cook, T., Erdogan, F., Stresses in bonded materials with a crack perpendicular to the interface. International Journal of Engineering Science 10 (1972) 667-696.

(Cow1971) Cowan G.R., Bergmann O.R., Holtzman A.H., Mechanism of Bond Zone Wave Formation in Explosive-Clad Metals, Metallurgical Transactions 2 (1971) 3145-3155. DOI: 10.1007/BF02814967

(Cra2007) Cravero, S., Ruggieri, C., Estimation procedure of J-resistance curves for SE(T) fracture specimens using unloading compliance. Engineering Fracture Mechanics 74 (2007) 2735–2757. DOI: 10.1016/j.engfracmech.2007.01.012

(Deh2011) Dehsorkhi, Reza Nasiri; Qods, Fathallah; Tajally, Mohammad, Investigation on microstructure and mechanical properties of Al-Zn composite during accumulative roll bonding (ARB) process, Materials Science and Engineering: A 530 (2011) 63-72. DOI: 10.1016/j.msea.2011.09.040

(Den2003) Denzer R., Barth F.J., Steinmann P., Studies in elastic fracture mechanics based on the material force method, International Journal for Numerical Methods in Engineering 58 (2003) 1817-1835. DOI: 10.1002/nme.834

(Doe1986) Doege, E., Meyer-Nolkemper, H., Saeed, I., Fließkurvenatlas metallischer Werkstoffe. Hanser Verlag München-Wien, 1986. ISBN 3-446-14427-7

(Doe2007) Doege, E., Behrens, B.A., Handbuch Umformtechnik - Grundlagen, Technologien, Maschinen, Springer-Verlag Berlin Heidelberg New York, 2007, ISBN 978-3-540-23441-8

(E1820-13) ASTM E1820-13, Standard Test Method for Measurement of Fracture Toughness. DOI: 10.1520/E1820-13

(Eiv2007) Eivani, A.R, Taheri, A.K., A new method for producing bimetallic rods, Materials Letters 61 (2007) 4110-4113. DOI: 10.1016/j.matlet.2007.01.046

(Eiz2008) Eizadjou M., Manesh H.D., Janghorban K., Investigation of roll bonding between aluminum alloy strips, Materials and Design 29 (2008) 909-913. DOI: 10.1016/j.matdes.2007.03.020

(Eiz2009) Eizadjou, M.; Danesh Manesh, H.; Janghorban, K., Mechanism of warm and cold roll bonding of aluminum alloy strips, Materials & Design 30 (2009) 4156-4161. DOI: 10.1016/j.matdes.2009.04.036

(Emb1967) Embury, J.D., Petch, N.J., Wraith, A.E., Wright, E.S. The fracture of mild steel laminates. Trans. Metall. Soc. AIME 239 (1967) 114-118.

(Eng2012) Engelhardt, M., Grittner, N., von Senden genannt Haverkamp, H., Reimche, W., Bormann, D., Bach, F-W., Extrusion of hybrid sheet metals, Journal of Materials Processing Technology 212 (2012) 1030-1038. DOI: 10.1016/j.jmatprotec.2011.12.013

(Erd1973) Erdogan F., Biricikoglu V., Two bonded half planes with a crack going through the interface. International Journal of Engineering Science 11 (1973) 745-66.

(Esh1951) Eshelby, J.D., The force on an elastic singularity. Philosophical Transactions of the Royal Society A 244 (1951) 87-112. DOI: 10.1098/rsta.1951.0016

(Esh1956) Eshelby, J.D., The Continuum Theory of Lattice Defects, Solid State Physics 3 (1956) 79-144. DOI: 10.1016/S0081-1947(08)60132-0

(Esh1970) Eshelby, J.D., Energy relations and the energy-momentum tensor in continuum mechanics. In: Kanninen M, Adler W, Rosenfield A, Jaffee R (eds), Inelastic behavior of solids. McGraw-Hill, New York (1970) 77-115.

(ESIS1992) ESIS PI-92, ESIS recommendations for determining the fracture resistance of ductile materials, European Structural Integrity Society (ESIS), Delft (1992)

(FEMM) Finite element magnetics, version 4.2. http://www.femm.info.

(Fis2007) Fischer F.D., Predan J., Kolednik O., Simha N.K., Application of material forces to fracture of inhomogeneous materials: illustrative examples, Archive of Applied Mechanics, Volume 77, Issue 2-3 (2007) 95-112. DOI: 10.1007/s00419-008-0254-1

(Fra2007) Fratzl, P.; Gupta, H. S.; Fischer, F. D.; Kolednik, O., Hindered Crack Propagation in Materials with Periodically Varying Young's Modulus-Lessons from Biological Materials, Advanced Materials 19 (2007) 2657-2661. DOI: 10.1002/adma.200602394

(Fre1986) Freund, L. B.; Hutchinson, J. W.; Lam, P. S., Analysis of high-strain-rate elastic-plastic crack growth, Engineering Fracture Mechanics 23 (1986) 119-129. DOI: 10.1016/0013-7944(86)90181-5

(Fuk2004) Fukaura, K., Yokoyama, Y., Yokoi, D., Tsujii, N., Ono, K., Fatigue of cold-work tool steels: Effect of heat treatment and carbide morphology on fatigue crack formation, life, and fracture surface observations, Metallurgical and Materials Transactions A 35 (2004) 1289-1300. DOI: 10.1007/s11661-004-0303-5

(Gar1988) Garg, Amar C.; Mai, Yiu-Wing, Failure mechanisms in toughened epoxy resins-A review, Composites Science and Technology 31 (1988), issue 3, 179-223

(GOM) https://www.gom.com/de/3d-software/gom-correlate/

(Gov2013) Govindaraj, N.V., Frydendahl, J.G., Holmedal, B., Layer continuity in accumulative roll bonding of dissimilar material combinations, Materials & Design 52 (2013) 905-915. DOI: 10.1016/j.matdes.2013.06.031

(Gro2011) Gross, D.; Seelig, T., Fracture Mechanics, Springer-Verlag Berlin Heidelberg (2011). DOI: 10.1007/978-3-642-19240-1

(Gur1996) Gurtin M.E., Podio-Guidugli P., Configurational forces and the basic laws for crack propagation. J. Mech. Phys. Solids 44 (1996) 905-927. DOI: 10.1016/0022-5096(96)00014-2

(Gur2000) Gurtin M.E., Configurational Forces as Basic Concepts of Continuum Physics. Springer, Berlin Heidelberg New York (2000)

(Gwy) http://gwyddion.net/download.php

(He1992) He, M.-Y., McMeeking, R., Zhang, N. Small scale yielding at a crack normal to the interface between an elastic and a yielding material. Materials Research Society Symposium Proceedings 239 (1992) 585-590. DOI: 10.1557/PROC-239-585

(Her2006) Hertzberg, R.W., Deformation and Fracture Mechanics of Engineering Materials, 4th edition, John Wiley & Sons (2006). ISBN 978-0-471-01214-6

(Hom) Homer K., The Iliad of Homer, Chicago, IL: University of Chicago Press (1951)

(Hut1968) Hutchinson, J.W., Singular Behavior at the End of a Tensile Crack Tip in a hardening Material, Journal of the Mechanics and Physics of Solids, Vol. 16 (1968) 13-31

(Irw1957) Irwin G.R., Analysis of Stresses and Strains near the End of a Crack Traversing a Plate. Journal of Applied Mechanics, Vol. 24 (1957) 361-364

(Irw1961) Irwin, G.R., Plastic Zone Near a Crack and Fracture Toughness. In: Sagamore Research Conference Proceedings, Vol. 4, Syracuse University Research Institute (1961) 63-78

(Jam2011) Jamaati, R., Toroghinejad, M.R., The Role of Surface Preparation Parameters on Cold Roll Bonding of Aluminum Strips, Journal of Materials Engineering and Performance 20 (2011) 191-197. DOI: 10.1007/s11665-010-9664-7

(Jin2008) Jindal, V.; Srivastava, V. C.; Ghosh, R. N., Development of IF steel-Al multilayer composite by repetitive roll bonding and annealing process, Materials Science and Technology 24 (2008) 798-802. DOI: 10.1179/174328406X148688

(Joh1965) Johnson, H. H., Calibrating the Electric Potential Method for Studying Slow Crack Growth, Materials Research & Standards 5 (1965) 442–445.

(Joy2003) Joyce, M.R; Reed, P.A.S; Syngellakis, S., Numerical modelling of crack shielding and deflection in a multi-layered material system, Materials Science and Engineering: A 342 (2003) 11-22. DOI: 10.1016/S0921-5093(02)00279-4

(Kai2006) Kainer, K.U., Metal Matrix Composites: Custom-made Materials for Automotive and Aerospace, WILEY-VCH, Weinheim (2006). ISBN: 978-3-527-31360-0

(Kas2014) Kasberger, R., Buchmayr, B., Production and Characterization of Multilayer Metallic Composites. In: Proceedings of MEFORM14, 26.-27.03.2014, Altenberg, Germany. ISBN: 978-3-86012-481-9

(Kaz1985) Kazakov, N. F., Diffusion welding. Pergamon, Oxford (1985). ISBN: 978-0-08-032550-7

(Kie2000) Kienzler R., Herrmann G., Mechanics in Material Space. Springer, Berlin Heidelberg New York (2000)

(Kim1997) Kim A.S., Suresh S., Shih C.F., Plasticity effects on fracture normal to interfaces with homogeneous and graded compositions, International Journal of Solids and Structures 34 (1997) 3415-3432. DOI: 10.1016/S0020-7683(96)00225-9

(Kol1985) Kolednik, O., Stüwe, H. P., The stereophotogrammetric determination of the critical crack tip opening displacement, Engineering Fracture Mechanics 21 (1985) 145-155. DOI: 10.1016/0013-7944(85)90061-X

(Kol1986) Kolednik, O.; Stüwe, H. P., An extensive analysis of a JIC-test, Engineering Fracture Mechanics 24 (1986) 277-290. DOI: 10.1016/0013-7944(86)90058-5

(Kol2000) Kolednik, O., The yield stress gradient effect in inhomogeneous materials. International Journal of Solids and Structures 37 (2000) 781-808. DOI: 10.1016/S0020-7683(99)00060-8

(Kol2009) Kolednik, O., Predan, J., Gubeljak, N., Fischer, D.F., Modeling fatigue crack growth in a bimaterial specimen with the configurational forces concept, Materials Science and Engineering: A 519 (2009) 172–183. DOI: 10.1016/j.msea.2009.04.059

(Kol2010) Kolednik, O., Predan, J., Fischer, F.D., Reprint of "Cracks in inhomogeneous materials: Comprehensive assessment using the configurational forces concept", Engineering Fracture Mechanics 77 (2010) 3611-3624. DOI: 10.1016/j.engfracmech.2010.10.010

(Kol2011) Kolednik O., Predan J., Fischer F.D., Fratzl P., Bioinspired Design Criteria for Damage-Resistant Materials with Periodically Varying Microstructure, Advanced Functional Materials 21 (2011) 3634-3641. DOI: 10.1002/adfm.201100443

(Kol2012) Kolednik, O., Fracture mechanics. In: Nicolais L, Borzacchiello A (eds) Wiley Encyclopedia of Composites, 2nd ed., John Wiley & Sons, Hoboken, New Jersey, USA (2012) pp 1126–1141. DOI: 10.1002/9781118097298.weoc096

(Kol2014) Kolednik, O.; Predan, J.; Fischer, F. D.; Fratzl, P., Improvements of strength and fracture resistance by spatial material property variations. Acta Materialia 68 (2014) 279-294. DOI: 10.1016/j.actamat.2014.01.034

(Kol2016) Kolednik, O.; Zechner, J.; Predan, J., Improvement of fatigue life by compliant and soft interlayers, Scripta Materialia 113 (2016) 1-5. DOI: 10.1016/j.scriptamat.2015.10.021

(Lee2007) Lee, J.J.W, Lloyd, I.K., Chai, H., Jung, Y.G., Lawn, B.R., Arrest, deflection, penetration and reinitiation of cracks in brittle layers across adhesive interlayers, Acta Materialia 55 (2007) 5859–5866. DOI: 10.1016/j.actamat.2007.06.038

(Les1996) Lesuer, D.R.; Syn, C.K.; Sherby, O.D.; Wadsworth, J.; Lewandowski, J.J.; Hunt, W.H., Mechanical behaviour of laminated metal composites, International Materials Reviews 41 (1996), issue 5, 169-197. DOI: 10.1179/imr.1996.41.5.169

(Li2008) Li, L.,. Nagai, K., Yin, F., Progress in cold roll bonding of metals, Science and Technology of Advanced Materials 9 (2008) 1-11. DOI: 10.1088/1468-6996/9/2/023001

(Li2011) Li, Long; Yin, Fu Xing; Nagai, Kotobu, Progress of Laminated Materials and Clad Steels Production, Materials Science Forum 675-677 (2011) 439-447. DOI: 10.4028/www.scientific.net/MSF.675-677.439

(Mau1993) Maugin G.A., Material Inhomogenieties in Elasticity. Chapman and Hall, London (1993)

(Mau1995) Maugin G.A, Material forces: concepts and applications. ASME Appl. Mech. Rev. 48 (1995) 213-245. DOI: 10.1115/1.3005101

(Mau2011) Maugin G.A., Configurational Forces: Thermomechanics, Physics, Mathematics, and Numerics. CRC Press, Boca Raton (2011)

(McE1962) McEwan K.J., Milner D.R., Pressure Welding of Dissimilar Metals, British Welding Journal 9 (1962) 406-420

(Mil1962) Milner, D.R., Rowe, G.W., Fundamentals of Solid Phase Welding, Metallurgical Reviews 7 (1962) 433-480. DOI: 10.1179/mtlr.1962.7.1.433

(Moh1975) Mohamed, H.A; Washburn, J., Mechanism of solid state pressure welding, Welding Journal 54 (1975) 302-310.

(Mor2013) Mori, K.I., Bay, N., Fratini, L., Micari, F., Tekkaya, A.E., Joining by plastic deformation, CIRP Annals - Manufacturing Technology 62 (2013) 673-694. DOI: 10.1016/j.cirp.2013.05.004

(Moz2010) Mozaffari, A.; Danesh Manesh, H.; Janghorban, K., Evaluation of mechanical properties and structure of multilayered Al/Ni composites produced by accumulative roll bonding (ARB) process, Journal of Alloys and Compounds 489 (2010) 103-109. DOI: 10.1016/j.jallcom.2009.09.022

(Mul2002) Müller R., Kolling S., Gross D., On configurational forces in the context of the finite element method. International Journal for Numerical Methods in Engineering 53 (2002) 1557-1574. DOI: 10.1002/nme.351

(Mul2004) Müller R., Gross D., Maugin G., Use of material forces in adaptive finite element methods. Computational Mechanics 33 (2004) 421-434. DOI: 10.1007/s00466-003-0543-z

(Mur1987) Murakami, Y., Stress intensity factors handbook. New York: Pergamon Press (1987)

(Mur2011) Murali, P., Bhandakkar, T.K.; Cheah, W. Li; Jhon, M.H.; Gao, H.; Ahluwalia, R., Role of modulus mismatch on crack propagation and toughness enhancement in bioinspired composites, Physical Review E 84 (2011). DOI: 10.1103/PhysRevE.84.015102

(Nak1988) Nakamura, T., Kondo, K., Sasahara, H., Nakamura, K., Research on pressure welding conditions of various work metals. Effects of contact pressure, surface expansion ratio and temperature, JSME International Journal Series III: Vibration, control engineering, engineering for industry (1988) 612-617. DOI: 10.1299/jsmec1988.31.612

(Par1953) Parks J.M., Recrystallization in welding, Welding Journal Research Supplement 32 (1953) 209-221

(Par1977) Parks, D.M., The virtual crack extension method for nonlinear material behavior, Computer Methods in Applied Mechanics and Engineering 12 (1977) 353-364. DOI: 10.1016/0045-7825(77)90023-8

(Par2014) Parab, N.D., Chen, W.W., Crack Propagation Through Interfaces in a Borosilicate Glass and a Glass Ceramic, International Journal of Applied Glass Science 5 (2014) 353–362. DOI: 10.1111/ijag.12093

(Raj2010) Rajan, T.P.D.; Pillai, R. M.; Pai, B. C., Characterization of centrifugal cast functionally graded aluminum-silicon carbide metal matrix composites, Materials Characterization 61 (2010), issue 10, 923-928. DOI: 10.1016/j.matchar.2010.06.002

(Rat2013) Rathmayr, G.B., Bachmaier, A., Pippan, R., Development of a New Testing Procedure for Performing Tensile Tests on Specimens with Sub-Millimetre Dimensions. Journal of Testing and Evaluation 41 (2013) 635-646. DOI: 10.1520/JTE20120175

(Ric1968a) Rice, J.R., A Path Independent Integral and the Approximate Analysis of Strain Concentration by Notches and Cracks, Journal of Applied Mechanics, Vol. 35 (1968) 379-386. DOI: 10.1115/1.3601206

(Ric1968b) Rice, J.R., Rosengren, G.F., Plane Strain Deformation near a Crack Tip in a Power-Law Hardening Material, Journal of the Mechanics and Physics of Solids, Vol. 16 (1968) 1-12

(Rom1995) Romeo, A., Ballarini, R., A crack very close to a bimaterial interface. Journal of Applied Mechanics 62 (1995) 614-619. DOI: 10.1115/1.2895990

(Rom1997) Romeo, A., Ballarini, R., A cohesive zone model for cracks terminating at a bimaterial interface. International Journal of Solids and Structures 34 (1997) 1307-1326. DOI: 10.1016/S0020-7683(96)00144-8

(Ros1983) Rosenfield, A. R.; Shetty, D. K., Cleavage fracture of steel in the upper ductile-brittle transition region, Engineering Fracture Mechanics 17 (1983) 461-470. DOI: 10.1016/0013-7944(83)90042-5

(Sai1999) Saito, Y.; Utsunomiya, H.; Tsuji, N.; Sakai, T., Novel ultra-high straining process for bulk materials - development of the accumulative roll-bonding (ARB) process, Acta Materialia 47 (1999) 579-583. DOI: 10.1016/S1359-6454(98)00365-6

(Seg1977) Segal V.M., Patent of the USSR, No. 575892 (1977)

(Seg1995) Segal, V.M, Materials processing by simple shear, Materials Science and Engineering A 197 (1995) 157-164. DOI: 10.1016/0921-5093(95)09705-8

(Seg2003) Segurado, J.; González, C.; LLorca J., A numerical investigation of the effect of particle clustering on the mechanical properties of composites, Acta Materialia 51 (2003), 2355-2369

(Sem1961) Semenov A.P., The phenomenon of seizure and its investigation, Wear 4 (1961) 1-9. DOI: 10.1016/0043-1648(61)90236-8

(She1990) Sherby, O.D, Lee, S., Koch, R., Sumi, T., Wolfenstine, J., Multilayered Composites based on Ultrahigh carbon steel and brass. Materials and Manufacturing Processes 5 (1990) 363-376. DOI: 10.1080/10426919008953258

(Shi1991) Shih, C. Cracks on bimaterial interfaces: elasticity and plasticity aspects. Materials Science and Engineering A 143 (1991) 77-90. DOI: 10.1016/0921-5093(91)90727-5

(Sim2003) Simha, N.K; Fischer, F.D; Kolednik, O.; Chen, C.R, Inhomogeneity effects on the crack driving force in elastic and elastic-plastic materials, Journal of the Mechanics and Physics of Solids 51 (2003) 209-240. DOI: 10.1016/S0022-5096(02)00025-X

(Sim2005) Simha, N.K., Predan, J., Kolednik, O., Fischer, F.D., Shan, G.X.: Crack tip shielding or anti-shielding due to smooth and discontinuous material inhomogeneities. Int. J. Fracture 135 (2005) 73-93. DOI: 10.1007/s10704-005-3944-5

(Sis2014) Sistaninia, M.; Kolednik, O., Effect of a single soft interlayer on the crack driving force, Engineering Fracture Mechanics 130 (2014) 21-41. DOI: 10.1016/j.engfracmech.2014.02.026

(Sis2017) Sistaninia, M.; Kolednik, O., Improving strength and toughness of materials by utilizing spatial variations of the yield stress, Acta Materialia 122 (2017) 207-219. DOI: 10.1016/j.actamat.2016.09.044

(Sis2018) Sistaninia, M.; Kasberger, R.; Kolednik, O., To the design of highly fracture-resistant composites by the application of the yield stress inhomogeneity effect, Composite Structures 185 (2018) 113-122. DOI: 10.1016/j.compstruct.2017.10.081

(Spi2009a) Spittel, M., Spittel, T., Flow stress of steel. In: Martienssen, Warlimont (Ed.), Metal Forming Data of Ferrous Alloys - deformation behaviour (2009) 23-56. DOI: 10.1007/978-3-540-44760-3_3

(Spi2009b) Spittel, M., Spittel, T., Steel symbol/number: DC04/1.0338. In: Martienssen, Warlimont (Ed.), Metal Forming Data of Ferrous Alloys - deformation behaviour (2009) 162-167. DOI: 10.1007/978-3-540-44760-3_18

(Sri2013) Srinivas, M.; Kamat, S. V., Effect of strain rate on fracture toughness of mild steel, Materials Science and Technology 17 (2013) 529-535. DOI: 10.1179/026708301101510375

(Sta1996a) Stampfl, J., Scherer, S., Berchthaler, M., Gruber, M., Kolednik, O., Determination of the fracture toughness by automatic image processing, International Journal of Fracture 78 (1996) 35-44.

(Sta1996b) Stampfl, J., Scherer, S., Gruber, M., Kolednik, O., Reconstruction of surface topographies by scanning electron microscopy for application in fracture research, Applied Physics A: Materials Science and Processing 63 (1996) 341-346.

(Sug1995) Sugimura, Y., Lim, P.G., Shih, C. F., Suresh, S. Fracture Normal to a Bimaterial Interface: Effects of Plasticity on Crack-Tip Shielding and Amplification. Acta Metallurgica et Materialia 43 (1995) 1157-1169. DOI: 10.1016/0956-7151(94)00295-S

(Tad1985) Tada, H., Paris, P.C., Irwin, G.R., The stress analysis of cracks handbook. St. Louis: Paris Productions Inc (1985)

(The1981) Theocaris, P. S.; Milios, J., Crack-arrest at a bimaterial interface, International Journal of Solids and Structures 17 (1981) 217–230. DOI: 10.1016/0020-7683(81)90077-9

(Vai1959) Vaidyanath L.R., Nicholas M.G., Miler D.R., Pressure Welding by Rolling, British Welding Journal 6 (1959) 13-28

(Wad2000) Wadsworth, J., Lesuer, D.R., Ancient and modern laminated composites - from the Great Pyramid of Gizeh to Y2K, Materials Characterization 45 (2000) 289-313. DOI: 10.1016/S1044-5803(00)00077-2

(Wan1997) Wang, G. Z.; Chen, J. H.; Li, Z. H., Further study on the mechanism of the ductile-to-brittle fracture transition in C-Mn base and weld steel, Metallurgical and Materials Transactions A 28 (1997) 1689-1698. DOI: 10.1007/s11661-997-0260-x

(Wan2000) Wang, T., Stähle, P. Stress state in front of a crack perpendicular to bimaterial interface. Acta Materialia 48 (2000) 4021-4033. DOI: 10.1016/S0013-7944(97)00150-1

(Web2013) Weber, R.P, Chawla, K.K, Miguez Suarez, J.C, Influence of notch orientation and temperature on the impact behavior of a dual hardness steel composite, Materials Science and Engineering: A 580 (2013) 279-287. DOI: 10.1016/j.msea.2013.05.026

(Wel1961) Wells, A.A., Unstable Crack Propagation in Metals: Cleavage and Fast Fracture, Proceedings of the Crack Propagation Symposium, Vol. 1, Paper 84, Cranfield, UK (1961)

(Wes1939) Westergaard H.M., Bearing Pressures and Cracks. Journal of Applied Mechanics, Vol. 6 (1939) 49-53

(Wil1957) Williams M.L., On the Stress Distribution at the Base of a Stationary Crack. Journal of Applied Mechanics, Vol. 24 (1957) 109-114

(Woe2006) Woesz, A., Weaver, J.C., Kazanci, M., Dauphin, Y., Aizenberg, J., Morse, D.E., Fratzl, P., Micromechanical properties of biological silica in skeletons of deep-sea sponges. Journal of Materials Research 21 (2006) 2068-2078. DOI: 10.1557/jmr.2006.0251

(Wu2015) Wu, Y., Feng, B., Xin, Y., Hong, R., Yu, H., Liu, Q., Microstructure and mechanical behavior of a Mg AZ31/Al 7050 laminate composite fabricated by extrusion, Materials Science and Engineering: A 640 (2015) 454-459. DOI: 10.1016/j.msea.2015.05.094

(Xin2015) Xin, Y., Hong, R., Feng, B., Yu, H., Wu, Y., Liu, Q, Fabrication of Mg/Al multilayer plates using an accumulative extrusion bonding process, Materials Science and Engineering: A 640 (2015) 210-216. DOI: 10.1016/j.msea.2015.06.008

(Yin2013) Yin, F. X.; Li, L.; Tanaka, Y.; Kishimoto, S.; Nagai, K., Hot rolling bonded multilayered composite steels and varied tensile deformation behaviour, Materials Science and Technology 28 (2013) 783-787. DOI: 10.1179/1743284711Y.0000000116

(Yu2013) Yu, H., Lu, C., Tieu, A.K. et al., Fabrication of ultra-thin nanostructured bimetallic foils by Accumulative Roll Bonding and Asymmetric Rolling. Scientific Reports 3 (2013) DOI: 10.1038/srep02373

(Zak1963) Zak, A., Williams, M., Crack point singularities at a bi-material interface. Journal of Applied Mechanics 30 (1963) 142-143.

(Zeb2011) Zebardast, M.; Taheri, A. Karimi, The cold welding of copper to aluminum using equal channel angular extrusion (ECAE) process, Journal of Materials Processing Technology 211 (2011) 1034-1043. DOI: 10.1016/j.jmatprotec.2011.01.004

(Zec2013) Zechner, J.; Kolednik, O., Fracture resistance of aluminum multilayer composites, Engineering Fracture Mechanics 110 (2013) 489-500. DOI: 10.1016/j.engfracmech.2012.11.007

(Zha1997) Zhang, W., Bay, N., Cold Welding - Experimental Investigation of the Surface Preparation Methods, Welding Journal Research Supplement 76 (1997) 326-330